FABRICATION AND ELECTROCHEMICAL CHARACTERIZATION OF HIGHLY EFFICIENT HIERARCHICALLY ASSEMBLED HYBRID TWO-DIMENSIONAL NANOINTERFACES FOR ELECTROCHEMICAL BIOSENSING AND BIOELECTRONICS

By

RENU KUMARI

Student number: 201505302

Thesis in fulfilment of the requirement for the degree

PHILOSOPHIAE DOCTOR

In

CHEMISTRY

In the

FACULTY OF SCIENCE

Of the

UNIVERSITY OF JOHANNESBURG

Supervisor: PROF PENNY P GOVENDER

DECEMBER, 2018

To My Beloved Brother Sahab

PUBLICATIONS AND PRESENTATIONS:

Conference Presentations

- R. Kumari, P. P. Govender, Stimuli-encoded graphene bioelectronics for development of on/off-switchable super-thin biosensors, **Poster presentation**, CHPC National meeting, CSIR Pretoria, South Africa, 30 November - 04 December 2015.
- R. Kumari, A. O. Osikoya, W. W. Anku, S. K. Shukla, and P. P. Govender, Hierarchically assembled two-dimensional hybrid nanointerfaces: a platform for bioelectronic applications, **Oral Presentation,** Department of Applied Chemistry 3rd Annual Postgraduate Research Event, University of Johannesburg, South Africa, 11 -12 September 2018.

Peer-reviewed Publications

- R. Kumari, A. O. Osikoya, W. W. Anku, S. K. Shukla, and P. P. Govender, Hierarchically assembled two-dimensional hybrid nanointerfaces: a platform for bioelectronic applications, *Electroanalysis*, **30** (2018) 2339–2348.
- R. Kumari, A. O. Osikoya, F. Opoku, W. W. Anku, S. K. Shukla, and P. P. Govender, Hierarchically assembled two-dimensional gold-boron nitride-tungsten disulphide nanohybrid interface system for electrobiocatalytic applications, *Materials Chemistry and Physics* **226** (2019) 129-140.
- R. Kumari, A. O. Osikoya, W. W. Anku, S. K. Shukla, and P. P. Govender, Hierarchically assembled of CVD grown graphene on WS_2 and AuNPs: a two dimensional nanohybrid interface for detection of H_2O_2, *Materials Research Bulletin.* (Under review).

ACKNOWLEDGEMENTS

My doctoral thesis is completed and it was possible because of the efforts of several people. I would like to express my sincere gratitude to all of them.

First of all, I would like to express my special appreciation and thanks to my supervisor Prof. Penny Govender for giving me the opportunity to pursue my PhD, her continuous support throughout the duration of my PhD study and related research. I am grateful for her patience, motivation and immense knowledge. I could not have imagined having a better advisor and mentor for my PhD than her. She also helped me and made it possible for me to obtain some of the best fellowship grants (GES and NRF) in UJ.

A very special thank you to Dr. Sudheesh K. Shukla for his invaluable advice and feedback on my research, for always being so supportive of my work and for helping to complete all my administrative works during my initial days in the university.

This PhD is a life-changing experience for me and it would have not been possible to do without the support and guidance that I have received from Dr. Adeniyi O. Osikoya. His guidance helped me in all the time of research and writing of this thesis and helped me to formulate the work plan, data collection for research papers and share his valuable viewpoints on my research work.

I greatly appreciate the support received from Dr. William W. Anku for giving great suggestions and sharing his knowledge and experience which made an invaluable contribution to my PhD research.

I am indebted to all my group mates Dr. Samuel Oppong, Dr. Martin M. Magu, Mr. Francis Opoku, Mr. Ephraim Muriithi, Mr. Chijioke Peter, Mr. Ephraim Marondedze, Ms. Nokuthula Ndaba, Mr. Wahab Olaide, Mr. Seiso Tsoeu, Mr. Sechaba Manyedi, Mr. Nkonde Mxolisi and Mr. Bongani Simelane for their constant support.

I owe my thanks to other colleagues Mr. Eric Ngigi, Mr. Tarekegn Dolla, Dr. Prabhakaran, Ms. Koki, Ms. Gao, Dr. Lawal, Mr. Idris and Mr. Siyasanga who supported me during my lab work and instrument access in UJ.

I am also very grateful to Prof Patrick N'dungu and Prof Kaushik Mallick for granting access to their respective labs which helped me to finish my research work on time in UJ.

I wish to thanks to Ms. Leah, Ms. Dereshni, and Mr. Sifiso for all the administrative help and Ms. Dudu and Mr. Tshediso for fellowship-related works. I gratefully acknowledge funding received from the Faculty of Science, University of Johannesburg and National Research Foundation for their financial assistance for my PhD research.

My deep appreciation goes out to Dr. Mikael Syarjarvi and Dr. Reza Yazdi for providing full support and their contributions to my research work during my stay at Linkoping University, Sweden. I would also like to say a heartfelt thank you to Biosensors and Bioelectronics lab members who created a healthy atmosphere for working there.

I met many friends during this journey of PhD and my utmost gratitude goes to all my friends, especially Sandra, Niharika, Nishu, Maitrayee, Manav, Sachin, Tim, Sourbh, Samarjeet, Sajan, Neeraj, Niladri sir, Meeankshi Di, Priya Di, Fariba, Zainab, Luana, Ceylan, Azhar. They make my stay blissful in both countries.

A special thanks to my best friends Compesh, Rashmi, Ajay and Neel for always taking care of me and encouraging me to follow my dreams and constant encouragement throughout my PhD. I am also grateful to Udai sir who encouraged me to do PhD outside India and Manju for her consistent support.

A special thanks to my family, I am really grateful to my mother and father for all the sacrifices that they have made and their prayers, which helped me survive so far. Thank you for believing in me. At the end, I would also like to thank you my sisters and brothers, for their unconditional love which always motivated me to strive towards my goal. They also helped me in whatever way they could during this challenging period.

SHIVA, Thank you for everything.

ABSTRACT

Two dimensional (2D) materials have provided a new era to biosensors research. Biosensors are functional biodevices which include the integration of biology with electronics. The integration of 2D materials with other nanomaterials has transformed the understanding of the biological and electronics world and has paved a way for the design and fabrication of novel 2D nanointerfaces. The use of 2D nanointerfaces has given great success to biosensors and bioelectronics field which ultimately impacts on biomedical diagnosis and sensing applications. The superior properties of 2D materials such as large surface area, ease of hybridization, good biocompatibility, and high electron transfer properties make them ideal interface materials for the design and fabrication of bioelectronic devices including biosensors.

The thesis focused on the fabrication of 2D nanointerfaces by combining two 2D hybrid materials and then nanostructuring with metal nanoparticles for better electron transfer within the interface which is followed by immobilization of enzyme as a bio-recognition element for biosensing purposes. The conjugation of the 2D hybrid nanointerface materials was achieved through the self-assembly technique.

Cyclic voltammetry (CV) and electrochemical impedance spectroscopy (EIS) were used in the study for characterization of the 2D hybrid nanointerface structures and chronoamperometry studies were employed to investigate the electrobiocatalytic properties of the 2D hybrid nanointerfaces structures. Structural characterization was done by using X-ray diffraction (XRD), transmission electron microscopy (TEM) and scanning electron microscopy (SEM) techniques for morphological details of 2D hybrid nanointerfaces structures. The fabrication of bioelectrodes was achieved by using the conjugated 2D hybrid nanointerface materials.

There are three different segments in this research study. All of these different segments involved the use of 2D materials for bioelectronics purposes.

The first phase involved the fabrication of smart hierarchically self-assembled 2D electrobiocatalytic interface system based on the combination of gold nanoparticles (AuNPs) doped graphene oxide (GO)-molybdenum disulfide (MoS_2) layered nanohybrid, conjugated with poly (N-isopropylacrylamide, PNIPAAm) resulting in GO/AuNPs/MoS_2/PNIPAAm interface. The introduction of PNIPAAm improved the stability of the self-assembled GO/AuNPs/MoS_2 interface structure.

Horseradish peroxidase (HRP) was subsequently immobilized on the GO/AuNPs/MoS_2/PNIPAAm interface through electrostatic interactions giving GO/AuNPs/MoS_2/PNIPAAm/Peroxidase electrobiocatalytic interface system as a platform for electrobiocatalysis reactions for biosensing applications. Morphological characterization of GO/AuNPs/MoS_2/PNIPAAm indicates that this 2D nanointerface structure has a wide surface area for enzyme immobilization due to their flake-like structure. CV showed diffusion-controlled electron transfer properties at the interface. The electrobiocatalytic activity of the nanohybrid interface structure was studied using hydrogen peroxide (H_2O_2) as a model analyte. The fabricated bioelectrode exhibits a wide linear response to the detection of H_2O_2 from 1.57 to 11.33 mM, with a detection limit of 3.34 mM (S/N=3) and a capacitance of 8.6 F/cm^2.

The second phase of the study involved the fabrication of hybrid dual 2D-nanohybrid structure through self-assembly combination AuNPs with hybrid 2D materials consisting of boron nitride (BN) and tungsten disulphide (WS_2) as a nanointerface system for electrochemical biosensing. HRP was immobilized on the hybrid dual 2D-nanoparticle systems to form a biointerface. Structural characterization showed high crystallinity in the fabricated structure, while morphological characterization confirmed

the high surface to volume area of the hybrid material and the presence of well-dispersed AuNPs. Electrochemical characterization also confirmed that the fabricated HRP/BN/WS_2/AuNPs/GC bioelectrode exhibited excellent electron transfer properties at the interface. The electrobiocatalytic activity of the nanohybrid interface structure was studied using H_2O_2 as a model analyte. The fabricated bioelectrode exhibited a wide linear range from 0.15 mM to 15.01 mM towards detection of H_2O_2 with a limit of detection of 3.0 mM (S/N = 3) and a sensitivity of 19.16 µA/mM/cm^2.

Theoretical studies of the BN/Au/WS_2(001) nanohybrid structure was carried out using density functional theory (DFT) calculation for confirming the charge transport mobility and conductivity of the fabricated material. DFT calculations combined with the experimental studies showed that the self-assembled combination of the BN/Au/WS_2(001) nanocomposite enhances the performance of the fabricated biosensor due to an introduced new electronic state emanating from the N 2p orbital.

The third phase of the study involved the synthesis of acetylene sourced graphene (Gr) by chemical vapour deposition (CVD) method. Self-assembly method was used to prepare the 2D nanohybrid interfaces, which consist of Gr, WS_2, AuNPs and HRP for fabricating electrochemical biosensor for detection of H_2O_2. The XRD results revealed that Gr/WS_2/AuNPs nanohybrid structure has good crystalline nature. CV and electrochemical impedance spectroscopy results showed that due to the incorporation of AuNPs, the redox properties of Gr/WS_2/AuNPs/HRP conjugate 2D hybrid structure improved in comparison to Gr/WS_2/HRP. The same trend was observed in the chronoamperometric results. The Gr/WS_2/AuNPs/HRP/GCE modified bioelectrode exhibited a good electrobiocatalytic performance towards the detection of H_2O_2 over a relatively wider linear range (0.40 mM to 23 mM), with a higher

sensitivity (11.07 µA/mM/cm^2) than that of Gr/WS_2/HRP/GCE modified bioelectrode (9.23 µA/mM/cm^2). The results have shown that electrobiocatalytic reactions can be controlled by modifying the nanohybrid interfaces.

TABLE OF CONTENTS

Section ***Page***

AFFIDAVIT ..... **ii**

DEDICATION ..... **iii**

PUBLICATIONS AND PRESENTATIONS: ..... **iv**

ACKNOWLEDGEMENTS ..... **v**

ABSTRACT ..... **viii**

TABLE OF CONTENTS ..... **xii**

LIST OF FIGURES ..... **xviii**

LIST OF TABLES ..... **xxv**

LIST OF SCHEMES ..... **xxvi**

LIST OF ABBREVIATIONS ..... **xxvii**

CHAPTER 1: INTRODUCTION **1**

1.1 BACKGROUND AND MOTIVATION 1

1.2 PROBLEM STATEMENT 8

1.3 JUSTIFICATION 9

1.4 AIM AND OBJECTIVES 10

1.4.1 Aim 10

1.4.2 Objectives 10

1.5 OUTLINE OF THE THESIS 11

1.6 REFERENCES 13

CHAPTER 2: LITERATURE REVIEW **23**

2.1 INTRODUCTION 23

2.2 BIOSENSORS 24

2.2.1 Types of biosensor/classification of biosensors 25
2.2.1.1 Classification based on bio-recognition elements used 26
2.2.1.1.1 Enzyme-based biosensors..... 26
2.2.1.1.2 Microbe/cell-based biosensors..... 27
2.2.1.1.3 Immunosensors/antigen-antibody based biosensors 28
2.2.1.1.4 Aptamers (synthetic oligonucleotides) based biosensor 28
2.2.1.1.5 DNA/Nucleic acid base biosensors 29
2.2.1.2 Classification based on signal transduction mechanism 30
2.2.1.2.1 Optical biosensors 30
2.2.1.2.2 Magnetic biosensors 30
2.2.1.2.3 Thermal/calorimetric detection biosensors..... 31
2.2.1.2.4 Piezoelectric/mechanical detection biosensors..... 32
2.2.1.2.5 Resonance detection biosensors 32
2.2.1.2.6 Ion-sensitive FET (ISFET) detection biosensors..... 33
2.2.1.2.7 Electrochemical biosensors 33
2.3 APPLICATIONS OF BIOSENSORS 36
2.4 PROBLEMS/CONCERNS OF BIOSENSOR EFFECTIVENESS 37
2.5 TWO DIMENSIONAL MATERIALS..... 38
2.5.1 Classification of 2D materials..... 40
2.5.1.1 2D layered inorganic nanomaterials (2D-LINs) 40
2.5.1.2 2D layered ionic solids 41
2.5.1.3 Graphene..... 41
2.5.2 Application of 2D materials in biosensing 43
2.5.2.1 Application of graphene and graphene-related materials in biosensing ……43
2.5.2.1.1 Application of graphene in biosensing 43
2.5.2.1.2 Application of graphene oxide in biosensing..... 45
2.5.2.1.3 Application of reduced graphene oxide in biosensing 46
2.5.2.2 Application of non-graphene 2D materials in biosensing 48
2.5.2.2.1 Application of molybdenum disulphide in biosensing..... 48
2.5.2.2.2 Application of tungsten disulphide in biosensing..... 52
2.5.2.2.3 Application of boron nitride in biosensing..... 56
2.6 ELECTROCHEMICAL TECHNIQUES 58
2.6.1 Overview of Electrode Processes 58

2.6.1.1 Electrochemical cells and reactions 59
2.6.1.2 Faradaic and non-faradaic processes 61
2.6.1.3 Electrode processes 62
2.6.1.4 Electrical Double Layer 64
2.6.2 VOLTAMMETRIC TECHNIQUES 67
2.6.2.1 Potential Step Voltammetry 67
2.6.2.2 Linear Sweep Voltammetry 68
2.6.2.3 Differential Pulse Voltammetry 70
2.6.2.4 Square Wave Voltammetry 70
2.6.2.5 Cyclic Voltammetry 71
2.6.2.5.1 Importance of the scan rate 74
2.6.3 CHRONOAMPEROMETRY TECHNIQUES 75
2.6.3.1 Chronoamperometry: Application 77
2.6.3.1.1 From Cottrell equation 77
2.6.3.1.2 Analytical performance of sensors 77
2.6.3.1.2.1 Sensitivity 78
2.6.3.1.2.2 Limit of Detection 79
2.6.3.1.2.3 Linear and dynamic range 79
2.6.3.1.2.4 Response time 79
2.6.4 ELECTROCHEMICAL IMPEDANCE SPECTROSCOPY 79
2.7 REFERENCES 85

CHAPTER 3: EXPERIMENTAL METHODOLOGY 104

3.1 INTRODUCTION 104
3.2 CHEMICALS AND MATERIALS 104
3.3 RESEARCH SCHEME 108
3.4 FABRICATION OF 2D BASED HIERARCHICALLY SELF-ASSEMBLED NANOHYBRID STRUCTURES 109
3.4.1 Preparation of GO/AuNPs/MoS_2/PNIPAAm/Peroxidase nanohybrid Interface structures 109
3.4.2 Fabrication of bioelectrodes 110
3.4.3 FABRICATION OF BN/WS_2/AuNPs/HRP NANOHYBRID 111

3.4.4 Preparation of BN/WS_2/AuNPs/HRP nanohybrid Interface structures INTERFACE STRUCTURES…….. 112
3.4.5 Preparation of modified bioelectrodes..... 113
3.4.6 Theoretical studies of BN/Au/WS_2 (001) nanohybrid structure..... 115
3.5 FABRICATION OF Gr/WS_2/AuNPs/HRP NANOHYBRID INTERFACE STRUCTURES…….. 115
3.5.1 Preparation of Gr/WS_2/AuNPs/HRP nanohybrid Interface structures ……116
3.5.1.1 Preparation of CVD-synthesized graphene..... 116
3.5.1.2 Preparation of Gr/WS_2/AuNPs/HRP nanohybrid Interface structures 117
3.5.1.3 Preparation of bioelectrodes 118
3.6 ELECTROCHEMICAL CHARACTERIZATIONS..... 120
3.6.1 Experimental set-up for the electrochemical experiment 120
3.6.1.1 Electrochemical cell and electrodes..... 120
3.6.1.2 Working electrode 120
3.6.1.3 Reference electrode..... 121
3.6.1.4 Counter electrode 122
3.6.1.5 Supporting electrolyte 122
3.6.2 Cyclic voltammetry experiment and solution preparation..... 122
3.6.2.1 Buffer solution preparation: 10mM phosphate buffer saline (PBS) 124
3.6.2.2 Preparation 10mM Ferri/Ferro cyanide 124
3.6.3 Analyte sensing..... 124
3.6.4 Analytical performance 125
3.7 MATERIALS CHARACTERIZATION 125
3.7.1 X-Ray Diffraction..... 125
3.7.1.1 Principle of XRD analysis..... 125
3.7.2 Transmission Electron Microscopy 127
3.7.3 Scanning Electron Microscopy..... 130
3.8 REFERENCES 132

CHAPTER 4: HIERARCHICALLY ASSEMBLED TWO-DIMENSIONAL HYBRID NANOINTERFACES: A PLATFORM FOR BIOELECTRONIC APPLICATIONS . 134

4.1 INTRODUCTION 134
4.2 EXPERIMENTAL 137
4.2.1 Characterizations 137
4.2.2 Preparation of monohybrid electrobiocatalytic interfaces structures ……..137
4.2.3 Fabrication of bioelectrodes 138
4.3 RESULTS AND DISCUSSION..... 138
4.4 SUB-CONCLUSION 156
4.5 REFERENCES 158

APPENDIX A1……..... 164

CHAPTER 5: HIERARCHICALLY ASSEMBLED TWO-DIMENSIONAL GOLD-BORON NITRIDE-TUNGSTEN DISULPHIDE NANOHYBRID INTERFACE SYSTEM FOR ELECTROCATALYTIC APPLICATIONS 168

5.1 INTRODUCTION 168
5.2 EXPERIMENTAL 171
5.2.1 Fabrication of BN/WS_2/AuNPs/HRP nanohybrid structure 171
5.2.2 Preparation of modified bioelectrodes..... 171
5.2.3 Computational details 171
5.3 RESULTS AND DISCUSSION..... 171
5.3.1 Theoretical studies..... 172
5.3.1.1 Theoretical calculation for the stability of BN/WS_2/AuNPs 172
5.3.1.2 Electronic properties 175
5.3.1.3 Density of State..... 177
5.3.1.4 Charge transfer and mechanism analysis..... 180
5.3.1.5 Work function..... 181
5.3.2 Materials characterization 183
5.3.3 Electrochemical behaviour of the modified bioelectrodes 185

5.3.4 Electrocatalysis of H_2O_2 at BN/WS_2/AuNPs/HRP/GCE 191
5.4 SUB-CONCLUSION 193
5.5 REFERENCES 195

Appendix A2…….. 202

CHAPTER 6: CVD GROWN GRAPHENE ON WS2 AND AuNPs: A TWO-DIMENSIONAL NANOHYBRID INTERFACE FOR DETECTION OF H2O2 203

6.1 INTRODUCTION 203
6.2 EXPERIMENTAL 207
6.2.1 Apparatus 207
6.2.2 Preparation of CVD-synthesized Graphene 207
6.2.3 Fabrication of graphene-WS_2-enzyme self-assembled nanohybrid structures ……207
6.2.4 Preparation of modified bioelectrodes..... 208
6.3 RESULTS AND DISCUSSION..... 208
6.4 SUB-CONCLUSION 216
6.5 REFERENCES 218

APPENDIX A3……..... 226

CHAPTER 7: CONCLUSION AND FUTURE PERSPECTIVES 227

LIST OF FIGURES

Figure	***Description***	***Page***
Figure 1.1	Scheme presentation of different components of a biosensor..	2
Figure 1. 2	Classification of biosensors.	3
Figure 2.1	Schematic diagram of a biosensor showing (a) biocatalyst, (b) transducer, (c) amplified output from the transducer, (d) processed signal and (e) displayed readable result	25
Figure 2.2	Different classifications of biosensors	26
Figure 2.3	The 2D materials library	39
Figure 2.4	Structure of graphene	42
Figure 2.5	(a) Schematic representation (b) capacitance (%) response on the graphene biosensor chip surface.	44
Figure 2.6	Preparation of the Hemin-graphene nanosheets/AuNP/GCE biosensor for the detection of hydrogen peroxide.	45
Figure 2.7	Schematic of the GO deposition on fiber optic sensor surface.	46
Figure 2.8	(a) Schematic diagram for the immobilization of Lac/AP-rGOs/Chit/GCE (b) current-time response of Lac/AP-rGOs/Chit/GCE of hydroquinone and catechol	47
Figure 2.9	Schematic diagram of the porphyrin graphene-based peptide sensor for cyclin A_2 detection	48
Figure 2.10	(a) Top view and (b) side view of the structure of MoS_2.....	49
Figure 2. 11	(a) Schematic diagram of experimental procedure for the preparation of anti-PSA on MoS_2 surface with PSA and (b) a pseudo double gate structure of a MoS_2 biosensor.	50
Figure 2. 12	(a) Schematic of a MoS_2 biosensor illustrating PSA antibody with the binding of PSA antigen with antibody receptors. (b) transfer characteristics of MoS_2 biosensor functionalized by anti-PSA under various PSA concentrations	51

Figure 2.13 Electrochemical characterization (a) cyclic voltammetry of AgNPs and AgNPs/MoS_2 electrodes at a scan rate of 0.1 V. s^{-1} (b) square wave voltammetry (SWV) curves of the AgNPs/MoS_2 electrode containing different concentration of glucose (c) the calibration curves (concentration vs current) of the biosensor. 52

Figure 2.14 (a) Top view and (b) side view of the structure of WS_2. 53

Figure 2.15 Schematic illustration of the electrochemical sensing for the detection of ATP or Hg^+ 54

Figure 2.16 (a) Schematic representation of the construction of GTA/Hb/1T-WS_2/GC electrode (not to scale) (b) cyclic voltammograms of ferri/ferrocyanide redox probe at various modified electrodes at scan rate 100 mVs^{-1} (c) chronoamperometric responses of the GTA/Hb/1T-WS_2/GC upon successive additions H_2O_2 (d) logarithmic relationship between the concentration of H_2O_2 and the catalytic current of the GTA/Hb/1T-WS_2/GC 55

Figure 2.17 Structure of BN. 56

Figure 2.18 (a) Illustration of the synthesis of AuNPs/BNS nanocomposites (b) cyclic voltammograms of different modified electrodes 0.1 M PBS at pH 7.4 in the presence of 10.0 mM H_2O_2 at scan rate 50 mV s^{-1} (c) chronoamperometry response of AuNPs/BNS/GCE to successive addition of H_2O_2 into PBS under stirring (The insert is the calibration curve) 57

Figure 2.19 The schematic representation of electrode processes. 63

Figure 2.20 A schematic diagram of a typical model of the double-layer region between the solution and metal with the negatively charged surface where x is the distance and ϕ is the inner potential 66

Figure 2.21 A schematic illustration of (a) potential step (b) corresponding current in potential step voltammetry 68

Figure 2.22 (a) Linear sweep voltammetry potential step (b) current response …. 69

Figure 2.23 (a) Schematic representation of potential sweep (b) corresponding current response in cyclic voltammetry. 71

Figure 2.24 Principle of chronoamperometry (a) change of potential with changing time and (b) resulting current response 77

Figure 2.25 (a) Illustration of a typical amperometric sensor response (b) Calibration plot showing the linear range, the dynamic range, and other relevant analytical useful parameters 78

Figure 2.26 (a) Nyquist plot (b) Randles equivalent circuit of a simple electrochemical system 83

Figure 3.1 Flow chart of Research Scheme 108

Figure 3.2 Schematic representation of the synthesis procedure of GO/AuNPs/MoS_2/PNIPAAm/Peroxidase nanohybrid interface structure. 111

Figure 3.3 Schematic representation of the fabrication procedure of BN/WS_2/AuNPs/HRP nanohybrid interface structure. 114

Figure 3.4 Schematic of the synthesis of graphene using CVD process. (Note: Image not drawn to scale) 117

Figure 3.5 Schematic representation of the synthesis procedure of fabricating Gr/WS_2/AuNPs/HRP nanohybrid interfaces. 119

Figure 3.6 Image of the electrochemical cell used in this study. 120

Figure 3.8 Images of reference electrodes (Ag/AgCl) used in this project. 121

Figure 3.9 Image of the counter electrode used in this study. 122

Figure 3.10 Typical electrochemical set up used in this study involving the three electrode cell system and Iviumstat potentiostat. 123

Figure 3.11 (a) Schematic representation of X-ray diffractometer (b) image of Shimadzu XD-3A X-ray diffractometer used in the project. 126

Figure 3.12 Schematic diagram showing the interaction of electrons with specimen 128

Figure 3.13 (a) A schematic diagram describing the path of an electron beam in a TEM (b) Image of installed JEOL (JEM-2100). 129

Figure 3.14 (a) TEM sample support mesh grid, and (b) a sample holder with vacuum rings..... 129

Figure 3.15 (a) Schematic diagram of SEM (b) Image of installed LEO 155 Gemini. 131

Figure 4.1 (a) Raman spectrum of the graphene oxide, (b) zeta potential measurement of the dispersed interface material in deionized water at pH 4–10, (c) AFM image of the dispersed graphene oxide on gold substrate, (d) AFM height profile distribution analysis spectra of the dispersed graphene oxide on gold substrate. 142

Figure 4.2 Morphological characterization of 2D-hetero hierarchically 3D self-assembled hybrid interfaces: SEM images of (a) AuNPs doped layered GO/MoS_2 2D nano-hetero interfaces and the inset shows AFM image of AuNPs doped layered GO/MoS_2 nano-heterostructures and (b) GO-AuNPs-MoS_2-PNIPAAm-Peroxidase bioelectrode. 143

Figure 4.3 Bioelectrode characterization showing (a) cyclic voltammetry response at 50 mV/s in 10 mM PBS and 10 mM $[Fe(CN)_6]^{3-/4-}$ for the bare GC and all modified electrodes; (b) effect of scan rate on the cathodic peak current I_{pc} and the anodic peak current I_{pa} ; (c) EIS Nyquist plot with Randles circuit equivalent diagram as an inset, and (d) charge transfer impedance histogram for the EIS. 145

Figure 4.4 Chronoamperometric response showing (a) current-time plot and (b) calibration curve response for the fabricated GO-AuNPs-MoS_2-PNIPAAm-Peroxidase bioelectrode and (c) current-time plot and (d) calibration curve response for the fabricated GO-AuNPs-MoS_2-Peroxidase at an applied potential of +0.6 V in 100 mM PBS. 152

Figure 4.5 Electrochemical performance of GO-AuNPs-MoS_2-PNIPAAm-Peroxidase bioelectrode showing areal capacitance vs potential (V) vs Ag/AgCl at scan rate 50 mV/s in 10 mM $[Fe(CN)_6]^{3-/4-}$ 156

Figure A1.1 TEM images of GO (a & b); SEM images of GO (c & d) 164

Figure A1.2 TEM images of MoS_2 nanosheets with different magnifications (a-d). 165

Figure A1.3 TEM images of MoS_2/AuNPs nanosheets with different magnifications (a-d). 166

Figure A1.4 Cyclic voltammetry response showing the effect of scan rates on the cathodic peak I_{pc}, and the anodic peak I_{pa}, in 10 mM PBS and 10 mM KCl and 10 mM $[Fe(CN)_6]^{3-/4-}$ vs Ag/AgCl reference electrode for (a) Bare GCE; (b) GO-MoS_2/GCE; (c) GO-Au-MoS_2/GCE; (d) GO-Au-MoS_2-PNIPAAM/GCE; (e) GO-Au-MoS_2-Peroxidase/GCE and (f) GO-Au-MoS_2-PNIPAAM-Peroxidase/GCE respectively. 167

Figure 5.1 The side view of the optimized structure of (a) Au/WS_2(001) and (b) BN/Au/WS_2(001) nanohybrid structure. 173

Figure 5.2 Calculated band structures of (a) WS_2 monolayer, (b) WS_2 (001), (c) pure Au, (d) Au(001), (e) BN sheet, (f) BN(001), (g) Au/WS_2(001) and (h) BN/Au/WS_2(001) nanohybrid structure. 175

Figure 5.3 Calculated PDOS of (a) WS_2 monolayer, (b) WS_2(001), (c) pure Au, (d) Au(001), (e) BN sheet, (f) BN(001), (g) Au/WS_2(001) and (h) BN/Au/WS_2(001) nanohybrid structure. 178

Figure 5.4 The charge density distribution plots of the HOL (a_1, a_2) and LUL (b_1, b_2) for the Au/WS_2(001) and BN/Au/WS_2(001) nanohybrid structure. The isovalue is 0.04 e $Å^{-3}$. 179

Figure 5.5 The 3D charge density difference of (a) Au/WS_2(001) and (b) BN/Au/WS_2(001) nanohybrid structure with an isovalue of 0.008 e $Å^{-3}$. 180

Figure 5.6 The calculated electrostatic potential of (a) WS_2(001), (b) Au(001), (c) BN(001), (d) Au/WS_2(001) and (e) BN/Au/WS_2(001) nanohybrid structure. 182

Figure 5.7 (a) TEM image of the BN/WS_2 hybrid structure, (b) TEM image of BN/WS_2/AuNPs nanohybrid structure, (c) SEM image of the BN/WS_2 2D hybrid structure and (d) XRD spectra for BN/WS_2 and BN/WS_2/AuNPs nanointerfaces structure. 185

Figure 5.8 Bioelectrode characterization showing (a) cyclic voltammetry response at 50 mV/s in 10 mM PBS and 10 mM $[Fe(CN)_6]^{3-/4-}$ for the bare GC and all modified electrodes; (b) effect of scan rate on the cathodic peak current I_{pc} and the anodic peak current I_{pa} ; (c) EIS Nyquist plot with Randles circuit equivalent diagram as inset, and (d) charge transfer impedance histogram for the EIS. 188

Figure 5.9 Chronoamperometry response showing current-time plot at an applied potential of + 0.6 V in 10 mM PBS and calibration curve for the chronoamperometric response for fabricated BN/WS_2/AuNPs/HRP/GCE (a & b) and BN/WS_2/AuNPs/GCE (c & d) nanohybrid structure. 192

Figure A2.1 Cyclic voltammetry response showing the effect of scan rates on the cathodic peak I_{pc}, and the anodic peak I_{pa}, in 10 mM PBS and 10 mM KCl and 10 mM $[Fe(CN)_6]^{3-/4-}$ vs Ag/AgCl reference electrode for (a) Bare GC electrode; (b) BN/WS_2/GCE; (c) BN/WS_2/AuNPs/GCE; (d) BN/WS_2/AuNPs/HRP/GCE respectively. 202

Figure 6.1 XRD spectra for Gr/WS_2/AuNPs nanointerface structure where * and # denote WS_2 and Gr peaks respectively..... 209

Figure 6.2 Bioelectrode characterization showing (I) CV responses ; (II) The effect of scan rates on the cathodic (I_{pc}) and anodic peaks (I_{pa}) of bare and all modified electrodes at 50 mV/s vs. Ag/AgCl reference electrode in 5 mM $[Fe(CN)_6]^{3-/4-}$ containing 0.1 M PBS and 0.1 M KCl. 210

Figure 6.3 EIS's Nyquist plots for the bare GC and all modified electrodes at 50 mV/s vs. Ag/AgCl reference electrode in 5 mM $[Fe(CN)_6]^{3-/4-}$ containing 0.1 M PBS and 0.1 M KCl. The inset is the equivalent of Randles circuit which is used to fit the data. 212

Figure 6.4 Chronoamperometry response showing current-time plot at an applied potential of +0.7 V in 0.1 M PBS and 0.1 M KCl and calibration curve for the chronoamperometric response for fabricated

Gr/HRP/GCE (a1, a2), Gr/WS_2/HRP/GCE (b1, b2) and Gr/WS_2/AuNPs/HRP/GCE (c1, c2) nanohybrid structures. 216

Figure A3.1 Cyclic voltammetry response showing the effect of scan rates on the cathodic peak I_{pc}, and the anodic peak I_{pa} in 0.1 M PBS and 0.1 M KCl and 5 mM $[Fe(CN)_6]^{3-/4-}$ vs Ag/AgCl reference electrode for (a) bare GC electrode; (b) Gr/GCE; (c) Gr/WS_2/HRP/GCE; (d) Gr/WS_2/AuNPs/HRP/GCE respectively. 226

LIST OF TABLES

Table	***Description***	***Page***
Table 2. 1	Examples of electrochemical biosensors, their working principles and types of electrodes employed.	35
Table 3. 1	List of chemicals and materials	105
Table 4.1	Randle circuit equivalent values	150
Table 4.2	Summary of electrobiocatalytic responses to stepwise H_2O_2 additions	154
Table 4.3	Comparative table showing the linear response similar studies	154
Table 6. 1	Summary of electrobiocatalytic responses of different modified bioelectrodes with H_2O_2 stepwise additions	215

LIST OF SCHEMES

Scheme	***Description***	***Page***
Scheme 3.1	Schematic representation of the fabricated GO/AuNPs MoS_2/PNIPAAm/Peroxidase 2D hierarchically self-assembled nanohybrid interfaces.	109
Scheme 3.2	Fabrication of hierarchical self-assembly interfaces of BN/WS_2/AuNPs/HRP nanohybrid structures.	112
Scheme 3.3	Fabrication of hierarchical self-assembly interfaces of Gr/WS_2/AuNPs/HRP nanohybrid structures	116
Scheme 4.1	2D-hetero hierarchically self-assembled hybrid interfaces: (a) AuNPs doped layered GO/MoS_2 2D nano-hetero interfaces (b) fabrication of GO/AuNPs/MoS_2/PNIPAAm/Peroxidase bioelectrode and electrobiocatalytic conversion of H_2O_2.	139
Scheme 5.1	Fabrication of hierarchical self-assembly interfaces of BN/WS_2/AuNPs/HRP nanohybrid structures showing H_2O_2 reduction at the interface.	172
Scheme 6.1	Schematic representation of AuNPs structuring on a CVD grown graphene and WS_2 interface and electron transfer process in the Gr/WS_2/AuNPs/HRP nanohybrid structure on the glassy carbon electrode in electrochemical cell which is connected to potentiostat. Note that Scheme 1 is not to scale.	208

LIST OF ABBREVIATIONS

2D	Two Dimensional
TMD	Transition Metal Dichalcogenides
GO	Graphene Oxide
MoS_2	Molybdenum Disulphide
BN	Boron Nitride
WS_2	Tungsten Disulphide
HRP	Peroxidase from Horseradish
AuNPs	Gold Nanoparticles
PNIPAAm	Poly (N-isopropylacrylamide)
H_2O_2	Hydrogen Peroxide
CV	Cyclic Voltammetry
EIS	Electrochemical Impedance Spectroscopy
DPV	Differential Pulse Voltammetry
PSV	Potential Step Voltammetry
SWV	Square-Wave Voltammetry
LoD	Limit of Detection
RE	Reference Electrode
CE	Counter Electrode
GCE	Glassy Carbon Electrode
RT	Room Temperature

DFT	Density Functional Theory
CASTEP	Cambridge Serial Total Energy Package
GGA	Generalized Gradient Approximation
CVD	Chemical Vapour Deposition
PBS	Phosphate Buffer Solution
Ag/AgCl	Silver/Silver Chloride
TEM	Transmission Electron Microscopy
SEM	Scanning Electron Microscopy
XRD	X-Ray Diffraction
I_{pc}	Cathodic Current
I_{pa}	Anodic Current
R_{ct}	Charge Transfer Resistance
E_{pc}	Cathodic Peak Potential
E_{pa}	Anodic Peak Potential
F	Faraday Constant
n	Number of Electrons
A	Surface Area
D	Diffusion Co-efficient
t	Time
ν	Scan Rate

CHAPTER 1

INTRODUCTION

1.1 BACKGROUND AND MOTIVATION

Sensors are devices which respond to changes in their environment, such as heat, motion, light, pressure or any other environmental phenomena and this response is converted into readable signals [1, 2]. Sensors are categorized into three types: (i) chemical sensors which are used for identifying different chemical substances; (ii) physical sensors for different physical properties for example temperature, position, pressure; and (iii) biosensors for biological substances. The term, 'biosensor' is one of type of sensor which involve the incorporation of biological entity like enzymes, antibodies or cells into the sensing device [1].

The concept of biosensors was first explained by L.C. Clark and C. Lyons in 1962 with an early invention of Clark oxygen electrode which was based on the concept that electrochemical detection of oxygen or H_2O_2 could be used as the basis for the detection of many analytes [3].

Biosensors are highly sensitive devices with simple and easy to use technology. Generally, biosensors are analytical devices integrating a biological sensing element with physicochemical transducers to produce an electronic signal that is proportional to the quantity (or concentration) of the analytes which is being detected or analyzed [4, 5].

A typical biosensor consists of five important components in which the first component is the analyte which needs to be detected. The second is the bioreceptor such as enzyme, cell, aptamers, antibodies and deoxyribonucleic acid (DNA), which is the

molecule that specifically recognizes the respective analytes [6, 7]. While the third component of the biosensor is the transducer whose role is to convert the bio-recognition event into a measurable or detectable signal [8, 9]. The fourth and fifth components are the electronics and display that processes the transduced signal and converts it into readable output results [10] as shown in Figure 1.1.

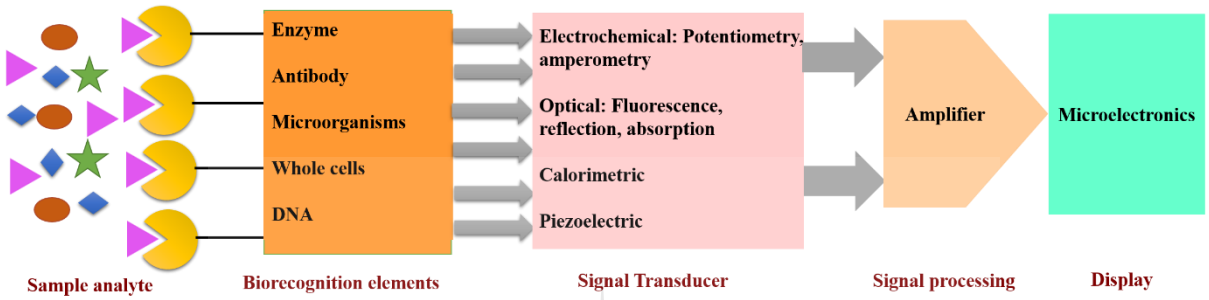

Figure 1.1 Schematic representation of different components of a biosensor. Redraw from [10].

The transducing system can be electrochemical, piezoelectric, magnetic, optical or acoustical and ion-sensitive. The bio-recognition element or bioreceptor consists of an immobilized biocomponent that detects the specific analytes, which deals with an event (chemical and electronic) between the analytes and the bio-recognition element and may result in flow of electrons, change in pH, change in mass, release of heat or other chemical changes which are transduced into electrical signals [11-13].

Historically, enzymes are the first known bio-recognition elements in electrochemical biosensors [3, 14] where the resulting enzymatic reaction (indicating the performance of the sensor) may be evaluated in terms of concentration change. Performance of biosensors depends upon the chemical and physical conditions of immobilized bio-recognition molecules and also on the stability of the respective electrode materials [15].

Based on bio-recognition element and the transduction element, biosensors can be classified [16] as shown in Figure 1.2.

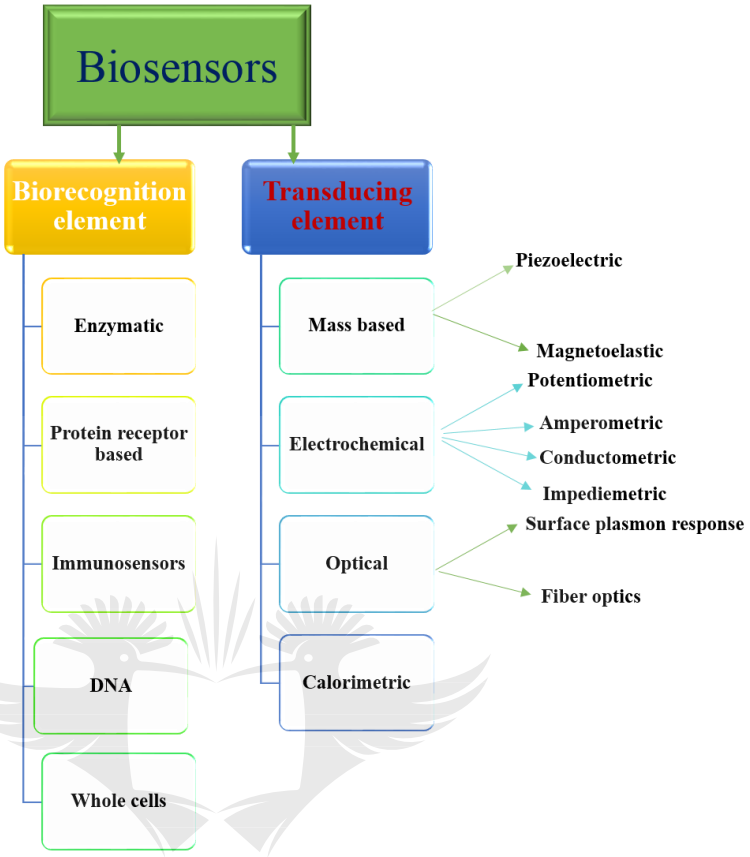

Figure 1. 2 Classification of biosensors. Redraw from [16].

The potential applications of biosensors cut across different areas ranging from industry to military applications (forensic and safety) [17]. They are currently most commonly applied in medical diagnostics, drug discovery, environmental monitoring and food safety [17-20]. In today's world, the development of functional devices are the highlight of growing research which opened different possibilities for the integration of electronic elements with biotechnology [22-24].

The recent progress being made relative to device development and fabrication in this field have enabled world-leading research groups to find a connection between the

living and artificial world with better understanding of various biochemical and/or biophysical events in these systems [25].

Recent trends in device fabrication and design are to make the devices lighter, with better durability, economical and [26, 27]. Various electrocatalytic bio-interfaces in different devices are helpful for the production, monitoring and regulation of biological reactions [28].

Biosensors have really been useful for upgrading the quality of life due to their various applications in health care technology for disease detection [4, 29-31]. The current research trend in the field of biosensors is towards the development of thin, flexible and highly sensitive bio-interface for efficient signal transduction [32].

Electrochemical biosensing is an interdisciplinary field of biosensors that fuses the knowledge of electrochemistry, nanotechnology and bioelectronics and has vast applications in healthcare, environmental monitoring, water analysis and energy (generation and storage). Consequently, there is a continuous need for the development of ultrafast and more highly sensitive next generation of biosensors that can easily be deployed in the field to target applications, with an accompanying fast response time and robust signals in real time sample monitoring.

In addition, the other focused areas for biosensing technique are the improvements in their sensing features, cost-effectiveness, efficiency and the miniaturization of the biosensing platforms. To achieve these promising features, there is a need to develop paper-formatted electrode technology, nanomaterial interfaced-electrode systems and nanohybrid interfaces that involve the incorporation of 2D materials into concept design for biosensing devices [33-35]. The combination of 2D materials is becoming the most versatile tool for attaining ultra-sensitive and selective novel nanobiosensors

[37, 38]. Consequently, recently, the fabrication of thinner, economical and flexible bioelectronic devices based on the use of 2D materials has become a major focus in biosensing [37-40].

The discovery of 2D materials has generated significant interest in the scientific community lately because of their exotic properties, which has made them the ideal materials for potential applications in biosensing, biomedical devices, energy storage and conversion electrochemical devices [34, 35, 40-45].

2D materials possess very high surface area, high electrocatalytic efficiency, tunable band gap and good biocompatibility [41, 46, 47]. In addition, 2D materials also offer an extensive platform for the utilization of their arrays of distinctive properties due to their electronic structure (hetero structuring), confinement effects [48] and their ability to be hybridized with other materials [19]. Due to their catalytic, electrical and optical properties [49, 50], 2D materials have rapidly gained research interest for the fabrication of biosensing platform.

Typically, 2D materials possess strong ionic or covalent intralayer forces and weak interlayer van der Waals forces which are responsible for their good stability [51] and anisotropic properties [52]. These van der Waals forces are the paramount contributor to the conventional lattice spacing and are responsible for the change in properties of the nanomaterials compared to their bulk counterpart.

Graphene is one of the most widely known members of 2D materials family. A single layer of graphene sheet consists of hexagonally arranged sp^2-hybridized carbon atoms. Graphene is usually classified as single layer graphene (SLG), few layer graphene (FLG) and multi-layer graphene (MLG), all of them with the outstanding properties, including high electrical and thermal conductivity [53], high specific surface

area (2630 m^2 g^{-1}), good carrier mobility at room temperature [33], high mechanical strength [54, 55], good absorption in the white light spectrum [56, 57], high enzyme loading [58, 59], and good tunable optical properties [60].

The sp^2-hybridization in graphene involves the mixing of 1 s-orbital and 2 p-orbitals (p_x and p_y) resulting in a trigonal planar structure with the formation of a σ-bond between carbon atoms [61]. The σ-bond is responsible for the vitality of the lattice structure in all allotropes of carbon. The π-bond is created due to p_z-electron and the π-bonds hybridize together to form the π-band and π*-band. These bonds are responsible for electronic properties and high in-plane conductivity of graphene due to the half-filled bond, which permits free-hopping electrons mechanism [56, 62].

Due to these diverse properties, graphene plays an important role in the field of energy generation and storage [59, 63, 64], high-speed electronic devices along with low cost. Graphene is also an ideal material for biosensors fabrication with better biosensing performance [65-67], especially due to its electronic properties. In recent era, the use of graphene based materials as immobilization matrixes have increased due to its high surface area which is ideal for the immobilization of bio-recognition elements resulting in improved biocatalytic processes [69-71].

Beyond graphene, the other well-known 2D materials are hexagonal boron nitride (h-BN) [72, 73], and transition metal dichalcogenides (TMDs) [38] with the general formula MX_2, where M is transition metal (e.g., Mo, W, Nb, Hf, Ta, Bi) and X is a chalcogen (e.g., S, Se, Te). TMD (MoS_2, WS_2, WSe_2, etc.) consist of a “sandwich” like structure of a transition metal (M) atom between two chalcogen atoms. These different non-graphene 2D materials have many salient features and divergent properties that

enhance the different potential applications of 2D materials [19, 35, 38, 42, 44, 46, 74-76].

Moreover, there is an obvious requirement to develop a higher surface area interface hybrid matrix that will result in greater sensitivity due to higher enzyme loading on the hybrid 2D interface matrix which will consequently lead to increase the electrobiocatalytic activity within the 2D layered hybrid interface materials. Research studies have also shown that the incorporation of novel 2D materials in the fabrication of biosensor system have resulted in highly efficient, ultra-sensitive, fast and smart biodevices.

Theoretical calculations were carried out in this study to confirm experimental data using quadratic configuration interaction or coupled cluster theory in the case of 2D nanohybrid structures. This helps to give more detailed information about the electronic interaction between different interfaces. The DFT which describes electron correlation energy was used to describe the coupling/correlation of electron motions [77] for these nanohybrid structures. First–principles calculation is an actual tool to unveil electronic interaction occurring at the nanohybrid structure interface [78] with the help of Cambridge Serial Total Energy Package 30 code [79] of the Materials Studio 2016 [80] software. The generalized gradient approximation function of the Perdew–Burke–Ernzerhof was adopted to account for the exchange–correlation effects and A Monkhorst–Pack 33 with k–points of 8 x 8 x 1 was used to optimize the crystal structure of the studied systems [81].

1.2 PROBLEM STATEMENT

In the last century, there have been many discoveries in the line of the interface between the biological and electronic world which has ultimately opened a novel field of bioelectronics, which is basically a development involving the integration of biotechnology with electronics [22, 25, 71, 82]. This also involves the use of biomolecule to catalyze a chemical reaction, which is then eventually translated into a readable signal. These discoveries have helped researchers to develop a deeper understanding of various biochemical as well as biophysical events in living systems [22, 24, 83, 84] and has also lead to the development of novel devices fabrication with applications in health, environmental and industrial purposes.

However, there are some limitations with the current bioelectronics devices being used in biosensing and other applications. These limitations include slow electron kinetics between the electrode and target analytes, low sensitivity, high cost and poor durability. Therefore, the fabrication of cheap, durable, fast and highly sensitive, super thin electrobiocatalytic interfaces has become a necessity for the development of next generation bioelectronics and biosensor devices [29, 85-89].

Consequently, it is very necessary that research is conducted into the possible incorporation of highly electrocatalytic and thin 2D nanohybrid materials into the design and fabrication of bioelectronic devices. Such research may possibly hold the answer to the fabrication of super thin, cheap, highly sensitive, lightweight, and ultrafast devices.

1.3 JUSTIFICATION

The recent focus and developments in 2D materials research makes it possible to achieve the design and fabrication of super thin and efficient biodevices including electrochemical biosensors. Additionally, research studies have shown that the integration of different materials, such as metallic nanoparticles, carbon dots, and polymers with 2D materials has led to improvement in the properties of the individual 2D materials [84, 90]. Recent research studies have reported that the incorporation of other 2D materials [74-76, 91] with graphene is a good way to overcome the zero band gap limitation of pristine graphene. In addition, incorporation of AuNPs in 2D hybrid structures has been reported to cause signal amplification in resultant fabricated devices [42-44].

This study involves the fabrication of hybrid 2D composite materials for the development of highly sensitive, fast and durable electrochemical interface as a platform for the fabrication of low-cost thin, flexible and highly sensitive electrochemical biosensor. This study will add an impact and make it possible to develop portable point-of-care diagnostic biodevices, portable handheld environmental monitoring sensors that can be deployed in rural communities for “on the spot” and easy to handle analysis of samples to avoid the time taken route for analysis of the sample in laboratories.

The effect of the combination of different 2D nanohybrid materials with the resultant superior electrocatalytic and electrobiocatalytic is the major focus of this study. The self-assembly approach has been extensively used for developing functional materials. The self-assembled hybrid structures along with proper design can provide

excellent materials with better performance. Here, the surface modified 2D materials will be chosen to construct a self-assembled structure for biosensing applications.

In this thesis, the self-assembly method is used to assemble 2D nanohybrid materials with enzyme and metal nanoparticles by hierarchical structuring using electrostatic and hydrophilic interactions respectively, for the fabrication of electrochemical biosensors platform.

1.4 AIM AND OBJECTIVES

1.4.1 Aim

The aim of this research is to fabricate hierarchically assembled 2D nanohybrid interfaces for thin bioelectronic systems.

1.4.2 Objectives

The objectives of this project include:

a) Fabrication of 2D nanohybrid interfaces for super thin bioelectronic systems using self-assembly structure approach.
b) Structural, electronic and morphological characterization of the fabricated 2D nanohybrid interface structure using X-ray diffraction, Raman spectroscopy, scanning electron microscopy and transmission electron microscopy.
c) Fabrication of modified bioelectrodes using the fabricated 2D based nanohybrid interface conjugated structures.

d) Examine and investigate the electrochemical behaviour of the fabricated 2D nanohybrid modified bioelectrodes through electrochemical techniques (CV and EIS).

e) Investigation of the interaction between different 2D materials and electronic structure and properties of the 2D nanohybrid interfaces using Material Studio 2016.

f) Exploration of the electrobiocatalytic activities of the fabricated bioelectrode by using chronoamperometric technique, with hydrogen peroxide as model analytes while horseradish peroxidase was used as sample bio-recognition element.

1.5 OUTLINE OF THE THESIS

The contents of the various chapters in this thesis are presented as follows:

Chapter 1 covers the **general introduction** along with background, problem statement, justification and aim and objectives of the thesis.

Chapter 2 provides an overview of the concept of biosensors and different types of biosensors. This chapter also includes recent updates on the background and review of two dimensional materials, their classification and their applications in the biosensing field. Additionally, this chapter also focuses on the basics of electrode processes and different electrochemical techniques.

Chapter 3 discusses the respective methods that have been used in the synthesis of materials, the reagents used, along with the information about material used with their origin and source. The chapter also discusses self-assembly structure methodology in

detail. This chapter provides a glimpse of principles and working procedures of characterization techniques used in this work.

Chapter 4 discusses the fabrication of 2D nanohybrid interfaces involving the conjugation of dual 2D material doped with metal nanoparticles (AuNPs) and conjugated with a polymer (GO/AuNPs/MoS_2/PNIPAAm/Peroxidase) as a novel interface system for bioreactors and electrobiocatalysis devices.

Chapter 5 presents the fabrication of BN/WS_2/AuNPs/HRP modified bioelectrodes with use of self-assembly procedure. In this work, BN and WS_2 are chosen as platform for the immobilization of HRP enzyme for fabrication of novel biosensor and analyzed electrochemical results. The electron transfer properties of conjugated material were also studied using the generalized gradient approximation (GGA) exchange correlation of the Cambridge Serial Total Energy Package (CASTEP).

Chapter 6 focusses on the fabrication of Gr, WS_2 and AuNPs with immobilized HRP (Gr/WS_2/AuNPs/HRP) modified bioelectrodes and characterization of these 2D nanohybrid materials with electrochemical measurements. This chapter also involves synthesis of graphene by CVD method.

Chapter 7 presents the general conclusion of this PhD study along with the future prospective based on the result obtained.

1.6 REFERENCES

[1] N. R. Council. Expanding the vision of sensor materials. *National Academies Press* (1995).

[2] J. K. Gimzewski, C. Gerber, E. Meyer and R. Schlittler. Observation of a chemical reaction using a micromechanical sensor. *Chemical Physics Letters* **217** (1994) 589-594.

[3] L. C. Clark, Jr. and C. Lyons. Electrode systems for continuous monitoring in cardiovascular surgery. *Annals of the New York Acedamy of Sciences* **102** (1962) 29-45.

[4] A. P. Turner. Biosensors: sense and sensibility. *Chemical Society Reviews* **42** (2013) 3184-3196.

[5] C. Lowe. An introduction to the concepts and technology of biosensors. *Biosensors* **1** (1985) 3-16.

[6] C. I. L. Justino, A. C. Freitas, R. Pereira, A. C. Duarte and T. A. P. R. Santos. Recent developments in recognition elements for chemical sensors and biosensors. *Trac-Trends in Analytical Chemistry* **68** (2015) 2-17.

[7] X. Wang, X. B. Lu and J. P. Chen. Development of biosensor technologies for analysis of environmental contaminants. *Trends in Environmental Analytical Chemistry* **2** (2014) 25-32.

[8] D. R. Thevenot, K. Toth, R. A. Durst and G. S. Wilson. Electrochemical biosensors: Recommended definitions and classification - (Technical Report). *Pure and Applied Chemistry* **71** (1999) 2333-2348.

[9] D. R. Thévenot, K. Toth, R. A. Durst and G. S. Wilson. Electrochemical biosensors: recommended definitions and classification1. *Biosensors and Bioelectronics* **16** (2001) 121-131.

[10] S. Singh, Nanofiber Electrodes for Biosensors. In: Barhoum A., Bechelany M., Makhlouf A. (eds) Handbook of Nanofibers. *Springer*, Cham (2018).

[11] A. Turner, I. Karube and G. S. Wilson. Biosensors: fundamentals and applications. *Oxford university press* (1987).

[12] A. Turner, W. Aston, I. Higgins, G. Davis and H. Hill. Applied aspects of bioelectrochemistry: fuel cells, sensors, and bioorganic synthesis, in *Biotechnol. Bioeng. Symp.;(United States)* **12**(1982).

[13] A. N. Sekretaryova, M. Eriksson and A. P. Turner. Bioelectrocatalytic systems for health applications. *Biotechnology advances* **34** (2016) 177-197.

[14] A. E. Cass, G. Davis, G. D. Francis, H. A. O. Hill, W. J. Aston, I. J. Higgins, E. V. Plotkin, L. D. Scott and A. P. Turner. Ferrocene-mediated enzyme electrode for amperometric determination of glucose. *Analytical chemistry* **56** (1984) 667-671.

[15] P. T. Kissinger. Biosensors—a perspective. *Biosensors and Bioelectronics* **20** (2005) 2512-2516.

[16] N. A. Mungroo, S. Neethirajan. Biosensors for the detection of antibiotics in poultry industry-a review. *Biosensors (Base*l) **4** (2014) 472-493.

[17] P. Yáñez-Sedeño, L. Agüí and J. M. Pingarrón. Biosensors in Forensic Analysis. *Forensic Science: A Multidisciplinary Approach* (2016).

[18] C. Chen, Q. J. Xie, D. W. Yang, H. L. Xiao, Y. C. Fu, Y. M. Tan and S. Z. Yao. Recent advances in electrochemical glucose biosensors: a review. *Rsc Advances* **3** (2013) 4473-4491.

[19] Y. Song, Y. Luo, C. Zhu, H. Li, D. Du and Y. Lin. Recent advances in electrochemical biosensors based on graphene two-dimensional nanomaterials. *Biosensors and Bioelectronics* **76** (2016) 195-212.

[20] S. Neethirajan, V. Ragavan, X. Weng and R. Chand. Biosensors for Sustainable Food Engineering: Challenges and Perspectives. *Biosensors* **8** (2018) 23.

[21] J. Yasmin, M. R. Ahmed and B.-K. Cho. Biosensors and their Applications in Food Safety: A Review. *Journal of Biosystems Engineering* **41** (2016) 240-254.

[22] I. Willner and E. Katz. Bioelectronics: From theory to applications. *John Wiley & Sons* (2006).

[23] E. Katz and I. Willner. Probing biomolecular interactions at conductive and semiconductive surfaces by impedance spectroscopy: routes to impedimetric immunosensors, DNA-sensors, and enzyme biosensors. *Electroanalysis* **15** (2003) 913-947.

[24] C. Joachim, J. K. Gimzewski and A. Aviram. Electronics using hybrid-molecular and mono-molecular devices. *Nature* **408** (2000) 541-548.

[25] A. Noy. Bionanoelectronics. *Advanced Materials* **23** (2011) 807-820.

[26] J.-H. Ahn and B. H. Hong. Graphene for displays that bend. *Nature Nanotechnology* **9** (2014) 737-738.

[27] F. Bonaccorso, Z. Sun, T. Hasan and A. Ferrari. Graphene photonics and optoelectronics. *Nature Photonics* **4** (2010) 611-622.

[28] N. Mohanty and V. Berry. Graphene-based single-bacterium resolution biodevice and DNA transistor: interfacing graphene derivatives with nanoscale and microscale biocomponents. *Nano Letters* **8** (2008) 4469-4476.

[29] J. Wang. Electrochemical glucose biosensors. *Chemical Reviews* **108** (2008) 814-825.

[30] V. Scognamiglio, F. Arduini, G. Palleschi and G. Rea. Biosensing technology for sustainable food safety. *TrAC Trends in Analytical Chemistry* **62** (2014) 1-10.

[31] P. Jolly, P. Damborsky, N. Madaboosi, R. R. Soares, V. Chu, J. P. Conde, J. Katrlik and P. Estrela. DNA aptamer-based sandwich microfluidic assays for dual quantification and multi-glycan profiling of cancer biomarkers. *Biosensors and Bioelectronics* **79** (2016) 313-319.

[32] M. Privman, T. K. Tam, M. Pita and E. Katz. Switchable electrode controlled by enzyme logic network system: approaching physiologically regulated bioelectronics. *Journal of the American Chemical Society* **131** (2008) 1314-1321.

[33] K. S. Novoselov, A. K. Geim, S. V. Morozov, D. Jiang, M. I. Katsnelson, I. V. Grigorieva, S. V. Dubonos and A. A. Firsov. Two-dimensional gas of massless Dirac fermions in graphene. *Nature* **438** (2005) 197-200.

[34] P. Bollella, G. Fusco, C. Tortolini, G. Sanzo, G. Favero, L. Gorton and R. Antiochia. Beyond graphene: Electrochemical sensors and biosensors for biomarkers detection. *Biosensors and Bioelectronics* **89** (2017) 152-166.

[35] G. Yang, C. Zhu, D. Du, J. Zhu and Y. Lin. Graphene-like two-dimensional layered nanomaterials: applications in biosensors and nanomedicine. *Nanoscale* **7** (2015) 14217-14231.

[36] S. Li, J. Singh, H. Li and I. A. Banerjee. Biosensor nanomaterials. *John Wiley & Sons* (2011).

[37] C. Jianrong, M. Yuqing, H. Nongyue, W. Xiaohua and L. Sijiao. Nanotechnology and biosensors. *Biotechnology Advances* **22** (2004) 505-518.

[38] Q. H. Wang, K. Kalantar-Zadeh, A. Kis, J. N. Coleman and M. S. Strano. Electronics and optoelectronics of two-dimensional transition metal dichalcogenides. *Nature Nanotechnology* **7** (2012) 699-712.

[39] K. Novoselov, D. Jiang, F. Schedin, T. Booth, V. Khotkevich, S. Morozov and A. Geim. Two-dimensional atomic crystals. *Proceedings of the National Academy of Sciences of the United States of America* **102** (2005) 10451-10453.

[40] D. Akinwande, N. Petrone and J. Hone. Two-dimensional flexible nanoelectronics. *Nature Communications* **5** (2014) 5678.

[41] X. Huang, C. Tan, Z. Yin and H. Zhang. 25th anniversary article: hybrid nanostructures based on two-dimensional nanomaterials. *Advanced Materials* **26** (2014) 2185-2204.

[42] C. Zhu, D. Du and Y. Lin. Graphene-like 2D nanomaterial-based biointerfaces for biosensing applications. *Biosensors and Bioelectronics* **89** (2017) 43-55.

[43] Z. Sun and H. Chang. Graphene and graphene-like two-dimensional materials in photodetection: mechanisms and methodology. *ACS Nano* **8** (2014) 4133-4156.

[44] M. Xu, T. Liang, M. Shi and H. Chen. Graphene-like two-dimensional materials. *Chemical Reviews* **113** (2013) 3766-3798.

[45] R. L. McCreery. Advanced carbon electrode materials for molecular electrochemistry. *Chemical Reviews* **108** (2008) 2646-2687.

[46] A. Gupta, T. Sakthivel and S. Seal. Recent development in 2D materials beyond graphene. *Progress in Materials Science* **73** (2015) 44-126.

[47] M. Chhowalla, H. S. Shin, G. Eda, L. J. Li, K. P. Loh and H. Zhang. The chemistry of two-dimensional layered transition metal dichalcogenide nanosheets. *Nature Chemistry* **5** (2013) 263-275.

[48] K. F. Mak, K. He, J. Shan and T. F. Heinz. Control of valley polarization in monolayer MoS_2 by optical helicity. *Nature Nanotechnology* **7** (2012) 494-498.

[49] R. Lv, J. A. Robinson, R. E. Schaak, D. Sun, Y. Sun, T. E. Mallouk and M. Terrones. Transition metal dichalcogenides and beyond: synthesis, properties, and applications of single-and few-layer nanosheets. *Accounts of chemical research* **48** (2014) 56-64.

[50] L. Britnell, R. Ribeiro, A. Eckmann, R. Jalil, B. Belle, A. Mishchenko, Y.-J. Kim, R. Gorbachev, T. Georgiou and S. Morozov. Strong light-matter interactions in heterostructures of atomically thin films. *Science* **340** (2013) 1311-1314.

[51] S. Das, J. A. Robinson, M. Dubey, H. Terrones and M. Terrones. Beyond graphene: progress in novel two-dimensional materials and van der Waals solids. *Annual Review of Materials Research* **45** (2015) 1-27.

[52] M. Pumera and A. H. Loo. Layered transition-metal dichalcogenides (MoS_2 and WS_2) for sensing and biosensing. *TrAC Trends in Analytical Chemistry* **61** (2014) 49-53.

[53] A. A. Balandin, S. Ghosh, W. Bao, I. Calizo, D. Teweldebrhan, F. Miao and C. N. Lau. Superior thermal conductivity of single-layer graphene. *Nano Letters* **8** (2008) 902-907.

[54] M. Fang, K. Wang, H. Lu, Y. Yang and S. Nutt. Covalent polymer functionalization of graphene nanosheets and mechanical properties of composites. *Journal of Materials Chemistry* **19** (2009) 7098-7105.

[55] C. Lee, X. Wei, J. W. Kysar and J. Hone. Measurement of the elastic properties and intrinsic strength of monolayer graphene. *Science* **321** (2008) 385-388.

[56] A. K. Geim. Graphene: status and prospects. *Science* **324** (2009) 1530-1534.

[57] R. R. Nair, P. Blake, A. N. Grigorenko, K. S. Novoselov, T. J. Booth, T. Stauber, N. M. Peres and A. K. Geim. Fine structure constant defines visual transparency of graphene. *Science* **320** (2008) 1308-1308.

[58] J. L. Zhang, F. Zhang, H. J. Yang, X. L. Huang, H. Liu, J. Y. Zhang and S. W. Guo. Graphene Oxide as a Matrix for Enzyme Immobilization. *Langmuir* **26** (2010) 6083-6085.

[59] D. A. Brownson and C. E. Banks. Graphene electrochemistry: an overview of potential applications. *Analyst* **135** (2010) 2768-2778.

[60] M. Liu, X. Yin, E. Ulin-Avila, B. Geng, T. Zentgraf, L. Ju, F. Wang and X. Zhang. A graphene-based broadband optical modulator. *Nature* **474** (2011) 64-67.

[61] A. C. Neto, F. Guinea, N. M. Peres, K. S. Novoselov and A. K. Geim. The electronic properties of graphene. *Reviews of Modern Physics* **81** (2009) 109.

[62] R. Saito, G. Dresselhaus and M. S. Dresselhaus. Physical properties of carbon nanotubes. *World Scientific* (1998).

[63] T. Kuila, S. Bose, P. Khanra, A. K. Mishra, N. H. Kim and J. H. Lee. Recent advances in graphene-based biosensors. *Biosensors and Bioelectronics* **26** (2011) 4637-4648.

[64] M. Pumera. Graphene-based nanomaterials for energy storage. *Energy & Environmental Science* **4** (2011) 668-674.

[65] E. B. Bahadır and M. K. Sezgintürk. Applications of graphene in electrochemical sensing and biosensing. *TrAC Trends in Analytical Chemistry* **76** (2016) 1-14.

[66] K. Yang, L. Feng, X. Shi and Z. Liu. Nano-graphene in biomedicine: theranostic applications. *Chemical Society Reviews* **42** (2013) 530-547.

[67] H. Jiang. Chemical preparation of graphene-based nanomaterials and their applications in chemical and biological sensors. *Small* **7** (2011) 2413-2427.

[68] C. H. Lu, H. H. Yang, C. L. Zhu, X. Chen and G. N. Chen. A graphene platform for sensing biomolecules. *Angewandte Chemie International Edition* **48** (2009) 4785-4787.

[69] Y. Liu, D. Yu, C. Zeng, Z. Miao and L. Dai. Biocompatible graphene oxide-based glucose biosensors. *Langmuir* **26** (2010) 6158-6160.

[70] T. Cohen-Karni, Q. Qing, Q. Li, Y. Fang and C. M. Lieber. Graphene and nanowire transistors for cellular interfaces and electrical recording. *Nano Letters* **10** (2010) 1098-1102.

[71] P. Nguyen and V. Berry. Graphene Interfaced with Biological Cells: Opportunities and Challenges. *Journal of Physical Chemistry Letters* **3** (2012) 1024-1029.

[72] T. Brugger, S. Günther, B. Wang, J. H. Dil, M.-L. Bocquet, J. Osterwalder, J. Wintterlin and T. Greber. Comparison of electronic structure and template function of single-layer graphene and a hexagonal boron nitride nanomesh on Ru (0001). *Physical Review B* **79** (2009) 045407.

[73] Y. Lin, T. V. Williams, T. B. Xu, W. Cao, H. E. Elsayed-Ali and J. W. Connell. Aqueous Dispersions of Few-Layered and Monolayered Hexagonal Boron Nitride Nanosheets from Sonication-Assisted Hydrolysis: Critical Role of Water. *Journal of Physical Chemistry C* **115** (2011) 2679-2685.

[74] H. Song, Y. Ni and S. Kokot. Investigations of an electrochemical platform based on the layered MoS_2–graphene and horseradish peroxidase nanocomposite for direct electrochemistry and electrocatalysis. *Biosensors and Bioelectronics* **56** (2014) 137-143.

[75] K.-J. Huang, Y.-J. Liu, J.-T. Cao and H.-B. Wang. An aptamer electrochemical assay for sensitive detection of immunoglobulin E based on tungsten disulfide–

graphene composites and gold nanoparticles. *RSC Advances* **4** (2014) 36742-36748.

[76] M. P. Levendorf, C. J. Kim, L. Brown, P. Y. Huang, R. W. Havener, D. A. Muller and J. Park. Graphene and boron nitride lateral heterostructures for atomically thin circuitry. *Nature* **488** (2012) 627-632.

[77] A. D. Becke. Perspective: Fifty years of density-functional theory in chemical physics. *Journal of Chemical Physics* **140** (2014) 18A301.

[78] V. Coropceanu, H. Li, P. Winget, L. Y. Zhu and J. L. Bredas. Electronic-Structure Theory of Organic Semiconductors: Charge-Transport Parameters and Metal/Organic Interfaces. *Annual Review of Materials Research* **43** (2013) 63-87.

[79] M. D. Segall, P. J. D. Lindan, M. J. Probert, C. J. Pickard, P. J. Hasnip, S. J. Clark and M. C. Payne. First-principles simulation: ideas, illustrations and the CASTEP code. *Journal of Physics-Condensed Matter* **14** (2002) 2717-2744.

[80] Materials Studio Simulation Environment. *Release 2016, Accelrys Software Inc*, *San Diego, CA* (2016)

[81] J. P. Perdew, K. Burke and M. Ernzerhof. Generalized gradient approximation made simple. *Physical Review Letters* **77** (1996) 3865-3868.

[82] M. Berggren and A. Richter-Dahlfors. Organic bioelectronics. *Advanced Materials* **19** (2007) 3201-3213.

[83] W. J. Aston and A. P. F. Turner. Biosensors and Biofuel Cells. *Biotechnology & Genetic Engineering Reviews* **1** (1984) 89-120.

[84] A. O. Osikoya and A. Tiwari. Recent advances in 2D bioelectronics. *Biosensors and Bioelectronics* **89** (2017) 1-7.

[85] O. Parlak, A. P. Turner and A. Tiwari. On/Off-Switchable Zipper-Like Bioelectronics on a Graphene Interface. *Advanced Materials* **26** (2014) 482-486.

[86] O. Parlak, A. P. Turner and A. Tiwari. pH-induced on/off-switchable graphene bioelectronics. *Journal of Materials Chemistry B* **3** (2015) 7434-7439.

[87] C. De las Heras Alarcón, S. Pennadam and C. Alexander. Stimuli responsive polymers for biomedical applications. *Chemical Society Reviews* **34** (2005) 276-285.

[88] D. Roy, J. N. Cambre and B. S. Sumerlin. Future perspectives and recent advances in stimuli-responsive materials. *Progress in Polymer Science* **35** (2010) 278-301.

[89] N. Karimian, M. H. A. Zavar, M. Chamsaz, A. P. Turner and A. Tiwari. On/off-switchable electrochemical folic acid sensor based on molecularly imprinted polymer electrode. *Electrochemistry Communications* **36** (2013) 92-95.

[90] O. Parlak and A. P. Turner. Switchable bioelectronics. *Biosensors and Bioelectronics* **76** (2016) 251-265.

[91] P. Mulpur, S. Yadavilli, A. M. Rao, V. Kamisetti and R. Podila. MoS_2/WS_2/BN-Silver Thin-Film Hybrid Architectures Displaying Enhanced Fluorescence via Surface Plasmon Coupled Emission for Sensing Applications. *Acs Sensors* **1** (2016) 826-833.

CHAPTER 2

LITERATURE REVIEW

2.1 INTRODUCTION

Accurate and timely detection of specific physiological and pathogenic molecules in the human body provides an opportunity for reduced cost and early diagnosis and treatment of disease. However, most of the assays used in these processes are expensive with slow responsivity. Deployment of biosensors in this area can serve as an appropriate substitute as they are expected to provide highly specific, cost-effective and extremely efficient tools for this purpose.

Significant efforts have been made by the scientific community to develop effective biosensors not only for biomedical purposes but also for other fields of life such as the military for defence purposes, drug discovery, agriculture, bioterrorism prevention and so on. Although major successes have been achieved in this respect, the developed biosensors still require improvements with regards to their miniaturization, specificity, independence of physical parameters such as pH and temperature, their reusability and their general effectiveness. Consequently, it has become relevant to understand the basic concepts of biosensing which will serve as the basis for the fabrication of more efficient biosensor devices.

This chapter contains literature on the basic concepts of biosensing, applications of biosensors in various aspects of life, problems of biosensor effectiveness, the use of 2D materials as transduction material, and some basic electrochemical processes that are commonly used in electrochemical sensing and electrocatalysis including CV, EIS and chronoamperometric techniques.

2.2 BIOSENSORS

A biosensor is a self-sufficient device consisting of an integrated bio-recognition element and a signal transduction element that performs a selective and quantitative determination of a biological analyte of interest [1]. Thus, a biosensor contains two major components: a bio-recognition element and a transduction element. The bio-recognition element can be one of the following: enzyme, antibody, nucleic acid, tissue, microorganisms or a polysaccharide. On the other hand, the transduction element can be either an electric current, potential, conductance, impedance, intensity and phase of electromagnetic radiation, mass, temperature or viscosity [2].

The two components of a biosensor (the bio-recognition and transduction elements) can be joined together in one of four different scheme names, membrane entrapment, matrix entrapment, covalent bonding and physical adsorption [2]. In the membrane entrapment arrangement, the biorecognition element and the analyte are separated by a semi-permeable membrane (through which the analyte diffuses) and the biorecognition element is attached to the transducer.

The matrix entrapment arrangement involves the formation of a permeable entrapment medium around the bio-recognition element which enhances its attachment to the transducer. While, the covalent bonding scheme entails treating the surface of the transducer as a reactive group on which the bio-recognition element binds.

The physical arrangement relies on the attachment of the bio-recognition element onto the transducer's surface through the combination of hydrogen bonds, van der Waals forces, hydrophobic forces and ionic forces [2].

In principle, the bio-recognition element of the biosensor recognises the analyte of interest and binds to it, producing a physicochemical response. The transducer element then converts the physicochemical response into a measurable electrical output or signal. The output signals is then amplified, processed and displayed. Figure 2.1 presents a schematic diagram of this process.

Apart from biological analytes such as protein, exosome, DNA, cells and so on, the analyte of interest can also be ions, toxin, dissolved gases and drugs [3].

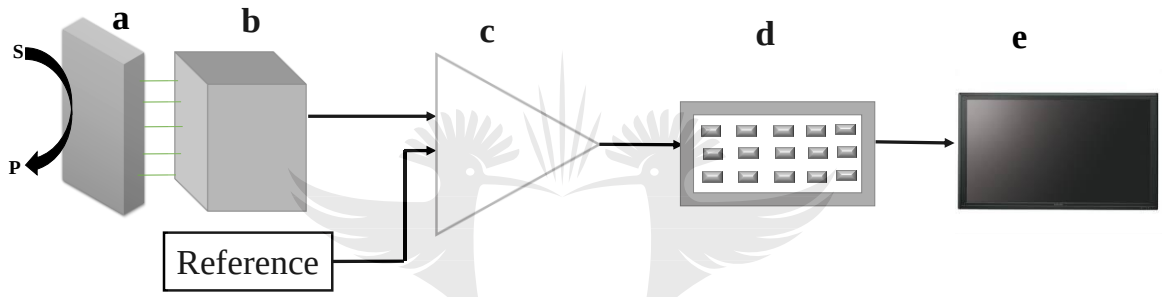

Figure 2.1 Schematic diagram of a biosensor showing (a) biocatalyst, (b) transducer, (c) amplified output from the transducer, (d) processed signal and (e) displayed readable result [4].

Based on the mechanism of transduction, biosensors can be categorised into various types.

2.2.1 Types of biosensor/classification of biosensors

Biosensors can be classified into two main groups. The first group of classification is based on the type of bio-recognition element used. That is, the biologically derived component of the biosensor that identifies, interacts and binds to the analyte under consideration. This type of biosensors includes a nucleic acid base, aptamer (synthetic oligonucleotides) based, immunosensor (antigen-antibody) based, enzyme-based and cell-based biosensors. The second group of classification is

based on the signal transduction mechanism of the biosensor. Thus, the mechanism by which the detector element converts the biological, chemical and physical signals resulting from the interaction between the bio-recognition element and the analyte into a measurable and quantifiable output signal. This type of biosensors include (i) resonant biosensors, (ii) optical-detection biosensors, (iii) thermal/calorimetric detection biosensors, (iv) ion-sensitive field electric transistor (ISFET) biosensors (v), mechanical/piezoelectric detection biosensors and (vi) electrochemical biosensors [5]. Figure 2.2 represents the different classifications of biosensors [6]. Detailed discussions of these two types of biosensors are provided in the ensuing sections.

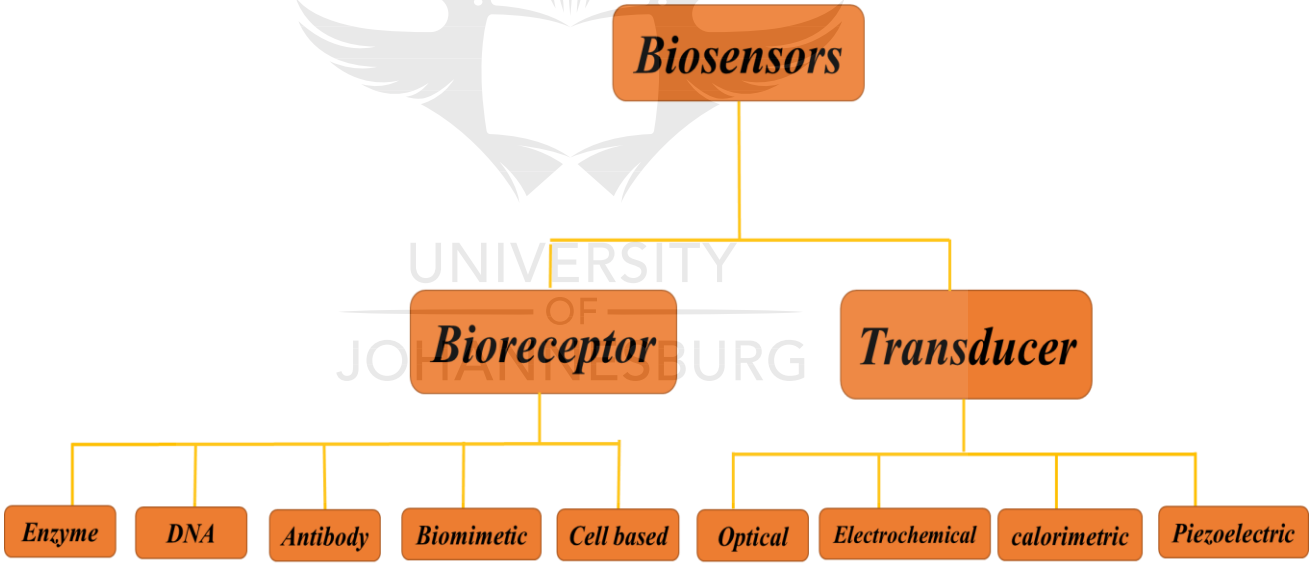

Figure 2.2 Different classifications of biosensors [6].

2.2.1.1 Classification based on bio-recognition elements used

2.2.1.1.1 Enzyme-based biosensors

This type of biosensor contains an enzyme as the bio-recognition element which is coupled with the transducer to generate a signal proportional to the concentration

of the analyte under consideration. Enzymes are regarded as an exceptional tool in biosensors development because of their unique tendency to particularly identify and catalyze the transformation of their substrates. Comparatively, this type of biosensors is more specific with faster response time as a result of their inherent shorter diffusion paths [5]. However, they tend to be relatively expensive to produce due to the tiresome purification processes or the difficulty in isolating the enzyme [7] and additionally, some might require cofactors/multi-enzymes for the generation of the quantifiable signal [8].

2.2.1.1.2 Microbe/cell-based biosensors

In microbe/cell-based biosensors, live cells constitute the bio-recognition element of the sensor. Its operation is based on the variations in the metabolism of the microorganisms, gene expression and pH which are measured as the response of the microbes to the target molecule of concern [9-11]. In most cases, the microorganisms are genetically engineered in order to attain the desired selectivity, sensitivity and the desired output signal [7]. Microbe-based biosensors are appropriate substitutes to enzyme-based biosensors because of their associated low-cost requirement and enhanced stability [12]. This system is also devoid of the tiresome purification processes. In addition, the microbes can be easily manipulated to withstand tough environmental conditions and can be produced in large quantities through simple cell culture process. Moreover, the essential cofactors are existent in the cells [13].

2.2.1.1.3 Immunosensors/antigen-antibody based biosensors

Immunosensors employ antigens and antibodies as the sensitive biological element and relies on the ability of the antibody (Ab) to bind with a matching antigen (Ag) with high specificity, stability and versatility [14]. It is grounded on Ag-Ab specific interactions through which the transducing element directly or indirectly detects their immunochemical reactions. They are mostly intended for the recognition of Abs or Ags. However, preference is given to the detection of Abs owing to the fact that the utilization of Abs as the bio-recognition element can result in diminished affinity since the Abs will immobilize onto the surface of the transducer [15, 16].

2.2.1.1.4 Aptamers (synthetic oligonucleotides) based biosensor

Aptamers are protein-binding oligonucleotides. They are single-stranded DNA or ribonucleic acid (RNA) sequences that are schemed to bind to a specific molecule with great specificity and affinity. They are regarded as suitable replacements for antibodies whereby they can bind to their targets by going through conformational changes [17]. Thus, an aptamer-based biosensor is the type where the bio-recognition element is a DNA, RNA or a man-made equivalent of a naturally occurring acid [17].

The possession of negative charges by the RNA and DNA strands makes them unique bio-recognition elements or target elements in biosensors. These type of biosensors are applied in various fields including identification of genes, detection of pathogens, forensic investigation and so on [18]. They possess certain advantages over other types of biosensors. These advantages include the avoidance of animal use, thus eliminating ethical issues. They are highly specific

with smaller sizes and with less complexity. They can be regenerated and possess the ability to be easily modified and immobilized [19]. However, aptamer-based biosensors are faced with the problem of structural pleomorphic (size and shape variability) and chemical simplicity which causes a reduction in the efficiency of the assay and increased cost of production [19].

2.2.1.1.5 DNA/Nucleic acid base biosensors

This type of biosensor employs nucleic acid as the bio-recognition element. It takes advantage of the high specific binding tendency between 2 single-stranded DNA chains resulting in the formation of double-stranded DNA. In other words, its principle is based on the ability of a single-stranded DNA chain to recognise a complementary strand, bind with it through hydrogen bonding to form a double-stranded DNA. This is achieved through immobilization of a single-stranded DNA chain as the probe with the base sequence as complementary to the considered target. Exposing the target to the probes causes the complementary single-stranded DNA chains to become hybridized resulting in the formation of double-stranded DNA. This process produces a reaction (biochemical) or a signal that is amplified by the transducer [20]. The bio-recognition element (nucleic acid) can be easily synthesized, is highly specific and can be reused several times after melting of the DNA duplex [21].

2.2.1.2 Classification based on signal transduction mechanism

2.2.1.2.1 Optical biosensors

In optical biosensors, light is the transduction signal measured in response to the physicochemical changes induced by the bio-recognition element as a result of the binding of a target molecule. The components measured include changes in the input light's amplitude, frequency, polarization or phase in response to the variations in the bio-recognition process [22, 23]. Hence, an optical biosensor consists of a light source, optical transmission medium, biological recognition element and optical detection system [24].

This type of biosensors has the advantage of being used in remote sensing, free from electromagnetic interference, fast, apart from being selective and specific [25].

The sensor can use two types of molecules namely: labelled or label-free molecules. The label-free sensor relies on the changes in the properties of the incident light, such as a refractive index to detect the binding of the considered molecule [2]. The measured signal is produced as a result of a direct communication between the analyzed material and the transduction element. On the other hand, label based sensors involve the use of a label to produce the optical signal either through luminescent, calorimetric or fluorescent methods [26].

2.2.1.2.2 Magnetic biosensors

In this type of sensors, either magnetic/super-paramagnetic particles or crystals are employed as the means of detection of biological reactions through the measurement of the changes in magnetic properties or the properties induced by

the magnetic effect such as variation in resistance, inductance, magnetic and optical properties [27]. This system consists of magnetic nanoparticles coated with a bio-receptor (e.g. Abs or nucleic acid).

The presence of the target molecule permits the binding of the magnetic nanoparticle with the surface of the magnetoresistance surface [28]. The binding produces a change in resistance, which is proportional to the concentration of the analyte. This change in resistance is then measured as a quantifiable output [29]. A major merit of this type of sensor is the tendency to enhance the interaction of the components through the manipulation of the magnetic particles in a magnetic field which intends to permit the movement of the particles to the surface of the sensor allowing the target to be rapidly detected [30].

2.2.1.2.3 Thermal/calorimetric detection biosensors

Thermal biosensors are designed on the basic properties of all biochemical reactions, which is the production and absorption of heat which subsequently changes the temperature of the reaction medium. They are composed of immobilized biomolecules and temperature sensors. In principle, the change in temperature produced as a result of the interaction of the bio-recognition element and the analyte is measured as a function of the concentration of the analyte [31]. This type of sensor has the advantage of being easily miniaturized with high stability and sensitivity [32]. Thermal biosensor can also be easily combined with microfluids for enhanced sensitivity [33].

2.2.1.2.4 Piezoelectric/mechanical detection biosensors

In piezoelectric biosensors, a piezoelectric material (material with the ability to generate voltage under mechanical stress) forms the sensor part (the transducer element) with the biosensor element coated on the piezoelectric material. It operates on the principle that a change in oscillation frequency occurs when there is a measureable change in the mass of materials bound on the surface of the piezoelectric material [34]. In general, excitation of the sensor occurs by changing the voltage on the surface of the electrodes. The change in voltage results in mechanical oscillation of the piezoelectric material. The frequency of the oscillation is measured when the oscillating material is placed in an external oscillation/ electric circuit [35]. Upon exposure of the analyte to the surface of the electrode located on the piezoelectric material, a change in oscillation frequency which is proportional to the mass of the analyte occurs [36, 37].

2.2.1.2.5 Resonance detection biosensors

Resonance biosensors utilize electromagnetic waves (surface plasmon waves) to sense the changes produced on the sensor during the interaction between the target analyte and the bio-recognition element. Upon exposure to any form of change, the resonance sensor produces a corresponding change in refractive index which is used as a measure of its sensitivity [37]. An interaction of the biomolecule with the analyte on the surface of the sensor causes a variation in the refractive index of the sensor [38]. This variation produces a corresponding change in the surface plasmon wave's propagation constant which is measured as the output signal. A significant advantage of a resonance sensor is that it is highly appropriate for real-time

monitoring as it operates as a label-free sensor without the use of fluorescence or radioactive materials [38].

2.2.1.2.6 Ion-sensitive FET (ISFET) detection biosensors

These are biosensors based on the combination of semiconductor sensitive field effect transistors with ion-sensitive surface. The construction of the ion-sensitive field effect transistors is achieved by wrapping the surface of the sensor with a polymer that has selective permeability for the respective ions. The polymer permits the diffusion of the ions through its pores and this diffusion creates an alteration in the field effect transistor potential. The electrical potential of the surface changes when an interaction occurs between the semiconductor and the ions, and this change in potential is measured [2].

2.2.1.2.7 Electrochemical biosensors

As far as electrochemical biosensors are concerned, the communication between the analyte and the biomolecule produces a chemical change proportional to the concentration of the analyte. This chemical change is converted to an electric signal which is measured. The transduction element is usually an electrode made of either platinum, gold, carbon, or silver [39]. Electrochemical biosensors possess many advantages such as simplicity, cost efficiency, portability, high specificity and selectivity [40, 41]. With regards to the signal transduction mechanism or the type of electrochemical variations detected during the interaction between the biomolecule and the analyte, the electrochemical biosensor can be classified as amperometric, conductometric, and potentiometric electrochemical biosensors.

Details of these type of electrochemical biosensors are presented in Table 2.1 below.

Table 2. 1 Examples of electrochemical biosensors, their working principles and types of electrodes employed.

Biosensor name	Working principle	Types of electrodes	References
Amperometric biosensor	Measurement of current as a function of time emanating from oxidation-reduction reaction in a biochemical reaction of the bioactive species. The magnitude of the current is dependent on the concentration of the analyte.	Working electrode (e.g. Au, C, Pt), reference electrode (e.g. Ag or Ag/AgCl) and counter electrode.	[42, 43]
Potentiometric biosensor	Measurement of electrical potential difference between the working and the reference electrodes which is produced during interaction between the bioactive material and the analyte when there is no or a negligible amount of current flowing through the electrode. The magnitude of the measured potential is proportional to the concentration of the analyte.	Working electrode (usually made of permselective ion-conductive membrane) and reference electrode.	[42, 43]
Conductometric biosensor	Measurement of the conductivity/ionic strength of an electrolyte solution between two electrodes due to enzymatic reaction in the electrode. The measured conductivity varies with changes in the concentration of the electrolyte/ionic species.	Working electrode and counter electrode	[44]

2.3 APPLICATIONS OF BIOSENSORS

Biosensors have found application in various fields including medical, pharmaceutical, agricultural, food and environmental fields. For instance, biosensors are applied in the clinical field for early detection of diseases. For example, Wang *et al.* [45] developed electrochemical biosensors for early detection of thyroid. Pesticides are known to exert negative effects on the nervous system. Hence, the identification of traces of these pesticides on crops in the agricultural industries will form a basis of an informed judgement whether the crops are safe for consumption or not. Consequently, biosensors meant for the detection of pesticides have also been developed including those developed by Ani *et al.* [46] and Ashish *et al.* [47].

Determination of the concentrations of individual ingredients in drugs is necessary to assess the efficacy or toxicity of a particular drug. This feat is now being achieved through the use of biosensors. For instance, Langdong *et al.* [48] designed a biosensor for recognition of STAT3 ligand concentration in herbal medicines. The existence of pathogens in the environment, particularly in water bodies can pose serious health-threatening consequences.

As a result, biosensors have been proposed for monitoring these organisms in the environment. An example of such a biosensor is those proposed by Foudeh *et al.* [49] for the detection of *Legionella pneumophila* and Enrico *et al.* [50] for the detection of E. coli in contaminated water samples. Similarly, biosensors for the detection of heavy metals such as mercury (Hg) [51], lead (Pb) [52] and so on have also been developed.

A number of biosensors have also been designed for sensing biological oxygen demand (BOD) and other water contaminants [53]. For their application in the food industry, biosensors for the quantification of amides, amines, carbohydrates, inorganic ions, acids etc. in food have been produced [54]. Again, for quality assurance purposes, the development of biosensors for the detection of microbes, bacteria and viruses has been extensively investigated [55]. An array of microbiological agents, chemicals and toxins have potential application in terrorist attacks and warfare. Hence, a dependable and fast/early recognition of this materials is of specific interest to security agents and health professionals to prevent and resolve issues related to biochemical weapons attack [56]. To achieve this aim, New Horizons Diagnostic Corporation (NHDC), for example, produced a biosensor for early and quick detection of botulinum toxin [57].

2.4 PROBLEMS/CONCERNS OF BIOSENSOR EFFECTIVENESS

To be regarded as efficient, a biosensor must possess certain valuable properties: It must demonstrate high specificity with regards to the analyte under consideration and be stable when stored under ordinary storage conditions. It must also be stable over a wide range of assays. Its activity should, as much as possible, not depend on physical factors such as pH and temperature so as to permit sample analysis with nominal pre-treatment. Additionally, a good sensor must have high sensitivity, a low limit of detection and a linear response in an accurate and precise manner over the suitable analytical range [55].

Although biosensors have been successfully applied in various aspects of life as mentioned in section 2.3, the majority of these sensors do not meet all of the

requirements of an effective biosensor and hence could have performed much better than their current performances. Efforts to address the problems of sensors inefficiency is being progressively pursued. One of the approaches being adopted to solve this problem is the use of 2D materials as components of biosensors as these materials are known to possess certain specific properties that can enhance the performances of the sensors. A detailed discussion of 2D materials with emphasis on their properties and their use in biosensors for enhanced efficiency is presented in the ensuing sections.

2.5 TWO DIMENSIONAL MATERIALS

Recent studies have shown that dimensionality plays a very important role in establishing the key properties of materials in addition to the arrangement of atoms in the material. A 2D material is defined as a material in which the bond strength and atomic arrangement along two-dimensions are similar and much stronger than along a third dimension [54]. These are the materials with few nanometers of thickness. The electrons in these materials experience free movement in the 2D plane but their movement in the third direction is restricted due to quantum mechanics [59].

2D materials have been one of the most studied classes of materials because of their unique physical phenomena which occur when charge and heat transport is confined to a plane [59].

The discovery of these newly found class of materials with their attendant exotic properties has been highlighted over the past decade due to the intense research activities that have been focused on them over other materials [60, 61] and recent

library of 2D materials as shown in Figure 2.3 [62]. These intense research activities by researchers all over the world have eventually led to a situation where around 140 hypothetical 2D materials have been discovered and studied till date [63, 64]. After the discovery of the first 2D material i.e. graphene in 2004, research studies in quite a number of other 2D materials have also been vigorously intensified.

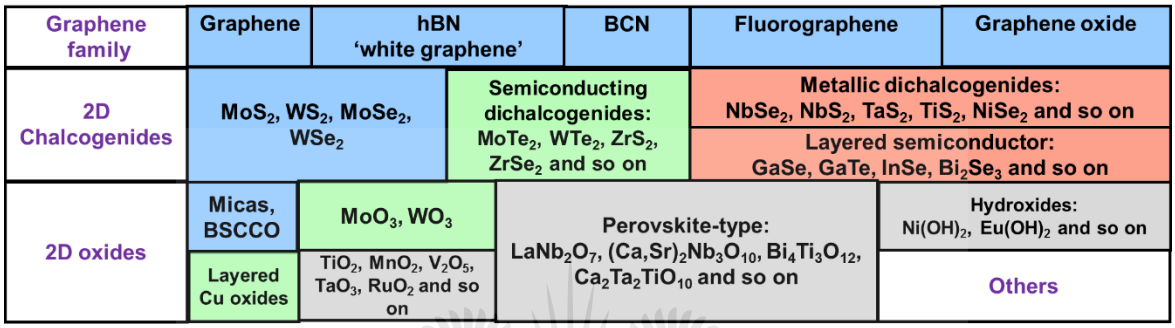

Figure 2.3 The 2D materials library [62].

Andre Geim and Konstantin Novoselov at the University of Manchester discovered graphene which led them to achieve a Nobel Prize in Physics in 2010 [65, 66]. Their ground breaking experiment which led to the isolation of the first single layer 2D material, graphene, through scotch tape exfoliation of graphite in 2004 [65, 66]. It showed that two-dimensional crystals might occur in a free-standing form and exhibit fascinating and unique physical properties [60].

But more than 80 years ago, researchers put forward their theory that due to the thermal fluctuations in low dimensional crystal lattices, atom displacement becomes comparable to interatomic distance at finite temperature [67]. They also theorized that with a decrease in thickness, the melting points of thin films decrease rapidly causing the films to segregate into islands with thickness of more than 12 atomic

layers [68, 69]. They concluded that 2D crystals were thermodynamically unstable and cannot exist without a three-dimensional base.

The existence of other layered 2D materials has since been made known, including TMDs and transition metal oxides (TMOs). TMDs possess the general formula MX_2 (X-M-X), where M could be any of the following metals including Hf, Zr, Ti, Mo, Ta, Bi, V and W; and X is a chalcogen (Se, S and Te) thus giving rise to an arrangement involving covalently bonded sheets with adjacent sheets attached by van der Waals forces. TMOs consist of transitional metals bonded to oxygen atoms [70, 71].

2.5.1 Classification of 2D materials

2.5.1.1 2D layered inorganic nanomaterials (2D-LINs)

2D-LINs consist of stacked sheets of inorganic nanomaterials with van der Waals forces between the layers. The 2D-LINs include hexagonal boron nitride (h-BN), MoS_2, WS_2, indium selenide (In_2Se_3), gallium selenide (GaSe), vanadium selenide (VSe_2), iron sulphide (FeS), tungsten selenide (WSe_2), molybdenum selenide ($MoSe_2$), gallium telluride (GaTe), and gallium sulphide (GaS) [72-74]. These materials have attracted attention, as new and novel inorganic layered materials due to their interesting physical and chemical properties. These materials exhibit weak van der Waal or hydrogen bonding (out of plane) and strong covalent or ionic bonding (in-plane).

2.5.1.2 2D layered ionic solids

These group of 2D materials consist of transition metal carbides and/or carbon nitrides labelled as MAX [75]. Their composition is generally represented as $M_{n+1}AX_n$, where M is a transition metal, A is groups 13 or 14 element, X is C and/or N, and n = 1, 2, or 3. Currently, more than 60 different pure MAX phases are known [76]. The bonds between the layers in the MAX phases are stronger in contrast to other layered 2D materials such as graphite and TMD which are made up of weak van der Waals interactions. The MAX family includes Ti_3C_2, Ti_2C, Nb_2C, V_2C, $(Ti_{0.5}, Nb_{0.5})_2C$, $(V_{0.5}, Cr_{0.5})_3C_2$, Ti_3CN, and Ta_4C_3 [74].

Another important class of 2D materials of layered ionic compounds consist of charged polyhedral layer sandwiched between hydroxide or halide layers by electrostatic forces. Exfoliated europium hydroxide such as $Eu(OH)_{2.5}(DS)_{0.5}$ [77] and perovskite-type oxides such as $KLnNb_2O_7$ and $RbLnTa_2O_7$ [78] are some examples.

2.5.1.3 Graphene

Graphene is an allotrope of carbon with sp^2 hybridized carbon atoms that are organised into a 2D honeycomb lattice with a C–C bond length of 0.142 nm (Figure 2.4) [79]. It is a zero-bandgap semiconductor with a conical band structure and an excellent in-plane conductivity [62]. The electrons in graphene act like massless relativistic particles with distinctive properties such as an anomalous quantum Hall effect [80] and ambipolar electric field effect along with ballistic conduction of charge carriers [81].

Apart from the above-mentioned properties, graphene sheets possess other peculiar properties that make them applicable in biosensors. Among these properties are a large surface area, greater elasticity, high mechanical strength, thermal conductivity and high electron mobility at room temperature [82]. In addition, graphene has the tendency to display voltage differences in the presence of a magnetic field at room temperature [50, 83]. It also exhibits excellent optical properties and tunable band gap with no existence of electron states. The comparatively low cost of production coupled with its environmentally friendly nature makes it more appropriate and a desirable material for the fabrication of biosensors [84, 85]. These properties of graphene endow graphene-based biosensors with enhanced performances.

Chemical functionalization of graphene prior to its use in biosensors is a necessary requirement. This process enhances its biocompatibility and hence ensures a successful biological receptor immobilization [85].

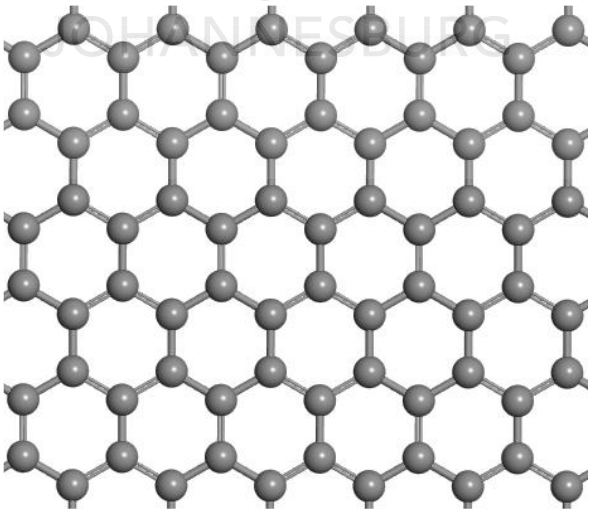

Figure 2.4 Structure of graphene (redrawn from [59]).

2.5.2 Application of 2D materials in biosensing

Following the discovery of graphene, research attention has been focused on the discovery of other 2D materials with exceptional and extraordinary properties. 2D materials have atomically-thin geometry with intrinsic flexibility and the ability to be easily integrated with various substrates due to the absence of surface dangling bonds. They also possess excellent electronic, optical and mechanical properties [86] and as a result, are considered as ideal materials for the design and fabrication of functional materials including biosensors. The next sections of this chapter discusses the progress that has been made in the utilization of graphene, layered ionic solids and layered inorganic nanomaterials as 2D material in enhancing the efficiencies of biosensors.

2.5.2.1 Application of graphene and graphene-related materials in biosensing

2.5.2.1.1 Application of graphene in biosensing

A number of graphene-based biosensors have been fabricated with reports indicating improved performances. For example, Afsahi *et al.* [87] developed a cheap and portable graphene-based biosensor for early recognition of Zika virus infection as shown in Figure 2.5. They applied the graphene-based biosensor in the detection of the Zika antigen in a human serum and attained a detection at a low concentration of 0.45 nM with high selectivity.

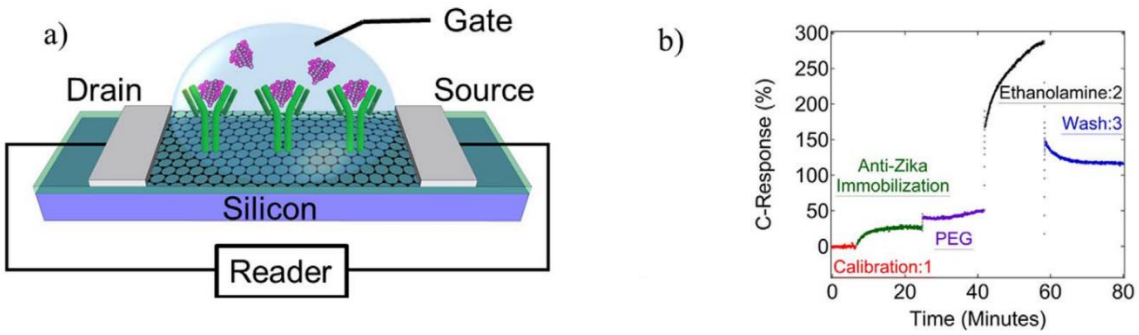

Figure 2.5 (a) Schematic representation (b) capacitance (%) response on the graphene biosensor chip surface [87].

Published data is available on the use of an enzymatic biosensor containing cerium oxide and graphene composite immobilized on glassy carbon electrode (GCE) [88]. The study was done comparatively using different electrodes consisting of cerium oxide and GCE, graphene and GCE, and cerium oxide-graphene GCEs. The efficiency of the sensor was observed to be higher in the electrodes containing the graphene, signifying the significance of graphene in the sensing mechanism. For the purposes of cholesterol detection, an enzymatic biosensor with graphene-based electrode has been developed [89]. Similarly, an electrochemical biosensor for H_2O_2 detection has also been reported [90] as shown in Figure 2.6. This sensor showed a linear response range of 0.3-1.8 nM, a detection limit of 0.11 µM, about 95 % steady state rapid response in 5s with a high sensitivity value of 2774.8 µA mM^{-1} cm^{-2}.

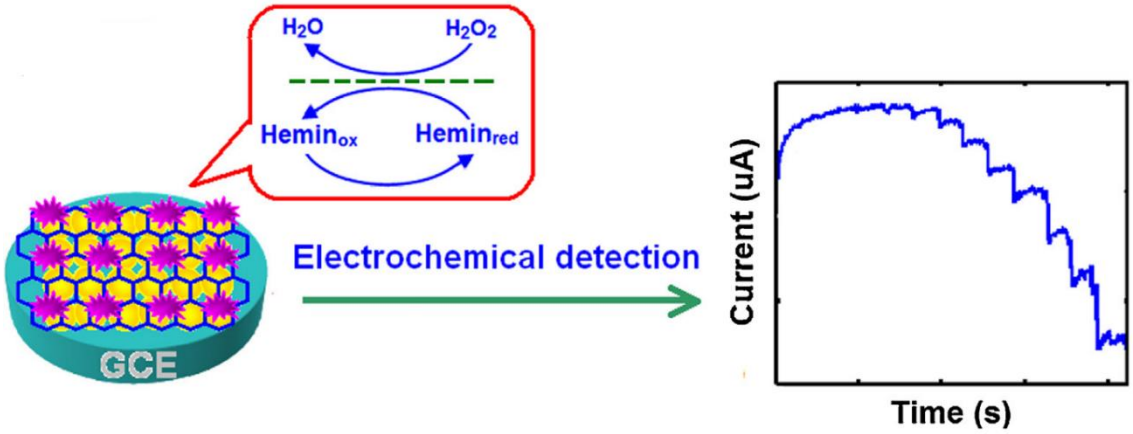

Figure 2.6 Preparation of the Hemin-graphene nanosheets/AuNP/GCE biosensor for the detection of hydrogen peroxide [90].

2.5.2.1.2 Application of graphene oxide in biosensing

GO is one of the graphene-related materials. Due to the existence of both hydrophobic and hydrophilic functional groups in its structure, GO disperses easily in water, displays high biocompatibility coupled with the ability to bind with a wide range of molecules. As a result, GO has been utilized in the fabrication of a number of biosensors. A GO-based label-free biosensor meant for aflatoxin B1 detection has been developed [91].

The GO was utilized in conjunction with AuNPs for the fabrication of the electrode on which the monoclonal antibody was covalently immobilized. The fabricated electrode was then used as the sensing platform for the detection of the aflatoxin antibody. A wide linear detection range of 0.5-5 ng mL, an impressive sensitivity of 639Ω/(ng/ml)/cm^2 with five weeks of storage stability were some of the attributes of the developed sensor [91]. Shaikh *et al.* [92] proposed a biosensor consisting of GO and a dual-peak long period grating meant for use as an immunosensor as shown in Figure 2.7.

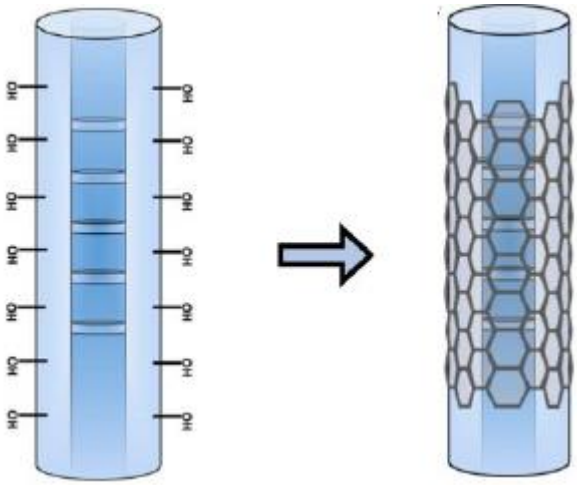

Figure 2.7 Schematic of the GO deposition on fiber optic sensor surface [92].

According to their study, the sensitivity of the dual-peak long period grating increased to about 150 % after it has been coated with GO. Upon immobilization of immunoglobulin G onto its surface, the GO-dual-peak long period grating based biosensor was deployed in detecting anti-immunoglobulin G and anti-prostate specific antigens. The performance of the sensor was impressive with high selectivity and sensitivity toward the respective antibodies [92]. A lectin immobilized-GO based label-free impedimetric biosensor for glycoproteins detection [93] and GO-based fluorescence sensor for estriol recognition [94] have also been performed with impressive sensitivity, selectivity and reproducibility results.

2.5.2.1.3 Application of reduced graphene oxide in biosensing

Reduced graphene oxide (rGO), another example of graphene-related materials, is viewed as one of the more suitable materials for biosensing application owing to its high electrical conductivity, and the fact that the deoxygenation procedure enhances the succeeding modification and immobilization of bio-recognition element onto its surface [95]. As a result, several rGO- based biosensors have been developed and

applied in the detection of various analytes. A study performed by Zhou *et al.* [96] involved the functionalization of 1-aminopyrene on rGO-GCE followed by immobilization of laccase onto the electrode as shown in Figure 2.8.

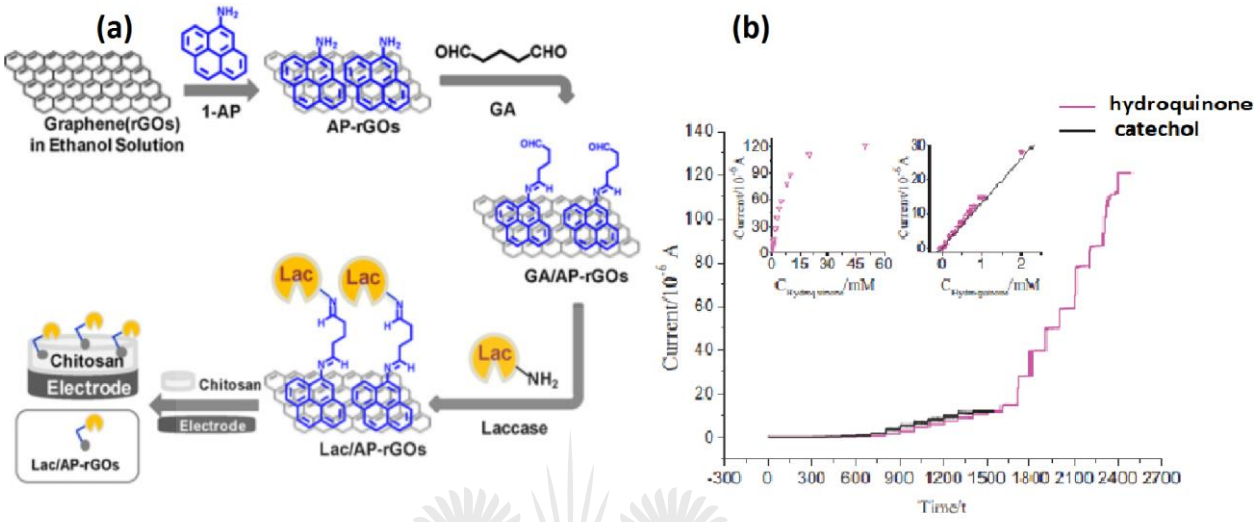

Figure 2.8 (a) Schematic diagram for the immobilization of Lac/AP-rGOs/Chit/GCE (b) current-time response of Lac/AP-rGOs/Chit/GCE of hydroquinone and catechol [96].

The fabricated biosensor was subsequently employed for the detection of hydroquinone and catechol. The sensitivity and linear range of the sensor were 14.16 μA mM^{-1} and 3–2000 μM respectively with respect to hydroquinone detection. For catechol detection, 15.79 μA mM^{-1} and 15–700 μM were the respective sensitivity and linear range results. The detection limits were measured to be 2 μM (hydroquinone) and 7 μM (catechol) within a response time of 5s. The sensor was stable for 7 days with more than 300 fold sensitivity and excellent repeatability with 3.96 % standard deviation [96].

Again, Zhou *et al.* [97] described the use of an rGO based electrochemical sensor on a GCE for the concurrent determination of four DNA bases. The analysis showed that the rGO-GCE electrode was more effective than the bare graphite and the GCE

electrodes as the rGO-GCE electrode displayed a comparatively higher electrochemical activity. In a similar manner, cyclin A_2 detection was performed through the use of rGO-porphyrin electrode as an electrochemical impedance sensor. The schematic representation is shown in Figure 2.9.

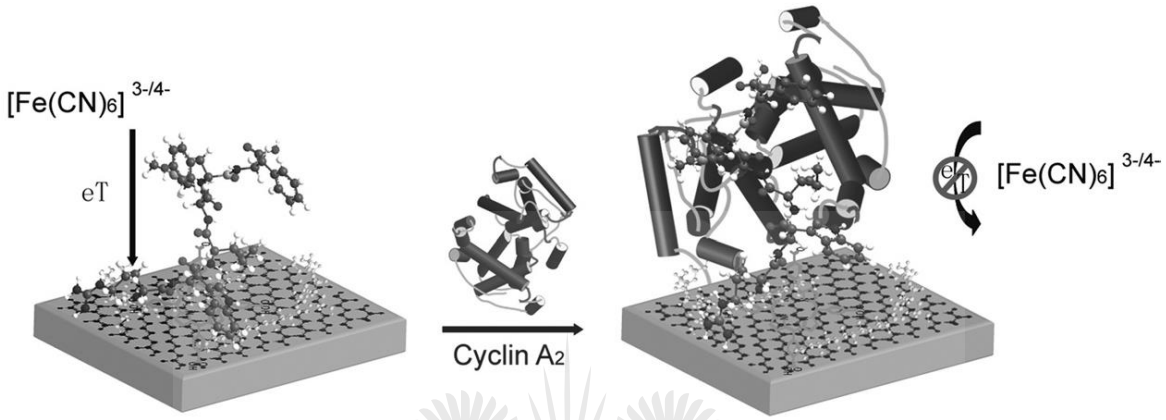

Figure 2.9 Schematic diagram of the porphyrin graphene-based peptide sensor for cyclin A_2 detection [98].

The fabrication and application of a 3-amino propyl triethoxy silane functionalized zirconium oxide (ZrO_2) coated rGO based biosensor for the detection of aflatoxin B1, a food toxin, has been carried out by Suveen *et al.* [99]. The electrochemical studies proved that the rGO based sensor was capable of detecting the aflatoxin B1 within a wide linear detection range of 0.1-2.5 ng/ml. The sensitivity and stability of the sensor were remarkably high with values of 1.2 mA mL ng^{-1} cm^{-2} sensitivity and up to eight weeks of stability.

2.5.2.2 Application of non-graphene 2D materials in biosensing

2.5.2.2.1 Application of molybdenum disulphide in biosensing

Various 2D non-graphene materials have been used in electrochemical biosensing for the detection of analytes such as glucose, dopamine, H_2O_2 and DNA [100]. An

example of these types of material is MoS_2. The structure of MoS_2 is made up of a Mo atom sandwiched between two atoms of S, with the three layers stacked together forming a layered structure (Figure 2.10) [61].

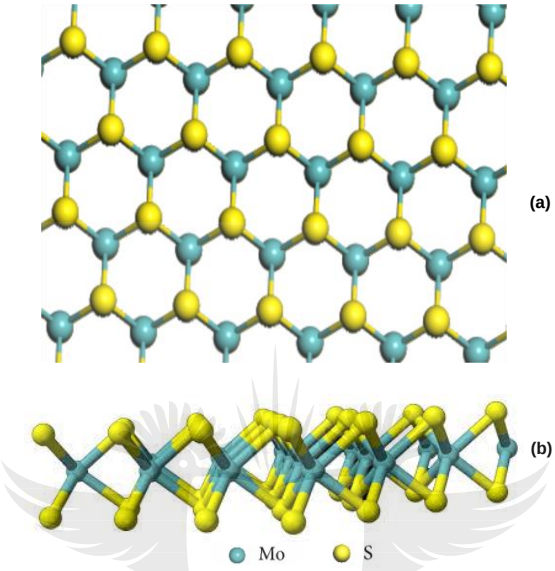

Figure 2.10 (a) Top view and (b) side view of the structure of MoS_2 (redrawn from [61]).

MoS_2 has been identified as an excellent functional material owing to the fact that the 2D electron-electron interactions among the Mo atoms in the structure help in promoting planar electric transport tendencies [101]. Consequently, MoS_2 has been used in a number of biosensing platforms [102-105].

A MoS_2 based field-effect transistor biosensor was developed (see in Figure 2.11) and applied in a quantitative prostate cancer antigen detection through the reduction of non-specific molecular binding events and the realization of even adsorption of the prostate cancer antigen onto the surface of the MoS_2 [106].

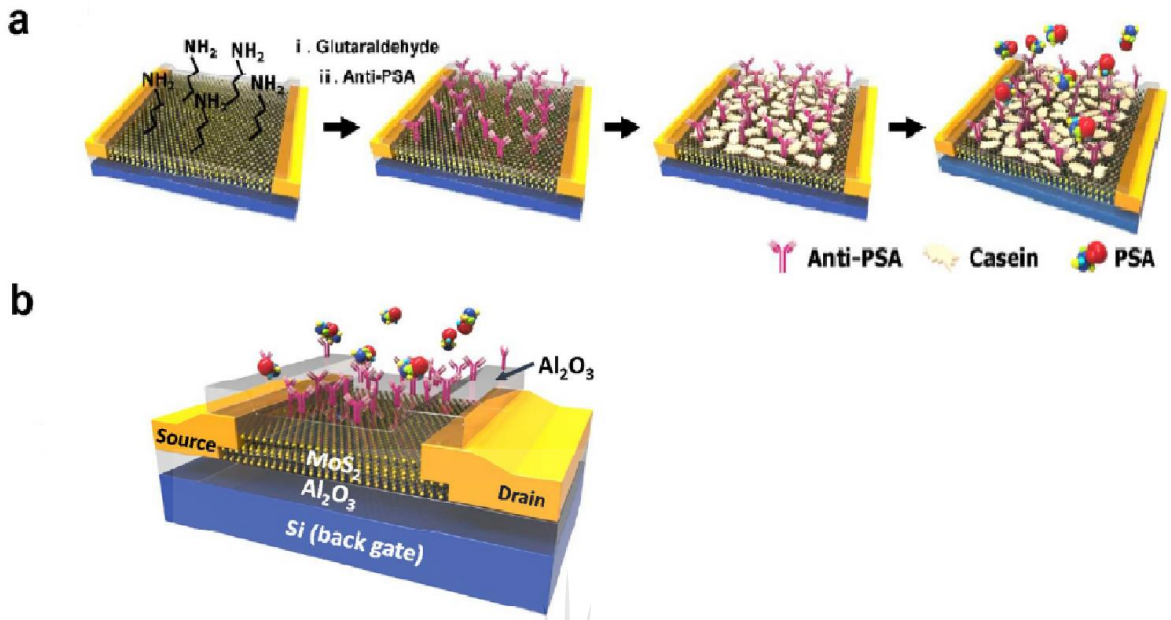

Figure 2. 11 (a) Schematic diagram of experimental procedure for the preparation of anti-PSA on MoS_2 surface with PSA and (b) a pseudo double gate structure of a MoS_2 biosensor [106].

The sensor detected a low concentration of the antigen (0.0001 ng/mL) with a 9% standard error apart from demonstrating excellent sensitivity and reproducibility and was proposed to be appropriate for diagnostic applications [106]. Similarly, a field-effect transistor biosensor for the detection of a prostate cancer antigen has been developed by Lee *et al.* [107] based on a multilayer MoS_2 through a back-gated scheme with no insulating oxide requirement (see Figure 2.12). In this sensor, the MoS_2 surface played the two roles of a transducer and the recognition element with a major enhancement in its sensitivity due to its hydrophobicity. The sensor achieved a minimum of 0.001 ng/mL limit of the prostate cancer antigen concentration, much below the acceptable clinical detection limit of 4 ng/mL [107].

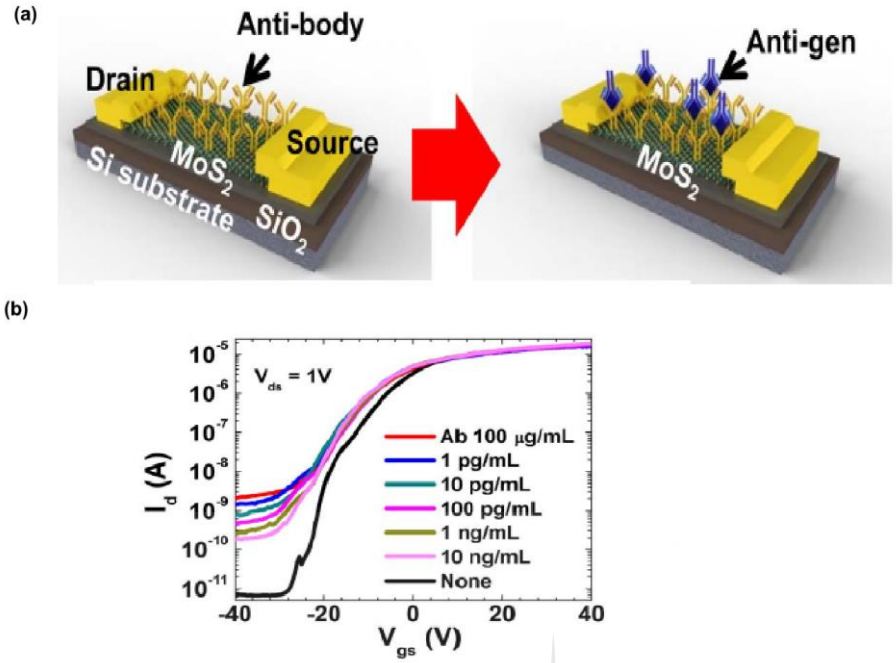

Figure 2. 12 (a) Schematic of a MoS_2 biosensor illustrating PSA antibody with the binding of PSA antigen with antibody receptors. (b) transfer characteristics of MoS_2 biosensor functionalized by anti-PSA under various PSA concentrations [107].

In their study, Shan *et al.* [108] fabricated a bilayer MoS_2 based FETs as a biosensor for glucose detection. The fabricated sensor was noted to respond linearly to increasing glucose concentration. The source-drain current was observed to increase in direct proportionality with glucose concentration [108]. The bilayer MoS_2-based FET sensor's sensitivity was determined to be 260.75 mA mM^{-1} with 300 nM as the detection limit. They noted that the developed biosensor exhibited certain advantages, including a short response time of less than 1 second, linear detection range between 300 nM and 30 mM and excellent stability. A similar glucose sensing platform was fabricated using silver nanoparticles (AgNPs) coated MoS_2 based interface system. This resulted in 97.5% reproducibility with a high stability for the fabricated sensor [109] as shown in Figure 2.13. The sensor also displayed

impressive sensitivity values of 9044.6 $\mu AmM^{-1}cm^{-2}$, a linear range of 0.1–1000 µM and a very low limit of detection of 0.03 µM [109].

Together with high selectivity, the sensor was regarded as being appropriate enough for application in glucose detection in human body fluids including saliva and sweat.

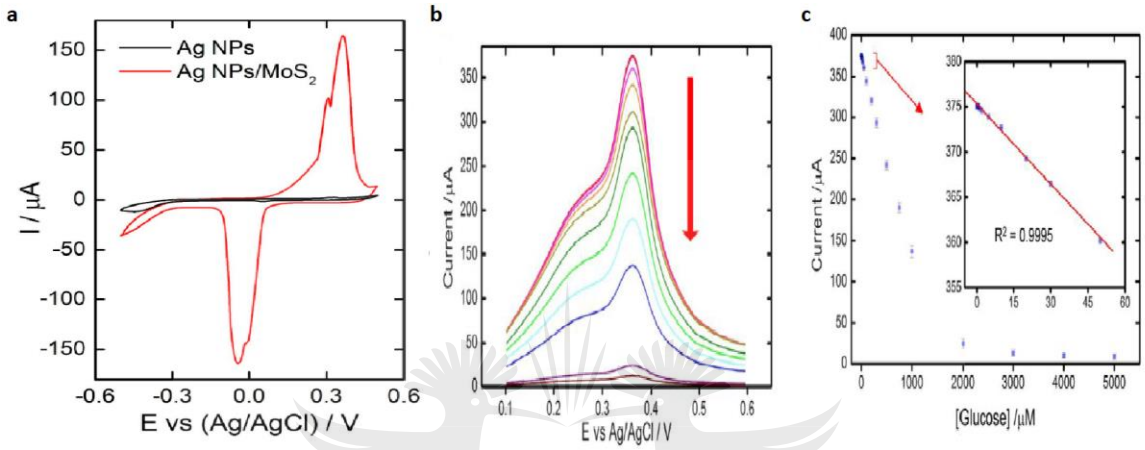

Figure 2.13 Electrochemical characterization (a) cyclic voltammetry of AgNPs and AgNPs/MoS_2 electrodes at a scan rate of 0.1 V. s^{-1} (b) square wave voltammetry (SWV) curves of the AgNPs/MoS_2 electrode containing different concentration of glucose (c) the calibration curves (concentration vs current) of the biosensor [109].

2.5.2.2.2 Application of tungsten disulphide in biosensing

Tungsten disulfide, WS_2, is a classic example of inorganic equivalents of graphene (see Figure 2.14) [62].

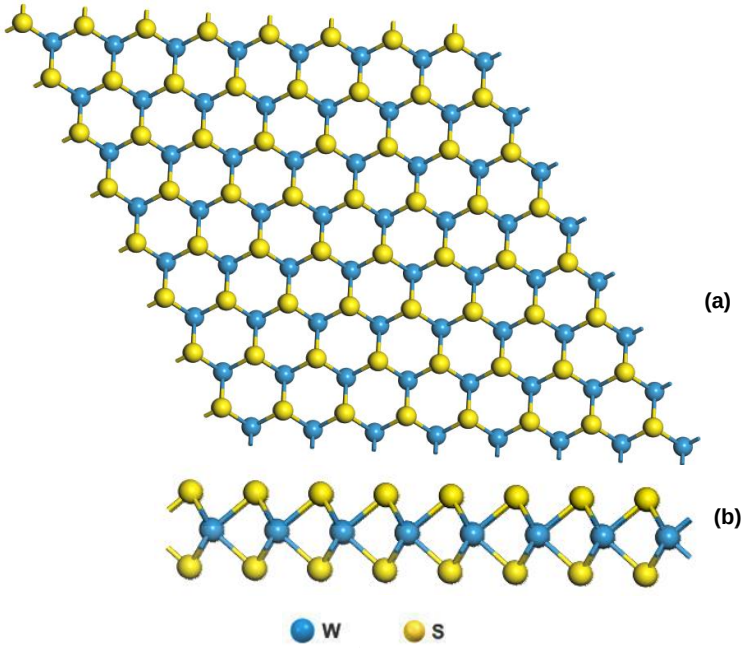

Figure 2.14 (a) Top view and (b) side view of the structure of WS_2 (redrawn from [110]).

Layered WS_2 has a trigonal prismatic coordination and comprises of sandwiched S–W–S bonds [111, 112]. WS_2 nanosheets can be produced in large quantities at a low cost. They have a large surface area to volume ratio and are reported to be highly conductive and exhibit catalytic and sensing ability. They are easily dispersed in aqueous solutions [113]. These properties make WS_2 nanosheets feasible for application in biosensors [113]. As a result of these interesting properties, several documented research works on the use of WS_2 based biosensors for the detection of many biological molecules are available. Among these documented research works is the one published by Li *et al.* [114]. They fabricated a biosensor consisting of WS_2 and single-stranded DNA (WS_2-ssDNA) for adenosine triphosphate (ATP) detection as shown in Figure 2.15. They initially immobilized the DNA sequence with –SH at one end on a gold electrode followed by the immobilization of WS_2 nanosheets on the surface of the gold-DNA/SH electrode.

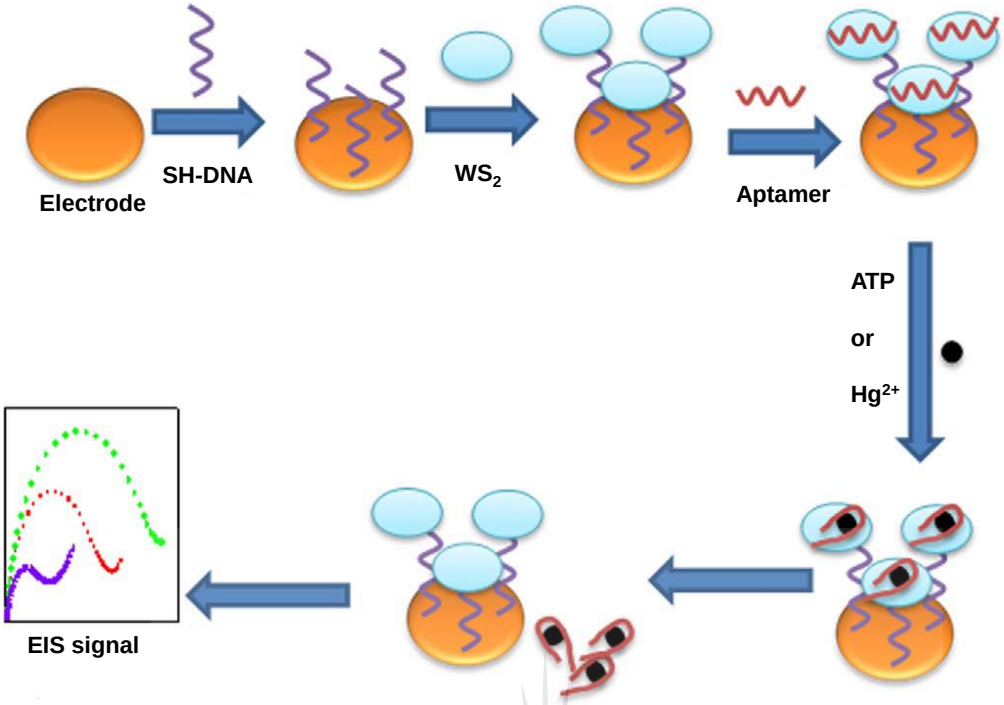

Figure 2.15 Schematic illustration of the electrochemical sensing for the detection of ATP or Hg^{+} [114].

Subsequently, the ATP binder was immobilized on the WS_2-Au-DNA/SH electrode. These immobilizations were possible because of the high attraction between the single-stranded DNA and the WS_2 [114]. The sensor was noted to be highly sensitive, selective and stable toward the detection of ATP due to the peculiar interaction within the WS_2-ssDNA interface and the explicit recognition between the aptamers and the target.

Again, a 1T phase WS_2 nanosheet has been used for the fabrication of a biosensor for H_2O_2 detection [115]. The sensor fabrication involved the immobilization of haemoglobin on the 1T phase WS_2 nanosheet and the subsequent entrapment of glutaraldehyde on the haemoglobin. The 1T-WS_2 nanosheet was identified to play a number of roles in the sensor's ability to detect H_2O_2. It provided a large surface area and a conductive surface for the immobilization of the haemoglobin, facilitated

the transfer of electrons to the surface of the electrode, and demonstrated electrocatalytic activity toward H_2O_2 reduction as shown in Figure 2.16.

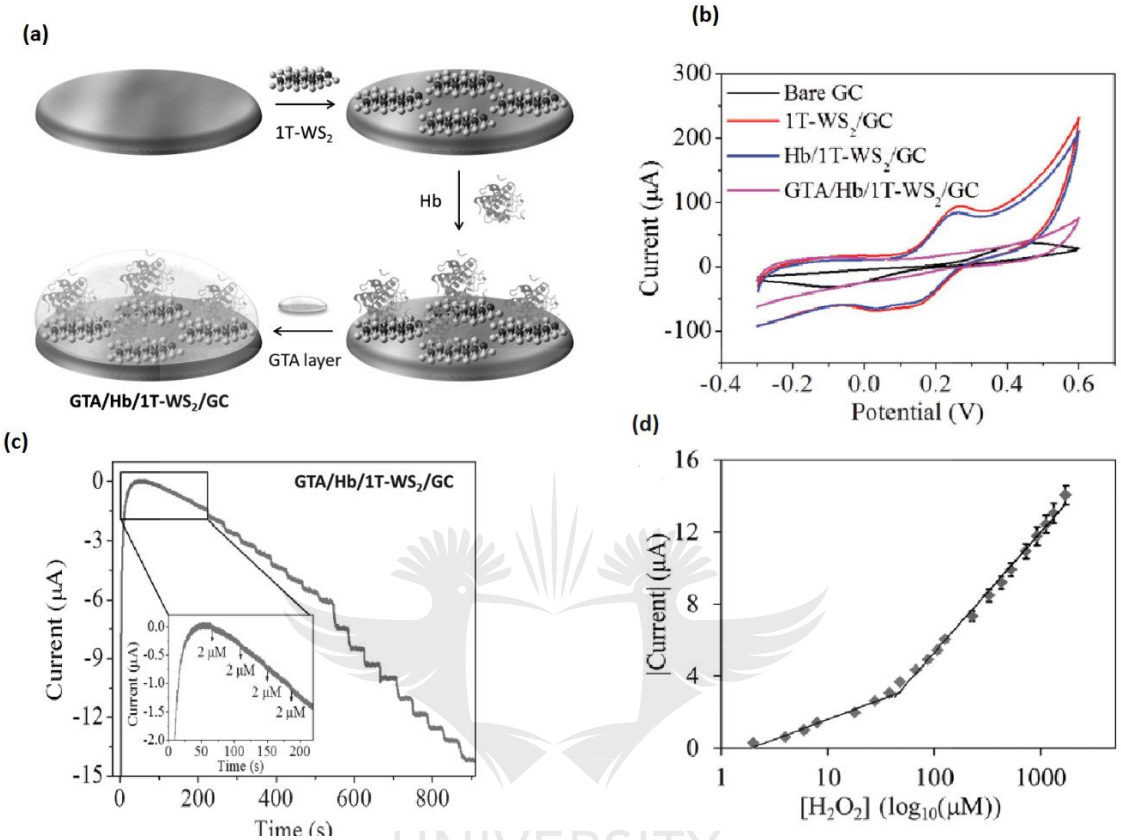

Figure 2.16 (a) Schematic representation of the construction of GTA/Hb/1T-WS_2/GC electrode (not to scale) (b) cyclic voltammograms of ferri/ferrocyanide redox probe at various modified electrodes at scan rate 100 mVs^{-1} (c) chronoamperometric responses of the GTA/Hb/1T-WS_2/GC upon successive additions H_2O_2 (d) logarithmic relationship between the concentration of H_2O_2 and the catalytic current of the GTA/Hb/1T-WS_2/GC [115].

WS_2 based biosensor displayed impressive results in terms of its ability to selectively sense the H_2O_2 over a wide range with high stability and reproducibility [115]. WS_2 has also been employed in designing a surface plasmon resonance biosensor which was used to sense glycerin solutions [116]. This analysis was done by employing both theoretical and experimental approaches. According to the result, the theoretical results corroborated those of the experimental ones confirming that the

presence of WS_2 enhanced the sensitivity of the sensor over 300 folds. They attributed this improved sensitivity to the excellent optical absorption property of the WS_2 which promoted the rate at which light energy was converted to electrical energy followed by enhanced resonance effect, and the fact that the WS_2 provided a large sensing surface area for adsorption of the analyte. A WS_2-CdS heterojunction based biosensor for the determination of glutathione has also been studied by Zang *et al.* [117].

2.5.2.2.3 Application of boron nitride in biosensing

BN, 'white graphene' as the structure of BN is analogous to graphene whose availability is quite economical and has potential applications in field of catalysis and sensing [103]. BN usually exists as flakes or sheets as shown in Figure 2.17.

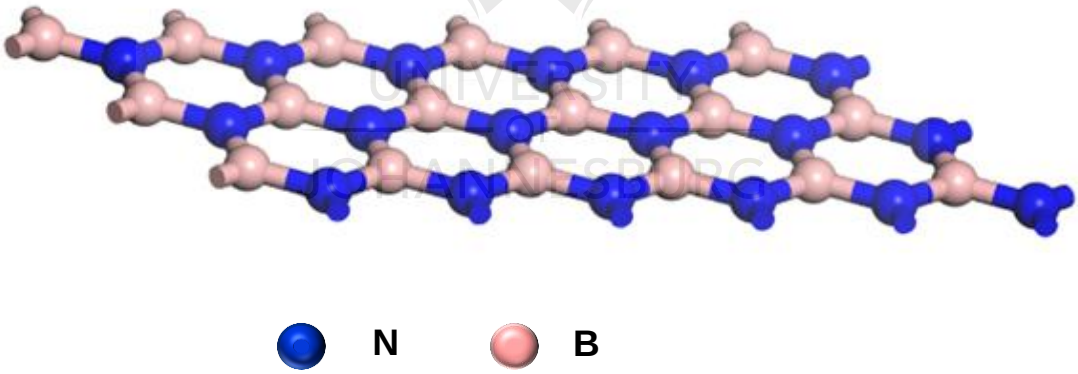

Figure 2.17 Structure of BN (redrawn from [62]).

The hexagonal polymorph of BN present as a semiconductor and has been applied in sensors. It is, however, important to note that BN has high hydrophobicity which renders it difficult to disperse in water. Thus, BN requires addition functionalization or surface treatment prior to its use as a component of a biosensor [118]. A study by Xu *et al.* [119] involved the functionalization of BN with chitosan that improved its hydrophilicity and

hence permitted the immobilization of catalase on its surface. The designed biosensor was then used for sensing for chlorfenuron within linear range and detection limits of 0.5–10 mM and 0.07 µM respectively. An electrochemical biosensor system containing BN nanosheet and AuNPs has also been reported for H_2O_2 detection [120] as shown in Figure 2.18.

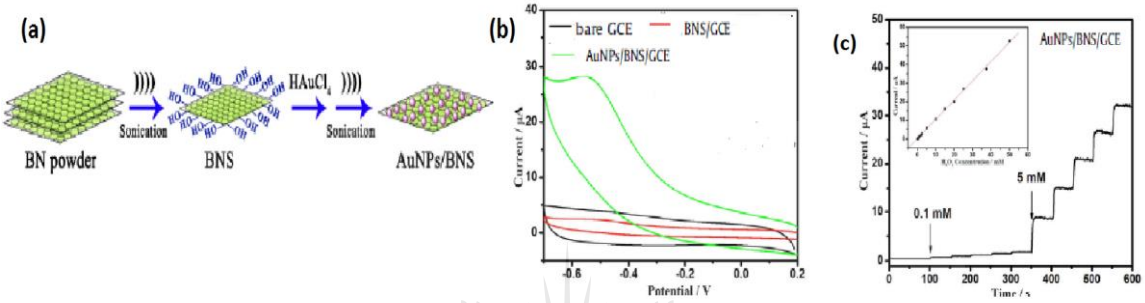

Figure 2.18 (a) Illustration of the synthesis of AuNPs/BNS nanocomposites (b) cyclic voltammograms of different modified electrodes 0.1 M PBS at pH 7.4 in the presence of 10.0 mM H_2O_2 at scan rate 50 mV s^{-1} (c) chronoamperometry response of AuNPs/BNS/GCE to successive addition of H_2O_2 into PBS under stirring (The insert is the calibration curve) [120].

Through fluorescence and electrochemical methods, another biosensor consisting of a hexagonal BN and AuNPs was developed and applied in detecting interleukin-6 [121]. Qun *et al.* [122] demonstrated the fabrication of an amperometric sensor through the use of a platinum nanoparticle (PtNP) and porous hexagonal BN whiskers. They noted that the fabricated electrode displayed a noteworthy amperometric response with regards to H_2O_2 reduction and oxidation processes and hence used it as a glucose sensor through the immobilization of glucose oxidase on its surface. The distinctive properties of the sensor include a fast response time of 5 s, 0.1–2.7 mM linear range, 14.1 µM detection limit with a sensitivity of 6.37 mA M^{-1} cm^{-2} [122].

2.6 ELECTROCHEMICAL TECHNIQUES

2.6.1 Overview of Electrode Processes

Electrochemistry is a branch of chemistry which involves the study of the chemical changes due to the passage of an electrical current and chemical reactions that results in the production of electrical energy. Electrochemistry is an efficient tool for probing reactions involving electron transfer and for understanding the kinetics and thermodynamics of electrode reactions.

Electrochemistry field involves the measurements of different electrical quantities, for instance, potential, current, charge, and also their connection to chemical parameters [123].

Electrochemical techniques have been divided into two major types namely; controlled current and controlled potential techniques. Electrolysis, coulometry and chronopotentiometry are examples of controlled current techniques. The controlled potential methods comprise mostly of other electrochemical techniques like potential step (chronoamperometry, chronocoulometry, and differential pulse voltammetry (DPV)), potential sweep (CV, anodic stripping voltammetry, rotating disk electrode) [124] and EIS.

The controlled potential techniques deal with charge transfer processes that take place at the electrode solution interface and has advantages like high selectivity and sensitivity towards electroactive species [125]. In these techniques, potentiostats are used in keeping the potential at a certain value while the current is measured. This kind of techniques is called voltammetric techniques.

The scope of electrochemistry has been increased over the years from basic concepts e.g. electrophoresis electroanalysis, corrosion, electrosynthesis, and metal electroplating to device application e.g. electrochemical sensors [126], energy storage (batteries and fuel cells) [127, 128] and energy conversion devices. To understand electrochemistry in detail, it is necessary to explore some basic concepts related to it.

2.6.1.1 Electrochemical cells and reactions

There are some processes which influence the transport of charges across the interface between an electrolyte and electrode. In an electrochemical system, two electrodes are separated by at least one electrolyte phase. The difference in electric potential that occurred between the electrodes is then measured by a high impedance voltmeter. Both electrodes are linked by conducting paths via ionic transport (through the electrolyte) and via electric wire externally for transportation of charge [129].

The electrode reactions are usually heterogeneous in nature and they occur at the interfacial region between a solution and an electrode. The electrode processes or reactions produce a very small unbalance in the electrode's electric charges, resulting in an interfacial potential difference. At an interface, the magnitude of the potential difference influences the relative energies of charge carriers of the different phases which control the rate and direction of charge transfer [123].

In an electrochemical cell, the cell potential (V) determines the collected differences in electric potential between all the different phases. So, the measurement of cell potential has become the most important aspect of experimental electrochemistry.

To understand the thermodynamic properties of electrode processes, it is necessary to know about the structure of the electrochemical cell. When an electrochemical reaction occurs at each electrode, the reaction is called half-cell reaction which means the presence of two electrodes in a typical cell. The overall chemical reaction is made up by combining two independent half-cell reactions. Each half-reaction represents the interfacial potential difference at the corresponding electrode.

For the occurrence of a redox reaction, the two materials in each half-cell are attached by a closed circuit in which electrons can flow from the reducing agent to the oxidizing agent.

For example, Zn(s) is constantly oxidized to produce Zn^{2+} (aq) as shown in equation (2.1):

$$Zn(s) \rightarrow Zn^{2+}(aq) + 2e^{-} \quad \text{.....(2.1)}$$

Again, Cu^{2+} is reduced in the cathode (equation 2.2):

$$Cu^{2+}(aq) + 2e^{-} \rightarrow Cu(s) \quad \text{.....(2.2)}$$

So this electrochemical cell is notated as in equation (2.3)

$$Zn\,(s) / Zn^{2+}\,(aq) // Cu^{2+}\,(aq) / Cu\,(s) \quad \text{.....(2.3)}$$

In this notation, / denotes a phase boundary, // represents the separation of the anode half reaction from the cathode half reaction. The state of the solution is written adjacent to its corresponding element. According to IUPAC convention, oxidation takes place at the anode (left half-cell) and reduction at the cathode (right half-cell) [130].

The Nernst equation for the whole cell is represented in equation (2.4)

$$E_{cell} = E^{o}{}_{cell} + \frac{RT}{nF} \ln \frac{a_{Cu^{2+}}}{a_{Zn^{2+}}} \quad \text{.....(2.4)}$$

This equation relates the activities of the oxidized and reduced species involved in the reaction with the electrode potential of the cell E_{cell}. Where $E^{o}{}_{cell}$ is the standard potential of the oxidized ($a_{Cu^{2+}}$) and reduced ($a_{Zn^{2+}}$) species and $a_{Cu^{2+}} = a_{Zn^{2+}} = 1$, n is the number of electrons transferred (here, n=2), the value of R is 8.314 J K^{-1} mol^{-1}(universal gas constant), the value of F is 96.485.33 C mol^{-1} (Faraday constant) and T denotes temperature (Kelvin).

An electrochemical cell in which electrical energy is obtained from spontaneous redox reactions which occurred within the cell is called galvanic or voltaic cell [123].

Oxidation is spontaneous at the anode which means that excess electrons are present at the electrode. Galvanic cell has many commercial applications especially non-rechargeable cells, rechargeable cells and fuel cells. On the other and, an electrochemical cell in which the electrical energy generated from external voltage source is used to deliver electrons and the corresponding energy regulates the direction of the electrode reactions is known as an electrolytic cell. The electrolytic cells have potential application in electrolytic syntheses (e.g., the production of aluminium and chlorine), electroplating (e.g., gold and silver) and electrorefining (e.g., copper).

2.6.1.2 Faradaic and non-faradaic processes

Two types of processes take place at the electrode. The first type is related to reactions in which transportation of charges happens across the electrode/solution

interface. The reactions obeyed Faraday's law which means the amount of charge generated (current flow) is directly proportional to the amount of chemical reaction taking place and it is known as faradaic process [123].

When some reactions are thermodynamically or kinetically unfavourable, then no charge transfer reactions occur, and this process is a non-faradaic electrode process. However, in a non-faradaic electrode reaction, adsorption and desorption processes occur and also the electrode-solution interface can be modified with varying potential or solution composition [123].

Both faradaic and non-faradaic processes may take place at an electrode. In a faradaic process, there is no change in bulk phase composition, voltage and electrode charge with applied constant current. Thus, a steady state current-voltage curve can be obtained experimentally. For a non-faradic (capacitive) process, charges are stored and also the electrode composition varies with time from which a charge-voltage curve may be obtained [131].

2.6.1.3 Electrode processes

It is important to study the transportation of species to the electrode surface and this can be accomplished by mass transport toward the electrode surface [132].

There are three possible different transport mechanisms

(a) Diffusion

(b) Migration

(c) Convection

In electroanalytical experiments**,** diffusion occurs at the electrode/electrolyte interface when redox reaction occurs at the electrode surface [123]. Figure 2.19 is the schematic representation of a typical electrode process.

The general electrochemical process has shown that electrode reaction rate depends upon mass transfer of oxidized species, transfer of charge from bulk solution to the electrode surface, several chemical reactions which contain dimerization or protonation processes and catalytic decomposition which happens on the surface of electrode and other desorption, adsorption, or crystallization and electron transfer at the surface of the electrode [123].

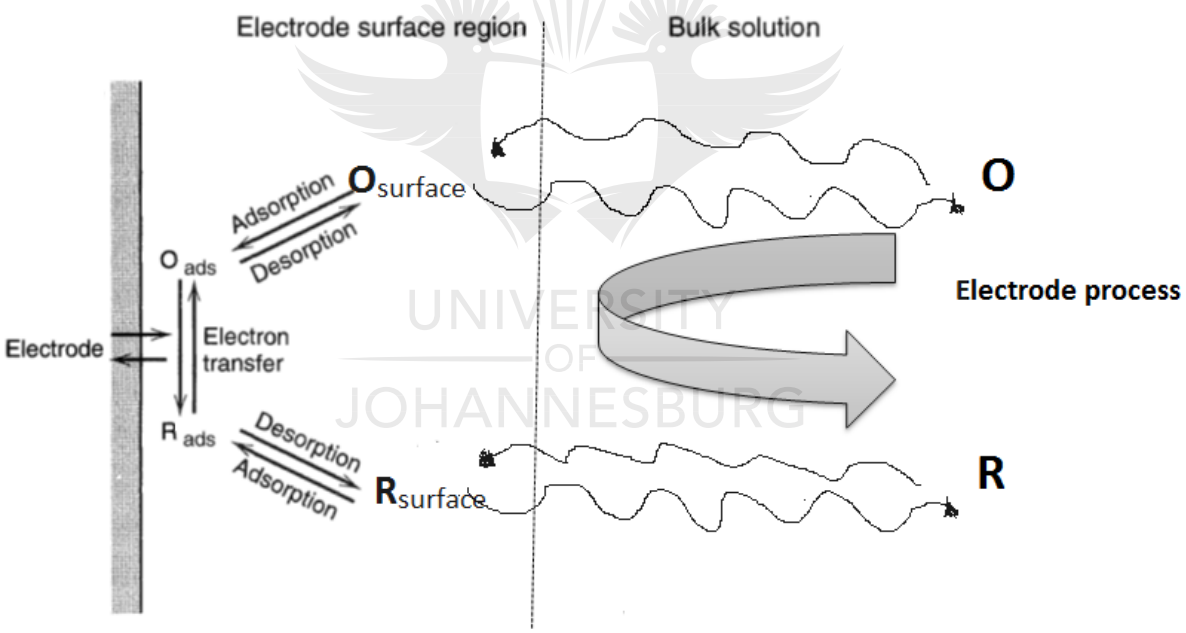

Figure 2.19 The schematic representation of electrode processes [123].

There are two types of electrode processes, one is that controlled by diffusion and the other one is controlled by kinetics of the electrode reaction as shown in Figure 2.19. In a diffusion controlled process, the rate of mass transport to the electrode surface is the slowest step of electrode processes which determines the rate of the

overall process. In kinetic controlled processes, diffusion is more prompt than electrode reaction hence the rate of the process is determined by kinetics [123].

2.6.1.4 Electrical Double Layer

It is important to understand the electron transfer between the analyte in solution and surface of the electrode. The structure of the electrode–solution interfacial region has been comprehensively studied. Firstly, Helmholtz considered the problem of a charged surface connected with an electrolyte solution which gave rise to the designation of double layer [133] and later Gouy and Chapman changed the classical model with the introduction of diffuse double layer. They concluded that the double layer with a flexible thickness in which ions are allowed to move freely into solution and the value of double layer capacity depends upon applied potential and electrolyte concentration [134, 135].

In 1924, Stern combined Helmholtz model and Gouy-Chapman model and proposed that the double layer was created by a dense layer of ions near electrode which is followed by a diffuse layer spreading into bulk solution [136]. Further work was carried out by Grahame, with the addition of one more region close to the electrode surface due to the existence of specific adsorption. Modern models of the double layer have considered the physical nature of the interfacial region [137]. Bockris, Devanathan and Müller model showed the majority of solvent molecules near the interface [138].

As shown in Figure. 2.20, the solution component vicinity of the electrode surface can be divided into several layers. The region close to the electrode, the inner layer contained absorbed solvent molecules and ions or molecules which is also known

as inner Helmholtz plane (IHP) which is the locus of the centre of absorbed species at a distance x_1, Outer Helmholtz plane (OHP) x_2, is the closest distance a solvated ion can get to the surface, which is the locus of the centres of these nearest solvated ions. The interaction of solvated ions with charged metal comprises of long-range electrostatic forces and these solvated ions are not specifically adsorbed. The non-specifically adsorbed species are spread to the diffuse layer which spreads from OHP into the bulk solution [139].

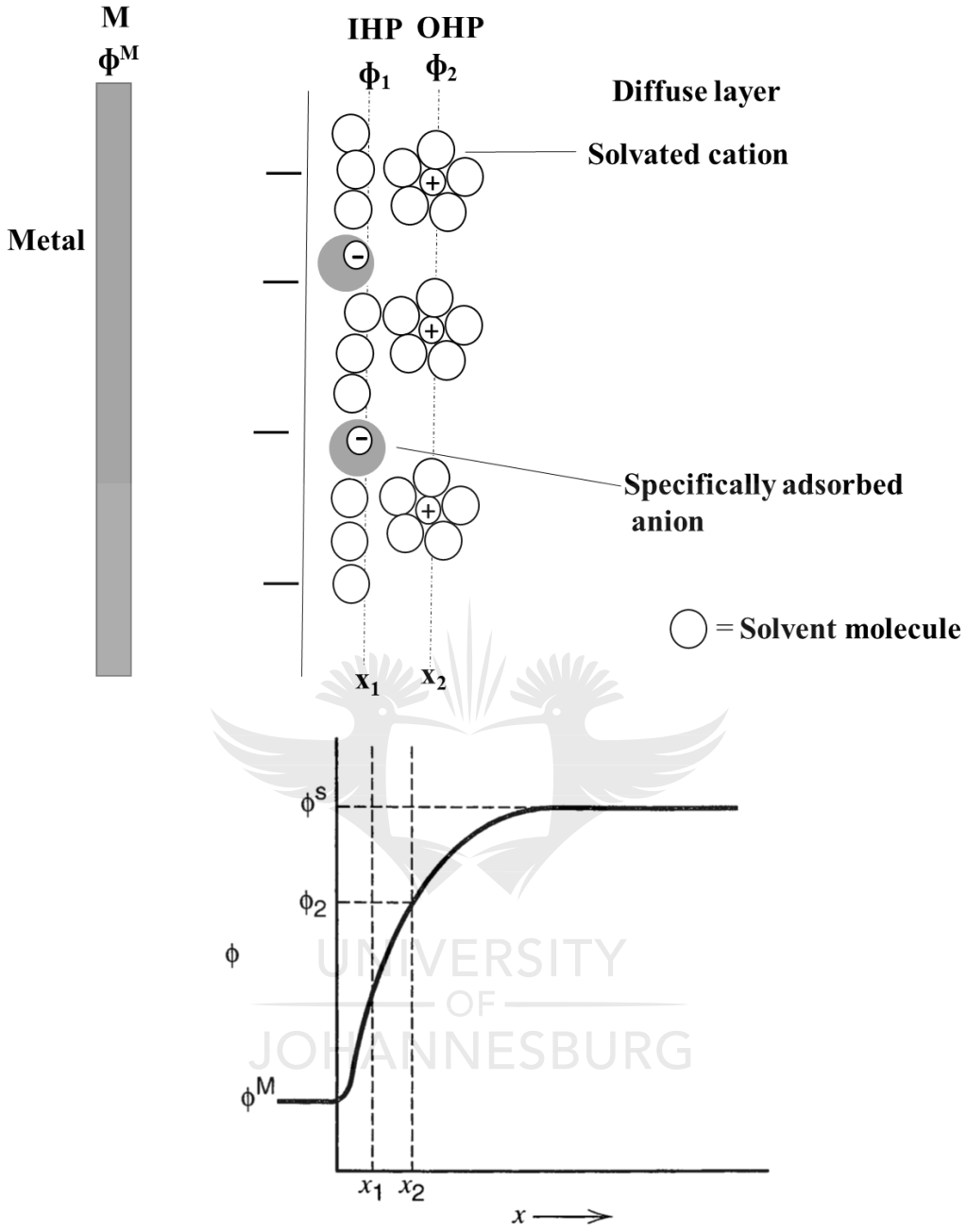

Figure 2.20 A schematic diagram of a typical model of the double-layer region between the solution and metal with the negatively charged surface where x is the distance and ϕ is the inner potential [123].

The double layer structure can interfere with the rates of electrode processes. When the electroactive species is non-specifically adsorbed, they can go toward the electrode till OHP. There is a potential drop from the electrode surface to the solvated molecules and the total potential is less than the potential between the

solution and the electrode by an amount ϕ_2-ϕ^S, which is referred to the potential drop across the diffuse layer. ϕ^S is the potential of the solution [123].

2.6.2 VOLTAMMETRIC TECHNIQUES

Voltammetry is an electrochemical analytical technique where the current versus potential behaviour at an electrode surface is assessed. Mostly, the applied potential (E) is varied or the current (I) is monitored over a period of time (t).

In voltammetric methods, the concentration of electroactive species is directly proportional to the current as a range of potentials are scanned. This change in concentration happens at the electrode surface due to oxidation or reduction process [123].

For the valuation of electrochemical sensors, numerous voltammetric methods, i.e., potential step voltammetry (PSV), linear sweep voltammetry (LSV), DPV, square-wave voltammetry (SWV) and CV have been used and discussed in detail later.

The following section summarizes some voltammetric techniques.

2.6.2.1 Potential Step Voltammetry

In an electrochemical cell, changing of the potential signal is implemented on a working electrode and this generates a typical current response which can be determined in a PSV method.

In potential step technique, the voltage applied to the electrode is increased from V_1 to V_2 and the corresponding current is measured as the function of time [140] as presented in Figure 2.21(a & b).

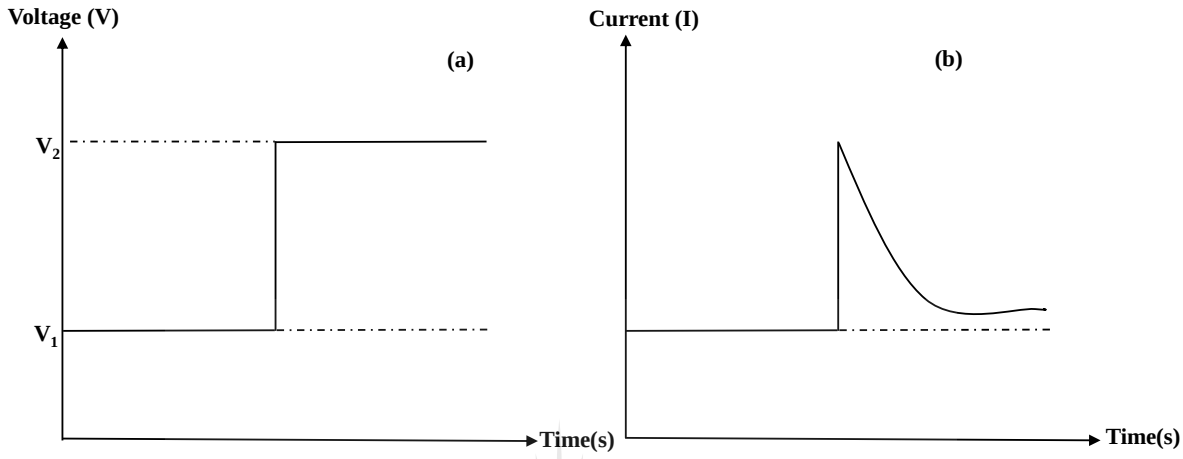

Figure 2.21 A schematic illustration of (a) potential step (b) corresponding current in potential step voltammetry [140].

Here, when the voltage is increased to V_2 then current starts rising sharply and then drops back as a function of time, due to slow diffusion of the electroactive species to the surface of the electrode.

The concentration gradient drops when the material can diffuse away from the electrode. The number of reactants decreases with the drop of the concentration gradient and therefore the current also decreases. Potential step voltammetry helps to estimate the diffusion coefficients of the species in the electrolyte [123].

2.6.2.2 Linear Sweep Voltammetry

In the LSV, the potential is applied over a certain range and current range is recorded as a function of sweep potential rather than time. The potential of the working electrode starts from value E_1 at which oxidation cannot go through

reduction to a potential E_2 where the reaction arises quickly as shown in Figure 2.22. Peak or trough formation in the current signal occurs due to reduction or oxidation of the species. The current begins to increase when the potential reaches the value at which electrode reaction can happen. Due to the quick electrode reaction at higher potentials, the current starts decreasing due to sluggish diffusion of electroactive species [141]. The LSV is more useful when the reaction is not reversible for example the production of methane from CO_2 [142].

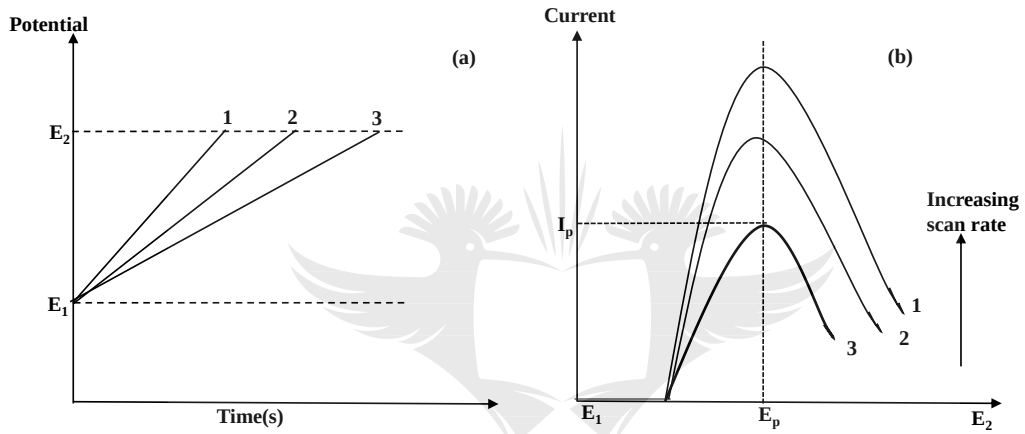

Figure 2.22 (a) Linear sweep voltammetry potential step (b) current response [141].

Unlike potential step measurements, the current response is measured as a function of potential rather than time in LSV measurements.

Figure 2.22 (b) displayed a sequence of linear sweep voltammograms recorded at different scan rates. With the change of scan rate, the response of current also changes and there is an increase in current with increasing scan rate. Consequently, the extent of the diffusion layer above the electrode surface will be changed with changing scan rate [142].

2.6.2.3 Differential Pulse Voltammetry

DPV is a derivative of staircase voltammetry or LSV. The potential is also scanned with a series of voltage pulses and each potential pulse of small amplitude is fixed and superimposed on altering base potential. Current is measured just before the pulse is applied and before it ends. For each potential pulse, the difference between current measurements is measured against the base potential. In contrast to linear single sweep voltammetry, which gives non-symmetric peaks, DPV gives symmetric peaks which start from zero-current values and finish at zero-current values. DPV is mainly useful for the determination of the formal electrode potentials of partially overlapping successive electron transfers [142] and very useful for the determination of trace concentrations of heavy metal ions.

2.6.2.4 Square Wave Voltammetry

SWV uses a combined square wave and staircase potential applied to a fixed electrode. The potential between the reference electrode and working electrode is swept linearly in time where current is measured in voltammetry experiment. The square wave voltammogram, as in DPV, is peak-shaped, but it consists of a differential curve between the current recorded in the forward half-cycle and the current recorded in the reverse half-cycle. SWV is very effective in solving nearly overlapping processes which provide information on the subsequent presence of chemical complications coupled to the electron transfers and is being used in detectors for liquid chromatography.

2.6.2.5 Cyclic Voltammetry

CV is a very useful technique for obtaining both qualitative and quantitative information about electrochemical reactions. The technique is capable of giving information about electron transfer reaction kinetics, redox process thermodynamics and understanding reaction intermediates. CV experiments usually involve the observation of the redox behaviour of electroactive species over a larger potential range.

CV is comparable to LSV. To typically evaluate redox reactions using CV, the potential is normally varied between two values (see below in Figure 2.23(a)) at a fixed rate. Typically the forward reaction is scanned from E_1 to E_2 when the potential reaches E_2 the scan is reversed and the potential is scanned back to E_1 as shown in Figure 2.23(a). A characteristic cyclic voltammogram measured for a reversible electrode reaction is presented in Figure 2.23 (b). The plot of current versus potential is labelled as cyclic voltammograms.

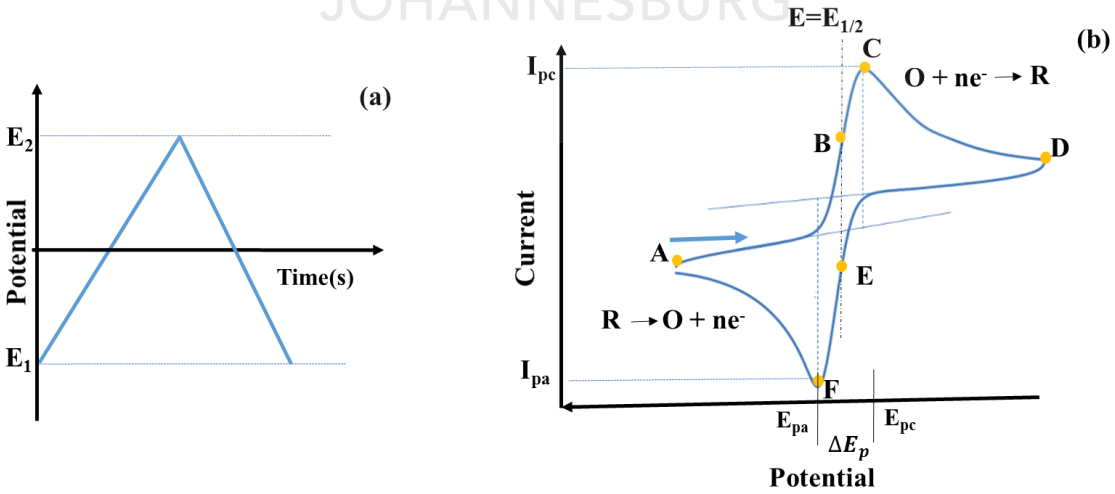

Figure 2.23 (a) Schematic representation of potential sweep (b) corresponding current response in cyclic voltammetry [143].

A typical example is the electro-reduction of hexacyanoferrate (III) to hexacyanoferrate (II) in aqueous solution as shown in equation 2.5 below.

$$Fe^{III}(CN)_6^{-3} + e \rightarrow Fe^{II}(CN)_6^{-4} \quad \text{.....(2.5)}$$

A typical example of a cyclic voltammogram is presented in Figure 2.23 (b). At first, the sweep direction is negative with observed faradic current and transport is by diffusion of the electroactive species. The potential is firstly scanned negatively (cathodically) from A to D, called forward scan as shown by the arrow in Figure 2.23 (b). When the potential starts increasing, the electrode reaction begins, thus increasing the cathodic current, this current increases rapidly until the concentration of $Fe^{III}(CN)_6^{-3}$ at the surface of the electrode is significantly reduced at point C, where the peak cathodic current (I_{pc}) is highest. Then the current decays as the solution near the electrode is depleted of $Fe^{III}(CN)_6^{-3}$ due to its electrolytic conversion to $Fe^{II}(CN)_6^{-4}$ (C→D). For the reverse scan (D→A), the potential is still suitably negative to reduce $Fe^{III}(CN)_6^{-3}$, so the cathodic current remains even though the potential is scanned in positive (anodic) direction. When the electrode become sufficiently strongly oxidative, $Fe^{II}(CN)_6^{-4}$, which has been collecting near the electrode, will now be easily oxidized by the electrode process (equation (2.6)).

$$Fe^{II}(CN)_6^{-4} \rightarrow Fe^{III}(CN)_6^{-3} + e \quad \text{.....(2.6)}$$

The process generates an anodic current which rapidly increases until the concentration of $Fe^{II}(CN)_6^{-4}$ on the surface is sufficiently reduced causing the current to peak (at point F). Then the current decays as the solution near the electrode is depleted of $Fe^{II}(CN)_6^{-4}$.

The ratio $\frac{Fe^{III}(CN)_6^{-3}}{Fe^{II}(CN)_6^{-4}}$ is the potential excitation signal at the electrode surface as given by the Nernst equation for a reversible system. The concentrations of $Fe^{III}(CN)_6^{-3}$ and $Fe^{II}(CN)_6^{-4}$ are equal at points B and E at the electrode surface, in accordance to Nernst equation (equation 2.7). Similarly, at halfway potential between the two resulting peaks C and F, E = $E_{1/2}$, (Figure 2.23(b)).

The electrochemical cell potential (E) relative to the standard potential of the redox species ($E^{o\prime}$) and the relative activities of redox analyte in the system at equilibrium the Nernst equation as expressed in equation (2.7).

$$E = E^{o\prime}_{Fe^{II}(CN)_6^{-4},Fe^{III}(CN)_6^{-3}} + \frac{0.059}{1}\log\frac{Fe^{III}(CN)_6^{-3}}{Fe^{II}(CN)_6^{-4}} \quad \text{.....(2.7)}$$

Here $E^{o\prime}$ is the formal reduction potential of the oxidized and reduced species. An initial value of *E* which is adequately positive of $E^{o\prime}$ results in a ratio in which $Fe^{III}(CN)_6^{-3}$ significantly dominates.

The logarithmic relation between E and $\frac{Fe^{III}(CN)_6^{-3}}{Fe^{II}(CN)_6^{-4}}$ is reflected by a rapid rate of change in the region where E = $E^{o\prime}$ i.e. $\frac{Fe^{III}(CN)_6^{-3}}{Fe^{II}(CN)_6^{-4}} = 1$. This causes rapid increase in cathodic current during forward scan.

In the forward scan, $Fe^{II}(CN)_6^{-4}$ is electrochemically produced from $Fe^{III}(CN)_6^{-3}$ as designated by the cathodic current. In the reverse scan this $Fe^{II}(CN)_6^{-4}$ is oxidized back to $Fe^{III}(CN)_6^{-3}$ as designated by the anodic current. Thus, CV is capable of promptly producing a new oxidation state during the forward scan and then probing its outcome on the reverse scan.

The important parameters in cyclic voltammogram are cathodic peak current (I_{pc}), anodic peak current (I_{pa}), cathodic peak potential (E_{pc}) and the anodic peak potential (E_{pa}) as shown in Figure 2.23 (b).

An electrochemical process where the oxidized and reduced species rapidly exchange electrons with the working electrode is designated an electrochemically reversible couple. The formal reduction potential $E^{o\prime}$ for a reversible couple is centred between E_{pa} and E_{pc} as represented in equation (2.8).

$$\mathrm{E}^{o\prime} = \frac{E_{pa}+E_{pc}}{2} \quad \text{.....(2.8)}$$

The peak potential separation is essential in the determination of the number of electrons (n) transferred in a typical redox reaction as shown in equation 2.9.

$$\Delta\mathrm{E_p} = E_{pa} - \mathrm{E}_{E_{pc}} \cong \frac{0.059}{\mathrm{n}} \quad \text{.....(2.9)}$$

Thus for a fast one-electron process, such as the reduction of $\mathrm{Fe^{III}(CN)_6^{-3}}$ to $\mathrm{Fe^{II}(CN)_6^{-4}}$, the value of ΔE_p is about 0.059 V. A sluggish electron transfer at the electrode surface results in irreversibility and leads to an increase in ΔE_p [144]. Thus, for a typical fast and reversible redox reaction, the ideal peak separation between the cathodic and anodic peak potential is around $\frac{59}{\mathrm{n}}$ mV, and the range between 60-70mV are usually acceptable in real experimental situations.

2.6.2.5.1 Importance of the scan rate

Higher current responses are observed with an increase in scan rate, which is an indication of the decrease of the diffusion layer [123]. The Randles- Sevcik equation

(equation 2.10) gives a description of the peak current for an electrochemically reversible system, at room temperature 25 °C [140, 145, 146].

$$I_P = (2.69x10^5)n^{\frac{2}{3}}AD^{\frac{1}{2}}Cv^{1/2} \quad \text{.....(2.10)}$$

where A is the electrode surface area (cm^2), I_P is the peak current (A), n is electron stoichiometry, D is the diffusion coefficient (cm^2/s), ν is scan rate (V/s) and C is the bulk concentration of the analyte (mol/dm^3).

According to equation (2.10), I_P is directly proportional to $\nu^{1/2}$ and it is also directly proportional to concentration. This relationship to concentration is very important when electrode mechanism is being studied. For a simple reversible couple, the values of I_{pa} and I_{pc} should be identical as shown in equation (2.11)

$$\frac{I_{pa}}{I_{pc}} = 1 \quad \text{.....(2.11)}$$

However, the ratio of the peak currents can be considerably affected by chemical reactions which are related to the electrode process.

It has been established that electrochemical irreversibility is mainly due to slow electron exchange between the redox species and the working electrode. In the situation where the reaction is electrochemically irreversible, then equations (2.8), (2.9), (2.10) and (2.11) are not applicable.

2.6.3 CHRONOAMPEROMETRY TECHNIQUES

The chronoamperometry technique is a controlled potential voltammetry, and it involves the measurement of currents as a function of time in response to a potential

pulse. Chronoamperometry technique is capable of being used for the identification of electrode mechanism relative to certain redox changes.

In a typical multi potential step chronoamperometry technique, the potential is stepped from a value at which no faradic reaction takes place to a potential where the surface concentration of active species is zero [147] as shown in Figure 2.24 (a).

The potential is initially stepped from E_1 where there is no oxidation or reduction reaction of electrochemically active species (no observed current) to E_2 where large current response occurs which is as a result of the electrode reaction. Similarly, there is an observed decay in the current [148] due to depletion of electroactive species near the surface of the electrode as shown in Figure 2.24 (b). The current-time plot shows that as time gradually increases, the diffusion layer also expands with the corresponding decay in current relative to the time at the electrode.

The Cottrell equation [123] shows the dependence of current on time for redox reactions after the application of a potential step and as indicated in equation (2.12).

$$I(t) = \frac{nFAcD^{1/2}}{\pi^{1/2}t^{1/2}} = kt^{-1/2} \quad \text{.....(2.12)}$$

Where F, n, D, c, A and t are the Faraday constant, number of electrons involved in the reaction, the diffusion coefficient of the electroactive species, concentration, electrode surface area and time respectively.

The current decays with time as shown in Figure 2.24 (b).

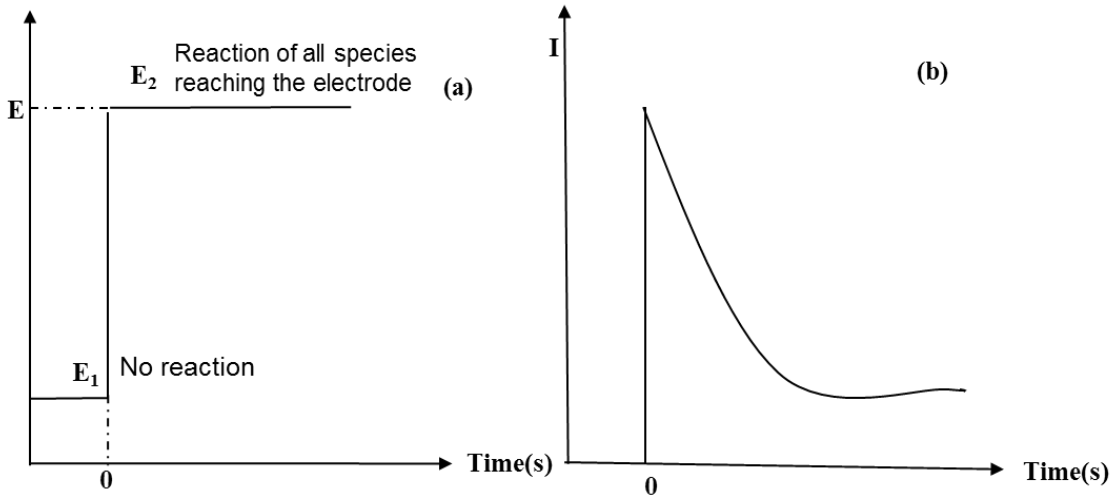

Figure 2.24 Principle of chronoamperometry (a) change of potential with changing time and (b) resulting current response [148].

2.6.3.1 Chronoamperometry: Application

2.6.3.1.1 From Cottrell equation

It is useful for:

(i) measurement of surface area (A)

(ii) measurement of diffusion coefficient (D)

(iii) measurement of analyte concentration

2.6.3.1.2 Analytical performance of sensors

Chronoamperometry experiment is usually used in the investigation of the electrocatalytic performance of modified bioelectrodes in electrochemical sensors while different parameters such as sensitivity, limit of detection, linear range and dynamic range are used for the evaluation of analyte concentration in the system.

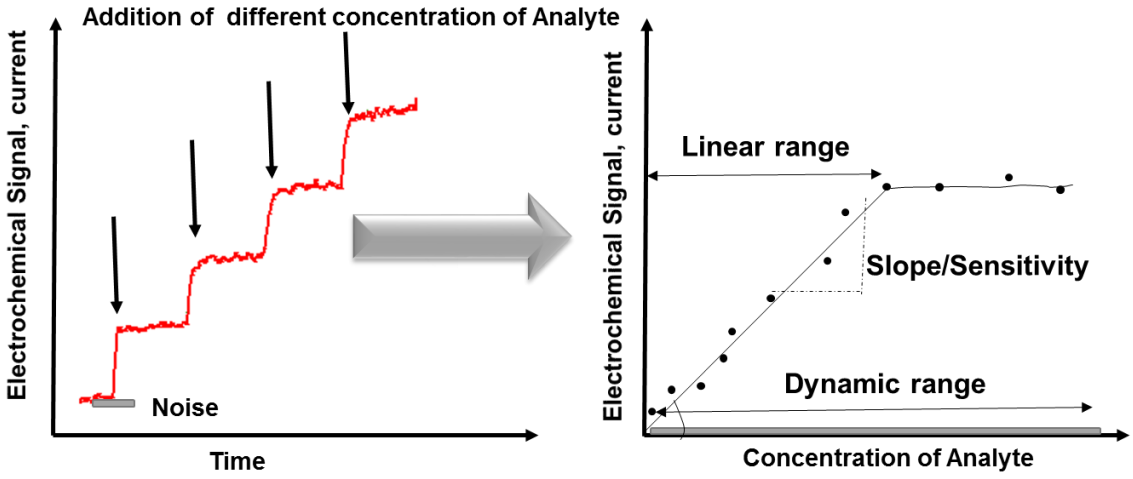

(a) (b)

Figure 2.25 (a) Illustration of a typical amperometric sensor response (b) Calibration plot showing the linear range, the dynamic range, and other relevant analytical useful parameters [149].

2.6.3.1.2.1 Sensitivity

The calibration graph (Figure 2.25 (b)) [149] (current versus concentration) was plotted for the determination of key parameters such as sensitivity, linear range, dynamic range and limit of detection (LoD).

The sensitivity of the electrode is defined as the slope of the calibration graph (b) as shown in Figure 2.25 relative to the effective electrode surface area as shown in equation (2.13).

$$Sensitivity\ (s) = \frac{Slope\ of\ the\ calibration\ curve)}{Surface\ area\ of\ the\ bare\ eelctrode} \quad \text{.....(2.13)}$$

Sensitivity is calculated over the linear portion of a calibration curve and with the improvement of electron transfer between the electrode surface and target redox species, there is an increase in sensitivity.

2.6.3.1.2.2 Limit of Detection

LoD is described as the lowest analyte concentration in the sample which is precisely measured by sensing electrode under an acceptable signal to noise (S/N) ratio.

The LoD is determined or calculated from calibration plots as three times the standard deviation of the current or potential signals (σ) as given in equation (2.14) [150].

$$LOD = \frac{3\sigma}{s} \quad \text{.....(2.14)}$$

2.6.3.1.2.3 Linear and dynamic range

The region where the current is directly proportional to the concentration within the working range of analyte concentration is called linear range while the dynamic range is the range of analyte concentrations where there is a calculable response to the addition of analyte [151] as shown in Figure 2.25 (b).

2.6.3.1.2.4 Response time

Response time is an important parameter for sensors, and it is defined as the time required for a response signal to reach 95 % of the steady-state value.

2.6.4 ELECTROCHEMICAL IMPEDANCE SPECTROSCOPY

In EIS, the electrode or cell impedance is plotted *vs.* frequency [152]. EIS is a sensitive, non-destructive technique which is used for the evaluation of electrochemical systems and processes like heterogeneous charge transfer

parameters and also for the study of double layer structures. EIS has been used for providing the electrode kinetic information for various types of materials like fuel cells and batteries [153].

The resistive and capacitive behaviour of the electrode–electrolyte interface can be studied by applying a small amplitude alternating current (ac) signal to the cell which is held at a constant voltage at equilibrium [153]. The response of the applied ac-signal is shown in a sinusoidal form. The analysis of electrode processes is achieved through the measurement of amplitude (i.e. impedance) and the phase difference. When the frequency of the ac-signal is changed, the impedance is then measured as a function of frequency.

The perturbation due to an applied potential at a frequency (ω) in the electrochemical cell may be expressed as given in equation (2.15) below:

$E = E_o$ sinωt……..…….....(2.15)

Where E_o is the voltage amplitude, V (t) is voltage at time t and ω is the radial frequency. The current response may then take the form of a phase shift denoted by ϕ which as shown in equation (2.16).

$I(t) = I_o$ sin (ωt+ ϕ)……..…….....(2.16)

Where I_o is the current amplitude, I (t) is the current at time t and ϕ is the phase shift. The impedance of the system is usually expressed as a complex number as given in equation 2.17 [123].

Z=$\frac{E_i}{I_i}$……..……...(2.17)

If the magnitude is expressed as $Z_o = V_o / I_o$ and the phase shift is (ϕ), the complex notation for impedance will then be as given in equation 2.18,

$$Z = Z_o (cos\ \phi + j\ sin\ \phi) = Z' + j\ Z'' \quad \text{.....(2.18)}$$

where, $j = \sqrt{(-1)}$, Z' is the real and Z" is the imaginary part of the impedance.

The impedance (Z) is expressed as given in equation 2.19.

$$Z = \frac{E}{I} = \frac{E_o \sin\omega t}{I_o \sin(\omega t + \phi)} = Z_o \frac{\sin\omega t}{\sin(\omega t + \phi)} \quad \text{.....(2.19)}$$

Where Z, ω and ϕ are impedance, radial frequency and phase shift respectively [122].

The variation of the impedance with frequency can be displayed in different ways. One representation is a Nyquist plot; which uses the plot of Z' *vs.* Z'' for different values of ω to interpret the impedance data of electrochemical results. The Nyquist plot usually displays two portions; one is the semi-circular portion and the other one is linear as shown in Figure 2.26 (a).

Similarly, an electrochemical system may be represented by parallel and series configuration of capacitors and resistors and this representation is called the equivalent circuit. The most frequently used circuit representation is called the Randles equivalent circuit [154] which is shown in Figure 2.25 (b).

In Nyquist plot, the semicircle portion refers to the higher frequency range electron-transfer-limited process which is denoted by R_{ct} whereas the linear portion of the Nyquist plot corresponds to the low frequency range diffusional-limited electron transfer process [123]. The diameter of the semi-circular portion of the Nyquist plot

equals the charge transfer resistance (R_{ct}) at the interface, the R_{ct} may equally be expressed according to the following equation (2.20):

$$Z_{(\omega)} = R_s + \frac{R_{ct} + \sigma\omega^{-1/2}}{(\sigma\omega^{1/2}C_d+1)^2 + \omega^2 C_d^2\left(R_{ct} + \sigma\omega^{-1/2}\right)^2} + j\frac{\left[\omega C_d\left(R_{ct} + \sigma\omega^{-1/2}\right)^2 + \sigma\omega^{-1/2}\left(C_d\sigma\omega^{1/2}+1\right)\right]}{\left(C_d\sigma\omega^{1/2}+1\right)^2 + \omega^2 C_d^2\left(R_{ct} + \sigma\omega^{-1/2}\right)^2} \quad \text{.....(2.20)}$$

where R_s is solution resistance, C_d is the double layer capacitance, ω is the $2\pi f$, where f is frequency, the second term is termed as Z' and the third term is Z'' in the above equation and σ is defined as shown in equation (2.21).

$$\sigma = \frac{RT}{\sqrt{2}n^2F^2A}\left(\frac{1}{D_O^{1/2}C_O} + \frac{1}{D_R^{1/2}C_R}\right) \quad \text{.....(2.21)}$$

Where A is the surface area of the electrode and D_O and D_R are the diffusion coefficients of the different species (oxidants and reactants), C_O and C_R represent the bulk concentrations of oxidants and reductants respectively and F is Faraday's constant, T is the temperature in Kelvin and R is the gas constant.

The components are represented as complex plane plot as shown in Figure 2.25 (a). It is quite useful to consider two limiting forms of equations (2.20) and (2.21) which may be expressed in terms of equations (2.22) and (2.23).

When $\omega \to 0$; then equations (2.20) and (2.21) may be respectively expressed as (2.22) and (2.23) below

$$Z' = R_s + R_{ct} + \sigma\omega^{-1/2} \quad \text{.....(2.22)}$$

$$Z'' = -\sigma\omega^{-\frac{1}{2}} - 2\sigma^2 C_d \quad \text{.....(2.23)}$$

The low frequency limit is the straight line of the unit slope, which when extrapolated to the real axis Z', gives an intercept of $R_s + R_{ct} - 2\sigma^2 C_d$. This line relates to diffusion controlled reaction and the impedance become Warburg impedance [154] with the phase angle being $\frac{\pi}{4}$ see Figure 2.26 (a).

The analogy is a resistor-capacitor (RC) parallel combination and the equation (2.18) becomes

$$\left(Z' - R_s - \frac{R_{ct}}{2}\right)^2 + (Z'')^2 = \left(\frac{R_{ct}}{2}\right)^2 \quad \text{.....(2.24)}$$

Equation 2.24 relates the circle of radius $\frac{R_{ct}}{2}$ with intercepts on the Z' axis of R_s ($\omega \to \infty$) and $R_s + R_{ct}$ ($\omega \to 0$) as shown in Figure 2.26 (a).

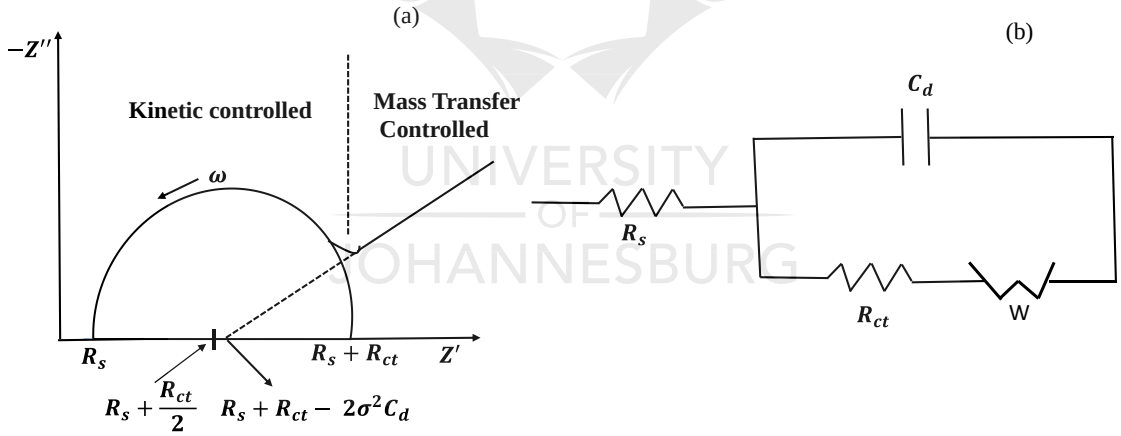

Figure 2.26 (a) Nyquist plot (b) Randles equivalent circuit of a simple electrochemical system [156].

To understand the physical significance of the semi-circle, it is pertinent to note that firstly, at very high frequency, Z'' ($= -\frac{1}{\omega C_d}$) become very small, then it starts to increase as frequency reduces. Conversely, at low frequency, current passes largely through R_{ct} which increases Z' and diminishes Z''.

Consequently, the final impedance of a cell in most electrochemical systems is mostly a combination of different processes including electron transfer kinetics, diffusion, and charge transfer impedance. Also to do a circuit equivalent fittings for the experimentally obtained Nyquist plots, Randles equivalent circuit usually include solution resistance (R_s), double layer capacitor C_d, R_{ct} and Warburg impedance W. Due to the relative value of the components R_{ct}, W and C_d, only the semicircle or only the straight line are observed [123].

2.7 REFERENCES

[1] D. R. Thevenot, K. Toth, R. A. Durst and G. S. Wilson. Electrochemical biosensors: recommended definitions and classification. *Pure and Applied Chemistry* **71** (1999) 2333-2348.

[2] S. P. Mohanty and E. Kougianos. Biosensors: a tutorial review. *Ieee Potentials* **25** (2006) 35-40.

[3] J. Kirsch, C. Siltanen, Q. Zhou, A. Revzin and A. Simonian. Biosensor technology: recent advances in threat agent detection and medicine. *Chemical Society Reviews* **42** (2013) 8733-8768.

[4] L. P. Wackett. Enzyme-based sensors: An annotated selection of World Wide Web sites relevant to the topics in microbial biotechnology. *Microbial Biotechnology* **9** (2016) 430-431.

[5] V. Perumal and U. Hashim. Advances in biosensors: Principle, architecture and applications. *Journal of Applied Biomedicine* **12** (2014) 1-15.

[6] N. A. Mungroo, S. Neethirajan. Biosensors for the detection of antibiotics in poultry industry-a review. Biosensors (Basel) 4 (2014) 472-493.

[7] C. R. Ispas, G. Crivat and S. Andreescu. Recent developments in enzyme-based biosensors for biomedical analysis. *Analytical Letters* **45** (2012) 168-186.

[8] M. Park, S.-L. Tsai and W. Chen. Microbial biosensors: engineered microorganisms as the sensing machinery. *Sensors* **13** (2013) 5777-5795.

[9] B. F. Pfleger, D. J. Pitera, J. D. Newman, V. J. Martin and J. D. Keasling. Microbial sensors for small molecules: development of a mevalonate biosensor. *Metabolic Engineering* **9** (2007) 30-38.

[10] E. Schultheiss, S. Weiss, E. Winterer, R. Maas, E. Heinzle and J. Jose. Esterase autodisplay: enzyme engineering and whole-cell activity determination in microplates with pH sensors. *Applied and Environmental Microbiology* **74** (2008) 4782-4791.

[11] A. Ivask, T. Rõlova and A. Kahru. A suite of recombinant luminescent bacterial strains for the quantification of bioavailable heavy metals and toxicity testing. *BMC Biotechnology* **9** (2009) 41.

[12] F. Lagarde and N. Jaffrezic-Renault. Cell-based electrochemical biosensors for water quality assessment. *Analytical and Bioanalytical Chemistry* **400** (2011) 947-964.

[13] L. Su, W. Jia, C. Hou and Y. Lei. Microbial biosensors: a review. *Biosensors and Bioelectronics* **26** (2011) 1788-1799.

[14] J. M. Fowler, D. K. Wong, H. B. Halsall and W. R. Heineman. Recent developments in electrochemical immunoassays and immunosensors. *Academic Press* (2008).

[15] P. J. Conroy, S. Hearty, P. Leonard and R. J. O'Kennedy. Antibody production, design and use for biosensor-based applications, *Seminars in Cell & Developmental Biology*, *Academic Press* **20** (2009) 10-26.

[16] P. D'Orazio. Biosensors in clinical chemistry—2011 update. *Clinica Chimica Acta* **412** (2011) 1749-1761.

[17] S. M. Nimjee, C. P. Rusconi and B. A. Sullenger. Aptamers: an emerging class of therapeutics. *Annual Review Medicine* **56** (2005) 555-583.

[18] P. Jolly, P. Estrela and M. Ladomery. Oligonucleotide-based systems: DNA, microRNAs, DNA/RNA aptamers. *Essays in biochemistry* **60** (2016) 27-35.

[19] H.-J. Schneider, S. Lim and R. M. Strongin. Biomimetic synthetic receptors as molecular recognition elements. *Recognition Receptors in Biosensors*. *Springer* (2010) 777-816.

[20] G. Parkinson and B. Pejcic. Using Biosensors to detect emerging infectious diseases. *Prepared for The Australian Biosecurity Cooperative Research Centre* (2005) 1-80.

[21] F. Teles and L. Fonseca. Trends in DNA biosensors. *Talanta* **77** (2008) 606-623.

[22] L. Lading, L. B. Nielsen and T. Sevel. Comparing biosensors, in Sensors, 2002. *Proceedings of IEEE* **1** (2002) 229-232.

[23] M. E. Bosch, A. J. R. Sánchez, F. S. Rojas and C. B. Ojeda. Recent development in optical fiber biosensors. *Sensors* **7** (2007) 797-859.

[24] P. N. Prasad. Introduction to biophotonics. *John Wiley & Sons*, (2004)

[25] M. Mehrvar, C. Bis, J. M. Scharer, M. Moo-Young and J. H. Luong. Fiber-optic biosensors-trends and advances. *Analytical sciences* **16** (2000) 677-692.

[26] P. Damborský, J. Švitel and J. Katrlík. Optical biosensors. *Essays in Biochemistry* **60** (2016) 91-100.

[27] I. Koh and L. Josephson. Magnetic nanoparticle sensors. *Sensors* **9** (2009) 8130-8145.

[28] V. D. Krishna, K. Wu, A. M. Perez and J.-P. Wang. Giant magnetoresistance-based biosensor for detection of influenza A virus. *Frontiers in Microbiology* **7** (2016) 400.

[29] I. Giouroudi and G. Kokkinis. Recent advances in magnetic microfluidic biosensors. *Nanomaterials* **7** (2017) 171.

[30] C. Jianrong, M. Yuqing, H. Nongyue, W. Xiaohua and L. Sijiao. Nanotechnology and biosensors. *Biotechnology Advances* **22** (2004) 505-518.

[31] B. Xie, K. Ramanathan and B. Danielsson. Principles of enzyme thermistor systems: Applications to biomedical and other measurements. *Thermal Biosensors, Bioactivity, Bioaffinitty. Springer* **64** (1999) 1-33.

[32] L. Ahmad, B. Towe, A. Wolf, F. Mertens and J. Lerchner. Binding event measurement using a chip calorimeter coupled to magnetic beads. *Sensors and Actuators B: Chemical* **145** (2010) 239-245.

[33] Y. Zhang and S. Tadigadapa. Calorimetric biosensors with integrated microfluidic channels. *Biosensors and Bioelectronics* **19** (2004) 1733-1743.

[34] J. Tichý, J. Erhart, E. Kittinger and J. Prívratská. Fundamentals of piezoelectric sensorics: mechanical, dielectric, and thermodynamical properties of piezoelectric materials. *Springer Science & Business Media*, (2010).

[35] G. García-Martinez, E. A. Bustabad, H. Perrot, C. Gabrielli, B. Bucur, M. Lazerges, D. Rose, L. Rodriguez-Pardo, J. Fariña and C. Compère. Development of a mass sensitive quartz crystal microbalance (QCM)-based DNA biosensor using a 50 MHz electronic oscillator circuit. *Sensors* **11** (2011) 7656-7664.

[36] G. Sauerbrey. Verwendung von Schwingquarzen zur Wägung dünner Schichten und zur Mikrowägung. *Zeitschrift für physik* **155** (1959) 206-222.

[37] C. Zhang, N. Liu, J. Yang and W. Chen. Thickness-shear vibration of AT-cut quartz plates carrying finite-size particles with rotational degree of freedom

and rotatory inertia. *IEEE Transactions on Ultrasonics, Ferroelectrics, and Frequency Control* **58** (2011) 666-670.

[38] T. Endo, S. Yamamura, K. Kerman and E. Tamiya. Label-free cell-based assay using localized surface plasmon resonance biosensor. *Analytica Chimica Acta* **614** (2008) 182-189.

[39] Y. Wang, H. Xu, J. Zhang and G. Li. Electrochemical sensors for clinic analysis. *Sensors* **8** (2008) 2043-2081.

[40] F. Faridbod, M. R. Ganjali, B. Larijani, P. Norouzi and M. Hosseini. Biosensors in Endocrinology-Review Article. *Iranian Journal of Public Health* **43** (2015) 94-104.

[41] S. Sanllorente-Mendez, O. Dominguez-Renedo and M. Arcos-Martinez. Development of acid phosphatase based amperometric biosensors for the inhibitive determination of As (V). *Talanta* **93** (2012) 301-306.

[42] R. F. Taylor and J. S. Schultz. Handbook of chemical and biological sensors. *CRC Press* (1996).

[43] A. Pizzariello, M. Stredanský, S. Stredanská and S. Miertuš. Urea biosensor based on amperometric pH-sensing with hematein as a pH-sensitive redox mediator. *Talanta* **54** (2001) 763-772.

[44] D. Grieshaber, R. MacKenzie, J. Voeroes and E. Reimhult. Electrochemical biosensors-sensor principles and architectures. *Sensors* **8** (2008) 1400-1458.

[45] H. Wang, X. Wu, P. Dong, C. Wang, J. Wang, Y. Liu and J. Chen. Electrochemical biosensor based on interdigitated electrodes for determination of thyroid stimulating hormone. *International Journal of Electrochemical Science* **9** (2014) 12-21.

[46] A. Mulyasuryani and M. Dofir. Enzyme biosensor for detection of organophosphate pesticide residues base on screen printed carbon electrode (SPCE)-bovine serum albumin (BSA). *Engineering* **6** (2014) 230-235.

[47] A. Gothwal, P. Beniwal, V. Dhull and V. Hooda. Preparation of electrochemical biosensor for detection of organophosphorus pesticides. *International Journal of Analytical Chemistry* **2014** (2014)

[48] L. Chen, D. Lv, X. Chen, M. Liu, D. Wang, Y. Liu, Z. Hong, Z. Zhu, X. Hu and Y. Cao. Biosensor-Based Active Ingredients Recognition System for Screening STAT3 Ligands from Medical Herbs. *Analytical Chemistry* **90** (2018) 8936-8945.

[49] A. M. Foudeh, H. Trigui, N. Mendis, S. P. Faucher, T. Veres and M. Tabrizian. Rapid and specific SPRi detection of L. pneumophila in complex environmental water samples. *Analytical and Bioanalytical Chemistry* **407** (2015) 5541-5545.

[50] M. G. Manera, G. Montagna, F. Cimaglia, M. Chiesa, P. Poltronieri, A. Santino and R. Rella. SPR based immunosensor for detection of Legionella pneumophila in water samples. *Optics Communications* **294** (2013) 420-426.

[51] F. Long, A. Zhu, H. Shi, H. Wang and J. Liu. Rapid on-site/in-situ detection of heavy metal ions in environmental water using a structure-switching DNA optical biosensor. *Scientific Reports* **3** (2013) 2308.

[52] A. Ravikumar, P. Panneerselvam, K. Radhakrishnan, N. Morad, C. Anuradha and S. Sivanesan. DNAzyme based amplified biosensor on ultrasensitive fluorescence detection of Pb (II) ions from aqueous system. *Journal of Fluorescence* **27** (2017) 2101-2109.

[53] N. Arora. Recent advances in biosensors technology: a review. *Octa Journal of Biosciences* **1** (2013) 147-150.

[54] G. Murugaboopathi, V. Parthasarathy, C. Chellaram, T. P. Anand and S. Vinurajkumar. Application of biosensors in food industry. *Biosciences Biotechnology Research Asia* **10** (2013) 711-714.

[55] L. Kenar. The use of biosensors for the detection of chemical and Biological Weapons. *Turkish Journal of Biochemistry* **35** (2010) 72-74.

[56] P. A. Emanuel, J. Dang, J. S. Gebhardt, J. Aldrich, E. A. Garber, H. Kulaga, P. Stopa, J. J. Valdes and A. Dion-Schultz. Recombinant antibodies: a new reagent for biological agent detection. *Biosensors and Bioelectronics* **14** (2000) 751-759.

[57] M. F. Chaplin and C. Bucke. Enzyme technology. *CUP Archive* (1990).

[58] F. Schwierz. Graphene transistors: status, prospects, and problems. *Proceedings of the IEEE* **101** (2013) 1567-1584.

[59] A. K. Geim and K. S. Novoselov. The rise of graphene. *Nature Materials* **6** (2007) 183-191.

[60] A. K. Geim. Graphene: status and prospects. *Science* **324** (2009) 1530-1534.

[61] Q. H. Wang, K. Kalantar-Zadeh, A. Kis, J. N. Coleman and M. S. Strano. Electronics and optoelectronics of two-dimensional transition metal dichalcogenides. *Nature Nanotechnology* **7** (2012) 699-712.

[62] A. K. Geim and I. V. Grigorieva. Van der Waals heterostructures. *Nature* **499** (2013) 419-425.

[63] P. Miro, M. Audiffred and T. Heine. An atlas of two-dimensional materials. *Chemical Society Reviews* **43** (2014) 6537-6554.

[64] M. Samadi, N. Sarikhani, M. Zirak, H. Zhang, H.-L. Zhang and A. Z. Moshfegh. Group 6 transition metal dichalcogenide nanomaterials: synthesis, applications and future perspectives. *Nanoscale Horizons* **3** (2018) 90-204.

[65] A. K. Geim. Random walk to graphene (Nobel lecture). *Angewandte Chemie International Edition* **50** (2011) 6966-6985.

[66] K. S. Novoselov, A. K. Geim, S. V. Morozov, D. Jiang, Y. Zhang, S. V. Dubonos, I. V. Grigorieva and A. A. Firsov. Electric field effect in atomically thin carbon films. *Science* **306** (2004) 666-669.

[67] L. D. Landau, E. M. Lifshitz and L. Pitaevskii. *Statistical physics, part I*, pergamon, Oxford (1980).

[68] J. Venables, G. Spiller and M. Hanbucken. Nucleation and growth of thin films. *Reports on Progress in Physics* **47** (1984) 399.

[69] L. Landau. Zur Theorie der phasenumwandlungen II. *Phys. Z. Sowjetunion* **11** (1937) 26-35.

[70] K. F. Mak, C. Lee, J. Hone, J. Shan and T. F. Heinz. Atomically thin MoS_2: a new direct-gap semiconductor. *Physics Review Letters* **105** (2010) 136805.

[71] H. Ramakrishna Matte, A. Gomathi, A. K. Manna, D. J. Late, R. Datta, S. K. Pati and C. Rao. MoS_2 and WS_2 analogues of graphene. *Angewandte Chemie International Edition* **49** (2010) 4059-4062.

[72] Y. Ma, Y. Dai, M. Guo, C. Niu, J. Lu and B. Huang. Electronic and magnetic properties of perfect, vacancy-doped, and nonmetal adsorbed $MoSe_2$, MoTe 2 and WS_2 monolayers. *Physical Chemistry Chemical Physics* **13** (2011) 15546-15553.

[73] M. Xu, T. Liang, M. Shi and H. Chen. Graphene-like two-dimensional materials. *Chemical Reviews* **113** (2013) 3766-3798.

[74] J. N. Coleman, M. Lotya, A. O'Neill, S. D. Bergin, P. J. King, U. Khan, K. Young, A. Gaucher, S. De, R. J. Smith, I. V. Shvets, S. K. Arora, G. Stanton, H. Y. Kim, K. Lee, G. T. Kim, G. S. Duesberg, T. Hallam, J. J. Boland, J. J. Wang, J. F. Donegan, J. C. Grunlan, G. Moriarty, A. Shmeliov, R. J. Nicholls, J. M. Perkins, E. M. Grieveson, K. Theuwissen, D. W. McComb, P. D. Nellist, and V. Nicolosi. Two-dimensional nanosheets produced by liquid exfoliation of layered materials. *Science* **331** (2011) 568-571.

[75] M. Naguib, V. N. Mochalin, M. W. Barsoum and Y. Gogotsi. 25th anniversary article: MXenes: a new family of two-dimensional materials. *Advanced Materials* **26** (2014) 992-1005.

[76] M. W. Barsoum. MAX phases: properties of machinable ternary carbides and nitrides. *John Wiley & Sons*, (2013)

[77] L. Hu, R. Ma, T. C. Ozawa and T. Sasaki. Exfoliation of layered europium hydroxide into unilamellar nanosheets. *Chemistry–An Asian Journal* **5** (2010) 248-251.

[78] S. Ida, C. Ogata, M. Eguchi, W. J. Youngblood, T. E. Mallouk and Y. Matsumoto. Photoluminescence of perovskite nanosheets prepared by exfoliation of layered oxides, $K_2Ln_2Ti_3O_{10}$, $KLnNb_2O_7$, and $RbLnTa_2O_7$ (Ln: lanthanide ion). *Journal of the American Chemical Society* **130** (2008) 7052-7059.

[79] J. C. Slonczewski and P. R. Weiss. Band Structure of Graphite. *Physical Review* **109** (1958) 272-279.

[80] K. S. Novoselov, Z. Jiang, Y. Zhang, S. V. Morozov, H. L. Stormer, U. Zeitler, J. C. Maan, G. S. Boebinger, P. Kim and A. K. Geim. Room-temperature quantum Hall effect in graphene. *Science* **315** (2007) 1379.

[81] K. Novoselov, D. Jiang, F. Schedin, T. Booth, V. Khotkevich, S. Morozov and A. Geim. Two-dimensional atomic crystals. *Proceedings of the National Academy of Sciences of the United States of America* **102** (2005) 10451-10453.

[82] A. S. Mayorov, R. V. Gorbachev, S. V. Morozov, L. Britnell, R. Jalil, L. A. Ponomarenko, P. Blake, K. S. Novoselov, K. Watanabe and T. Taniguchi. Micrometer-scale ballistic transport in encapsulated graphene at room temperature. *Nano Letters* **11** (2011) 2396-2399.

[83] K. S. Novoselov, A. K. Geim, S. V. Morozov, D. Jiang, M. I. Katsnelson, I. V. Grigorieva, S. V. Dubonos and A. A. Firsov. Two-dimensional gas of massless Dirac fermions in graphene. *Nature* **438** (2005) 197-200.

[84] T. Kuila, S. Bose, P. Khanra, A. K. Mishra, N. H. Kim and J. H. Lee. Recent advances in graphene-based biosensors. *Biosensors and Bioelectronics* **26** (2011) 4637-4648.

[85] M. Pumera. Graphene in biosensing. *Materials Today* **14** (2011) 308-315.

[86] Y. Guo, K. Xu, C. Wu, J. Zhao and Y. Xie. Surface chemical-modification for engineering the intrinsic physical properties of inorganic two-dimensional nanomaterials. *Chemical Society Reviews* **44** (2015) 637-646.

[87] S. Afsahi, M. B. Lerner, J. M. Goldstein, J. Lee, X. Tang, D. A. Bagarozzi Jr, D. Pan, L. Locascio, A. Walker and F. Barron. Novel graphene-based biosensor for early detection of Zika virus infection. *Biosensors and Bioelectronics* **100** (2018) 85-88.

[88] M. Zhang, R. Yuan, Y. Chai, C. Wang and X. Wu. Cerium oxide–graphene as the matrix for cholesterol sensor. *Analytical Biochemistry* **436** (2013) 69-74.

[89] R. Manjunatha, G. S. Suresh, J. S. Melo, S. F. D'Souza and T. V. Venkatesha. An amperometric bienzymatic cholesterol biosensor based on functionalized graphene modified electrode and its electrocatalytic activity towards total cholesterol determination. *Talanta* **99** (2012) 302-309.

[90] H. Song, Y. Ni and S. Kokot. A novel electrochemical biosensor based on the hemin-graphene nano-sheets and gold nano-particles hybrid film for the analysis of hydrogen peroxide. *Analytica Chimica Acta* **788** (2013) 24-31.

[91] S. Srivastava, M. A. Ali, S. Umrao, U. K. Parashar, A. Srivastava, G. Sumana, B. Malhotra, S. S. Pandey and S. Hayase. Graphene oxide-based biosensor for food toxin detection. *Applied Biochemistry and Biotechnology* **174** (2014) 960-970.

[92] M. Shaikh, C. Liu, M. Partridge, S. James, W. Zhu and X. Chen. Highly sensitive and selective biosensor based on graphene oxide coated long period grating, *Optical Fibers and Sensors for Medical Diagnostics and Treatment Applications XVII, International Society for Optics and Photonics* **10058** (2017) 100580G.

[93] L. Klukova, J. Filip, S. Belicky, A. Vikartovska and J. Tkac. Graphene oxide-based electrochemical label-free detection of glycoproteins down to aM level using a lectin biosensor. *Analyst* **141** (2016) 4278-4282.

[94] H. Kushwaha, R. Sao and R. Vaish. Label free selective detection of estriol using graphene oxide-based fluorescence sensor. *Journal of Applied Physics* **116** (2014) 034701.

[95] M. Zhou, Y. Wang, Y. Zhai, J. Zhai, W. Ren, F. Wang and S. Dong. Controlled synthesis of large-area and patterned electrochemically reduced graphene oxide films. *Chemistry–A European Journal* **15** (2009) 6116-6120.

[96] X.-H. Zhou, L.-H. Liu, X. Bai and H.-C. Shi. A reduced graphene oxide based biosensor for high-sensitive detection of phenols in water samples. *Sensors and Actuators B: Chemical* **181** (2013) 661-667.

[97] M. Zhou, Y. Zhai and S. Dong. Electrochemical sensing and biosensing platform based on chemically reduced graphene oxide. *Analytical Chemistry* **81** (2009) 5603-5613.

[98] L. Feng, L. Wu, J. Wang, J. Ren, D. Miyoshi, N. Sugimoto and X. Qu. Detection of a Prognostic Indicator in Early-Stage Cancer Using Functionalized Graphene-Based Peptide Sensors. *Advanced Materials* **24** (2012) 125-131.

[99] S. Kumar, J. G. Sharma, S. Maji and B. D. Malhotra. Nanostructured zirconia decorated reduced graphene oxide based efficient biosensing platform for non-invasive oral cancer detection. *Biosensors and Bioelectronics* **78** (2016) 497-504.

[100] P. Bollella, G. Fusco, C. Tortolini, G. Sanzo, G. Favero, L. Gorton and R. Antiochia. Beyond graphene: Electrochemical sensors and biosensors for biomarkers detection. *Biosensors and Bioelectronics* **89** (2017) 152-166.

[101] D. J. Late, Y.-K. Huang, B. Liu, J. Acharya, S. N. Shirodkar, J. Luo, A. Yan, D. Charles, U. V. Waghmare and V. P. Dravid. Sensing behavior of atomically thin-layered MoS_2 transistors. *Acs Nano* **7** (2013) 4879-4891.

[102] O. Parlak, A. İncel, L. Uzun, A. P. Turner and A. Tiwari. Structuring Au nanoparticles on two-dimensional MoS_2 nanosheets for electrochemical glucose biosensors. *Biosensors and Bioelectronics* **89** (2017) 545-550.

[103] G.-X. Wang, W.-J. Bao, J. Wang, Q.-Q. Lu and X.-H. Xia. Immobilization and catalytic activity of horseradish peroxidase on molybdenum disulfide nanosheets modified electrode. *Electrochemistry Communications* **35** (2013) 146-148.

[104] G. Yang, C. Zhu, D. Du, J. Zhu and Y. Lin. Graphene-like two-dimensional layered nanomaterials: applications in biosensors and nanomedicine. *Nanoscale* **7** (2015) 14217-14231.

[105] X. Gan, H. Zhao and X. Quan. Two-dimensional MoS_2: A promising building block for biosensors. *Biosensors and Bioelectronics* **89** (2017) 56-71.

[106] H. Park, G. Han, S. W. Lee, H. Lee, S. H. Jeong, M. Naqi, A. AlMutairi, Y. J. Kim, J. Lee and W.-j. Kim. Label-Free and Recalibrated Multilayer MoS_2 Biosensor for Point-of-Care Diagnostics. *ACS Applied Materials & Interfaces* **9** (2017) 43490-43497.

[107] J. Lee, P. Dak, Y. Lee, H. Park, W. Choi, M. A. Alam and S. Kim. Two-dimensional layered MoS_2 biosensors enable highly sensitive detection of biomolecules. *Scientific reports* **4** (2014) 7352.

[108] J. Shan, J. Li, X. Chu, M. Xu, F. Jin, X. Wang, L. Ma, X. Fang, Z. Wei and X. Wang. High sensitivity glucose detection at extremely low concentrations using a MoS_2-based field-effect transistor. *RSC Advances* **8** (2018) 7942-7948.

[109] K. Anderson, B. Poulter, J. Dudgeon, S.-E. Li and X. Ma. A highly sensitive nonenzymatic glucose biosensor based on the regulatory effect of glucose

on electrochemical behaviors of colloidal silver nanoparticles on MoS_2. *Sensors* **17** (2017) 1807.

[110] Q. Wang, P. Wu, G. Cao and M. Huang. First-principles study of the structural and electronic properties of MoS_2–WS_2 and MoS_2–$MoTe_2$ monolayer heterostructures. *Journal of Physics D: Applied Physics* **46** (2013) 505308.

[111] W. Zhao, Z. Ghorannevis, L. Chu, M. Toh, C. Kloc, P.-H. Tan and G. Eda. Evolution of electronic structure in atomically thin sheets of WS_2 and WSe_2. *ACS Nano* **7** (2012) 791-797.

[112] M. Bernardi, M. Palummo and J. C. Grossman. Extraordinary sunlight absorption and one nanometer thick photovoltaics using two-dimensional monolayer materials. *Nano Letters* **13** (2013) 3664-3670.

[113] X. Liu, J. Ge, X. Wang, Z. Wu, G. Shen and R. Yu. Development of a highly sensitive sensing platform for T4 polynucleotide kinase phosphatase and its inhibitors based on WS_2 nanosheets. *Analytical Methods* **6** (2014) 7212-7217.

[114] A. Li, J. Zhang, J. Qiu, Z. Zhao, C. Wang, C. Zhao and H. Liu. A novel aptameric biosensor based on the self-assembled DNA–WS_2 nanosheet architecture. *Talanta* **163** (2017) 78-84.

[115] R. J. Toh, C. C. Mayorga-Martinez, Z. Sofer and M. Pumera. 1T-Phase WS_2 Protein-Based Biosensor. *Advanced Functional Materials* **27** (2017) 1604923.

[116] Q. Ouyang, N. Panwar, S. Zeng, X. Wang, L. Jiang, X.-Q. Dinh, B. K. Tay, P. Coquet and K.-T. Yong. Monolayer WS_2 Enhanced High Sensitivity Plasmonic Biosensor based on Phase Modulation, *CLEO: Science and Innovations,* Optical Society of America (2017) SM1C. 4.

[117] Y. Zang, X. Hu, H. Zhou, Q. Xu, P. Huan and H. Xue. Enhanced photoelectrochemical behavior of CdS/WS_2 heterojunction for sensitive glutathione biosensing in human serum. *International Journal of Electrochemical Science* **13** (2018) 7558-7570.

[118] K. Uosaki, G. Elumalai, H. Noguchi, T. Masuda, A. Lyalin, A. Nakayama and T. Taketsugu. Boron nitride nanosheet on gold as an electrocatalyst for oxygen reduction reaction: Theoretical suggestion and experimental proof. *Journal of the American Chemical Society* **136** (2014) 6542-6545.

[119] Q. Xu, L. Cai, H. Zhao, J. Tang, Y. Shen, X. Hu and H. Zeng. Forchlorfenuron detection based on its inhibitory effect towards catalase immobilized on boron nitride substrate. *Biosensors and Bioelectronics* **63** (2015) 294-300.

[120] G.-H. Yang, A. Abulizi and J.-J. Zhu. Sonochemical fabrication of gold nanoparticles–boron nitride sheets nanocomposites for enzymeless hydrogen peroxide detection. *Ultrasonics Sonochemistry* **21** (2014) 1958-1963.

[121] G.-H. Yang, J.-J. Shi, S. Wang, W.-W. Xiong, L.-P. Jiang, C. Burda and J.-J. Zhu. Fabrication of a boron nitride–gold nanocluster composite and its versatile application for immunoassays. *Chemical Communications* **49** (2013) 10757-10759.

[122] Q. Li, W. Luo, L. Su, J. Chen, K.-C. Chou and X. Hou. An amperometric glucose enzyme biosensor based on porous hexagonal boron nitride whiskers decorated with Pt nanoparticles. *RSC Advances* **6** (2016) 92748-92753.

[123] A. J. Bard, L. R. Faulkner, J. Leddy and C. G. Zoski. Electrochemical methods: fundamentals and applications. *Wiley New York*, (1980)

[124] M. Ciobanu, J. P. Wilburn, M. L. Krim and D. E. Cliffel. Fundamentals. *Handbook of Electrochemistry*. *Elsevier* (2007) 3-29.

[125] P. M. Monk. Fundamentals of electroanalytical chemistry. *John Wiley & Sons* (2008).

[126] G. R. Bhimanapati, Z. Lin, V. Meunier, Y. Jung, J. Cha, S. Das, D. Xiao, Y. Son, M. S. Strano, V. R. Cooper, L. Liang, S. G. Louie, E. Ringe, W. Zhou, S. S. Kim, R. R. Naik, B. G. Sumpter, H. Terrones, F. Xia, Y. Wang, J. Zhu, D. Akinwande, N. Alem, J. A. Schuller, R. E. Schaak, M. Terrones, and J. A. Robinson. Recent Advances in Two-Dimensional Materials beyond Graphene. *ACS Nano* **9** (2015) 11509-11539.

[127] B. Conway. Electrochemical Capacitors: Scientific Fundamentals and Technology Applications. *Springer* (1999).

[128] R. J. Brodd, K. R. Bullock, R. A. Leising, R. L. Middaugh, J. R. Miller and E. Takeuchi. Batteries, 1977 to 2002. *Journal of the Electrochemical Society* **151** (2004) K1-K11.

[129] J. O. M. Bockris, B. E. Conway and R. E. White. Modern aspects of electrochemistry. *Springer Science & Business Media* (2012).

[130] D. C. Grahame. Electrode processes and the electrical double layer. *Annual Review of Physical Chemistry* **6** (1955) 337-358.

[131] P. Biesheuvel and J. Dykstra. The difference between Faradaic and Nonfaradaic processes in Electrochemistry. *arXiv preprint arXiv:1809.02930* (2018).

[132] B. E. Conway and R. Greef. Theory and principles of electrode processes, *Journal of The Electrochemical Society* **113** (1966) 325C-326C.

[133] H. Von Helmholtz. Studies of electric boundary layers. *Wiedemamm Annalen* **7** (1879) 337-382.

[134] M. Gouy. Sur la constitution de la charge électrique à la surface d'un électrolyte. *Journal of Theoretical and Applied Physics* **9** (1910) 457-468.

[135] D. L. Chapman. LI. A contribution to the theory of electrocapillarity. *The London, Edinburgh, and Dublin philosophical magazine and journal of science* **25** (1913) 475-481.

[136] O. Stern. The theory of the electrolytic double-layer. *Z. Elektrochem* **30** (1924) 1014-1020.

[137] D. Grahame. *Chemical Review* **41** (1947) 441.

[138] J. Bockris, M. Devanathan and K. Muller. Thermodynamic characterization of metal dissolution and inhibitor adsorption processes in the low carbon steel/mimosa tannin/sulfuric acid system. *Proceedings of the Royal Society A* **274** (1963) 55-79.

[139] P. Attard. Electrolytes and the electric double layer. *Advances in Chemical Physics* **92** (1996) 1-160.

[140] R. G. Compton and C. E. Banks. Understanding voltammetry. *World Scientific* (2011) .

[141] A. Fisher. Electrode Dynamics. *Oxford University Press* (1996).

[142] P. Zanello. Inorganic electrochemistry: theory, practice and application. *Royal Society of Chemistry* (2007).

[143] N. Elgrishi, K. J. Rountree, B. D. McCarthy, E. S. Rountree, T. T. Eisenhart and J. L. Dempsey. A Practical Beginner's Guide to Cyclic Voltammetry. *Journal of Chemical Education* **95** (2017) 197-206.

[144] P. T. Kissinger and W. R. Heineman. Cyclic voltammetry. *Journal of Chemical Education* **60** (1983) 702-706.

[145] J. Randles. A cathode ray polarograph. *Transactions of the Faraday Society* **44** (1948) 322-327.

[146] J. E. Randles. A cathode ray polarograph. Part II.—The current-voltage curves. *Transactions of the Faraday Society* **44** (1948) 327-338.

[147] C. M. Brett and A. O. Brett. Electrochemistry: Principles, Methods and Applications *Oxford University Press (1993)*.

[148] R. Murray. Chronoamperometry, chronocoulometry, and chronopotentiometry. *Physical Methods of Chemistry Volume II: Electrochemical Methods* (1986).

[149] J. Millerand and J. C. Miller. Statistics and chemometrics for analytical chemistry, *Pearson Education* (2005).

[150] A. Shrivastava and V. B. Gupta. Methods for the determination of limit of detection and limit of quantitation of the analytical methods. *Chronicles of Young Scientists* **2** (2011) 21-25.

[151] D. Harris. Calibration methods. *Harris DC. Quantitative chemical analysis. 6th edition. New York: WH Freeman and Company* (2003) 80-98.

[152] D. Macdonald. Transient techniques in electrochemistry. *Springer Science & Business Media* (2012).

[153] M. E. Orazem and B. Tribollet. Electrochemical impedance spectroscopy. *John Wiley & Sons* (2011).

[154] J. E. B. Randles. Kinetics of rapid electrode reactions. *Discussions of the Faraday Society* **1** (1947) 11-19.

[155] E. Warburg. Ueber die polarisationscapacität des platins. *Annalen der Physik* **311** (1901) 125-135.

[156] C. Brett and A. M. Oliveira Brett. Electrochemistry: principles, methods, and applications. *Oxford University Press* (1993).

CHAPTER 3

EXPERIMENTAL METHODOLOGY

3.1 INTRODUCTION

This chapter gives detailed information on the chemicals and materials that were used in the study, and the preparation procedures that have been used to achieve the objectives of this research. A detailed description of the different instruments used in the study is also presented.

3.2 CHEMICALS AND MATERIALS

All the chemicals used in this research work were procured from reliable suppliers. They are of analytical grade and were used without further purification. Aqueous solutions were prepared with Milli-Q water (18.2 MΩ.cm) obtained with Millipore system. All the materials used are listed in Table 3.1.

Table 3.1 List of chemicals and materials

Chemical/Materials	Formula/Description	Purity (%)	Source
Graphene oxide	GO, 0.3–0.7 µm flake size, 1 atomic Layer thickness	Not applicable (NA)	Graphene Supermarket
Molybdenum disulphide	MoS_2, 100-400 nm flake size, 1-8 monolayers thickness	>99.0%	Graphene Supermarket
Boron nitride	BN, 50-200 nm flake size, 1-5 monolayers thickness	>99.0%	Graphene Supermarket
Tungsten disulphide	WS_2, 50-150 nm flake size, 1-4 monolayers thickness	>99.0%	Graphene Supermarket
Gold nanoparticles solution	10 nm diameter, $6X10^{12}$ particles/mL, reactant free	NA	Sigma Aldrich
Peroxidase from horseradish (HRP)	Type II, essentially salt-free, lyophilized powder, 150-250 units/mg solid	NA	Sigma Aldrich
Poly(N-isopropylacrylamide), amine terminated	$(C_6H_{11}NO)_nSCH_2CH_2NH_2$ (PNIPAAm, average mol wt=2500	NA	Sigma Aldrich

Hydrogen peroxide	H_2O_2, ACS reagent, 30 wt% in H_2O	NA	Sigma Aldrich
Potassium dihydrogen phosphate	KH_2PO_4	99.99%	Sigma Aldrich
Dipotassium hydrogen phosphate	K_2HPO_4	99.0%	Sigma Aldrich
Disodium hydrogen phosphate	Na_2HPO_4	99.0%	Sigma Aldrich
Potassium chloride	KCl	99.0%	Sigma Aldrich
Sodium chloride	NaCl	99.0%	Sigma Aldrich
Potassium ferricyanide	$K_4[Fe(CN)_6]$	99.0%	Sigma Aldrich
Potassium ferrocyanide	$K_3[Fe(CN)_6]$	98.5%	Sigma Aldrich
Ethanol	C_2H_5OH	99.0%	Sigma Aldrich
Micro-polish Alumina Slurry	1.0 µm, 0.5 µm and 0.03 µm	NA	Buehler
Micro-cloth	PSA, 10 Inch	NA	Buehler
Reference electrode: Silver/Silver Chloride (3M KCl)	Ag/AgCl	NA	ALS Co., Ltd
Counter electrode: Platinum Wire	Pt wire	NA	ALS Co., Ltd

Working electrode: Glassy Carbon Electrode	GCE, diameter, 3mm	NA	ALS Co., Ltd
Copper sheet	Cu, 1 mm x 15.0 cm x 15.0 cm	99.9%	Alfa Aesar

3.3 RESEARCH SCHEME

The research scheme of the experimental work mainly consisted of the fabrication of 2D based nanohybrid electrobiocatalytic interfaces using self-assembly approach, preparation of bioelectrodes, and the structural and morphological characterization of the self-assembled interface system and finally the electrochemical characterization of the as-fabricated nanohybrid electrobiocatalytic interfaces. Figure 3.1 elucidates the overall research scheme of this work.

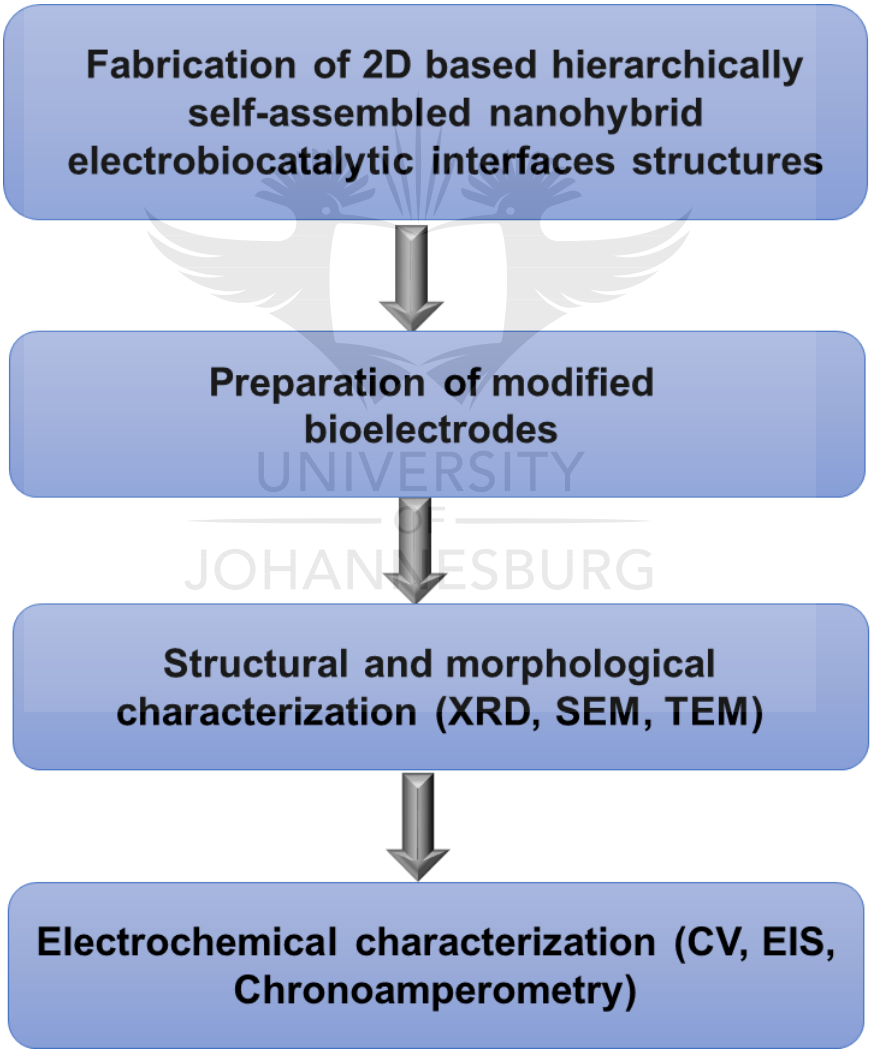

Figure 3.1 Flow chart of Research Scheme

3.4 FABRICATION OF 2D BASED HIERARCHICALLY SELF-ASSEMBLED NANOHYBRID STRUCTURES

A self-assembled method was used to assemble GO/MoS_2 nanohybrid structure with metal nanoparticles (AuNPs), polymer (PNIPAAm), and the immobilization of enzyme (Horseradish Peroxidase, HRP) using non–covalent interactions [1] as shown in Scheme 3.1.

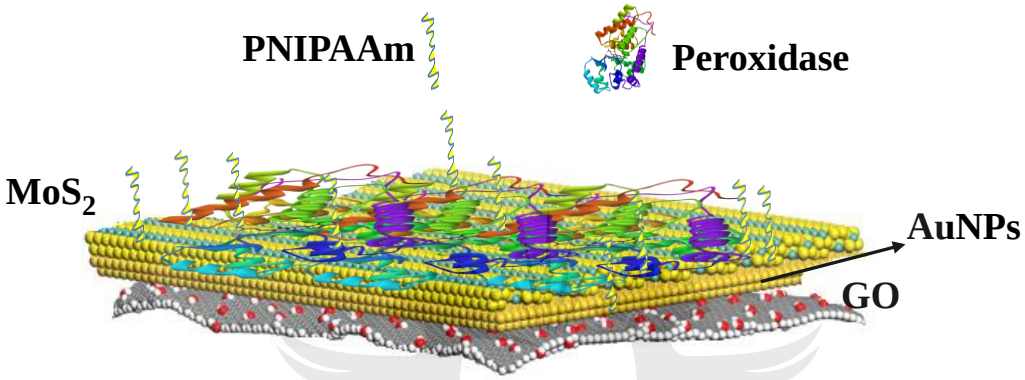

Scheme 3.1 Schematic representation of the fabricated GO/AuNPs MoS_2/PNIPAAm/Peroxidase 2D hierarchically self-assembled nanohybrid interfaces. (Note: Scheme not drawn to scale)

3.4.1 Preparation of GO/AuNPs/MoS_2/PNIPAAm/Peroxidase nanohybrid Interface structures

100 µL of the AuNPs solution (6×10^{12} particles/mL) was added to 15 µL of the aqueous GO solution (0.5 mg/mL) and the mixture was sonicated for 1 hour at room temperature (RT). This was immediately followed by the introduction of 100 µL of an aqueous solution of MoS_2 (0.018 mg/mL, dispersed in water), and the mixture was again sonicated for 1 hour. The resultant suspension was centrifuged three times (at 4000 rpm) to isolate AuNPs-MoS_2 decorated graphene oxide nanosheets. The resultant GO-AuNP-MoS_2 hybrid nanosheets structure was mixed with 10 µL of Poly (N-isopropyl acrylamide), amine (PNIPAAm) solution (10 mg/mL), washed with

distilled water to remove excess PNIPAAm and dried at RT prior to conjugation with enzyme peroxidase (10 mg/mL).

The GO-AuNP-MoS_2-PNIPAAm hybrid structure was subsequently conjugated with the peroxidase enzyme as follows: 10 mg of peroxidase was dissolved in 1 mL of deionized water; and the mixture was incubated for 3 hours at RT. 10 µL of peroxidase solution (10mg/1mL) was added to the GO-AuNP-MoS_2-PNIPAAm hybrid structure. The mixture was then centrifuged at 5000 rpm for 30 min after which the precipitate was washed with PBS and centrifuged successively (three times) to remove loosely attached enzymes from graphene oxide surface. The various stages involved in the fabrication of the GO-AuNPs-MoS_2-PNIPAAm-peroxidase is shown in Figure 3.2 (step 1).

3.4.2 Fabrication of bioelectrodes

GCE were carefully polished using 1.0 µm, 0.3 µm and 0.05 µm alumina slurry on polishing micro-clothes. They were then rinsed with deionized water (DI) and ethanol, sonicated for a few minutes in double-distilled water, and were allowed to dry at room temperature. The steps involved in purifying the GCE are presented in Figure 3.2 (step 2).

The nanohybrid solution containing a mixture of the GO-AuNPs-MoS_2-PNIPAAm-peroxidase enzyme was sonicated for 5 minutes to achieve a homogeneous dispersion. Subsequently, 10 µL of this suspension was drop-cast on the surface of the pre-cleaned GCE and dried for 8 hours at 4 °C as shown in Figure 3.2 (step 3). The other electrodes, such as those with/without enzyme, were prepared by the same procedures described above.

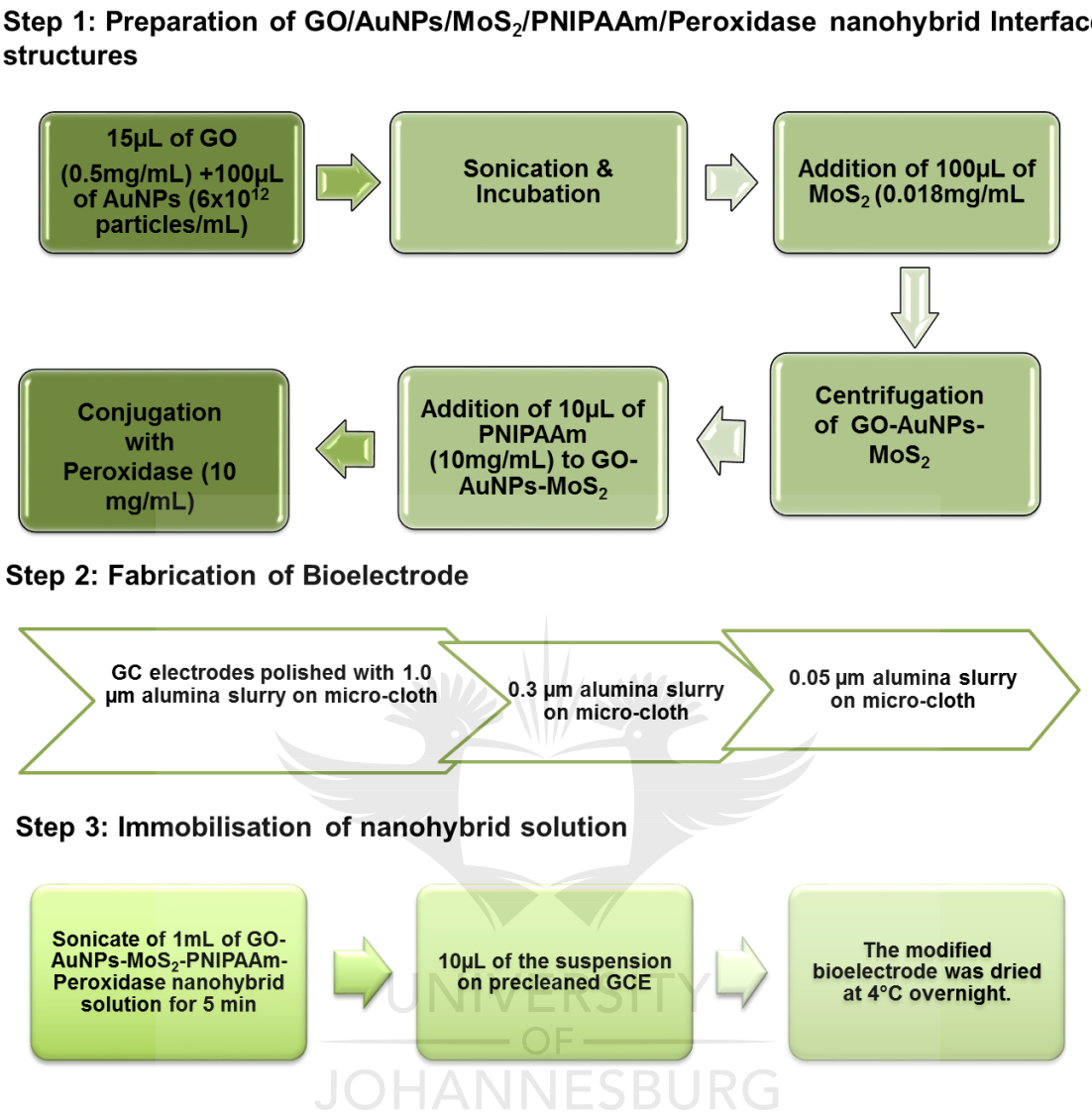

Figure 3.2 **Schematic representation of the synthesis procedure of GO/AuNPs/MoS_2/PNIPAAm/Peroxidase nanohybrid interface structure.**

3.4.3 FABRICATION OF BN/WS_2/AuNPs/HRP NANOHYBRID INTERFACE STRUCTURES

A self-assembled method was used to assemble BN/WS_2 nanohybrid structure with AuNPs and then immobilized HRP using non-covalent interactions [1-2] as shown in Scheme 3.2.

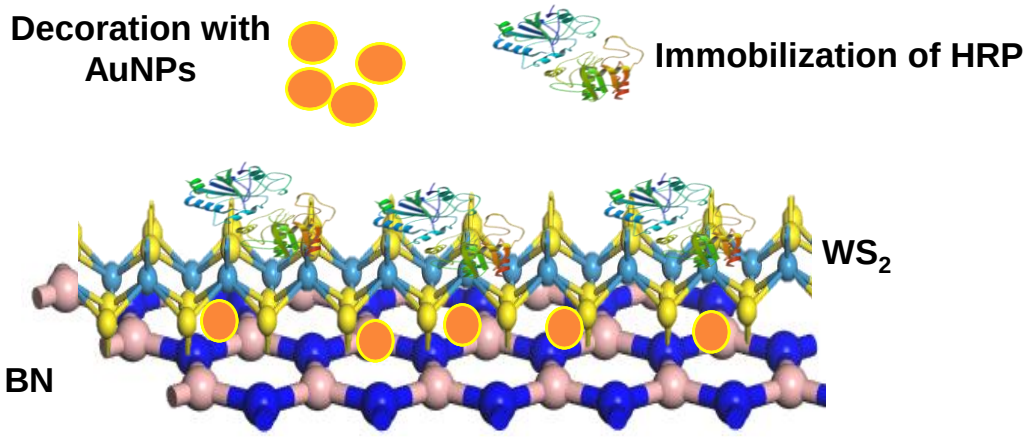

Scheme 3.2 Fabrication of hierarchical self-assembly interfaces of BN/WS_2/AuNPs/HRP nanohybrid structures. (Note: Scheme not drawn to scale)

3.4.4 Preparation of BN/WS_2/AuNPs/HRP nanohybrid Interface structures

The schematic presentation of the synthesis procedure of BN/WS_2/AuNPs/HRP 2D hierarchically self-assembled nanohybrid interfaces is shown in Figure 3.3 (a). The assembly of the BN/WS_2/AuNPs nanohybrid structure was achieved by adding 15 µL each of the aqueous solution of BN (5.4 mg/L) and AuNPs ($6X10^{12}$ particles/mL) to 15 µL of the aqueous solution of WS_2 (26 mg/L). The composite solution was then ultra-sonicated for 2 hours so as to produce a homogenous mixture of BN/WS_2/AuNPs. The resulting suspension was centrifuged three times for 5 minutes each at 4000 rpm to isolate unassociated and loose BN flakes, which were then separated from the hybrid structure.

A fresh 10 mg of HRP was dissolved in 1mL of deionized water. Subsequently, HRP was non-covalently immobilized onto BN/WS_2/AuNPs by adding 15 µL of an aqueous solution of HRP (10 mg/mL) to the prepared mixture of BN/WS_2/AuNPs, followed by sonication for 30 minutes to achieve a homogeneous dispersion of the

HRP/BN/WS_2/AuNPs nanohybrid structure. These samples were stored at 4 °C for further use.

3.4.5 Preparation of modified bioelectrodes

The GCE were carefully polished in three stages with 1.0 µm, 0.3 µm and 0.05 µm alumina slurry respectively on Buehler polishing micro-clothes. The polished GCE were successively rinsed with deionized water and ethanol in an ultrasonic bath. The cleaned GCE were then dried with nitrogen gas.

Subsequently, 15 µL of BN/WS_2/AuNPs/HRP suspension was drop-cast on the surface of the pre-cleaned GCE and dried overnight at 4 °C. The other electrodes, such as those with/without enzyme, were prepared by the same procedures described above. The stages involved in the preparation of the modified bioelectrodes are depicted in Figure 3.3 (b).

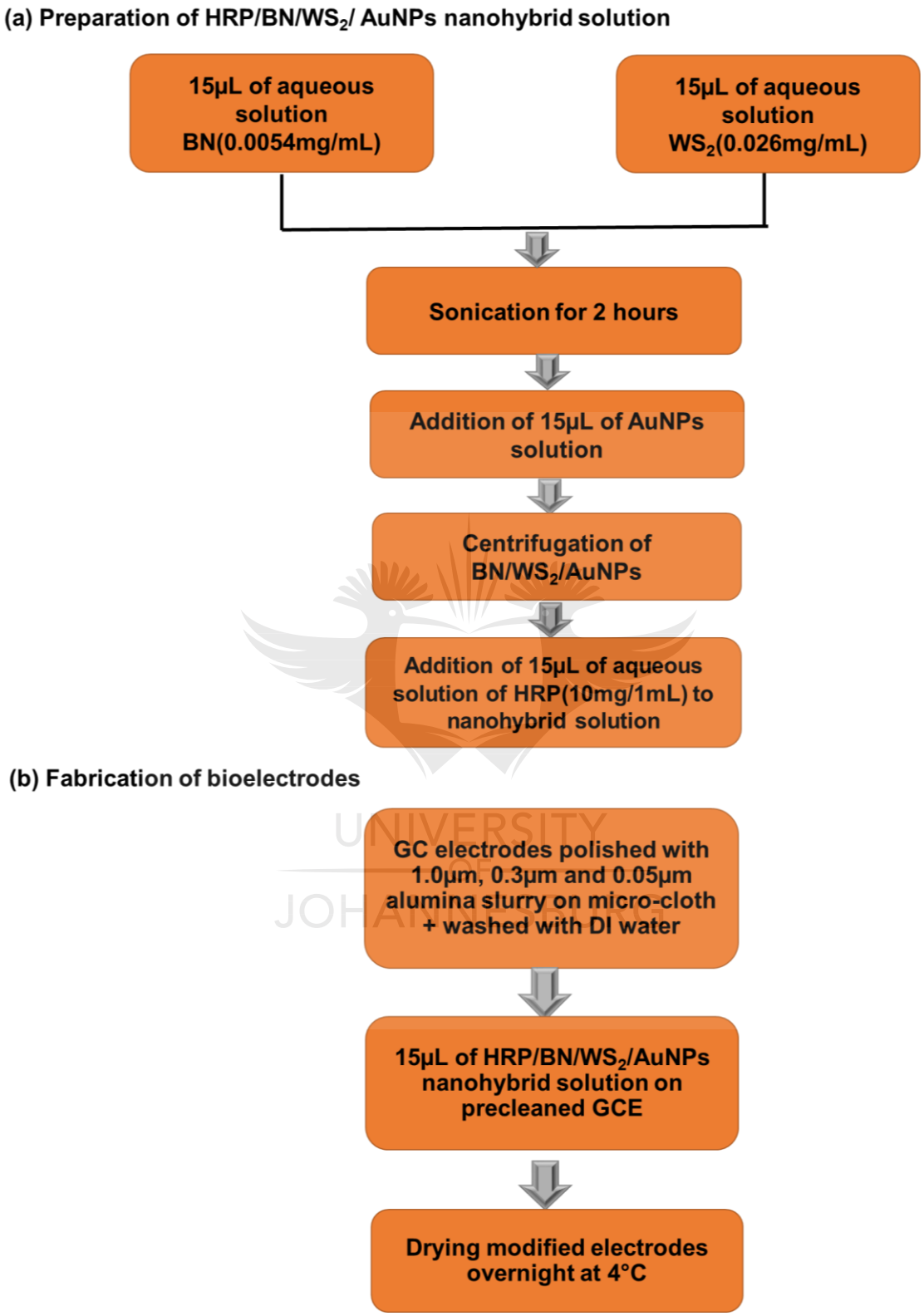

Figure 3.3 Schematic representation of the fabrication procedure of BN/WS_2/AuNPs/HRP nanohybrid interface structure.

3.4.6 Theoretical studies of BN/Au/WS_2 (001) nanohybrid structure

Theoretical studies of the BN/Au/WS_2(001) was done using first principle calculations. First–principles calculations reveal the nature of the electronic interaction occurring at the nanohybrid structure interface [3]. First–principles calculations were done for detailed study of the properties of BN/Au/WS_2(001) nanohybrid structure to obtain the theoretical perspective for its biosensing properties.

All the calculations were implemented using the CASTEP [4] code of the Materials Studio 2016 [4]. The GGA function of the Perdew–Burke–Ernzerhof were used to account for the exchange–correlation effects [5]. A Monkhorst–Pack [6] with *k*–points of 8 x 8 x 1 was used to optimise the crystal structure of the studied systems. The wavefunction of the valence electrons ($4f^{14}$ $5d^{10}$ $6s^1$ for Au, $4f^{14}$ $5d^4$ $6s^2$ for W, $3s^2$ $3p^4$ for S, $2s^2$ $2p^3$ for B and $2s^2$ $2p^5$ for N) were expanded using a plane wave cut–off energy of 400 eV. The atomic positions and the lattice parameters were fully relaxed using the Broyden–Fletcher–Goldfarb–Shanno approach [7] up until the convergence criteria of force and energy were less than 0.3 eV A^{-1} and 10^6 eV, respectively. To accurately describe the electronic properties, a hybrid Heyd−Scuseria− Ernzerhof functional was used [8].

3.5 FABRICATION OF Gr/WS_2/AuNPs/HRP NANOHYBRID INTERFACE STRUCTURES

In this section, a self-assembly fabrication of Gr/WS_2/AuNPs/HRP nanohybrid interface structure was achieved through the conjugation of CVD grown Gr with another 2D material (WS_2) decorated with AuNPs, followed by the immobilization of

HRP on the nanohybrid 2D materials using non-covalent interactions as shown in Scheme 3.3.

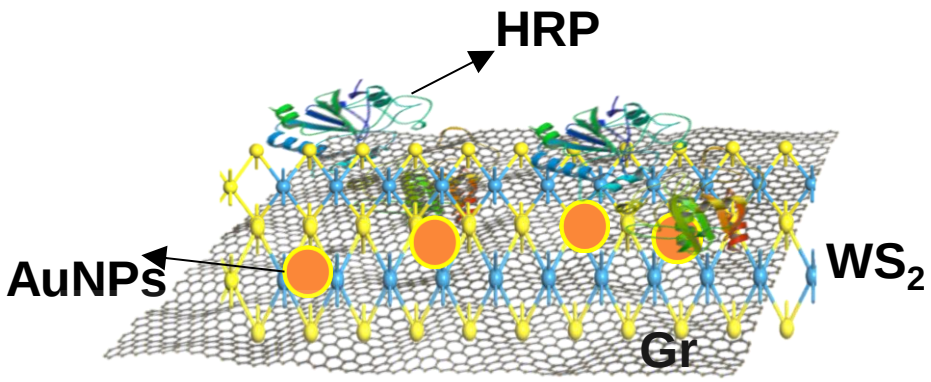

Scheme 3.3 Fabrication of hierarchical self-assembly interfaces of Gr/WS_2/AuNPs/HRP nanohybrid structures (Note: Scheme not drawn to scale)

3.5.1 Preparation of Gr/WS_2/AuNPs/HRP nanohybrid Interface structures

The synthesis procedure of fabrication of Gr/WS_2/AuNPs/HRP 2D hierarchically self-assembled nanohybrid interfaces consist of three steps and represented in Figure 3.4.

3.5.1.1 Preparation of CVD-synthesized graphene

The synthesis procedure of acetylene (C_2H_2) sourced CVD grown graphene has been reported by Osikoya *et al.* [9]. Firstly, the copper sheet (2x6 cm, 1mm thickness) was cleaned with ethanol thoroughly. The Cu metal strip was inserted in the middle of a horizontal tube furnace connected with the mass flow controller. The deposition of graphene on Cu sheet was achieved using a mixture of argon (Ar) and nitrogen (N_2) as carrier gases at flow rates of 350 cm^3/min and 250 cm^3/min,

respectively. C_2H_2 was used as the carbon source. The process involved purging the quartz tube with argon gas flowing at the rate of 50 cm^3/min for 30 min, after which the temperature controller had started heating the CVD system. The synthesis reaction was started by the introduction of acetylene gas at the flow rate of 10 cm^3/min for 2 minutes and was ended by stopping the acetylene gas flow. The reaction products were allowed to cool to 500 °C under the inert gas mixture of Ar and N_2 and they were then cooled to room temperature under nitrogen gas flow (alone) at a flow rate of 50 cm^3/min as shown in Figure 3.4.

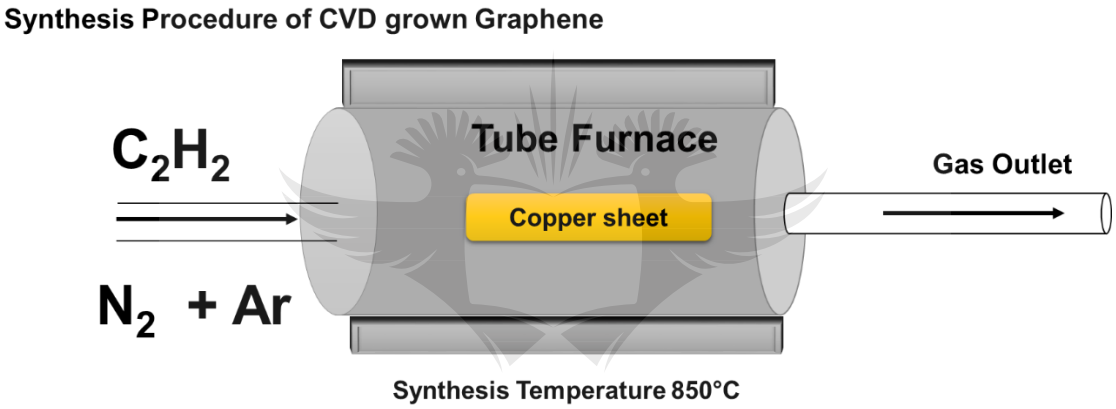

Figure 3.4 Schematic of the synthesis of graphene using CVD process. (Note: Image not drawn to scale)

3.5.1.2 Preparation of Gr/WS_2/AuNPs/HRP nanohybrid Interface structures

A 1 mg of the as synthesized graphene powder was dispersed in 1 mL of deionized water. The dispersed graphene was sonicated for 2 hours to produce a homogenous mixture. The resulting suspension was centrifuged 3-4 times for 10 minutes at 5000 rpm, to isolate monolayer graphene from multilayer graphene.

The graphene-WS_2 assembly was prepared by adding 20 µL of the dispersed graphene (1 mg/1mL) to 10 µL of the aqueous solution of WS_2 (0.026 mg/1mL). To prepare Gr/WS_2/AuNPs nanohybrid solution, 20 µL of 10 nm sized AuNPs solution

was added to the Gr/WS_2 composite. The 2D nanohybrid solution was mixed for 10 minutes to make a composite solution of Gr/WS_2/AuNPs.

A fresh 1 mg of HRP was dissolved in 1 mL of deionized water. Consequently, HRP was non-covalently immobilized onto Gr/WS_2/AuNPs by adding 10 µL of aqueous solution of HRP (1 mg/mL) to the 2D nanohybrid solution, followed by mixing for 1 min to achieve homogeneous dispersion of the Gr/WS_2/AuNPs/HRP nanohybrid structure. These samples were stored at 4 °C for further use. The procedure described above is depicted in Figure 3.5 (a).

3.5.1.3 Preparation of bioelectrodes

The glassy carbon electrode was polished with 1 µm, 0.3 µm and 0.05 µm alumina slurry sequentially. It was then sonicated in (1:1) ethanol and deionized water. After that, the GCE was dried in air and Gr/WS_2/AuNPs/HRP dispersion (10 µL) was drop cast onto it and dried overnight. This procedure is presented in Figure 3.4 (b). The other modified electrodes were similarly prepared with/without enzyme using the same procedure described above.

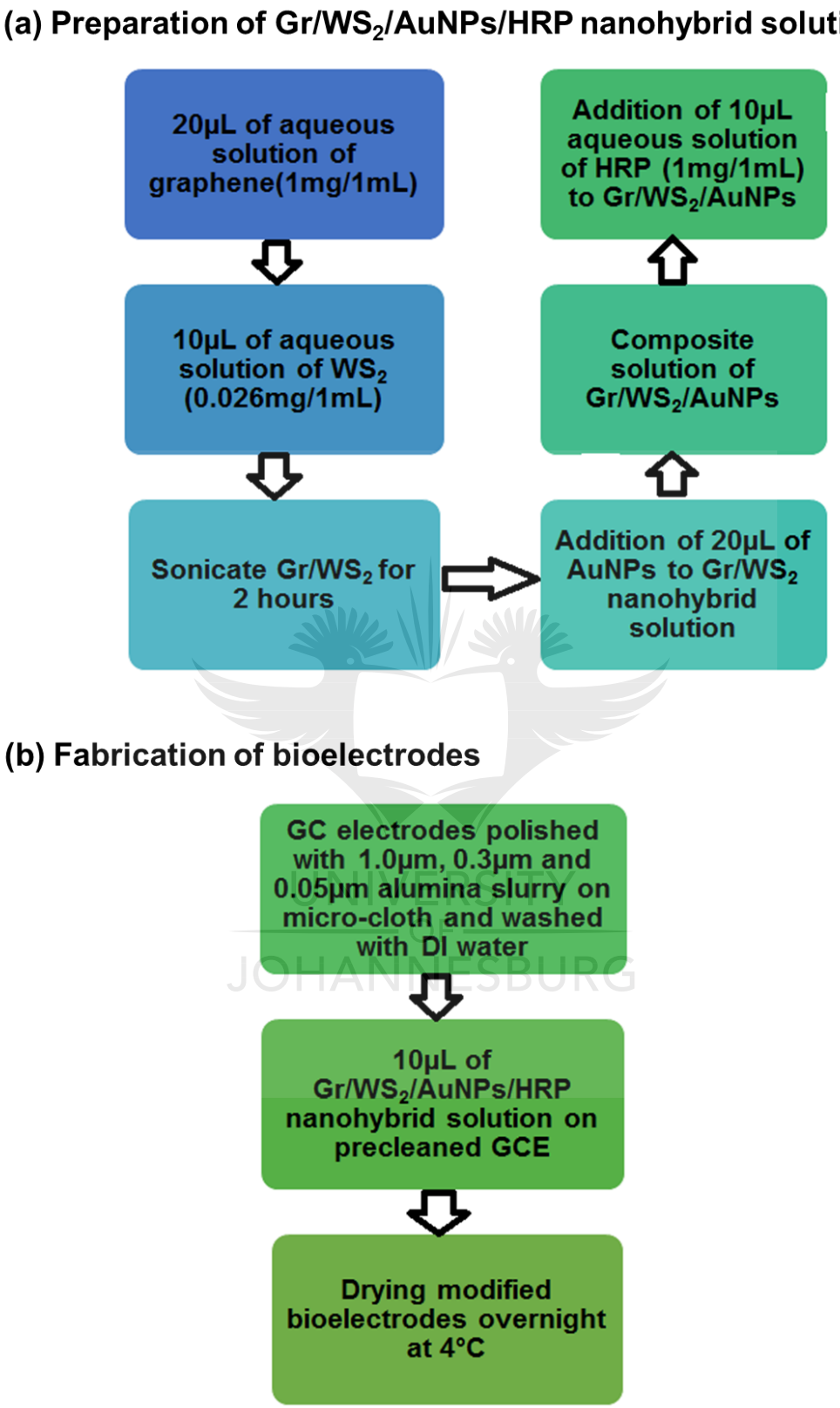

Figure 3.5 Schematic representation of the synthesis procedure of fabricating Gr/WS2/AuNPs/HRP nanohybrid interfaces.

3.6 ELECTROCHEMICAL CHARACTERIZATIONS

3.6.1 Experimental set-up for the electrochemical experiment

3.6.1.1 Electrochemical cell and electrodes

The electrochemical cell consists of a working electrode (WE), a reference electrode (RE), and usually a counter (auxiliary) electrode (CE) as shown in Figure 3.6.

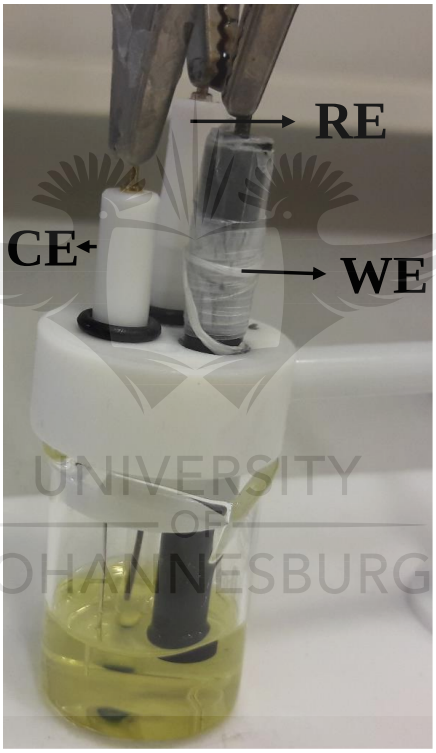

Figure 3.6 Image of the electrochemical cell used in this study.

3.6.1.2 Working electrode

The working electrode is made of a glassy carbon, with a well-defined surface area as shown in Figure 3.7.

Figure 3.7 Image of glassy carbon electrode used in this project.

3.6.1.3 Reference electrode

The reference electrode used in this study is the silver/silver chloride electrode (Ag/AgCl) as shown in Figure 3.8.

Figure 3.7 Images of reference electrodes (Ag/AgCl) used in this project.

3.6.1.4 Counter electrode

The counter electrode is made of platinum wire. The counter electrode used in this study is shown in Figure 3.9.

Figure 3.8 Image of the counter electrode used in this study.

3.6.1.5 Supporting electrolyte

Phosphate buffer solution (PBS) was used as the supporting electrolyte in this project. **The detailed procedure for preparing of PBS is described in 3.6.2.1**

3.6.2 Cyclic voltammetry experiment and solution preparation

As shown in Figure 3.7, GCE was used throughout this project. The cleaning of these electrodes was done by mechanical polishing with alumina slurry. The CE were used as available and they were rinsed in deionized water before and after each use. The reference electrode, Ag/AgCl, was always stored in a solution of 3M KCl when not in use and also rinsed with deionized water before each use.

The CV experiment was performed in 10 mM ferro/ferri cyanide solution containing 10mM PBS (pH=7.4) as a redox probe by scanning a potential -0.2 to 0.8 V with

E_{start} =0.8 V at different scan rates which ranges from 10 to 100 mV/s and current range of 100 µA is selected as shown in Figure 3.10.

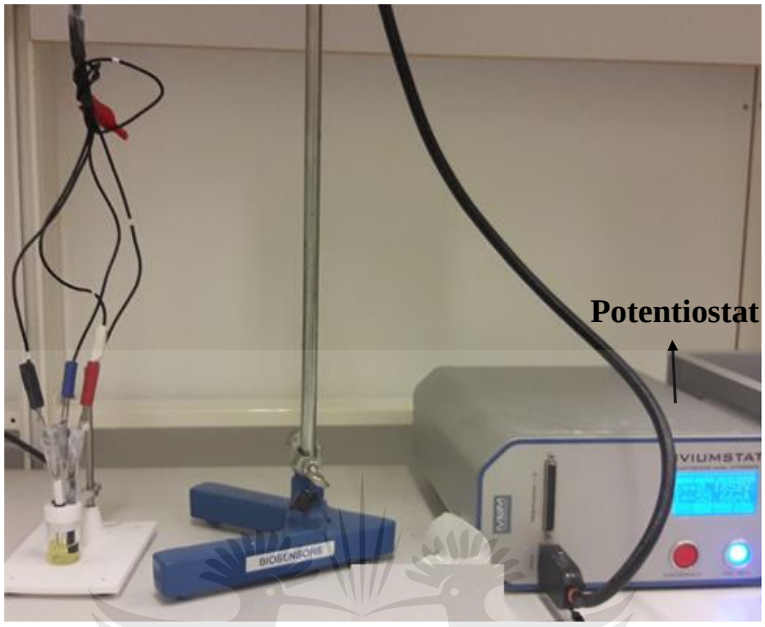

Figure 3.9 Typical electrochemical set up used in this study involving the three electrode cell system and Iviumstat potentiostat.

Equations (3.1) and (3.2) were used in the calculation of solution concentrations used in the study.

$$Concentration\ \left(\frac{mol}{L}\right) = \frac{Mass\ (g)}{Molcular\ weight\left(\frac{g}{mol}\right) \times Volume\ (L)} \quad \text{.....(3.1)}$$

Where dilute solutions are required, equation (3.2) was used in diluting the stock solutions to the required concentrations.

$$C_1V_1 = C_2V_2 \quad \text{.....(3.2)}$$

Where C_1 is the starting concentration and V_1 is the starting volume and C_2 is the final concentration and V_2 is the final volume.

3.6.2.1 Buffer solution preparation: 10mM phosphate buffer saline (PBS)

A 250 mL PBS (10mM) stock solution was prepared by dissolving 0.36 g of Na_2HPO_4, 0.06 g of KH_2PO_4, 0.05 g of KCl, 2.0 g of NaCl in 200 mL of deionized water. Also, 0.1 M NaOH and 0.1 M HCl were separately prepared respectively for adjusting the pH of the PBS to 7.4 by adding them as required. After adjusting to the required pH of 7.4, the solution is topped up to 250 mL by adding deionized water.

3.6.2.2 Preparation 10mM Ferri/Ferro cyanide

For preparing 100 mL of ferri/ferro cyanide ($[Fe(CN)_6^{3-/4-}]$) stock solution, 0.329 g of $K_3Fe(CN)_6$ and 0.422 g of $K_4Fe(CN)_6$ were dissolved in 80 mL of 10 mM PBS of pH 7.4 and subsequently made up to 100 mL (with the prepared 10 mM PBS). The prepared solution was used as the redox probe in this project.

During the CV and EIS measurements, certain volume of prepared electrolyte (10 mM $[Fe(CN)_6^{3-/4-}]$ and 10 mM PBS) were put into the electrochemical cell. The 10 mM PBS and 10 mM KCl supporting electrolyte were used in all chronoamperometry experiments.

3.6.3 Analyte sensing

H_2O_2 was used as the model target analyte in the study to demonstrate the electrobiocatalytic and biosensing ability of the differently modified bioelectrodes (as mentioned in sections 3.4.2, 3.5.2 and 3.6.1.3.1). Different concentration of H_2O_2 was prepared by using equation (3.2).

3.6.4 Analytical performance

The efficiency and applicability of the fabricated sensors were determined from chronoamperometry experiment.

3.7 MATERIALS CHARACTERIZATION

Structural and morphology characterization of the synthesized nanohybrid structures were carried out using different techniques i.e. XRD, TEM and SEM. On the other hand, electrochemical characterization of the different modified electrodes was done by CV and EIS.

3.7.1 X-Ray Diffraction

XRD is a versatile, non-destructive analytical technique capable of giving information about structural features and phase determination of materials under analysis. The crystallite size and shape of crystalline materials could also be determined with XRD technique.

3.7.1.1 Principle of XRD analysis

X-rays are electromagnetic radiations with wavelengths of about 1 Å (10^{-10} m). The X-rays are generated form cathode ray tube (see Figure 3.11) and filtered to produce monochromatic x-ray which is then focused on the sample. The incident ray is diffracted in accordance with Bragg's law as stated in equation (3.3). The diffraction angle and intensity of the diffracted ray is then detected and measured.

This law (Bragg's law) expresses the relationship between the wavelength of electromagnetic radiation to the diffraction angle and the lattice spacing in a crystalline sample.

$$n\lambda = 2d\ sin\theta \quad \text{.....(3.3)}$$

Where n, λ, d and θ describes an order of reflection, wavelength, the distance between different planes of atoms in the crystal lattice, and the angle of diffraction, respectively.

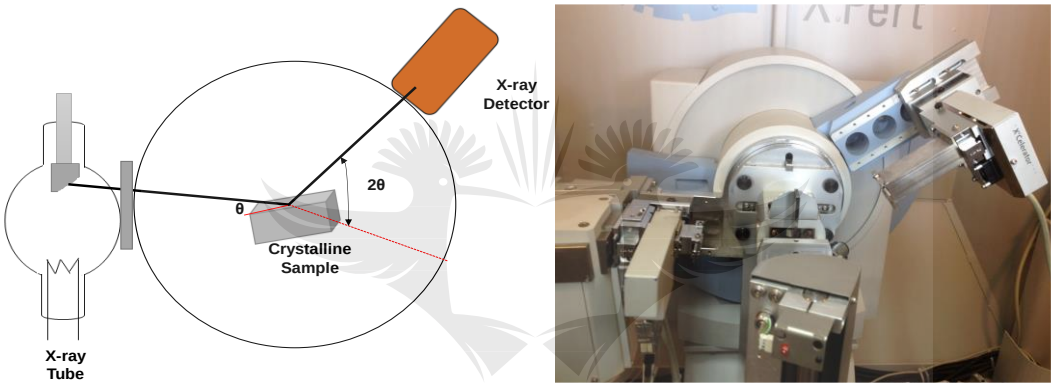

(a) (b)

Figure 3.10 (a) Schematic representation of X-ray diffractometer (b) image of Shimadzu XD-3A X-ray diffractometer used in the project.

Bragg's equation gives the relationship between the wavelengths of electromagnetic radiation (λ), lattice spacing in crystalline sample (d) and the diffraction angles (θ) [9].

Different diffraction patterns are produced with different crystalline samples due to different kinds of arrangement of atoms present in particular crystal structure which in turn determine peak intensities and peak positions at a particular diffraction angle of 2θ.

The following information could be obtained from x-ray diffraction pattern:

(i) Unit cell structure, lattice parameters and Miller indices.

(ii) Phase identification

(iii) Crystalline size from the width of the peak in a particular pattern.

The XRD of all the fabricated nanohybrid structures in this study were investigated using Shimadzu XD-3A X-ray diffractometer (Figure 3.11(b)) at 20 kV using Cu-Kα radiation (k =0.1542 nm) within the diffraction angle range (2θ) from 4° to 90°.

3.7.2 Transmission Electron Microscopy

Due to their versatility and high spatial resolution, electron microscopes have evolved as great tools for the characterization of a wide range of materials. The two main types of electron microscopes are the transmission electron microscope and the scanning electron microscope.

The TEM principle is to use the transmitted electrons; the electrons which are passing through the specimen before they are collected as shown in Figure 3.12 [10].

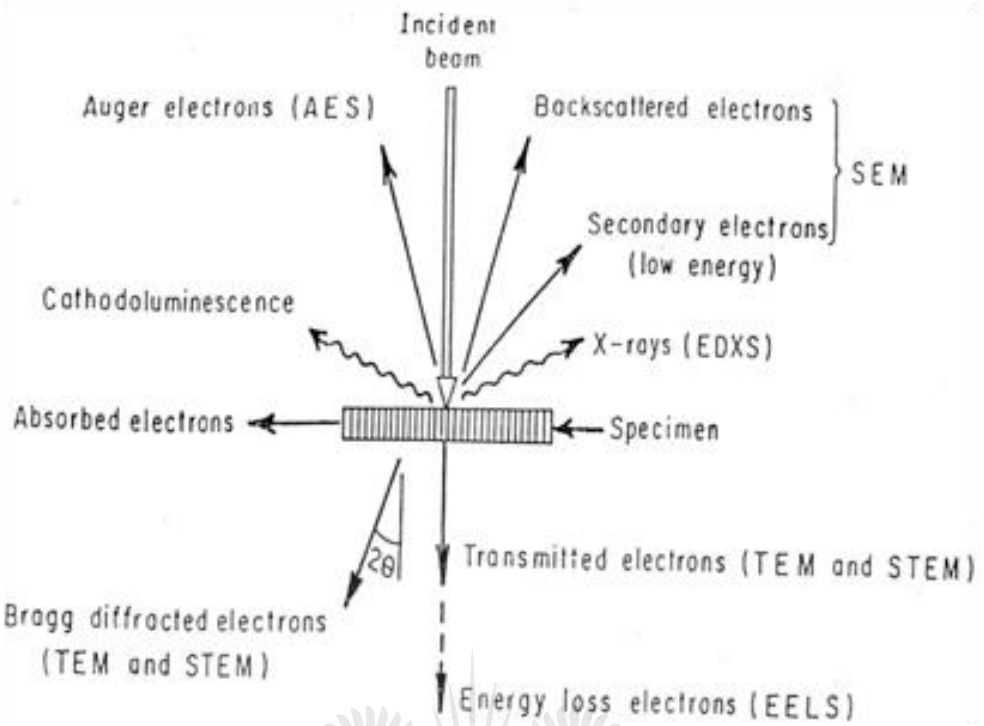

Figure 3.11 Schematic diagram showing the interaction of electrons with specimen [10].

A beam of electron is transmitted through a very thin lens which interacts with the specimen. Due to the interaction of the electrons transmitted through the specimen, an image is formed and then this image is magnified and focused on a fluorescent screen or detected by light-sensitive charged-coupled device (CCD) camera. The detected image is shown in real time on a monitor or via a computer [11] as indicated in Figure 3.13.

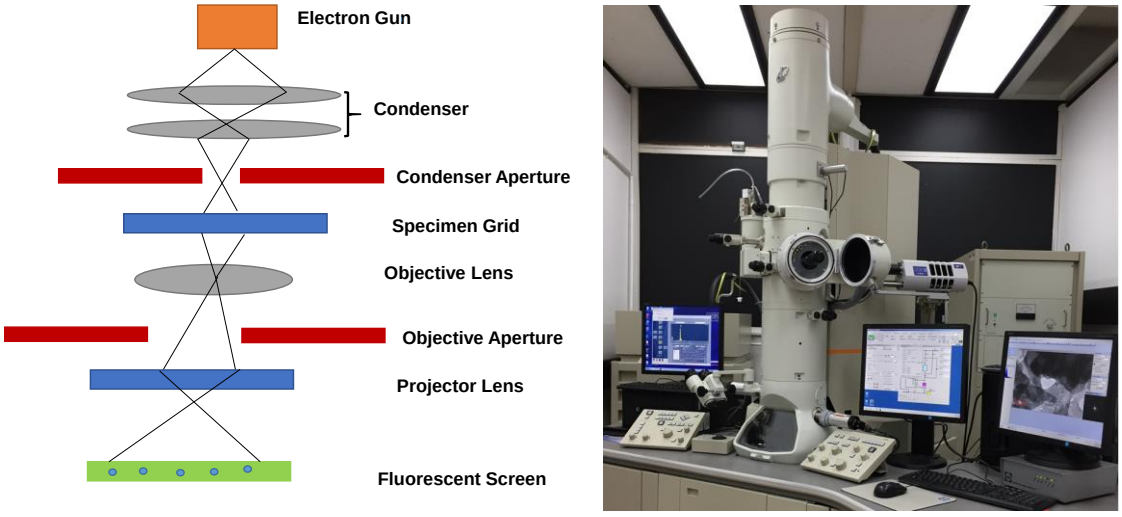

(a) (b)

Figure 3.12 (a) A schematic diagram describing the path of an electron beam in a TEM (b) Image of installed JEOL (JEM-2100).

TEM provides very important and valuable information on the inner structure of the sample, such as crystal structure [12].

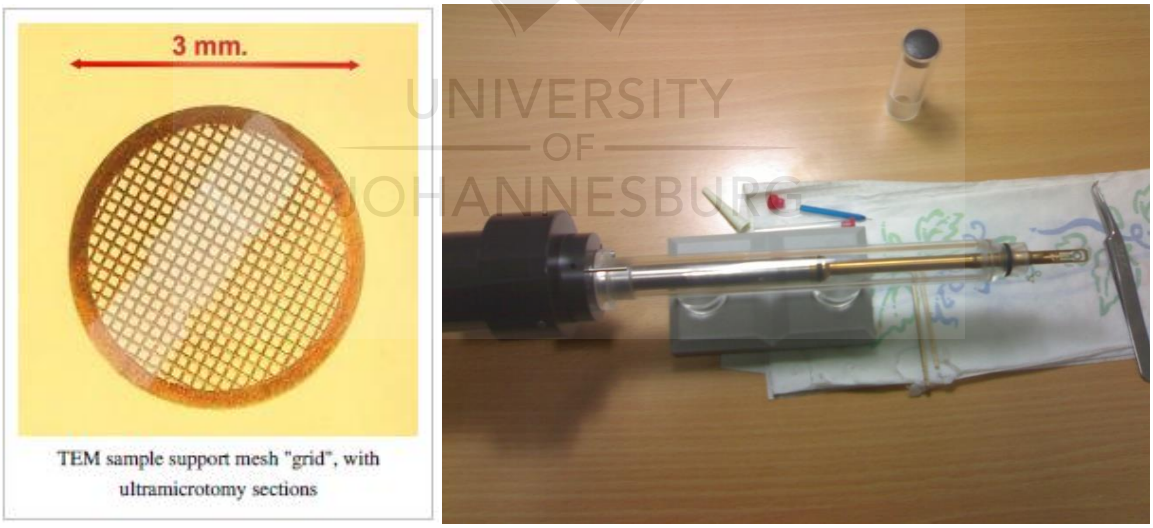

(a) (b)

Figure 3.13 (a) TEM sample support mesh grid, and (b) a sample holder with vacuum rings.

The specimen stage of TEM contain airlocks which allow the insertion of the specimen holder into the vacuum. The specimen holders are used to hold a

standard size of the grid. The sample is placed onto the inner meshed area having a diameter of approximately 2.5 mm and the usual grid materials are copper, molybdenum, gold or platinum (Figure 3.14 (a)). This grid is placed into the sample holder (as shown in Figure 3.14(b)) which is paired with the specimen stage.

In this study, the sample for TEM was prepared by drop-casting 20 µL of the sample hybrid material onto a Cu-grid coated with a lacy carbon film.

3.7.3 Scanning Electron Microscopy

In contrast to the TEM technique, the electrons are not transmitted through the sample in SEM. In SEM, two types of electrons are primarily detected: (a) backscattered electrons (BSE) and (b) secondary electrons (SE) as shown in Figure 3.12. SE are as a result of inelastic interactions between the electron beam and the sample. Thus, SE come from surface regions and backscattered electrons are reflected back after elastic interactions between the beam and the sample while BSE originates from deeper regions of the sample.

The SEM produces images by probing the specimen with a focused electron beam which is scanned across a rectangular area of the specimen and so images are produced by detecting secondary electrons and the detector captures the image by mapping the detecting signal based on beam position as presented in Figure 3.15 (a). SEM has the advantage of revealing three-dimensional images [13].

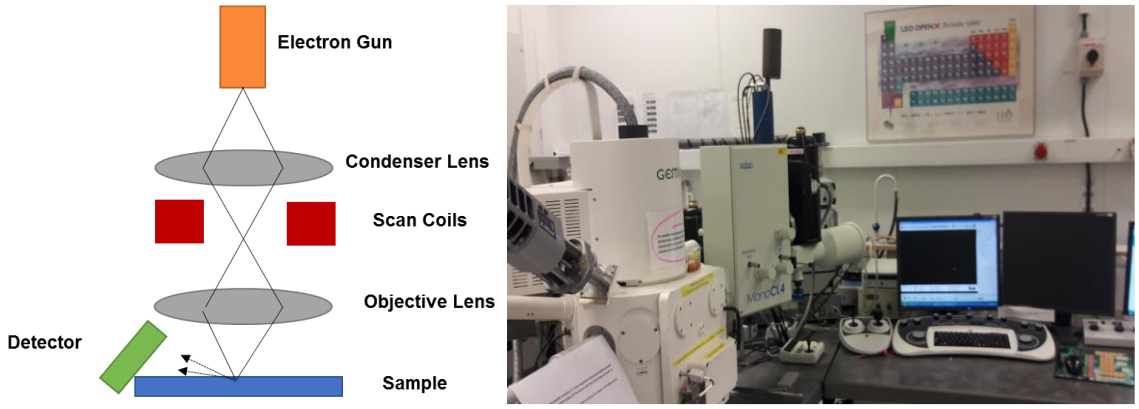

(a) (b)

Figure 3.14 (a) Schematic diagram of SEM (b) Image of installed LEO 155 Gemini.

The surface morphologies and elemental analysis of the samples used in this study were examined using a scanning electron microscopy (LEO 155 Gemini) under a 20 kV electron acceleration voltage as shown in Figure 3.15 (b).

3.8 REFERENCES

[1] O. Parlak, A. Tiwari, A. P. Turner and A. Tiwari. Template-directed hierarchical self-assembly of graphene based hybrid structure for electrochemical biosensing. *Biosensors and Bioelectronics* **49** (2013) 53-62.

[2] O. Parlak, P. Seshadri, I. Lundström, A. P. Turner and A. Tiwari. Two-Dimensional Gold-Tungsten Disulphide Bio-Interface for High-Throughput Electrocatalytic Nano-Bioreactors. *Advanced Materials Interfaces* **1** (2014) 1400136.

[3] V. Coropceanu, H. Li, P. Winget, L. Zhu and J.-L. Brédas. Electronic-structure theory of organic semiconductors: charge-transport parameters and metal/organic interfaces. *Annual Review of Materials Research* **43** (2013) 63-87.

[4] M. Segall, P. J. Lindan, M. a. Probert, C. J. Pickard, P. J. Hasnip, S. Clark and M. Payne. First-principles simulation: ideas, illustrations and the CASTEP code. *Journal of Physics: Condensed Matter* **14** (2002) 2717.

[5] J. P. Perdew, K. Burke and M. Ernzerhof. Generalized gradient approximation made simple. *Physical Review Letters* **77** (1996) 3865-3868.

[6] J. D. Pack and H. J. Monkhorst. Special points for Brillouin-zone integrations—a reply. *Physical Review B* **16** (1977) 1748-1749.

[7] D. C. Liu and J. Nocedal. On the limited memory BFGS method for large scale optimization. *Mathematical Programming* **45** (1989) 503-528.

[8] J. Heyd, G. E. Scuseria and M. Ernzerhof. Hybrid functionals based on a screened Coulomb potential. *The Journal of Chemical Physics* **118** (2003) 8207-8215.

[9] A. O. Osikoya, O. Parlak, N. A. Murugan, E. D. Dikio, H. Moloto, L. Uzun, A. P. Turner and A. Tiwari. Acetylene-sourced CVD-synthesised catalytically active graphene for electrochemical biosensing. *Biosensors and Bioelectronics* **89** (2017) 496-504.

[10] L. Reimer. Electron-Specimen Interactions. In: Transmission Electron Microscopy. Springer Series in Optical Sciences, vol 36. *Springer*, Berlin, Heidelberg (1984).

[11] B. D. Cullity and S. R. Stock. Elements of X-ray Diffraction. *Pearson Education* (2014).

[12] J. Eberhart. Structural and chemical analysis of materials. X-ray, electron, and neutron diffraction; X-ray, electron, and ion spectrometry; electron microscopy. *Journal of Applied Crystallography* **26** (1993) 145.

[13] O. C. Wells. Method and apparatus for detecting low loss electrons in a scanning electron microscope, US Patents, 1995.

CHAPTER 4

HIERARCHICALLY ASSEMBLED TWO-DIMENSIONAL HYBRID NANOINTERFACES: A PLATFORM FOR BIOELECTRONIC APPLICATIONS

4.1 INTRODUCTION

The design and fabrication of two-dimensional nanointerfaces for bioelectronic systems has recently become a major focus in bioelectronics applications and devices due to the superior electrical, thermal, optical and mechanical properties of nano-structured 2D materials over their three-dimensional (3D) and bulk counterparts [1-3]. The atomic thinness of these 2D materials makes it possible to easily integrate them in bioelectronic device design as advance interface materials. Additionally, their flexibility, electron transport properties, good biocompatibility, large surface area, notable electron transfer and ease of hybridization [4-8] make them the ideal interface materials in devices designs where flatness, sensitivity and high efficiency are requirements [3, 9].

Some of the materials with the potential applicability in the fabrication of two-dimensional nano-interfaces for bioelectronic systems are graphene/graphene oxide and MoS_2 [10]. Graphene possesses excellent electron mobility of about 120000 cm^2/Vs which makes it a very effective material for application in nanoelectronics, electrobiocatalytic reactors and biosensors [11-13]. GO, an oxidized form of graphene, with oxygen-containing functional groups (such as epoxy, hydroxyl, carbonyl and carboxyl groups) on the basal and edge planes, is more compatible with biomolecules thus, making it an excellent platform for electrobiocatalysis reactions [14-17].

The work presented in this chapter has been published in the *Electroanalysis,* **30** (2018) 2339-2348.

Similarly, layered TMDs, with the generalized formula MX_2, where M is a transition metal of groups IV, V, and VI, and X is a chalcogen such as S, Se, and Te, mostly possesses graphene-like structural features leading to similar electron mobility features in their nanosized forms. MoS_2, a typical TMD with structural feature involving a Mo atom sandwiched between two S atoms (S-Mo-S), with the S-Mo-S repeating units chemically bonded to form nanosheets [11, 18, 19], possesses quite a number of outstanding properties.

These properties include tunable energy band gap, high electron mobility, relatively low toxicity, good chemical stability and large specific surface area [20]. Due to its catalytically active sites, MoS_2 is suitable for capturing various biomolecules which provide the excellent increase in signal amplification which is quite essential in the operations and functions of bioelectronic devices [7, 11]. The combination of two hybrid 2D materials i.e. GO and MoS_2 hybrid structures offer the possibility to create devices with broad functionalities with better electrochemical performance due to improvement in electron transport features and good biocompatibility with biomolecules [20-22]. GO-MoS_2 nanohybrid combination will facilitate efficiency by preserving the effective carrier mobility of graphene while facilitating electron transfer at the interface [9, 10].

Studies have shown that the incorporation of AuNPs at the interfaces of nanohybrid leads to an increase in the electrobiocatalytic activities of such devices [23]. This is due to the introduction of current amplification features by the AuNPs at the interface, and the synergistic effect of the smart nanohybrid combinations leading to improved conductivity, good stability and high electrocatalytic activity [23-26].

It is a known fact that the presence of oxygenated functional groups in the GO, (though enhances biocompatibility through improved hydrophilicity) leads to decreased conductivity [18, 27-29]. Consequently, the GO-MoS_2 hybrid interface structure was decorated with AuNPs to improve the conductivity and interface electron transfer.

Poly (N-isopropylacrylamide, PNIPAAm) was subsequently conjugated with the hybrid nano interface materials through both covalent and non-covalent interactions to enhance the stability of the interface material and reduce leaching at the electrode surface [27, 28]. A suitable bio-recognition element (HRP) was eventually immobilized on the polymer-nanohybrid interface materials and the resultant bioconjugate structure was immobilized on pre-cleaned electrode GCE for the electrochemical detection of the model target analyte (H_2O_2) to demonstrate biosensing ability of the fabricated bioconjugate interface material.

We, therefore, report the fabrication of dual 2D system consisting of AuNPs doped GO/MoS_2/PNIPAAm/HRP conjugated hybrid structures as a platform for electrobiocatalytic reactions for the fabrication of sensitive biodevices. Using electrochemical techniques, we demonstrated by using H_2O_2 as a model analyte, that the dual 2D nanohybrid electrobiocatalytic interface structure can be used as a platform for efficient electrobiocatalytic reactions in bioreactors, biosensing and bioelectronics applications.

4.2 EXPERIMENTAL

4.2.1 Characterizations

The zeta potential of the graphene oxide dispersions before and after surface modification with enzyme was determined using a Nano ZS dynamic light scattering (DLS) Zeta potential instrument (Malvern Instruments, Worcestershire, UK). For the morphology of the sample, we used a SEM instrument (Jeol XL30, MA, USA) with image magnification range of x5–x1,000,000; a resolution of 2 nm and an accelerating voltage of 1–30 keV using an aluminium stub.

The GO was characterized with Raman spectroscopy, SEM, TEM and atomic force microscopy (AFM). The surface charge analysis was done by using zeta potential measurement. The fabricated modified bioelectrodes were characterized to assess the electron transfer properties at the interface, by using CV and EIS, while the electrobiocatalytic activity of the fabricated modified bioelectrodes towards the reduction of H_2O_2 was done via chronoamperometric measurements. The detailed procedures followed in the characterization of all the samples using CV, EIS, chronoamperometry, TEM and SEM are discussed in sections 3.7.2, 3.7.2.2, 3.7.3, 3.8.2 and 3.8.3 respectively.

4.2.2 Preparation of monohybrid electrobiocatalytic interfaces structures

Chapter 3, section 3.4.1 provides a detail description of the preparation.

4.2.3 Fabrication of bioelectrodes

The bioelectrodes fabrication procedures are discussed in chapter 3, section 3.4.2.

4.3 RESULTS AND DISCUSSION

The hierarchically self-assembled AuNPs doped GO-MoS_2-PNIPAAm-Peroxidase hetero structure interface system is presented in Scheme 4.1(a) with the correspondent electrobiocatalytic reduction of H_2O_2 via the nano-constructed interface bioelectrode in Scheme 4.1(b).

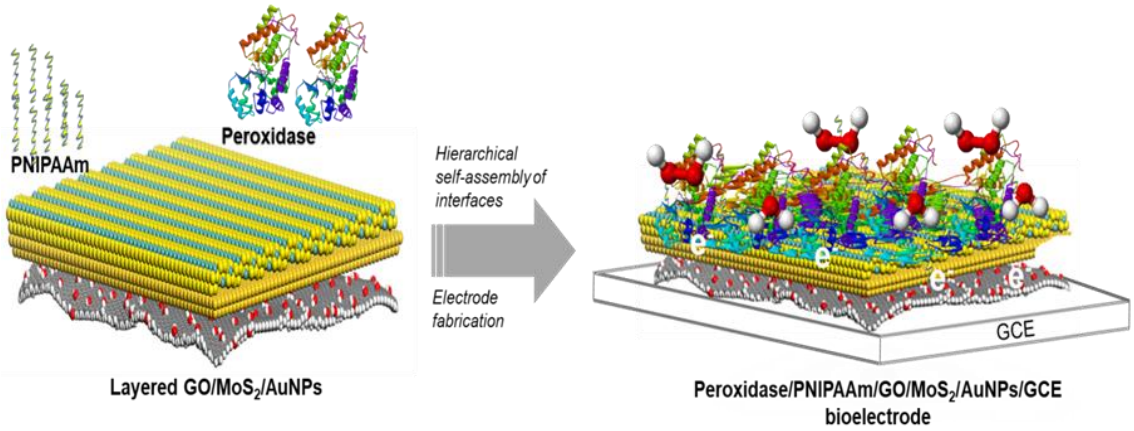

Scheme 4.1 2D-hetero hierarchically self-assembled hybrid interfaces: (a) AuNPs doped layered GO/MoS_2 2D nano-hetero interfaces (b) fabrication of GO/AuNPs/MoS_2/PNIPAAm/Peroxidase bioelectrode and electrobiocatalytic conversion of H_2O_2. (Note: Scheme not drawn to scale)

Raman spectroscopy result of the GO is presented in Figure 4.1(a), showing the presence of the D-band at 1347 cm^{-1} and the G-band at 1591 cm^{-1} respectively. Raman spectroscopy is one of the key tools for the characterization of sp^2 hybridized carbon nanomaterials [11], the technique is non-destructive, and it is capable of being utilized in the structural and electronic assay of the material.

Experimental results have shown that Raman spectroscopy is quite useful for studying the electron-defect scattering, electron-electron and electron-phonon phenomenon in graphene at variable carrier density. The presence of the D-band indicates the presence of a chemical bond, edges, and symmetry breaking perturbations in the sample, it basically requires the presence of lattice defects to be Raman active [30, 31]. The G-band in carbon nanomaterials including graphene is as a result of sp^2 hybridized C-C bond stretching, corresponding to the first-order scattering of the E_{2g} mode [32-34].

The surface charge analysis (zeta potential) result for the 2D nanohybrid interface materials is presented in Figure 4.1(b). The zeta potential of a colloidal system is quite important for understanding the electrochemical equilibrium of the interface material, giving information about the effect of pH on the surface charge at the interface, and consequently the colloidal stability of the dispersed material. The isoelectric point (IEP) of the colloidal system (which is the pH at which the electrical charge at the interface is neutral) could also be determined through the zeta potential measurements.

In the present study, the surface of the GO nanosheets was first modified with a metallic nanoparticle, then with a metallic sulphide. These surface modifications altered the initially observed surface charge of the GO nanosheets due to the electrostatic interaction between the electronegative oxygenated functional groups in the GO and the electropositively charged metallic substances. The zeta potential of the unmodified GO was observed to decrease with increasing pH from - 4.36 mV to - 74.53 mV, this may be due to the hydrolysis of C-O and carbonyl (C=O) groups in the GO by the alkaline environment to carboxylic ($-COO^-$) group.

However, after modification with metallic AuNPs, the surface charge at the strongly acidic pH 2 was observed to be 43.5 mV. This observation may be due to the overall influence of the acidic protons (H^+) coupled with the metal particles to produce overall highly electropositive charge which will be attracted to the electronegative surface of the GO, resulting in the observed highly electropositive surface charge at low pH. This surface charge (of the GO) was observed to decrease with increasing basicity and at pH 10, the surface charge was observed to be - 32.8 mV, which might be due to the neutralizing effect of the base on the metallic charge in the

strongly basic medium, the formation of the –COO group. These results clearly showed that the surface charge characteristic at the interface can be tuned by modifying the pH of the system.

The surface morphology and the height profile for the GO nanosheets were characterized by AFM (Figure 4.1(c) & (d)). AFM has the unique advantage of being able to provide an image for both conducting and non-conducting substances. It can measure the topography of samples at sub-nanometer resolutions, and thus the AFM characterization provides information about the suitability and the availability of large aspect ratio on the 2D material for the immobilization of enzyme or other bio-recognition elements. This information is quite important for the understanding of the electron transfer reaction at the interface.

In this study, the sample for the AFM characterization was prepared by dispersing 1 mg of the GO powder in 10 mL of deionized water. The mixture was sonicated for 30 minutes for even dispersion of the GO nanosheets in the aqueous medium, and the mixture (20 µL) was subsequently drop cast on a gold substrate and allowed to dry in the fume hood for about 8 hours before taking the AFM measurement. The AFM image (Figure 4.1(c)) shows flat nanosheets with large aspect ratio, while the height profile plot (Figure 4.1(d)) shows a maximum height of about 4 nm.

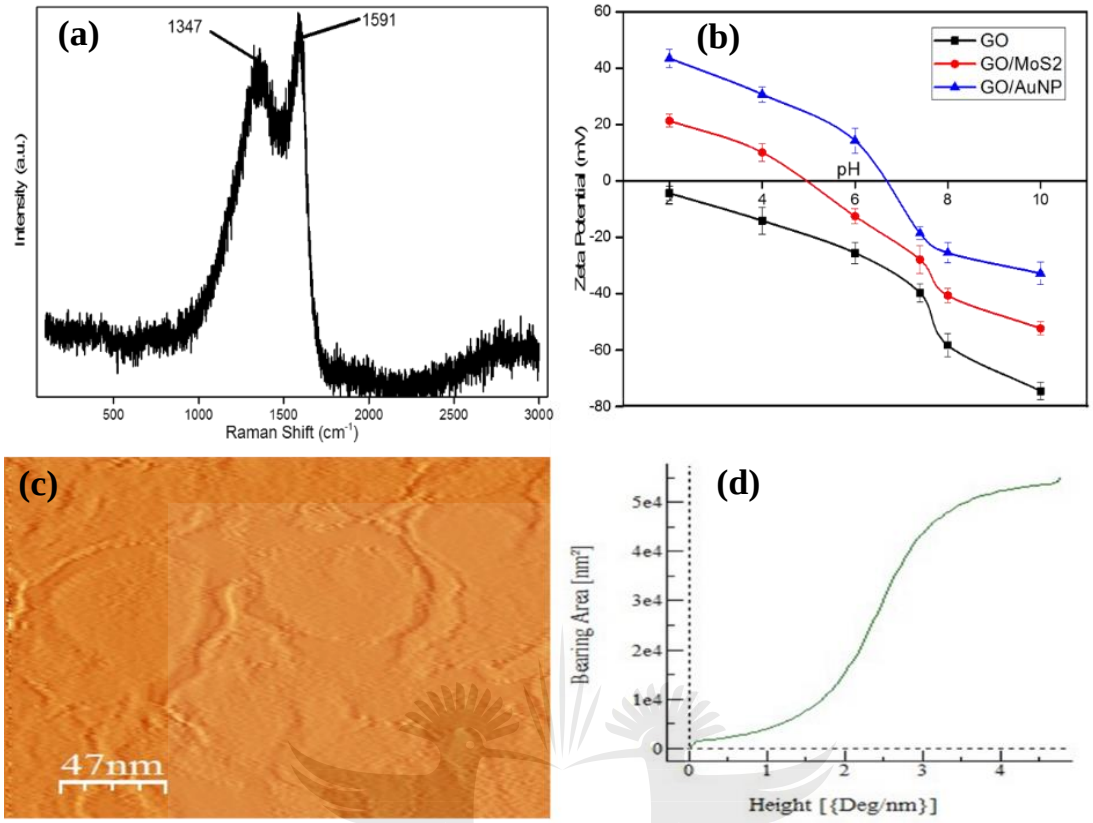

Figure 4.1 **(a) Raman spectrum of the graphene oxide, (b) zeta potential measurement of the dispersed interface material in deionized water at pH 4–10, (c) AFM image of the dispersed graphene oxide on gold substrate, (d) AFM height profile distribution analysis spectra of the dispersed graphene oxide on gold substrate.**

Morphological characterization of the 2D hierarchically assembled hetero structures (containing AuNPs doped GO-MoS_2) was done using SEM (Figure 4.2(a)). The figure shows thin flake-like structures with high aspect ratio, thus indicating a very good platform for enzyme immobilization and a wide area for interface electron transfer activities, while the inset shows a high magnification AFM image showing the amorphous nature of the self-assembly layered interface structures.

Figure 4.2(b) is the SEM image of the resulting 3D structure after the immobilization of polymer and enzyme PNIPAAm and peroxidase) on the layered self- assembled 2D interface structure showing a rough and undulating amorphous surface providing a very wide surface area for contact with the substrate which is a recipe for good electron transfer.

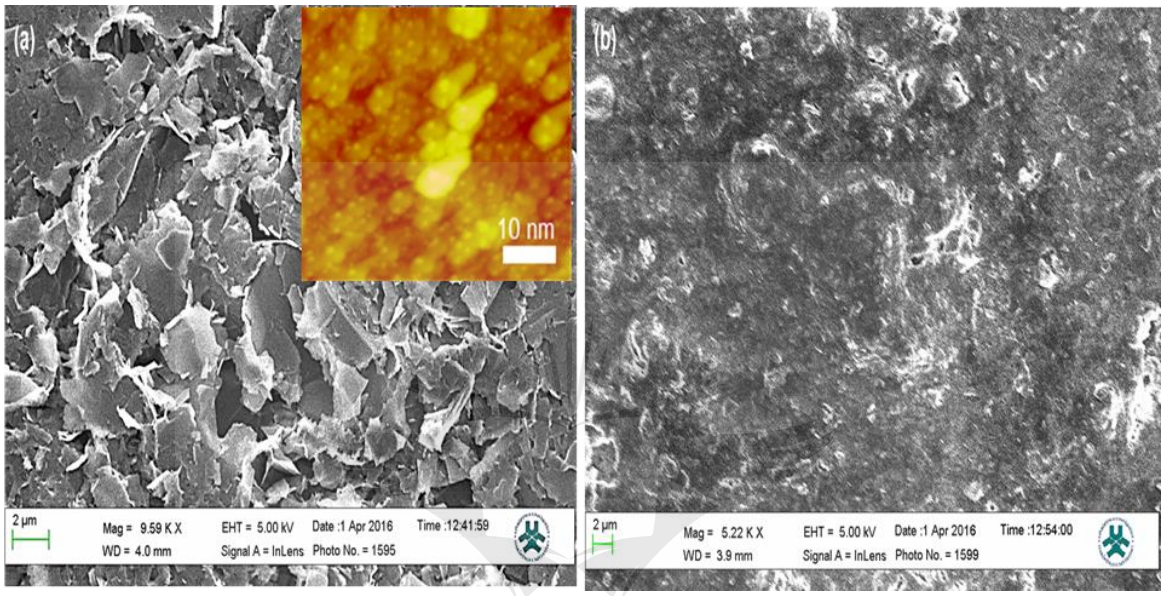

Figure 4.2 Morphological characterization of 2D-hetero hierarchically 3D self-assembled hybrid interfaces: SEM images of (a) AuNPs doped layered GO/MoS_2 2D nano-hetero interfaces and the inset shows AFM image of AuNPs doped layered GO/MoS_2 nano-heterostructures and (b) GO-AuNPs-MoS_2-PNIPAAm-Peroxidase bioelectrode.

Further material characterizations was done and presented in Figures A1.1; A1.2; and A1.3 (Appendix A1). Figure A1.1 (a) (Appendix A1) is the TEM image of the GO showing a crumpled structured material agglomerate around the 3 mm copper grid used for the analysis, while Figure A1.1 (b) (Appendix A1) shows the material to be like folded sheets. Further analysis of some other sections of the material using SEM shows an almost smooth, thin plane with a wide aspect ratio (Figure A1.1(c) Appendix A1) and a petal-like assemblage (Figure A1.1(d) Appendix A1).

The TEM image of the 2D MoS_2 nanosheets at different magnification is presented in Figure A1.2 (a–d) Appendix A1. Figure A1.2 (a & b) shows agglomerated nanosheets flakes of the material while the high-resolution image of the materials showed that the material is highly crystalline in nature Figure A1.2 (c & d) Appendix A1. Also, the TEM images (at different magnifications) of the dispersed spherically shaped AuNPs on the MoS_2 nanosheets is presented in Figure A1.3 (a–d).

Using 10 mM ferro/ferricyanide $[Fe(CN)_6]^{3-/4-}$ solution in 10 mM PBS as redox probe, the bare and modified bioelectrodes were characterized using CV and EIS (Figure 4.3 (a–d); and Figure A4 (a–f), Appendix A1) respectively. The CV response displays the classical sigmoidal shape while exhibiting narrow peak to peak potential separation (ΔE_p) for all the AuNPs doped GO and MoS_2 modified electrodes which is an indication of fast electron transfer kinetics which can be attributed to the wide surface area presented by the 2D graphene system and the 2D TMD (MoS_2) and their reported fast electron transport properties [7, 10, 35].

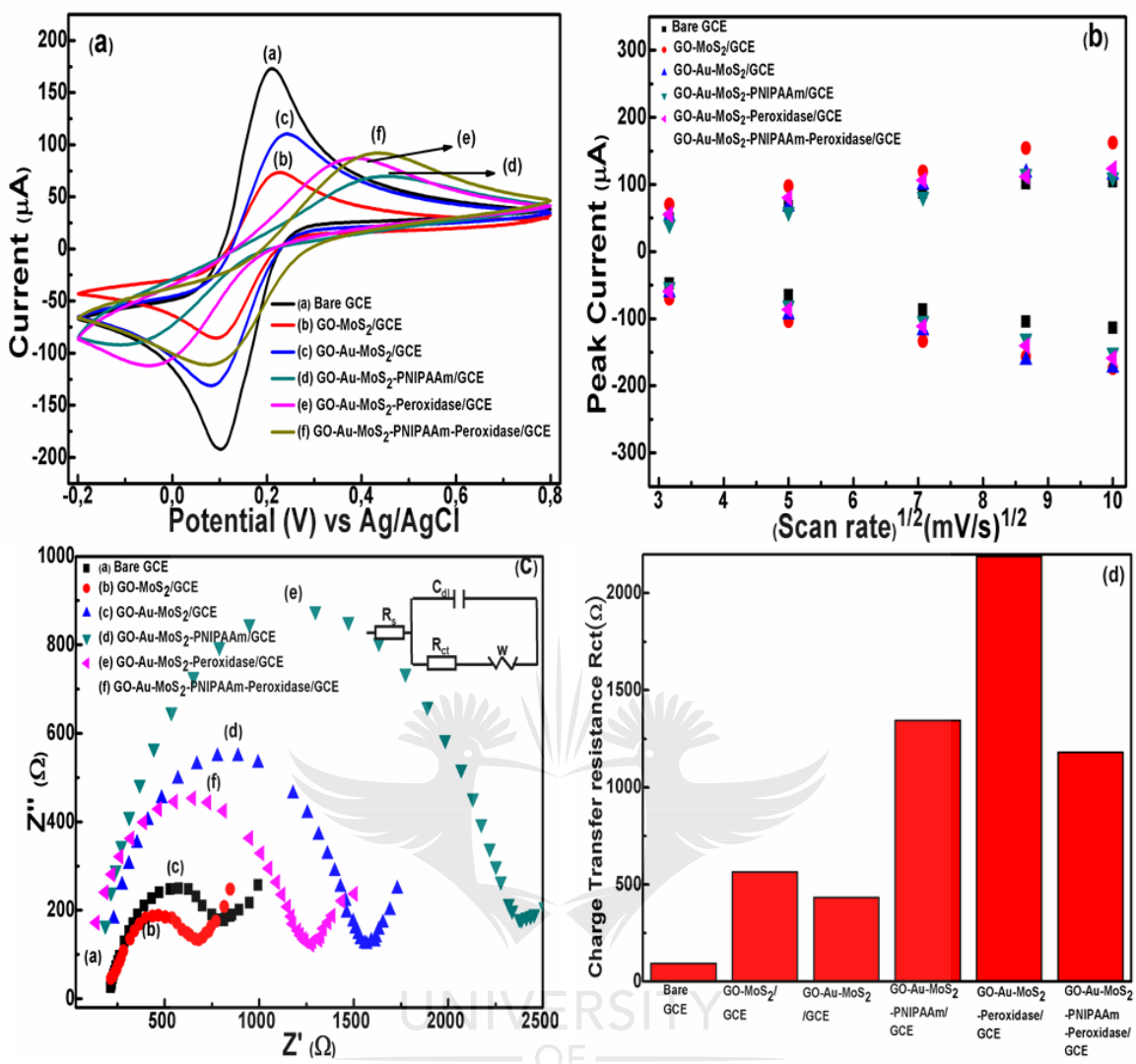

Figure 4.3 **Bioelectrode characterization showing (a) cyclic voltammetry response at 50 mV/s in 10 mM PBS and 10 mM $[Fe(CN)_6]^{3-/4-}$ for the bare GC and all modified electrodes; (b) effect of scan rate on the cathodic peak current I_{pc} and the anodic peak current I_{pa}; (c) EIS Nyquist plot with Randles circuit equivalent diagram as an inset, and (d) charge transfer impedance histogram for the EIS.**

Similarly, the peak current of the nanohybrid assembly of AuNPs doped GO-MoS_2 fabricated electrode is higher compared to the assembly without the doped AuNPs. This is an indication that the presence of the AuNPs contributed to increasing the effective electroactive surface area in agreement with Randle-Sevcik equation (equation 4.1) from which it can be seen that the peak current (I_p) is directly

proportional to the effective electrode surface area (A) and based on the assumption that mass transport is diffusion controlled

$$I_P = 2.69 \times 10^{-5} A D^{1/2} n^{3/2} \gamma^{1/2} C \quad \text{.....(4.1)}$$

where D is the diffusion coefficient of the molecules (6.70×10^{-6} cm^2/s), n is the number of electrons transferred, γ is the scan rate in V/s and C is the concentration of the redox probe solution in mol/dm^3.

It is also observed that the reduction peak potential (E_{pc}) after the immobilization of PNIPAAm and peroxidase on the nano-hybrid assemble modified electrodes, shifted to negative values (Figure 4.3(a)) thus indicating that the forward (reduction) reaction requires more activation energy than similar reaction without the presence of PNIPAAm and peroxidase. This fact is also reinforced by the increased ΔE_p observed for the CV scans for the modified electrodes involving PNIPAAm and peroxidase [34-38].

The effect of scan rates on the reduction (forward) reaction peak current and the oxidation peak current was equally evaluated using cyclic voltammetry measurements in 10 mM ferri-ferro cyanide probe and 10 mM PBS and the results presented in Figure 4.3(b) and Figure A1.4 (a–f) Appendix A1. The cathodic peak current (I_{pc}) and the anodic peak current (I_{pa}) for the bare GC and all modified electrodes increase linearly with increasing scan rates from 10–100 mV/s, thus indicating a diffusion-controlled electrode process at the interface.

EIS in a solution of ferro/ferricyanide redox probe was also used to characterize the treated modified electrodes (Figure 4.3(c)). It is widely known that the double-layer

capacitance (C_{dl}) and interfacial electron transfer resistance of the electrode surface can be changed by modifying the electrode using polymers, nanomaterials and semiconducting materials. To do correct fitting of the Nyquist plots, it was needed to replace C_{dl} with a constant phase element (CPE) in the Randles equivalent circuit. Due to the presence of CPE in the Nyquist plots, there is a microscopic roughness, which causes an inhomogeneous distribution in both C_{dl} and bulk electrolyte solution resistance (R_s) [39].

The Nyquist plot of the EIS (Figure 4.3(c)) displays the presence of kinetic controlled impedance, (the semicircular part) and the diffusion controlled impedance (the linear part, which is notably quite small in this impedance measurement) at lower frequencies in the electrochemical system, while the Randles circuit equivalent fittings (Figure 4.3(c) inset) showed the presence of solution resistance R_s, charge transfer resistance R_{ct}, the constant phase element corresponding to the double-layer capacitance CPE_{dl}, and the frequency dependent Warburg impedance *w*. At higher frequencies, the diameter of the semi-circular part is equivalent to the electron transfer resistance (R_{ct}) in the electrochemical system, and the value of the R_{ct} as an inverse relationship with the electrochemical activity of the specimen.

In an electrochemical system, the solution resistance R_s results from the ohmic resistance of the electrolyte solution, while the double layer capacitance is a non-faradaic component which comes from the charging of the dielectric features at the electrode-electrolyte interface which is dependent on the surface modification of the electrode. The frequency dependent Warburg impedance w, is as a result of the diffusion of the ionic species in the redox probe to the interface for charge transfer to occur in a faradaic system, while the charge transfer resistance R_{ct} is the

activation energy in a faradaic electrochemical system that must be overcome for electron transfer to occur at the interface and it is also dependent on the surface modification of the electrode [40-42].

The R_{ct} is a measure of the kinetic controlled resistance (or the interfacial electron transfer rate) between the redox probe electroactive species and the electrode surface of the modified electrode system. In this study, the comparative R_{ct} values for the bare and all modified electrodes were evaluated based on the diameter of the semi-circular part of the Nyquist plot (Figure 4.3(c)) and a histogram representation of the respective values is presented in Figure 4.3d [41]. The R_{ct} may also be evaluated using equation 4.2.

$$Z_{(\omega)} = R_s + \frac{R_{ct} + \sigma\omega^{-1/2}}{(\sigma\omega^{1/2}C_d+1)^2 + \omega^2 C_d^2\left(R_{ct} + \sigma\omega^{-1/2}\right)^2} + j\frac{\left[\omega C_d\left(R_{ct} + \sigma\omega^{-1/2}\right)^2 + \sigma\omega^{-1/2}\left(C_d\sigma\omega^{1/2}+1\right)\right]}{\left(C_d\sigma\omega^{1/2}+1\right)^2 + \omega^2 C_d^2\left(R_{ct} + \sigma\omega^{-1/2}\right)^2} \quad \text{.....(4.2)}$$

Where w=2πf, f=frequency, C_d is the double layer capacitance and σ is expressed as given in equation 4.3.

$$\sigma = \frac{RT}{\sqrt{2n^2F^2A}}\left(\frac{1}{D_O^{1/2}C_O} + \frac{1}{D_R^{1/2}C_R}\right) \quad \text{.....(4.3)}$$

Where R is the gas constant, T is the temperature in Kelvin, F is Faraday's constant, A is electrode surface area, D_o and D_R are respectively the diffusion coefficients of oxidants and reductants, C_o and C_R are the concentrations of the oxidants and reductant respectively.

Significant changes in the impedance spectra were observed after different treatments. The equivalent circuit compatible with the Nyquist diagram has been shown as inset Figure 4.3(c). The circuit element that is most pertinent to this work is R_{ct}. This is because it often relates directly to the accessibility of the modified electrode and also reflects the flow of charge across the modified interface into the substrate electrode.

The ohmic R_{ct}, for the layered structured modified electrode, was calculated to be 565.2 Ω, which is higher than that of the bare GC electrode (92.8 Ω), thereby signifying that the introduction or the presence of the electronegative oxygenated groups (C=Os and COO^- s) in GO and the sulphide (S_2^-) group in the MoS_2 causes a resistance to electron transfer between the redox couple at the interface. However, when the layered matrix was doped with AuNPs, there was a marginal reduction in R_{ct} value to 433.1 Ω, signifying the role of AuNPs in enhancing electron transfer kinetics at the interface [5, 6]. A summary of the circuit element representation and the corresponding ohmic resistance and CPE values are presented in Table 4.1.

Table 4.1 Randle circuit equivalent values

Circuit Element	GO-MoS_2/GCE	GO-Au-MoS_2/GCE	GO-Au-MoS_2-Peroxidase/GCE	GO-Au-MoS_2-PNIPAAm/GCE	GO-Au-MoS_2-PNIPAAm Peroxidase/GCE
R_s/ohm	207.9	215.4	136.4	163.4	66.35
CPE-T/F	7.858×10^{-5}	6.505×10^{-5}	3.613×10^{-6}	3.310×10^{-6}	3.7553×10^{-6}
CPE-P/F	0.7776	0.7867	0.8636	0.8585	0.8467
R_{ct}/ohm	702.4	525.8	2206.0	1379	1161.0

Further modification of the electrodes through the introduction of the polymer matrix (PNIPAAm) resulted in a considerable increase in the R_{ct} value to 1345.0 Ω, which is an indication of the insulating effect of the terminated amine group polymer matrix at the interface. However, after conjugation of the matrix with the peroxidase enzyme, the R_{ct} value was reduced to 1130.0 Ω, thus indicating that the enzyme conjugation mitigated against the insulating effect of the polymer matrix at the interface. Moreover, an increase of membrane capacitance was observed with modified electrodes in absence of the polymer matrix (PNIPAAm) and peroxidase enzyme in comparison with treated electrodes, probably due to the increase of the dielectric constant caused by electronegative oxygenated groups in GO and/or sulphide (S_2^-) group in the MoS_2.

The electrobiocatalytic activity of the fabricated modified GO-AuNPs-MoS_2-PNIPAAm-Peroxidase-GC bioelectrode was investigated using chronoamperometry at a constant applied potential of +0.60 V (vs. Ag/AgCl) using 100 mM PBS and 100 mM potassium chloride (KCl) as supporting electrolyte. To establish reproducibility, the sensing experiments were repeated three times and the standard deviation of the current response was calculated and plotted as current range in the calibration curves (Figure 4.4(a) and 4.4(b)), the average standard deviation was calculated to be 0.023 %. Similarly, to evaluate the contribution of PNIPAAm in the assembled nano interface hybrid, the chronoamperometric measurement experiments were repeated without PNIPAAm in the electrode matrix (Figure 4.4(c) and 4.4(d)). The fabricated bioelectrode exhibited a fast response (reaching a steady state current in about 5s) towards the successive addition of

H_2O_2. The current time plots for the chronoamperometric response are presented in Figure 4.4(a) and 4.4(c) while the corresponding calibration curves are presented in Figure 4.4(b) and 4.4(d). The GO-AuNPs-MoS_2-PNIPAAm-Peroxidase-GC fabricated bioelectrodes exhibited a wide linear range from 1.57 mM to 11.33 mM and dynamic range from 0.19 mM to 13.94 mM towards hydrogen peroxide detection with a limit of detection of 2.432 mM (S/N=3) and a sensitivity of 14.237 μA/mM/cm^2. The sensitivity of the bioelectrode was calculated by dividing the slope of the calibration curve with the surface area of the electrode.

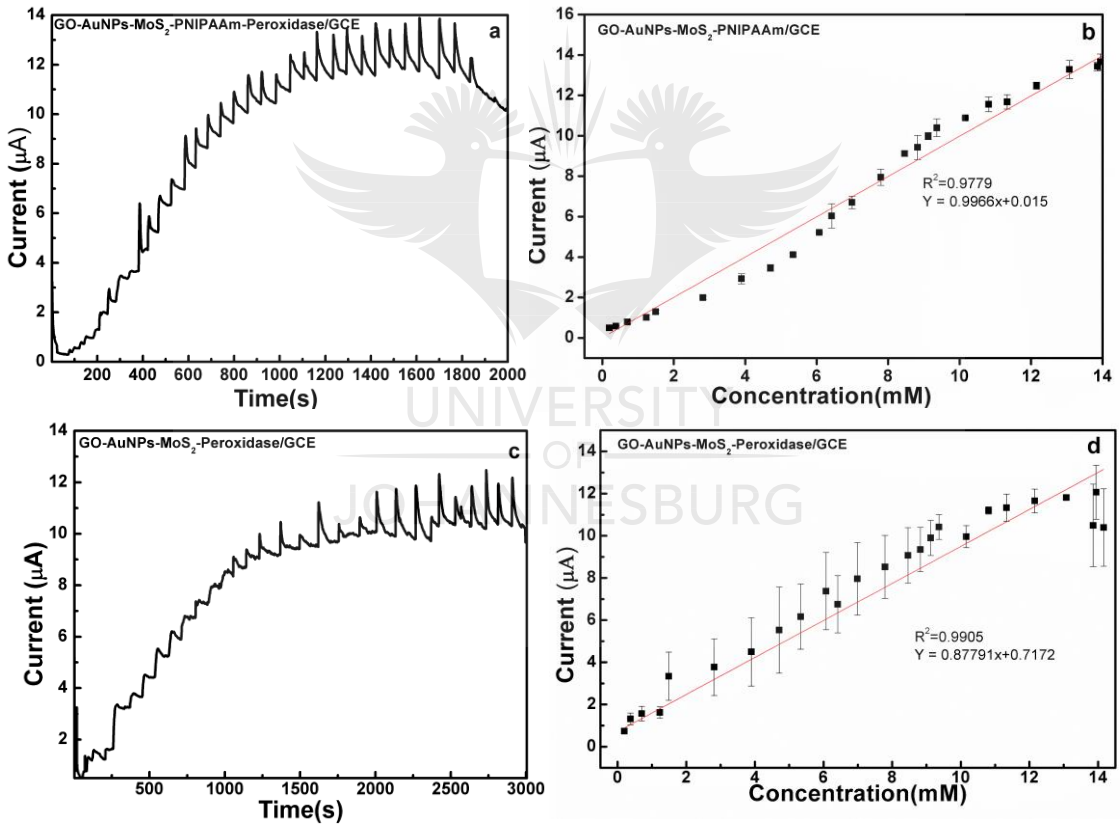

Figure 4.4 Chronoamperometric response showing (a) current-time plot and (b) calibration curve response for the fabricated GO-AuNPs-MoS_2-PNIPAAm-Peroxidase bioelectrode and (c) current-time plot and (d) calibration curve response for the fabricated GO-AuNPs-MoS_2-Peroxidase at an applied potential of +0.6 V in 100 mM PBS.

The GO-AuNPs-MoS_2-Peroxidase-GC fabricated bioelectrodes also exhibited a fast response to successive addition of H_2O_2 reaching a study state current in 4 s. The GO-AuNPs-MoS_2-Peroxidase-GC bioelectrode also exhibited a linear range from 1.23 mM to 9.41 mM; a dynamic range from 0.11 mM to 14.12 mM with a limit of detection of 3.34 mM (S/N=3) and a sensitivity of 12.542 µA/mM/cm^2.

It was observed that the GO-AuNPs-MoS_2-Peroxidase-GC modified bioelectrode (without PNIPAAm) is more prone to leaching during the chronoamperometric experimental measurements. Also, the experiments involving GO-AuNPs-MoS_2-PNIPAAm-Peroxidase-GC modified bioelectrodes showed a more consistent current response (as can be seen in the current range bars in Figure 4.4(b)) than the current responses from the GO-AuNPs-MoS_2-peroxidase-GC fabricated modified bioelectrodes (as seen in the current range bars in Figure 4.4(d)). The average standard deviation for three separate measurements for the detection of H_2O_2 under similar conditions is 24.23%. This may be attributed to the stabilizing effect of the PNIPAAm.

It was equally observed that in all repeated comparative experiments, the GO-AuNPs-MoS_2-PNIPAAm-peroxidase-GC modified bioelectrodes always exhibited a wider linear range than the GO-AuNPs-MoS_2-peroxidase-GC fabricated modified bioelectrode. A comparative summary of the responses from the modified bioelectrode matrices in this study is given in Table 4.2.

Table 4.2 Summary of electrobiocatalytic responses to stepwise H_2O_2 additions

	GCE/GO-AuNPs-MoS_2-PNIPAAm-HRP	GCE/GO-AuNPs-MoS_2-HRP
LoD	2.432	3.34
Linear range (mM)	1.57 – 11.33	1.23 - 9,41
Dynamic range (mM)	0.19 – 13.94	0.11 – 14.12
Sensitivity ($\mu A/mM/cm^2$)	14.237	12.542
Regression (R^2)	0.9779	0.9905

Similarly, a comparative table showing the linear response of similar studies as compared to this study is presented in Table 4.3.

Table 4.3 Comparative table showing the linear response similar studies

Immobilization Matrix	Sensing target	Linear Range [mM]	Ref.
HRP/MoS_2/Graphene/GCE	H_2O_2	0.0002 - 1.103	[43]
Mb-HSG-SN-CNTs/GCE	H_2O_2	0.002 -1.2	[44]
MoS_2/GR-MWCNTs/GCE	H_2O_2	0.005 – 0.145	[45]
Hb-AuNPs@MoS_2/GCE	H_2O_2	0.01 - 0.3	[46]
PEG-MoS_2 nanosheets	H_2O_2	0.00286–0.286	[47]
HRP/graphene/GCE	H_2O_2	0.00033-0.014	[48]
hemin/GO/CNT-modified GCE	H_2O_2	0.0006-7.2	[49]
GO/AuNPs/MoS_2/HRP/PNIPAAm/ Peroxidase	H_2O_2	1.57-11.33	Present Work

The Table 4.3 shows that the GO-AuNPs-MoS_2-peroxidase-GC of this study displayed a wider linear response compared to the other mentioned systems. The stability of the GO-AuNPs-MoS_2-PNIPAAm-Peroxidase-GC modified bioelectrodes

was studied over a 5-day period by measuring the current response to 10 mM H_2O_2 in 100 mM PBS and 100 mM KCl supporting electrolyte while the modified bioelectrode is stored at 4 °C after each usage. It was observed that there were no significant changes to the current response over this 5-day period. This result is an indication that the fabricated modified bioelectrode is stable over the 5-day period of the stability test.

The specific capacitance of GO-AuNPs-MoS_2-PNIPAAm-Peroxidase bioelectrode can be calculated from CV plots (Figure 4.3(a), f) using equation 4.4.

$$C_{sp} = \frac{\sqrt{(I(V)dv)}}{vA\Delta V} \quad \text{.....(4.4)}$$

Where $\sqrt{I(V)}$ is equal to the integrated area under the CV plot, and v is the scan rate, A is the electrode area and ΔV is the potential window. Figure 4.5 plots areal capacitance with potential (V) Vs Ag/AgCl for scan rate 50 mV/s.

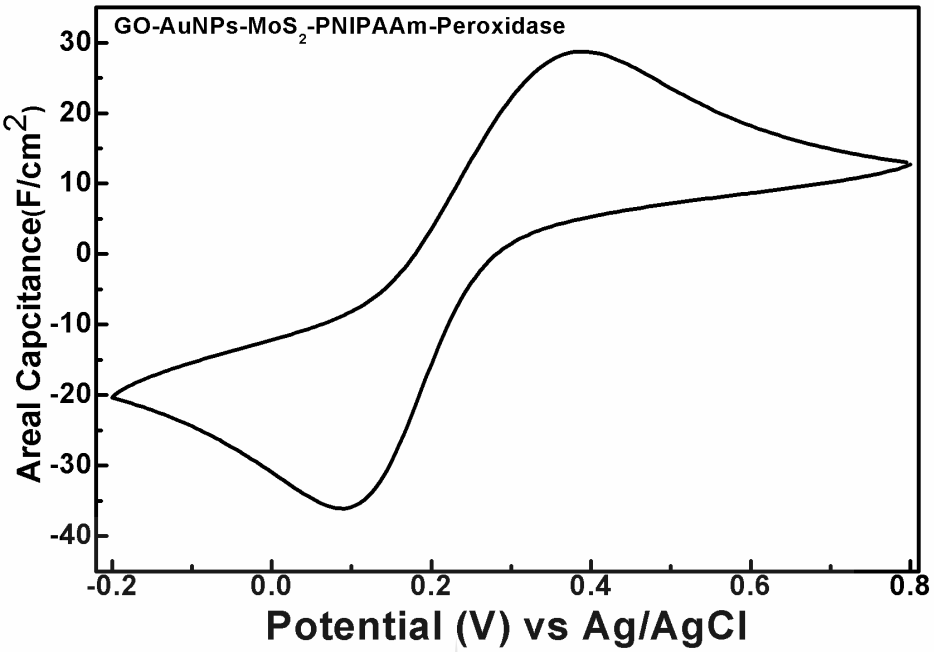

Figure 4.5 Electrochemical performance of GO-AuNPs-MoS_2-PNIPAAm-Peroxidase bioelectrode showing areal capacitance vs potential (V) vs Ag/AgCl at scan rate 50 mV/s in 10 mM $[Fe(CN)_6]^{3-/4-}$.

The calculated specific capacitance of GO-AuNPs-MoS_2-PNIPAAm-Peroxidase bioelectrode is 8.6 F/cm^2 for scan rate 50 mV/s. The performance of this bioelectrode suggests that hierarchically assembled two-dimensional hybrid nanointerfaces can readily be incorporated as a platform for electrobiocatalytic reactions in biosensors and other bioreactors.

4.4 SUB-CONCLUSION

In this study, we have successfully combined dual 2D hybrid layered structures including GO and MoS_2, then doped the layered structure with AuNPs, followed by the immobilization of the polymer (PNIPAAm) and the bio-recognition element (peroxidase) leading to the fabrication of an electrode material with very high surface area coupled with the known excellent electron transport properties of these 2D

materials. We have exploited the biocompatibility and hydrophilicity of the GO, coupled with the wide surface area and conductivity MoS_2 and combined this with the signal enhancement of the AuNPs. This nanohybrid matrix was stabilized by the introduction of PNIPAAm. HRP was subsequently immobilized as the bio-recognition element for the detection of H_2O_2 as a model analyte. Thus, we have set the stage for the fabrication of stable electrobiocatalysis interface platform using the advantages of the hybrid multi nano 2D polymer-enzyme bioconjugate framework for the design and fabrication of thin, flexible, fast, and sensitive bioelectronics, bioreactors and biosensors.

4.5 REFERENCES

[1] Z. L. Wang. Self-powered nanosensors and nanosystems. *Advanced Materials* **24** (2012) 280-285.

[2] L. Zhang, M. Zhou and S. Dong. A self-powered acetaldehyde sensor based on biofuel cell. *Analytical Chemistry* **84** (2012) 10345-10349.

[3] L. Deng and S. Dong. The Self-Powered Biosensors Based on Biofuel Cells. *Electrochemical Biosensors. Pan Stanford* **3** (2015) 371-387.

[4] M. Zhou and J. Wang. Biofuel Cells for Self-Powered Electrochemical Biosensing and Logic Biosensing: A Review. *Electroanalysis* **24** (2012) 197-209.

[5] A. P. Turner. Biosensors: sense and sensibility. *Chemical Society Reviews* **42** (2013) 3184-3196.

[6] A. Tiwari and A. N. Nordin. Advanced biomaterials and biodevices. *John Wiley & Sons* (2014).

[7] A. Tiwari and M. SyvÃ. Advanced 2D materials. *John Wiley & Sons* (2016)

[8] A. O. Osikoya and A. Tiwari. Recent advances in 2D bioelectronics. *Biosensors & Bioelectronics* **89** (2017) 1-7.

[9] A. Tiwari and M. SyvÃ. Graphene materials: fundamentals and emerging applications. *John Wiley & Sons* (2015)

[10] S. Patra, E. Roy, A. Tiwari, R. Madhuri and P. K. Sharma. 2-Dimensional graphene as a route for emergence of additional dimension nanomaterials. *Biosensors and Bioelectronics* **89** (2017) 8-27.

[11] A. O. Osikoya, O. Parlak, N. A. Murugan, E. D. Dikio, H. Moloto, L. Uzun, A. P. Turner and A. Tiwari. Acetylene-sourced CVD-synthesised catalytically

active graphene for electrochemical biosensing. *Biosensors and Bioelectronics* **89** (2017) 496-504.

[12] A. Tiwari and A. P. Turner. Biosensors nanotechnology. *John Wiley & Sons* (2014)

[13] A. Tiwari, H. K. Patra and A. P. Turner. Advanced bioelectronic materials. *John Wiley & Sons* (2015).

[14] A. Tiwari and M. M. Demir. Advanced Sensor and Detection Materials. *John Wiley & Sons*, (2014)

[15] F. Kim, L. J. Cote and J. Huang. Graphene oxide: surface activity and two-dimensional assembly. *Advanced Materials* **22** (2010) 1954-1958.

[16] O. Parlak and A. P. Turner. Switchable bioelectronics. *Biosensors and Bioelectronics* **76** (2016) 251-265.

[17] O. Parlak, A. P. Turner and A. Tiwari. On/Off-Switchable Zipper-Like Bioelectronics on a Graphene Interface. *Advanced Materials* **26** (2014) 482-486.

[18] M. Osada and T. Sasaki. Two-dimensional dielectric nanosheets: novel nanoelectronics from nanocrystal building blocks. *Advanced Materials* **24** (2012) 210-228.

[19] R. Tenne. Advances in the synthesis of inorganic nanotubes and fullerene-like nanoparticles. *Angewandte Chemie International Edition* **42** (2003) 5124-5132.

[20] B. Radisavljevic, A. Radenovic, J. Brivio, i. V. Giacometti and A. Kis. Single-layer MoS_2 transistors. *Nature Nanotechnology* **6** (2011) 147-150.

[21] K. Roy, M. Padmanabhan, S. Goswami, T. P. Sai, G. Ramalingam, S. Raghavan and A. Ghosh. Graphene–MoS_2 hybrid structures for

multifunctional photoresponsive memory devices. *Nature nanotechnology* **8** (2013) 826-830.

[22] J. Yoon, J.-W. Shin, J. Lim, M. Mohammadniaei, G. B. Bapurao, T. Lee and J.-W. Choi. Electrochemical nitric oxide biosensor based on amine-modified MoS_2/graphene oxide/myoglobin hybrid. *Colloids and Surfaces B: Biointerfaces* **159** (2017) 729-736.

[23] O. Parlak, A. İncel, L. Uzun, A. P. Turner and A. Tiwari. Structuring Au nanoparticles on two-dimensional MoS_2 nanosheets for electrochemical glucose biosensors. *Biosensors and Bioelectronics* **89** (2017) 545-550.

[24] O. Parlak, A. Tiwari, A. P. Turner and A. Tiwari. Template-directed hierarchical self-assembly of graphene based hybrid structure for electrochemical biosensing. *Biosensors and Bioelectronics* **49** (2013) 53-62.

[25] Y. Liu, D. Yu, C. Zeng, Z. Miao and L. Dai. Biocompatible graphene oxide-based glucose biosensors. *Langmuir* **26** (2010) 6158-6160.

[26] M. Pumera, A. Ambrosi, A. Bonanni, E. L. K. Chng and H. L. Poh. Graphene for electrochemical sensing and biosensing. *TrAC Trends in Analytical Chemistry* **29** (2010) 954-965.

[27] M. Fang, K. Wang, H. Lu, Y. Yang and S. Nutt. Covalent polymer functionalization of graphene nanosheets and mechanical properties of composites. *Journal of Materials Chemistry* **19** (2009) 7098-7105.

[28] J. Zhang, P. Du, D. Xu, Y. Li, W. Peng, G. Zhang, F. Zhang and X. Fan. Near-Infrared Responsive MoS_2/Poly (N-isopropylacrylamide) Hydrogels for Remote Light-Controlled Microvalves. *Industrial & Engineering Chemistry Research* **55** (2016) 4526-4531.

[29] B. Unnikrishnan, S. Palanisamy and S.-M. Chen. A simple electrochemical approach to fabricate a glucose biosensor based on graphene–glucose oxidase biocomposite. *Biosensors and Bioelectronics* **39** (2013) 70-75.

[30] S. S. Nanda, M. J. Kim, K. S. Yeom, S. S. A. An, H. Ju and D. K. Yi. Raman spectrum of graphene with its versatile future perspectives. *TrAC Trends in Analytical Chemistry* **80** (2016) 125-131.

[31] K.-i. Sasaki, Y. Tokura and T. Sogawa. The origin of Raman D band: bonding and antibonding orbitals in graphene. *Crystals* **3** (2013) 120-140.

[32] M. S. Dresselhaus, A. Jorio, M. Hofmann, G. Dresselhaus and R. Saito. Perspectives on carbon nanotubes and graphene Raman spectroscopy. *Nano letters* **10** (2010) 751-758.

[33] D. Yang, A. Velamakanni, G. Bozoklu, S. Park, M. Stoller, R. D. Piner, S. Stankovich, I. Jung, D. A. Field and C. A. Ventrice Jr. Chemical analysis of graphene oxide films after heat and chemical treatments by X-ray photoelectron and Micro-Raman spectroscopy. *Carbon* **47** (2009) 145-152.

[34] A. C. Ferrari. Raman spectroscopy of graphene and graphite: disorder, electron–phonon coupling, doping and nonadiabatic effects. *Solid state communications* **143** (2007) 47-57.

[35] R. S. Nicholson. Theory and application of cyclic voltammetry for measurement of electrode reaction kinetics. *Analytical Chemistry* **37** (1965) 1351-1355.

[36] M. Levi and D. Aurbach. Simultaneous measurements and modeling of the electrochemical impedance and the cyclic voltammetric characteristics of graphite electrodes doped with lithium. *The Journal of Physical Chemistry B* **101** (1997) 4630-4640.

[37] P. T. Kissinger and W. R. Heineman. Cyclic voltammetry. *Journal of Chemical Education* **60** (1983) 702-706.

[38] O. Parlak, P. Seshadri, I. Lundström, A. P. Turner and A. Tiwari. Two-Dimensional Gold-Tungsten Disulphide Bio-Interface for High-Throughput Electrocatalytic Nano-Bioreactors. *Advanced Materials Interfaces* **1** (2014) 1400136.

[39] M. D. Stoller, S. Park, Y. Zhu, J. An and R. S. Ruoff. Graphene-based ultracapacitors. *Nano Letters* **8** (2008) 3498-3502.

[40] L. Alfonta, A. Bardea, O. Khersonsky, E. Katz and I. Willner. Chronopotentiometry and Faradaic impedance spectroscopy as signal transduction methods for the biocatalytic precipitation of an insoluble product on electrode supports: routes for enzyme sensors, immunosensors and DNA sensors. *Biosensors and Bioelectronics* **16** (2001) 675-687.

[41] B.-Y. Chang and S.-M. Park. Electrochemical impedance spectroscopy. *Annual Review of Analytical Chemistry* **3** (2010) 207-229.

[42] A. Tiwari and L. Uzun. Advanced molecularly imprinting materials. *John Wiley & Sons* (2016).

[43] H. Song, Y. Ni and S. Kokot. Investigations of an electrochemical platform based on the layered MoS_2–graphene and horseradish peroxidase nanocomposite for direct electrochemistry and electrocatalysis. *Biosensors and Bioelectronics* **56** (2014) 137-143.

[44] C.-Y. Liu and J.-M. Hu. Hydrogen peroxide biosensor based on the direct electrochemistry of myoglobin immobilized on silver nanoparticles doped carbon nanotubes film. *Biosensors and Bioelectronics* **24** (2009) 2149-2154.

[45] V. Mani, S.-M. Chen, K. Raj and M. Kesavan. MoS_2 flowers grown on graphene/carbon nanotubes: a versatile substrate for electrochemical determination of hydrogen peroxide. *International Journal Electrochemical Science* **11** (2016) 2954-2961.

[46] J. Chao, M. Zou, C. Zhang, H. Sun, D. Pan, H. Pei, S. Su, L. Yuwen, C. Fan and L. Wang. A MoS_2–based system for efficient immobilization of hemoglobin and biosensing applications. *Nanotechnology* **26** (2015) 274005.

[47] H. Zhao, Y. Li, B. Tan, Y. Zhang, X. Chen and X. Quan. PEGylated molybdenum dichalcogenide (PEG-MoS_2) nanosheets with enhanced peroxidase-like activity for the colorimetric detection of H_2O_2. *New Journal of Chemistry* **41** (2017) 6700-6708.

[48] M. Li, S. Xu, M. Tang, L. Liu, F. Gao and Y. Wang. Direct electrochemistry of horseradish peroxidase on graphene-modified electrode for electrocatalytic reduction towards H_2O_2. *Electrochimica Acta* **56** (2011) 1144-1149.

[49] Y. Zhang, Z. Xia, H. Liu, M. Yang, L. Lin and Q. Li. Hemin-graphene oxide-pristine carbon nanotubes complexes with intrinsic peroxidase-like activity for the detection of H_2O_2 and simultaneous determination for Trp, AA, DA, and UA. *Sensors and Actuators B: Chemical* **188** (2013) 496-501.

APPENDIX A1

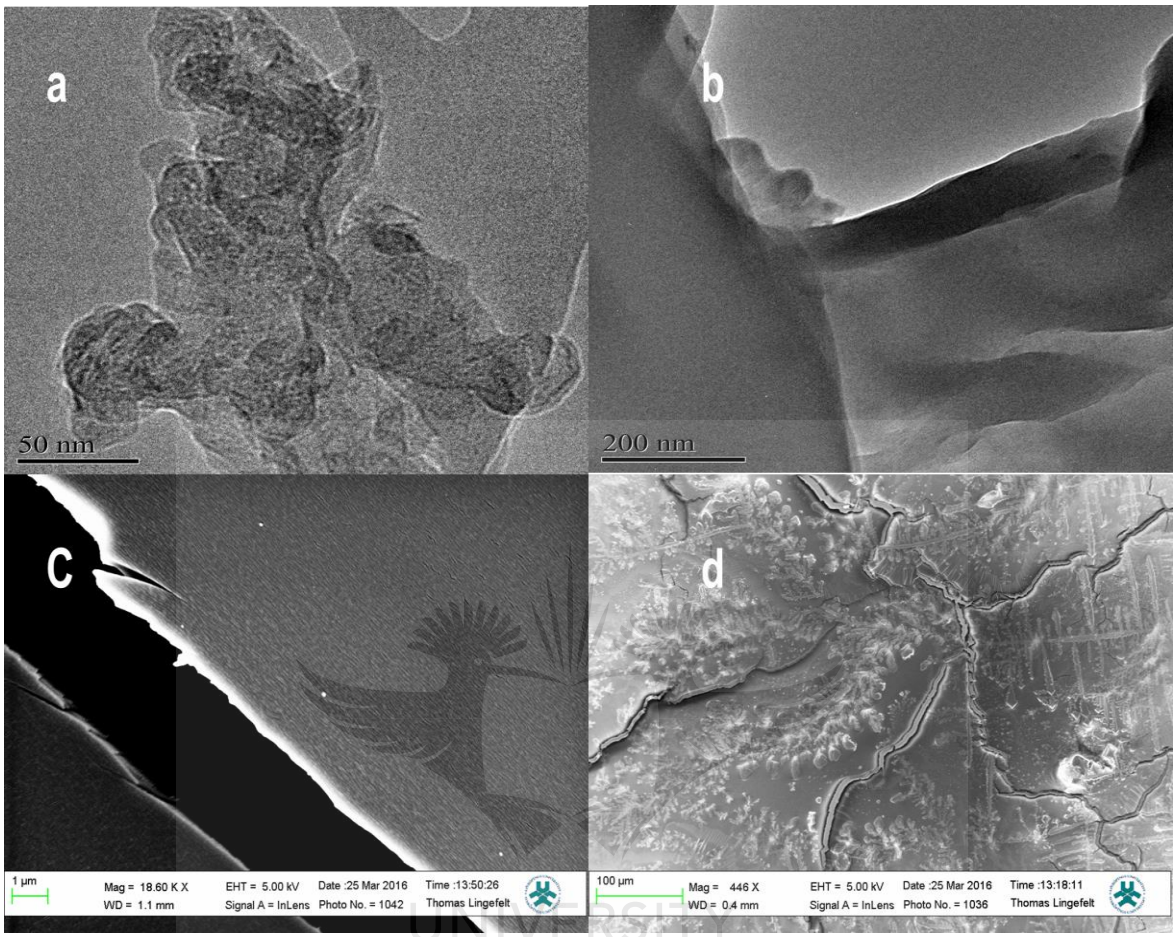

Figure A1.1 TEM images of GO (a & b); SEM images of GO (c & d)

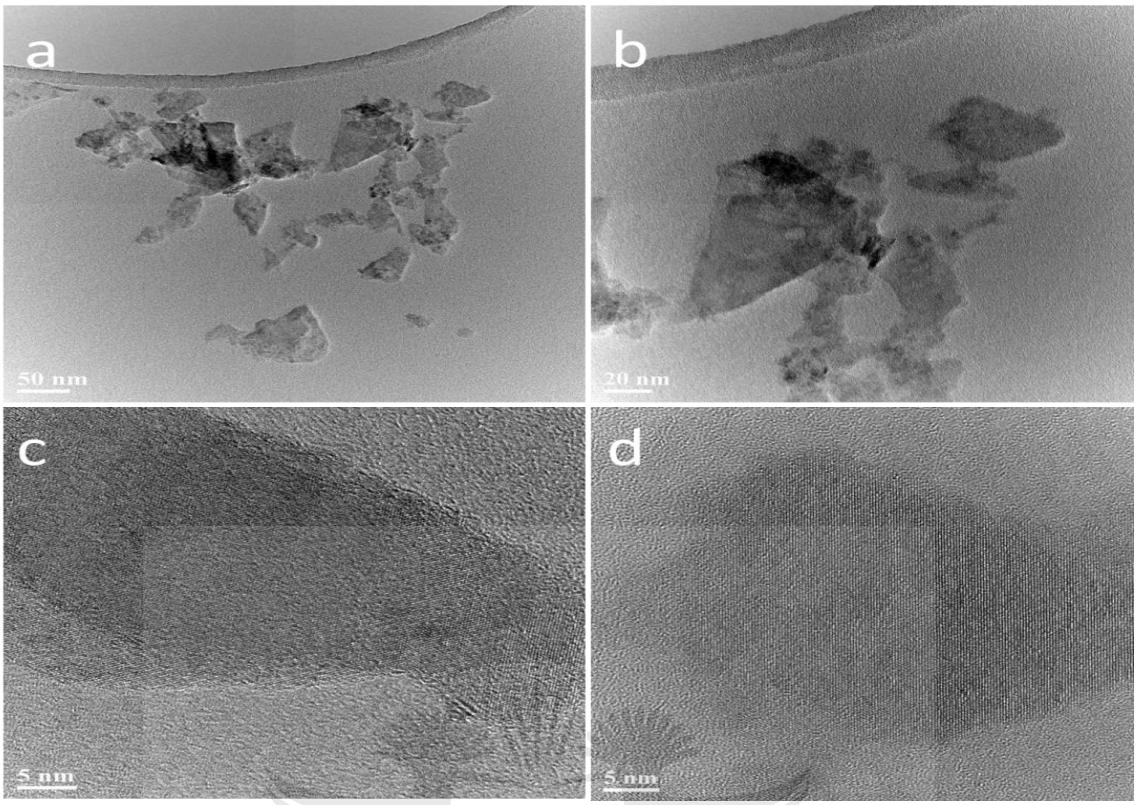

Figure A1.2 TEM images of MoS_2 nanosheets with different magnifications (a-d).

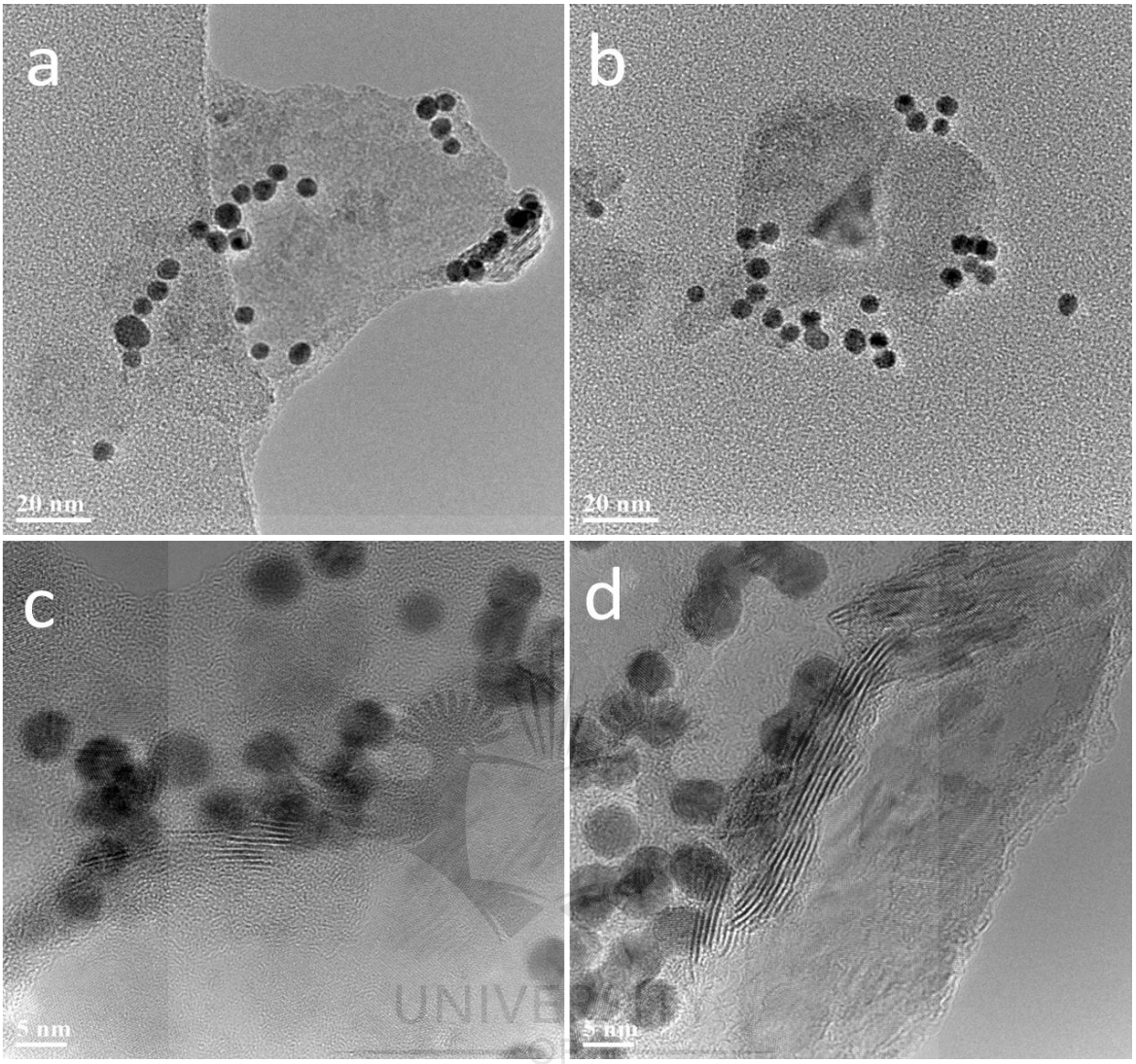

Figure A1.3 TEM images of MoS_2/AuNPs nanosheets with different magnifications (a-d).

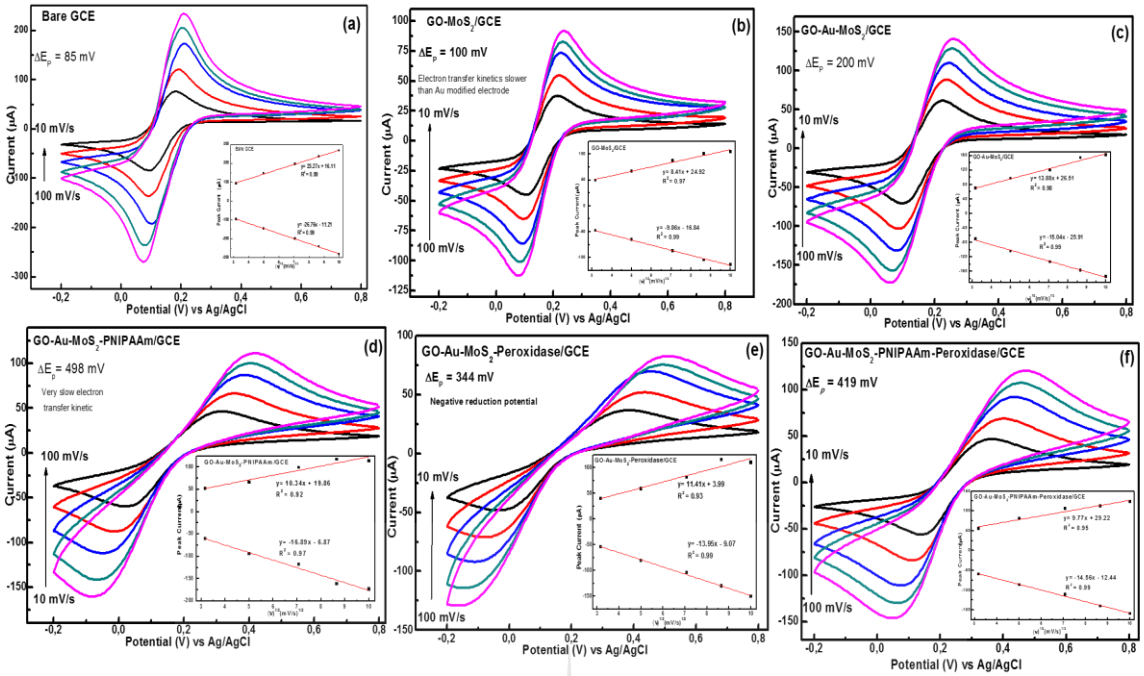

Figure A1.4 Cyclic voltammetry response showing the effect of scan rates on the cathodic peak I_{pc}, and the anodic peak I_{pa}, in 10 mM PBS and 10 mM KCl and 10 mM $[Fe(CN)_6]^{3-/4-}$ vs Ag/AgCl reference electrode for (a) Bare GCE; (b) GO-MoS_2/GCE; (c) GO-Au-MoS_2/GCE; (d) GO-Au-MoS_2-PNIPAAM/GCE; (e) GO-Au-MoS_2-Peroxidase/GCE and (f) GO-Au-MoS_2-PNIPAAM-Peroxidase/GCE respectively.

CHAPTER 5

HIERARCHICALLY ASSEMBLED TWO-DIMENSIONAL GOLD-BORON NITRIDE-TUNGSTEN DISULPHIDE NANOHYBRID INTERFACE SYSTEM FOR ELECTROCATALYTIC APPLICATIONS

5.1 INTRODUCTION

The focus in devices fabrication has recently been towards making slimmer, smarter devices with excellent performances. As a result of this, the use of 2D materials in concept design for nano bioreactors are fast gaining ground as a platform for biodevices fabrication which mostly combined the advantages of 2D material in electronic transport properties, flexibility, durability and biocompatibility with those of biotechnology.

It can be said that the discovery of graphene has been mainly responsible for the focus on 2D materials for device fabrication. And quite naturally, after the initial excitement about the discovery of graphene had subsided, and with the realization that graphene, with all its wonderful properties, has its own limitation as a choice material for device fabrication (particularly the possession of zero band-gap in single layer graphene), research focus among material scientists are now shifting to beyond graphene era [1-3]. This has led to the discovery of quite a number of non-graphene 2D materials, some of which possess some properties that are absent in graphene which makes them promising for quite a number of applications. Studies on the applications of these 2D non-graphene materials are still in their infant stages and detailed research studies on their uses and applications are still quite rare.

The work presented in this chapter has been published in the journal of *Materials Chemistry and Physics* ***226*** *(2019) 129-140.*

Some of these graphene-like 2D materials are layered TMD, metal oxides and other 2D compounds such as BN, Bi_2Te_3, Bi_2Se_3, $TaSe_2$, MoS_2 and WS_2 etc. [4]. Studies have shown that these non-graphene 2D materials generally possess excellent mechanical strength of up to 1.0 TPa, very good thermal conductivity of between 3080 to 5150 W/mK, excellent electrical conductivity (200 S/m), superior thermal stability with oxidation resistance temperature properties of the as-prepared nanohybrid structures. The ability of 2D TMD nanosheets to facilitate rapid electron transfer at the electrode-electrolyte interface has been established by several research studies [5-8].

BN has been reported to have a wide electrical band gap of 5.9 eV [9], excellent ultraviolet photoluminescence, excellent thermal conductivity and stability, superb in-plane mechanical strength, good resistance to oxidation and chemical inertness [10, 11] and it is thus a good candidate for the provision of good stability features in fabricated electrobiocatalytic devices.

Similarly, WS_2, with a band gap of 2.1 eV [12] has been shown in several studies as a material that is capable of overcoming the gapless band structure limitation of graphene. It possesses very wide in plane length and a nanoscale dimension in thickness [13]. Structurally, WS_2 is a hexagonally arranged layered material where, in each layer, one W atom is six-fold coordinated and hexagonally packed between two trigonal coordinated sulphur atoms [14]. Each S-W-S layer is bonded to seceding layers via weak Van der Waal forces. WS_2 possesses outstanding physico-chemical properties including large surface area, very high charge density, outstanding electron mobility and very high electronic density of state [15], causing

it to be regarded as an inorganic graphene. Additionally, WS_2 possesses good biocompatibility and it is highly dispersible [16] in water, making it a good candidate for the fabrication of hybrid self-assembled layered structures in conjunction with other materials [13].

Consequently, a nanohybrid composite consisting of BN and WS_2 layered dual 2D structure as developed in this study. Gold nanoparticle was subsequently introduced into the dual 2D system to strengthen the electron transfer properties of the composite structured materials to obtain a self-assembled structured dual 2D-nanomaterial composite.

Horseradish peroxidase was chosen as a model bio-recognition element and immobilized on the self-assembled dual 2D-Nanomaterial composite structure, thus obtaining HRP/BN/WS_2/AuNPs dual 2D-nanomaterial biointerface structure as a platform for the design of novel efficient and fast bioreactors and electrobiocatalysis devices thus demonstrating a new and unique design concept in biodevices fabrication to overcome the obvious setbacks of limited durability, slow interface electron transfer activities and low sensitivity of existing biodevices.

The immobilization of the HRP on the dual 2D-AuNPs matrix was achieved through electrostatic attraction under physiological conditions because of the attraction of the residual net charges between HRP and the dual 2D hybrid matrix.

As a novel concept, we have used a combination of experimental and theoretical studies to correlate the charge transport mobility and conductivity of BN/Au/WS_2(001) nanohybrid structure as biosensing interface material. The theoretical study was performed using a hybrid DFT calculation to offer a

fundamental interpretation of the experimental data, as well as to elucidate the chemical nature, stability, electronic and structural properties of the as-prepared nanohybrid structure.

5.2 EXPERIMENTAL

5.2.1 Fabrication of BN/WS_2/AuNPs/HRP nanohybrid structure

The synthesis procedure of BN/WS_2/AuNPs/HRP nanohybrid structure is presented in section 3.4.4.

5.2.2 Preparation of modified bioelectrodes

The followed methods for preparation of modified bioelectrodes are discussed in section 3.4.5.

5.2.3 Computational details

The computational details of BN/WS_2/AuNPs nanohybrid structures were given in section 3.4.6.

5.3 RESULTS AND DISCUSSION

The bioelectrode fabrication steps are illustrated in scheme 5.1. Firstly, hybrid 2D heterostructure was formed via self-assembly of BN and WS_2, followed by the dispersion of metallic AuNPs via electrostatic attraction to the nitride and sulphide ions of the self-assembled hybrid 2D heterostructures. This was followed by the immobilization of the bio-recognition element on the self-assembled nanohybrid structure and finally the immobilization of the entire structure on pre-cleaned GC

electrode and eventually culminating in the electrobiocatalytic detection of H_2O_2 at the interface as represented by equation 5.1.

$$2H_2O_2 + 2e \rightarrow H_2O + O_2 \quad \text{.....(5.1)}$$

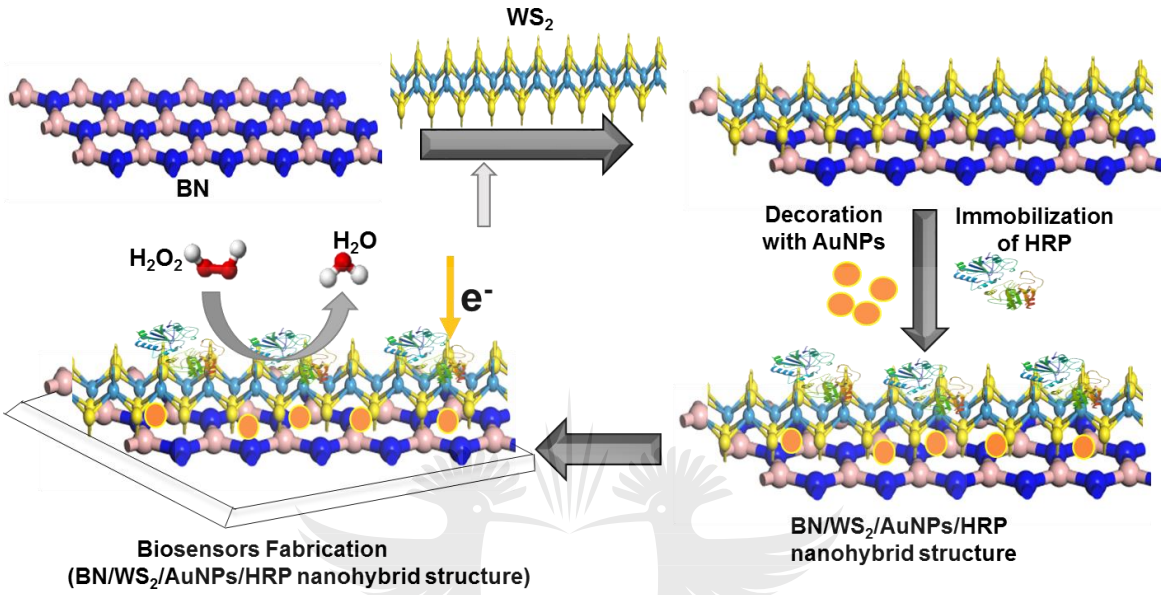

Scheme 5.1 Fabrication of hierarchical self-assembly interfaces of BN/WS_2/AuNPs/HRP nanohybrid structures showing H_2O_2 reduction at the interface. (Note: Scheme not drawn to scale)

The stability of the self-assembled nanohybrid interface material was firstly assessed through theoretical computational studies.

5.3.1 Theoretical studies

5.3.1.1 Theoretical calculation for the stability of BN/WS_2/AuNPs

Before the Au/WS_2(001) and BN/Au/WS_2(001) nanocomposites were built, the geometry of WS_2, pure Au and BN sheet were initially optimized. The optimized lattice constants were $a = b = 2.498$ Å, $c = 6.634$ Å for BN sheet, $a = b = 3.153$ Å, $c = 14.323$ Å for WS_2 monolayer, and $a = b = c = 4.078$ Å for pure Au. These

optimised lattice parameters were in good agreement with earlier studies (a = b = 2.504 Å, c = 6.653 Å for BN [17], a = b = 3.153 Å, c = 12.323 Å for WS_2 monolayer [18], and a = b = c = 4.070 Å for pure Au [19]). The bond lengths of W–S, B–N, Au–Au and S–S were calculated as 2.40, 2.85, 1.40 and 3.13 Å, respectively, and the S–W–S bond angle was 81.35°. These values were in agreement with earlier theoretical studies [20-22]. This indicates the validity and accuracy of the parameters used in this study. The Au/WS_2(001) and BN/Au/WS_2(001) nanohybrid structures were constructed using a 4 x 4 supercell of WS_2 monolayer (16 W and 32 S atoms), a 3 x 3 supercell of pure Au (18 Au atoms), and a 5 x 5 supercell of BN sheets (25 B and 25 N atoms). The resulting lattice mismatch was –2.99 (2.09 %) between Au and WS_2 monolayer (BN sheet). The periodic interaction between the adjacent systems of the nanocomposites was prevented using a vacuum region of 20 Å. The optimized structures are shown in Figure 5.1.

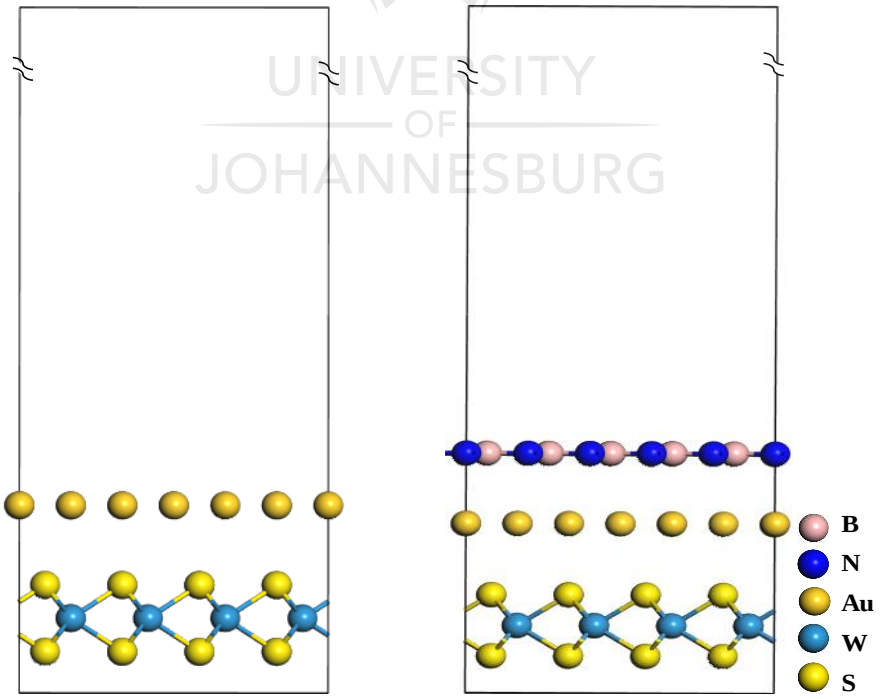

Figure 5.1 The side view of the optimized structure of (a) Au/WS_2(001) and (b) BN/Au/WS_2(001) nanohybrid structure.

The equilibrium distance between Au and WS_2 was 4.98 Å, while the interlayer spacing between BN and Au was 2.13 Å for the BN/Au/WS_2(001) nanohybrid structure. Moreover, the interlayer spacing between Au and WS_2 was 4.51 Å for the Au/WS_2(001) nanohybrid structure. The adsorption stability of the as–fabricated BN/Au/WS_2(001) nanohybrid structure was evaluated by calculating the interface adhesion energy (E_{ad}) [23]:

$$E_{ad} = \left[E_{\mathrm{BN/Au/WS_2(001)}} - E_{\mathrm{BN}} - E_{\mathrm{Au}} - E_{\mathrm{WS_2}}\right]/S \quad \text{.....(5.2)}$$

where $E_{\mathrm{BN/Au/WS_2(001)}}$, E_{BN}, E_{Au}, and $E_{\mathrm{WS_2}}$ are the total energies of the relaxed BN/Au/ WS_2(001) nanohybrid structure, BN sheets, pure Au, and WS_2 monolayer respectively, and S is the surface area. The adhesion energies of the Au/WS_2(001) and BN/Au/WS_2(001) nanohybrid structures was calculated as –1.20 and –1.89 eV Å^2, respectively. The negative adhesion energies show that both BN and Au could form a stable interface with the WS_2 substrates. The interlayer binding energy of the Au/WS_2(001) and BN/Au/WS_2(001) nanohybrid structure was calculated to assess the nature of the interaction between the monolayers of these as–prepared nanohybrid structures:

$$E_b = -\left[E_{\mathrm{BN/Au/WS_2(001)}} - E_{\mathrm{BN}} - E_{\mathrm{Au}} - E_{\mathrm{WS_2}}\right]/\mathrm{nW} \quad \text{.....(5.3)}$$

Here, nW is the number of W atoms per supercell. From equation. 5.3, the interface binding energy was 1.86 and 2.94 eV per WS_2 for the Au/WS_2(001) and BN/Au/WS_2(001) nanohybrid structure, respectively. The small binding energies indicate that BN sheets, pure Au, and WS_2 monolayer bind together through physical adsorption due to the long–range van der Waals interactions.

5.3.1.2 Electronic properties

To comprehend how BN sheet and Au influence the conductivity of WS_2–based sensors, we studied their electronic structures. The band structures of BN sheets, BN(001) surface, pure Au, WS_2 monolayer, WS_2(001) surface, Au/WS_2(001) and BN/Au/WS_2(001) nanohybrid structure were calculated with the results depicted in Figure 5.2.

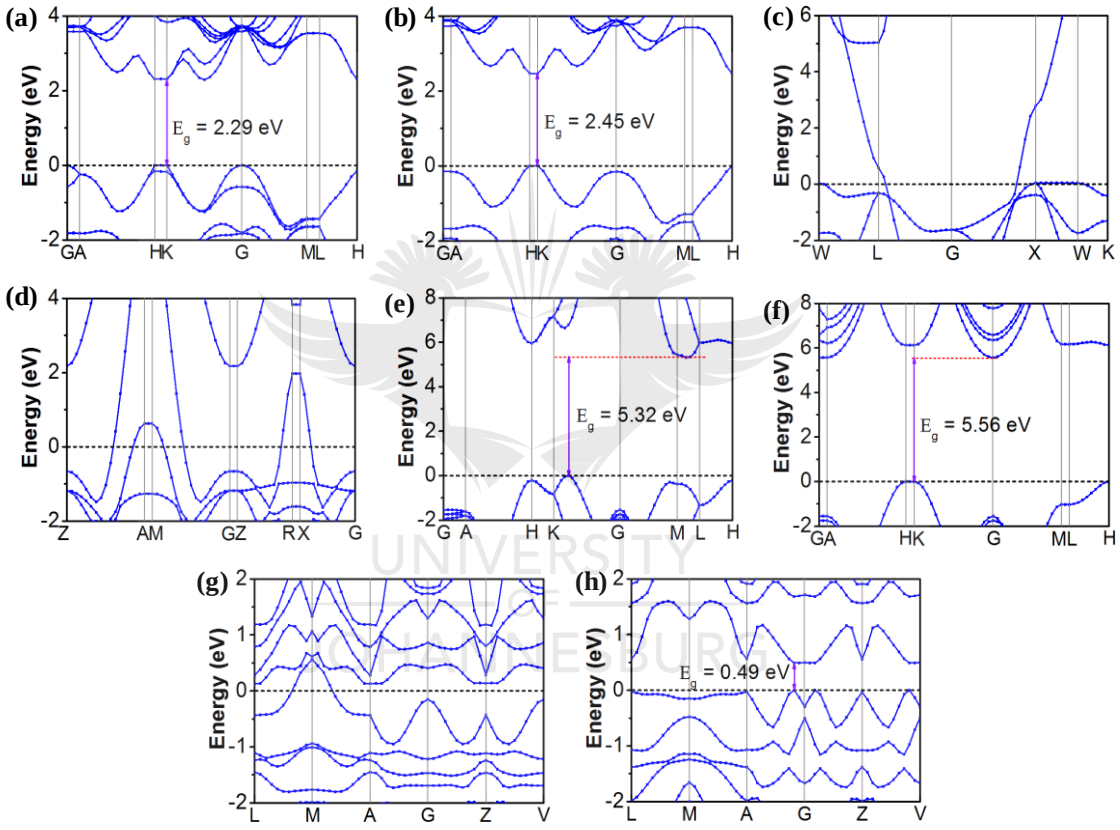

Figure 5.2 Calculated band structures of (a) WS_2 monolayer, (b) WS_2 (001), (c) pure Au, (d) Au(001), (e) BN sheet, (f) BN(001), (g) Au/WS_2(001) and (h) BN/Au/WS_2(001) nanohybrid structure.

Our calculations show that pristine WS_2 monolayer was a direct bandgap semiconductor with both the valence band maximum (VBM) and conduction band minimum (CBM) positioned on the *K* point. The calculated bandgap value of 2.29 eV, seen in Figure 5.2(a) was in agreement with earlier theoretical and

experimental results [24]. When the WS_2 monolayer was exposed along the 001 surface, a direct bandgap energy of 2.45 eV was obtained (Figure 5.2(b)). This was ascribed to the quantum–confinement effects induced by the thickness limit of the (001) surface. For pure gold, the gapless characteristic was retained with Dirac points of the partially occupied band crossing the Fermi energy level near the vicinity of *L* and *G* points in the Brillouin Zone (Figure 5.2(c)), thereby forming a ‘‘half’’ Dirac cone. The zero bandgap confirms the metallicity of Au. The electronic band structure of pure Au was analogous to that of graphene sheet [25], hence its inherent dispersion was gapless. The Dirac cone formation feature near the Fermi energy level still remains in the Au(001) surface (Figure 5.2(d)).

Bulk BN sheet was an indirect bandgap with a value of 5.32 eV. This value is within the experimental band gap range of 3.8–5.9 eV [26]. The indirect band gap of BN(100) surface was 5.56 eV, and this was located at the *K* and *G* points. The Au/WS_2(001) nanohybrid structure shows a metallic band structure due to the introduction of spherical Au nanoparticles and the weak interlayer interactions. Thus, the Dirac cone shape was preserved. The metallic band of Au/WS_2(001) nanohybrid structure was considerably flattened and this indicates that the effective mass of electron becomes higher compared to the clean edges. Based on the semi classical Drude model, the large effective electron mass might lower its electrical conductivity [27, 28]. Upon the formation of the hybrid interface, the bandgap value of BN/Au/WS_2(001) nanohybrid structure was about 0.49 eV. Due to the sub lattice symmetry breaking caused by the coupled BN sheets, the interactions among BN, Au and WS_2 induce a bandgap opening at the Dirac point of Au (Figure 5.2(d)). Thus, the bandgap opening causes the BN sheets to generate inhomogeneity in the Au electrostatic potential [29] and this can change the periodicity of Au, thereby

breaking the degeneracy of band at the *M* point. Moreover, the introduction of BN sheets much increases the thermal conductivity of BN/Au/WS_2(001) nanohybrid structure. This indicates that BN sheets may be a suitable substrate for WS_2 in sensors (Figure 5.2(a)-(h)).

5.3.1.3 Density of State

Since the electronic band structure of nanohybrid structure mostly relies on the interfacial interactions of the individual monolayers, the nature of orbitals and variation of electronic properties of Au/WS_2(001) and BN/Au/WS_2(001) nanohybrid structure, the total density of states (TDOS) and partial density of states (PDOS) was calculated. For comparison, the TDOS and PDOS of the individual BN, Au, WS_2 and their surfaces before the formation of the interface was also calculated as shown in Figure 5.3(a)-(h).

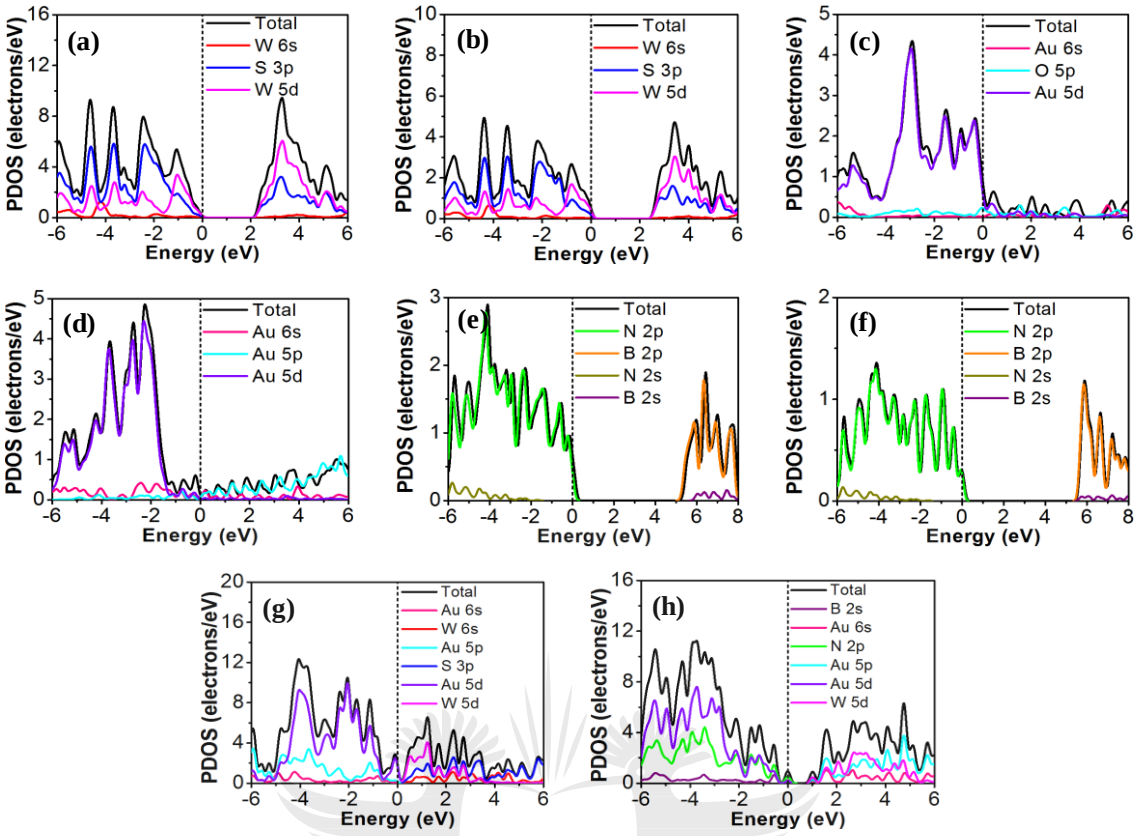

Figure 5.3 Calculated PDOS of (a) WS_2 monolayer, (b) WS_2(001), (c) pure Au, (d) Au(001), (e) BN sheet, (f) BN(001), (g) Au/WS_2(001) and (h) BN/Au/WS_2(001) nanohybrid structure.

From the PDOS of the WS_2 and WS_2(001) sheets (Figure 5.3 (a) and (b)), the CBM and VBM primarily consisted of W 5d state with some contribution from S 3p state. The PDOS results agree well with earlier theoretical studies [30]. For pure Au and Au(001) surface (Figure 5.3 (c) and (d)), the VBM was primarily contributed by Au 5d state, while the CBM was mainly dominated by Au 5p state. The same observation was made in earlier studies [31]. For pure BN sheet and BN(001) surface (Figure 5.3(e) and (f)), the VBM was mainly occupied by N 2p state, whereas the CBM was dominated by B 2p state and this was in agreement with earlier studies [32, 33]. Figure 5.3 (g) demonstrates that the density of the VBM distributes around the Au 5d state, while that of the CBM was around the W 5d state. The PDOS results showed that the metallic states originate largely from the Au 5d state on the edges.

Based on the PDOS of BN/Au/WS_2(001) nanohybrid structure (Figure 5.3(h)), we can draw a conclusion that the VBM was dominated by the N 2p and Au 5p states, whereas the CBM was contributed by W 5d state of the WS_2 monolayer.

The charge density distribution of the lowest unoccupied and highest occupied levels (LUL and HOL) was calculated to shed more insights on the PDOS results. The results are shown in Figure 5.4.

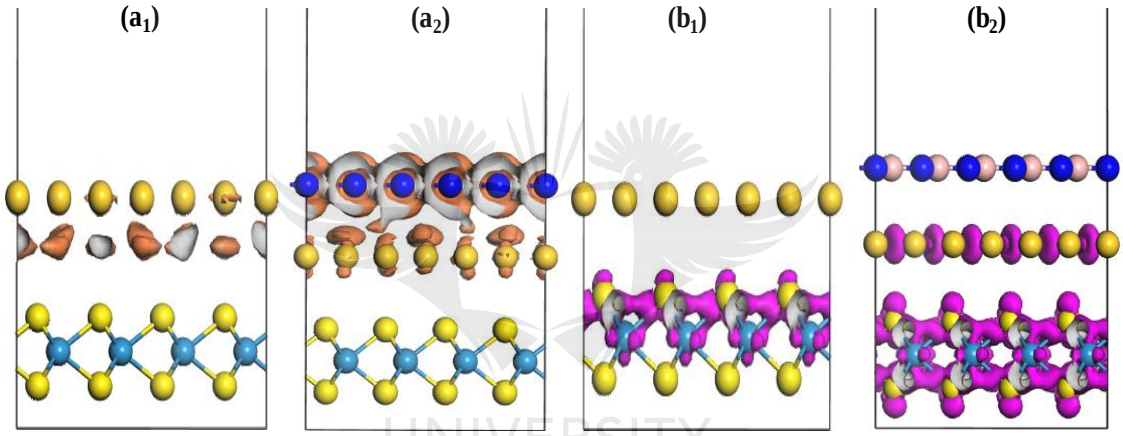

Figure 5.4 The charge density distribution plots of the HOL (a_1, a_2) and LUL (b_1, b_2) for the Au/WS_2(001) and BN/Au/WS_2(001) nanohybrid structure. The isovalue is 0.04 e $Å^{-3}$.

In the Au/WS_2(001) nanohybrid structure (Figure 5.4(a_1)), the HOL was contributed by Au, while the LUL was almost localised on the WS_2 sheets. However, the charge distributions of BN/Au/WS_2(001) nanohybrid structure was different with the HOL comprising of states from BN sheets and Au (see Figure 5.4(a_2)), while the LUL was composed of W 5d states hybridized with a small Au 5p state localized mostly around the Au atoms (Figure 5.4(b_2)). As shown in Figure 5.4(a_2) and (b_2), although the charge density for both the HOL and LUL were mainly distributed in the BN sheets and WS_2 monolayers, there was considerable charge density of the HOL and

LUL being localised on the Au surface. This induces orbital hybridization between Au and BN sheets or WS_2 monolayers.

5.3.1.4 Charge transfer and mechanism analysis

The Fermi energies of Au, BN sheets, WS_2 monolayers, Au/WS_2(001) and BN/Au/WS_2(001) nanohybrid structures were calculated as –4.64, –2.86, –2.56, –2.40 and –1.76 eV, respectively. Such Fermi energy shift indicates a redistribution of charges between the involved monolayers. The charge transfer was visualised by the three–dimensional (3D) charge density difference plot, see Figure 5.5((a), (b)).

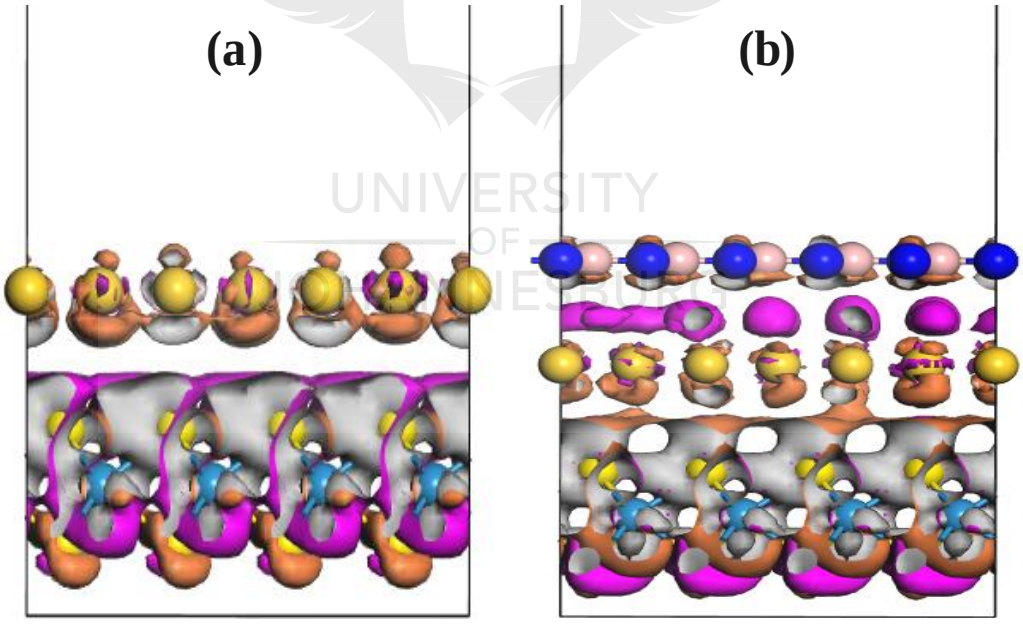

Figure 5.5 The 3D charge density difference of (a) Au/WS_2(001) and (b) BN/Au/WS_2(001) nanohybrid structure with an isovalue of 0.008 e Å^{-3}.

The orange and magenta isosurfaces are the charge accumulation and depletion, respectively. The charge density redistributions occur at the interface region of

BN/Au/WS_2(001) nanohybrid structure. As shown in Figure 5.5(b), the electrons were mainly accumulated on the bottom of BN sheets and Au, while the electron depletion appears around the top–most Au atoms, as well as the bottom–most WS_2 monolayer. The charge density redistribution revealed the electron acceptor–transporter role played by Au in the interfacial layer of BN sheet and WS_2 monolayer. Therefore, in this study, Au could act as a sensitizer and a co–catalyst in the BN/Au/WS_2(001) nanohybrid structure to enhance its performance as sensors. Nevertheless, for the Au/WS_2(001) nanohybrid structure, the electrons and holes were accumulated on the Au and WS_2 monolayer, respectively. Figure 5.6 showed that the charge distribution at the interface of Au and WS_2 in BN/Au/WS_2(001) nanohybrid structure was more enhanced than in the Au/WS_2(001) composite. A Mulliken population charge analysis revealed that the total charge migrating from BN sheets via Au to the bottom WS_2 monolayer was 1.60 |e|. Moreover, the Mulliken population charge analysis indicates a charge transfer of 0.64 electrons from Au to W atoms of the WS_2 sheets. The larger charge transfer in the BN/Au/WS_2(001) nanohybrid structure was due to the increased interlayer and adhesion energies.

5.3.1.5 Work function

The work function of a surface is a vital parameter in evaluating the charge transfer at the nanohybrid structure interface [23]. Therefore, to further understand the source of such interfacial electron migration, the work function of the monolayers BN(001), Au(001), and WS_2(001) were evaluated by aligning the Fermi level to the vacuum level [34].

$$\Phi = E_{vac} - E_F \quad \text{.....(5.4)}$$

where Φ is the work function, E_{vac} represent the electrostatic potential of the vacuum energy level, and E_F is the Fermi energy level. The calculated work function for monolayers BN(001), Au(001), WS_2(001), and the Au/WS_2(001) and BN/Au/WS_2(001) nanohybrid structures are given in Figure 5.6.

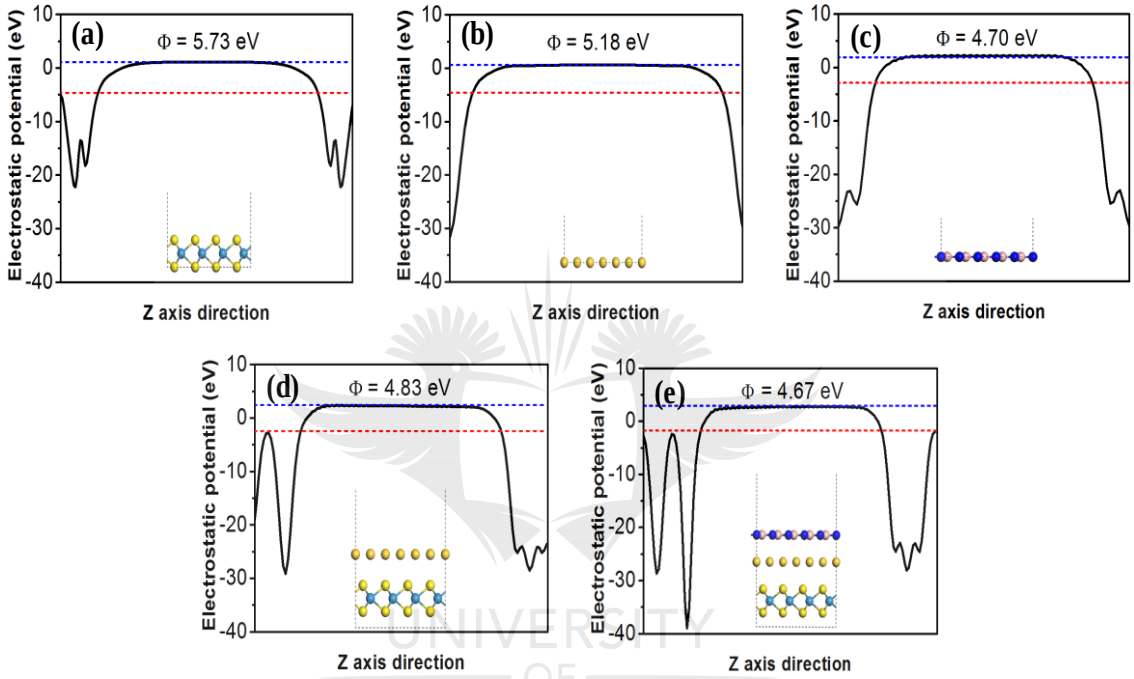

Figure 5.6 The calculated electrostatic potential of (a) WS_2(001), (b) Au(001), (c) BN(001), (d) Au/WS_2(001) and (e) BN/Au/WS_2(001) nanohybrid structure.

Based on equation 5.4, the work functions of WS_2(001), Au(001), BN(001), Au/WS_2(001) and BN/Au/WS_2(001) nanohybrid structures were calculated as 5.73, 5.18, 4.70, 4.83 and 4.67 eV, respectively. The obtained work functions for WS_2 monolayer was slightly comparable with an earlier theoretical calculation of WS_2 monolayer (5.89 eV) [35], BN sheet (4.70 eV) [36] and clean gold (5.20 eV) [36]. The work function of the WS_2 monolayer was larger than that of Au and BN sheet. Hence, when WS_2 monolayer comes into contact with Au and BN sheet, electrons

may flow from both Au and BN sheet to WS_2. Therefore, both Au and BN sheet were positively charged relative to WS_2 near the interface due to electrostatic interaction of the nano conjugated materials. This results in an electron depletion at the BN surface, as revealed by the charge density difference plot, while making the WS_2 environment electron–rich [30]. Subsequently, a built–in electric field perpendicular to the nanohybrid structure was induced due to the electron transfer between these monolayers. The calculated work function of Au/WS_2(001) and BN/Au/WS_2(001) nanohybrid structures were 4.83 and 4.67 eV, respectively and this was much lower than that of the WS_2 monolayer. It implies an easier transfer of electrons in the Au/WS_2(001) and BN/Au/WS_2(001) nanohybrid structure. The Fermi energy level of WS_2, Au and BN sheets shifts upward by 1.06, 0.51 and 0.03 eV for BN/Au/WS_2(001) nanohybrid structure. However, for the Au/WS_2(001) nanohybrid structure, the Fermi energy level of WS_2 and Au shifts upward by 0.9 and 0.36 eV, while the Fermi energy level of BN sheet shifts downward by 0.15 eV.

5.3.2 Materials characterization

Materials characterization for hybrid 2D nanointerfaces structure (BN-WS_2-AuNPs) was performed using TEM and SEM for morphological characterization while XRD was used for structural characterization (Figure 5.7((a)-(d)). Figure 5.7(a) shows the TEM image of the dual 2D structure comprising BN and WS_2 hybrid structure. The image showed layered structures with wide specific surface area which are quite desirable for the immobilization of bio-recognition element and for achieving good electrobiocatalysis. Figure 5.7(b) shows the TEM image of the dual 2D hybrid structure (BN/WS_2) after the dispersion AuNPs on the hybrid structure. It is observed that the AuNPs were well dispersed on the layered dual 2D hybrid structure and

consequently led to increasing the available surface area of the interface structure. Figure 5.7(c) is the SEM image of the 2D hybrid interface structure. The image equally showed flat layered materials with wide aspect ratio which is in agreement with the observations of the TEM image of the hybrid structure as shown in Figure 5.7(a).

The structural characterization of the nanointerface structure was done using XRD and presented in Figure 5.7(d). The XRD is a non-destructive characterization which is used to determine the crystal structure and phase of crystalline samples. The lattice planes and geometry and size of structures of the sample are determined by the angular positions of the X-ray diffraction peaks. BN/WS_2 and BN/WS_2/AuNPs nanohybrid structures have been prepared by dispersing 500 µL of both composite solutions on silica disk with low background. Figure 5.7 (d) shows that the X-ray diffractograms of BN/WS_2 and BN/WS_2/AuNPs nanohybrid structure have crystalline structures. The reflections observed for BN/WS_2 (2θ=12.84, 14.65, 16.54, 20.93, 25.86, 26.76, 29.55, 33.41, 39.22, 42.5, 53.1°) can be indexed to combination of BN and WS_2 and the reflections observed for BN/WS_2/AuNPs (2θ=12.90, 16.54, 26.74, 29.18, 31.69, 33.37, 38.58, 45.47, 51.08, 52.85, 64.76°) can be indexed to a combination of BN, WS_2 and Au and match with database JCPDS file no. 073-2095 of BN and JCPDS no. 84-1398 of WS_2 as evaluated by X'pert software [37-39] as shown in Figure 5.7. The plot for BN/WS_2/AuNPs resembles the combined profiles of the (111) and (220) of Bragg peaks seen in the theoretical diffraction pattern of metallic gold nanoparticles [40]. These observations are consistent with the presence of BN, WS_2 and AuNPs in nanohybrid structures.

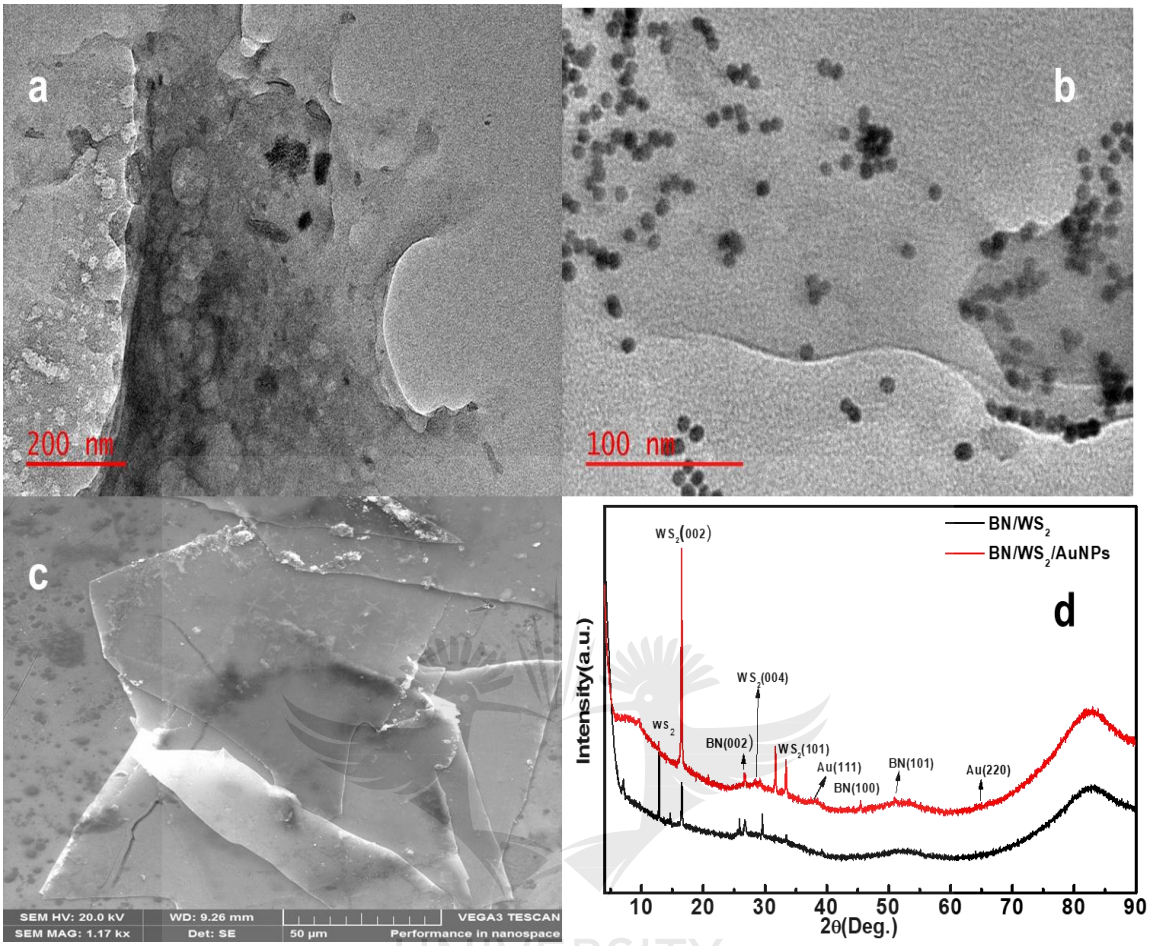

Figure 5.7 **(a) TEM image of the BN/WS_2 hybrid structure, (b) TEM image of BN/WS_2/AuNPs nanohybrid structure, (c) SEM image of the BN/WS_2 2D hybrid structure and (d) XRD spectra for BN/WS_2 and BN/WS_2/AuNPs nanointerfaces structure.**

5.3.3 Electrochemical behaviour of the modified bioelectrodes

The fabricated modified bioelectrodes were characterized using CV and EIS (Figure A2.1 ((a)-(d)) Appendix A2 and Figure 5.8((a)-(d)). The CV curves for the bare GC and all the fabricated modified bioelectrodes exhibited the classical sigmoidal shape (Figure 5.8(a)), thus indicating that faradaic electron transfer process took place at the interface in 10 mM $[Fe(CN)_6]^{3-/4-}$ solution redox probe and 10 mM PBS as

supporting electrolyte. Figure A2.1 ((a)-(d)) Appendix A2 shows the CV scan response at different scan rates for the bare GC and all modified electrodes.

It was observed that the anodic peak current (I_{p_a}) and the cathodic peak current (I_{p_c}) increases with increase in scan rates. Figure 5.8(a) (1-IV) is the CV response for the bare GC and all the modified electrodes at 50 mV/s also shows the classical sigmoidal shape with different peak to peak potential separations (ΔE_p) [41]. The bare GCE displayed narrow ΔE_p of 100mV and I_{p_a} versus I_{p_c} ratio of 1 (Figure 5.8(a) (1)). The narrow ΔE_p is an indication of fast electron transfer kinetics at the electrode-electrolyte interface, while the I_{p_a}- I_{p_c} ratio of 1 is an indication of the reversibility of the redox reaction of the $[Fe(CN)_6]^{3-/4-}$ solution redox probe. The BN/WS_2/GCE (Figure 5.8(b) (II)) equally displayed a well-defined redox peaks that indicate the occurrence of faradaic process at the interface. The ΔE_p value for the BN/WS_2/GCE is quite wider (398 mV) than that of the bare GC electrode, while the I_{p_a}/I_{p_c} ratio is ~ 1 which is an indication of a slower electron transfer kinetics at the modified electrode surface compared to the bare GCE. This slow electron transfer can be attributed to the quasi reversible nature of the redox reaction at the BN/WS_2/GCE surface [42]. The peak to peak potential separation for BN/WS_2/AuNPs/GCE (Figure 5.8 (a) (III)) is considerably lower (199 mV) than that of the BN/WS_2 without AuNPs, thus signifying that the incorporation of Au nanoparticles led to improved electron transfer kinetics. Also, the increased current response indicated that AuNPs equally acted as a current booster due to the increase in effective surface area of the BN/WS_2/AuNPs/GCE electrode compared to BN/WS_2/GCE [43]. After immobilization of enzyme HRP on the surface of the modified electrode containing BN/WS_2/AuNPs, peak potential separation ΔE_p is

observed to increase to 321 mV (Figure 5.8 (a) (IV)) and the I_{p_a}/I_{p_c} ratio is calculated to be ~ 1.4, thus indicating that the presence of the HRP layer caused a reduction in available surface area and consequently led to the lowering of the electron transfer kinetics at the interface and thus leading to a quasi-reversible redox process.

Similarly, the redox peak potentials were also observed to shift (anodic peak potential toward positive and cathodic peak potential toward negative) with increasing scan rates (Figure 5.8(b)). Also, the plot of the oxidation and reduction peak currents as a function of the square root of scan rates exhibited linear relationships (Figure 5.8(b)). This is in agreement with the Nernstian equation which shows interfacial activities of electro-active components in the process of adsorption and desorption [41, 44, 45]. The observed shift in potential coupled with the linear increase in I_{p_a} and I_{p_c} relative to the square root of the scan rate is an indication that mass transfer is diffusion controlled at the interface [46] in agreement with Randles–Sevcik equation as given in equation 5.5.

$$I_p = 2.69\, x10^{-5}\, AD^{1/2} n^{3/2} \gamma^{1/2} C \quad \text{.....(5.5)}$$

Where I_p is the peak current and it is directly proportional to the effective electrode surface area (A), concentration (C), and the square root of scan rates $(\gamma^{1/2})$ respectively of the modified electrode where mass transport is diffusion (D) controlled.

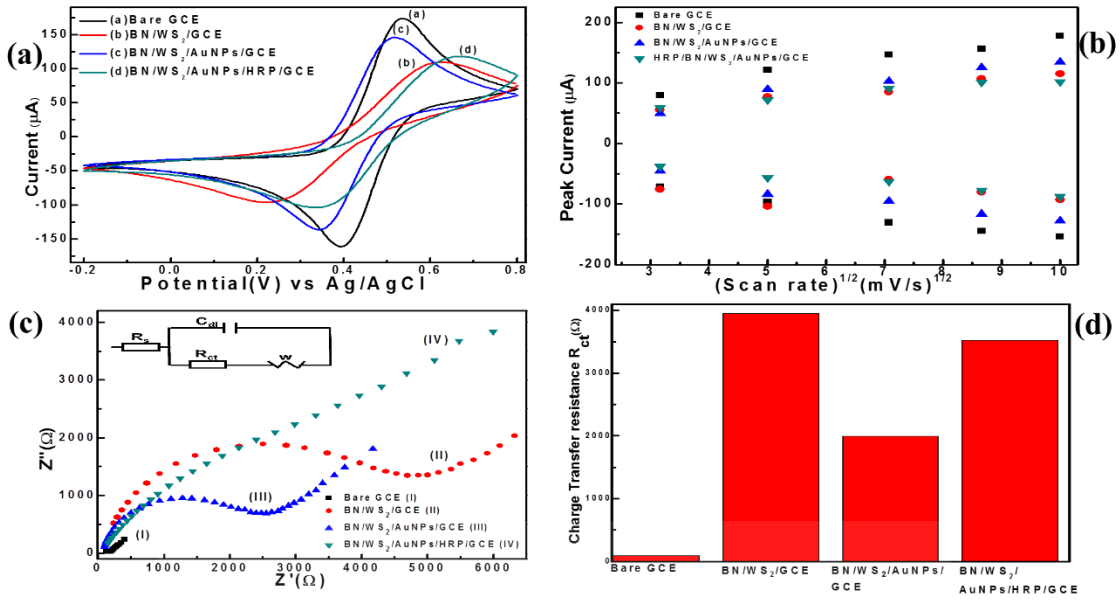

Figure 5.8 Bioelectrode characterization showing (a) cyclic voltammetry response at 50 mV/s in 10 mM PBS and 10 mM $[Fe(CN)_6]^{3-/4-}$ for the bare GC and all modified electrodes; (b) effect of scan rate on the cathodic peak current I_{pc} and the anodic peak current I_{pa}; (c) EIS Nyquist plot with Randles circuit equivalent diagram as inset, and (d) charge transfer impedance histogram for the EIS.

The fabricated modified bioelectrodes were further characterized using EIS. It is commonly known that current flowing through the interface during an electrochemical reaction always contains the faradaic and non-faradaic component. The faradaic component is due to electron transfer when a redox reaction takes place and the transferring electron overcomes a certain activation barrier (usually referred to as R_{ct} which is basically dependent on the environment at the surface of the electrode and an uncompensated solution resistance (R_s) [47].

Similarly, the mass transport of reactants and products to the interface give rise to another class of resistance known as Warburg impedance (Z_w). The non-faradaic current results in the charging of the double layer capacitance (C_{dl}). Levi and Aurbach [48] in their study, established the relationship between R_{ct} and the

thickness of materials at the electrode surface. Thus, EIS is an excellent way of evaluating the effect of electrode modification on electron transfer process during an electrochemical reaction. The complex EIS is usually presented as a plot of real (Z') versus imaginary (Z'') components arising from resistance and capacitance of the cell respectively [49].

The EIS characterization for the bare and all modified electrodes in this study is presented as Nyquist plot (Figure 5.8 (c) (I-IV)) showing the semi-circle region and the linear region, while the Randles circuit equivalent fittings for the electrochemical cell is presented as an inset to Figure 5.8 (c). The semicircle portion of the Nyquist plot corresponds to the higher frequency range electron-transfer-limited process which is denoted by R_{ct} whereas the linear portion of the Nyquist plot corresponds to low frequency range diffusional-limited electron transfer process [49]. The diameter of the semi-circular portion of the Nyquist plot equals the charge transfer resistance (R_{ct}) at the interface [47-49], the R_{ct} may equally be expressed according to the following [47] equation 5.6 and 5.7 [47, 50].

$$Z_{(\omega)} = R_s + \frac{R_{ct} + \sigma\omega^{-1/2}}{(\sigma\omega^{1/2}C_d+1)^2 + \omega^2 C_d^2\left(R_{ct} + \sigma\omega^{-1/2}\right)^2} + j\frac{\left[\omega C_d\left(R_{ct} + \sigma\omega^{-1/2}\right)^2 + \sigma\omega^{-1/2}(C_d\sigma\omega^{1/2}+1)\right]}{(C_d\sigma\omega^{1/2}+1)^2 + \omega^2 C_d^2\left(R_{ct} + \sigma\omega^{-1/2}\right)^2} \quad \text{.....(5.6)}$$

ω is defined as $2\pi f$, where f is frequency, and $j = (-1)^{1/2}$ and

$$\sigma = \frac{RT}{\sqrt{2n^2F^2A}}\left(\frac{1}{D_0^{1/2}C_0(x,t)} + \frac{1}{D_R^{1/2}C_R(x,t)}\right) \quad \text{.....(5.7)}$$

where A is electrode surface area and Cs are the different concentrations of the different species at a distance x and t is time. Also, the Warburg impedance is related to σ according to the following equation 5.8 [47].

$$Z_w = \left(\frac{2}{\omega}\right)^{1/2} \sigma \quad \text{.....(5.8)}$$

In this study, the R_{ct} for the bare GC electrode was evaluated to be 92.8 Ω (Figure 5.8(c) (I)) but this was substantially increased to 3946 Ω after the modification of the electrode with BN/WS_2 hybrid (Figure 5.8(c) (II)), this may be due to the electrostatic repulsion between S^{2-} ion in the WS_2 and the electron being transferred from the redox couple [50].

Similarly, the wide bandgap and hydrophobic nature of BN could also be a contributor to this observed large difference between the R_{ct} values for the bare and BN/WS_2 modified electrodes. It was however observed that when AuNPs was added to the dual 2D hybrid structure, the calculated R_{ct} value for the resulting BN/WS_2/AuNPs modified electrode was 1990 Ω (Figure 5.8 (c) (III)). This observed reduction in R_{ct} value maybe attributed to the signal amplification properties of AuNPs due to increased effective electrode surface area introduced by the presence of the AuNPs [13, 51].

However, after the immobilization of HRP on the dual 2D nanoparticle hybrid structure to obtain BN/WS_2/AuNPs/HRP/GCE (Figure 5.8 (c) (IV)), it was observed that the R_{ct} value was increased to 3523 Ω, indicating that the enzyme exhibited an insulating property at the interface in the redox probe. This observation is in agreement with what was reported by Parlak *et al.* [50].

5.3.4 Electrocatalysis of H_2O_2 at BN/WS_2/AuNPs/HRP/GCE

The electrobiocatalytic properties of the fabricated BN/WS_2/AuNPs/HRP/GCE were evaluated using H_2O_2 as a model analyte. It is well known that H_2O_2 is a substrate or side product in many enzyme-catalyzed reactions. Consequently, many reports on oxidase based biosensors rely on the detection of H_2O_2 produced by enzymatic reactions because the amount of H_2O_2 produced by such enzymatic reactions is normally directly proportional to the quantity of the substrate generating it. As a result, using chronoamperometric technique, the activity of the fabricated modified BN/WS_2/AuNPs/HRP/GCE towards the detection of H_2O_2 was investigated and the results are presented in Figure 5.9((a)-(d)).

The current-time response curve to successive addition of H_2O_2 in 10 mM PBS and at a constant potential of 0.6 V is presented in Figure 5.9 (a) while the corresponding calibration curve is presented in Figure 5.9 (b). The fabricated bioelectrode exhibited a fast response to successive addition of the analytes with a wide linear range from 0.15 mM to 15.01 mM, a sensitivity of 19.16 µA/mM/cm^2 and the limit of detection (LoD) was calculated to be 3 mM. To assess repeatability, the biosensing experiments were performed 3 times and the average standard deviation for each measurement was calculated to be around 2% and it was plotted as the current range in the calibration curve (Figure 5.9 (b)).

The electrocatalysis experiments were again repeated using fabricated BN/WS_2/AuNPs/GCE (without HRP), the results are presented in Figure 5.9((c)-(d)) (Current-time and calibration curves respectively), to assess the role of HRP in the electrocatalysis reaction. It was observed that the current response is considerably lower which could be as a result of low conversion of the analyte. The response time

is equally slower, and the sensitivity is lower (3.19 µA/mM/cm^2). Similarly, the chronoamperometric measurements were also repeated 3 times, the average standard deviation was calculated to be 33%. This is an indication that the repeatability of the reaction is far less reliable without the presence of the bio-recognition element to aid the detection process.

The stability of the fabricated modified BN/WS_2/AuNPs/HRP/GCE was evaluated over a one month period during which the electrodes were stored at 4 ^oC. It was observed that there was no appreciable change in current response during the month long stability evaluation period. These results showed that the fabricated bioelectrodes were quite stable over a one month period.

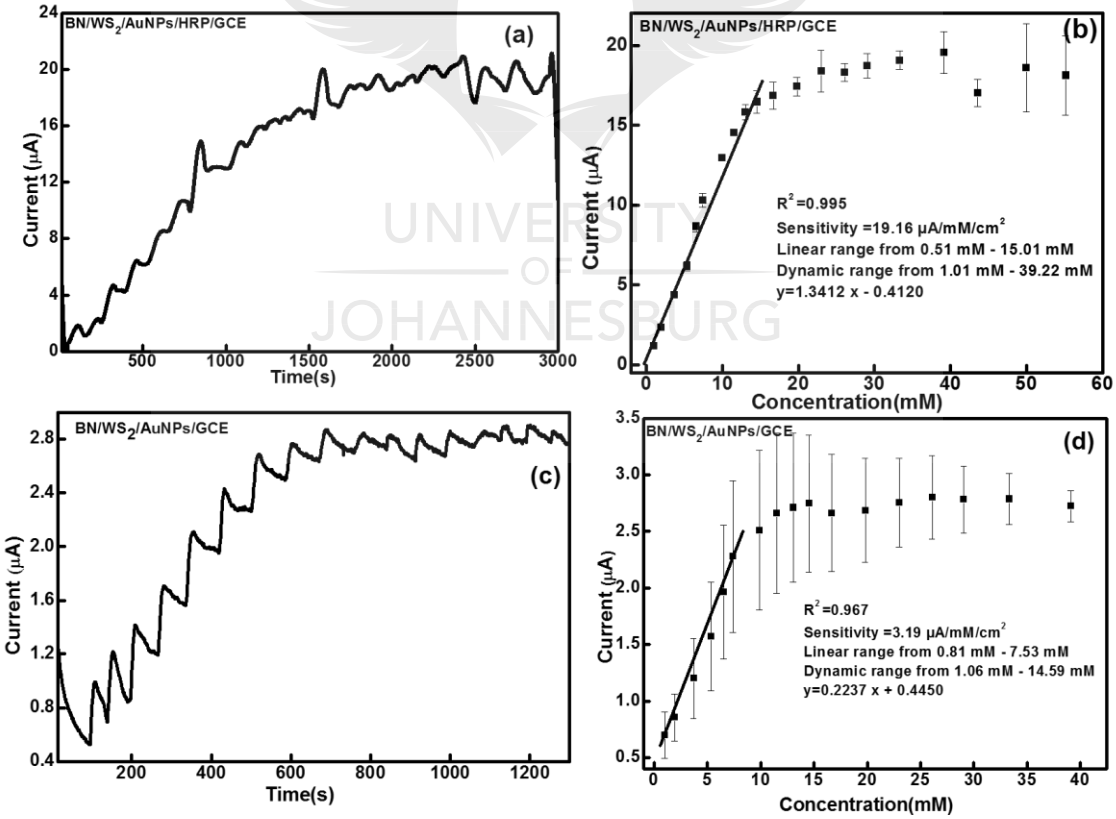

Figure 5.9 Chronoamperometry response showing current-time plot at an applied potential of + 0.6 V in 10 mM PBS and calibration curve for the chronoamperometric response for fabricated

BN/WS_2/AuNPs/HRP/GCE (a & b) and BN/WS_2/AuNPs/GCE (c & d) nanohybrid structure.

5.4 SUB-CONCLUSION

In this study, we report for the first time the fabrication of dual 2D hybrid interface system for applications in bioreactors, bioelectronics and biosensors. To increase signal amplification, AuNPs were conjugated with the 2D hybrid structure to form a hybrid nanointerface structure. To form a biointerface structure, HRP was subsequently immobilized on the nanointerface material. H_2O_2 was used as a model analyte to assess the electrobiocatalytic performance of the resultant fabricated modified BN/WS_2/AuNPs/HRP/GCE.

Additionally, the charge transfer, conductivity, electronic structure and stability of Au/WS_2(001) and BN/Au/WS_2(001) nanohybrid structures were investigated using hybrid DFT calculations. We found that both Au and BN sheet can adsorb on the WS_2 monolayer by weak van der Waals forces with higher thermodynamic stability. Due to the intrinsic interlayer dipole, the linear band structure of Au/WS_2(001) nanohybrid structure was disrupted and further widened to 0.49 eV when BN sheets were coupled with Au and WS_2 monolayers.

The first–principle calculations revealed that the BN sheets acted as an electron donor, while the noble metal Au served as an electron bridge with monolayer WS_2 acted as electron acceptors. The synergistic effects of BN sheets, metallic Au and monolayer WS_2 contributed to the enhanced performance of BN/Au/WS_2(001) nanohybrid structure as biosensors. These theoretical studies not only rationalise the experimental findings obtained in this study but also offer an efficient route to design future 2D–based biosensors.

Using chronoamperometric measurements, the fabricated electrochemical biointerface structure exhibited a fast response towards the detection of hydrogen peroxide reaching a steady state current within a few seconds after the successive addition of the analyte, with a wide linear range from 0.51 mM to 15.01 mM and a sensitivity of 19.16 μA/mM/cm^2. The fabricated biointerface structure also exhibited remarkable stability with no appreciable current response loss when tested for about 14 days while being stored at 4 °C. This has thus set the stage for the use of BN/WS_2/AuNPs hybrid nanointerface structure in the design and fabrication of bioreactors, biosensors and bioelectronics devices.

5.5 REFERENCES

[1] A. Gupta, T. Sakthivel and S. Seal. Recent development in 2D materials beyond graphene. *Progress in Materials Science* **73** (2015) 44-126.

[2] K. Shavanova, Y. Bakakina, I. Burkova, I. Shtepliuk, R. Viter, A. Ubelis, V. Beni, N. Starodub, R. Yakimova and V. Khranovskyy. Application of 2D non-graphene materials and 2D oxide nanostructures for biosensing technology. *Sensors (Switzerland)* **16** (2016) 223.

[3] B. Nichols, A. Mazzoni, M. Chin, P. Shah, S. Najmaei, R. Burke and M. Dubey. Advances in 2D Materials for Electronic Devices. *Semiconductors and Semimetals. Elsevier* **95** (2016) 221-277.

[4] A. O. Osikoya and A. Tiwari. Recent advances in 2D bioelectronics. *Biosensors & Bioelectronics* **89** (2017) 1-7.

[5] A. K. Geim and K. S. Novoselov. The rise of graphene. *Nature Materials* **6** (2007) 183-191.

[6] S. Das, R. Gulotty, A. V. Sumant and A. Roelofs. All two-dimensional, flexible, transparent, and thinnest thin film transistor. *Nano Letters* **14** (2014) 2861-2866.

[7] B. Radisavljevic, A. Radenovic, J. Brivio, i. V. Giacometti and A. Kis. Single-layer MoS_2 transistors. *Nature Nanotechnology* **6** (2011) 147-150.

[8] F. Schwierz, J. Pezoldt and R. Granzner. Two-dimensional materials and their prospects in transistor electronics. *Nanoscale* **7** (2015) 8261-8283.

[9] K. Watanabe, T. Taniguchi and H. Kanda. Direct-bandgap properties and evidence for ultraviolet lasing of hexagonal boron nitride single crystal. *Nature Materials* **3** (2004) 404-409.

[10] Z.-G. Chen, J. Zou, G. Liu, F. Li, Y. Wang, L. Wang, X.-L. Yuan, T. Sekiguchi, H.-M. Cheng and G. Q. Lu. Novel boron nitride hollow nanoribbons. *ACS Nano* **2** (2008) 2183-2191.

[11] C. Jin, F. Lin, K. Suenaga and S. Iijima. Fabrication of a freestanding boron nitride single layer and its defect assignments. *Physical Review Letters* **102** (2009) 195505.

[12] H. Zeng, G.-B. Liu, J. Dai, Y. Yan, B. Zhu, R. He, L. Xie, S. Xu, X. Chen and W. Yao. Optical signature of symmetry variations and spin-valley coupling in atomically thin tungsten dichalcogenides. *Scientific Reports* **3** (2013) 1608.

[13] O. Parlak, P. Seshadri, I. Lundström, A. P. Turner and A. Tiwari. Two-Dimensional Gold-Tungsten Disulphide Bio-Interface for High-Throughput Electrocatalytic Nano-Bioreactors. *Advanced Materials Interfaces* **1** (2014) 1400136.

[14] W. Zhao, Z. Ghorannevis, L. Chu, M. Toh, C. Kloc, P. H. Tan and G. Eda. Evolution of electronic structure in atomically thin sheets of WS_2 and WSe_2. *ACS Nano* **7** (2013) 791-797.

[15] W. Sik Hwang, M. Remskar, R. Yan, V. Protasenko, K. Tahy, S. Doo Chae, P. Zhao, A. Konar, H. Xing and A. Seabaugh. Transistors with chemically synthesized layered semiconductor WS_2 exhibiting 105 room temperature modulation and ambipolar behavior. *Applied Physics Letters* **101** (2012) 013107.

[16] Y. Yuan, R. Li and Z. Liu. Establishing water-soluble layered WS_2 nanosheet as a platform for biosensing. *Analytical chemistry* **86** (2014) 3610-3615.

[17] W. Paszkowicz, J. Pelka, M. Knapp, T. Szyszko and S. Podsiadlo. Lattice parameters and anisotropic thermal expansion of hexagonal boron nitride in the 10–297.5 K temperature range. *Applied Physics A* **75** (2002) 431-435.

[18] A. Molina-Sanchez and L. Wirtz. Phonons in single-layer and few-layer MoS_2 and WS_2. *Physical Review B* **84** (2011) 155413.

[19] E. R. Jette and F. Foote. Precision determination of lattice constants. *The Journal of Chemical Physics* **3** (1935) 605-616.

[20] F. Opoku, K. K. Govender, C. G. C. E. van Sittert and P. P. Govender. Role of MoS_2 and WS_2 monolayers on photocatalytic hydrogen production and the pollutant degradation of monoclinic $BiVO_4$: a first-principles study. *New Journal of Chemistry* **41** (2017) 11701-11713.

[21] H. M. Lee, M. Ge, B. Sahu, P. Tarakeshwar and K. S. Kim. Geometrical and electronic structures of gold, silver, and gold− silver binary clusters: Origins of ductility of gold and gold− silver alloy formation. *The Journal of Physical Chemistry B* **107** (2003) 9994-10005.

[22] J. Zhou, Q. Wang, Q. Sun and P. Jena. Electronic and magnetic properties of a BN sheet decorated with hydrogen and fluorine. *Physical Review B* **81** (2010) 085442.

[23] J. Liu, B. Cheng and J. Yu. A new understanding of the photocatalytic mechanism of the direct Z-scheme gC_3N_4/TiO_2 heterostructure. *Physical Chemistry Chemical Physics* **18** (2016) 31175-31183.

[24] Y. Yan, C. Zhang, W. Gu, C. Ding, X. Li and Y. Xian. Facile synthesis of water-soluble WS_2 quantum dots for turn-on fluorescent measurement of lipoic acid. *The Journal of Physical Chemistry C* **120** (2016) 12170-12177.

[25] N. Drummond, V. Zolyomi and V. Fal'Ko. Electrically tunable band gap in silicene. *Physical Review B* **85** (2012) 075423.

[26] C. E. Dreyer, J. L. Lyons, A. Janotti and C. G. Van de Walle. Band alignments and polarization properties of BN polymorphs. *Applied Physics Express* **7** (2014) 031001.

[27] P. Drude. Zur elektronentheorie der metalle; II. Teil. galvanomagnetische und thermomagnetische effecte. *Annalen der Physik* **308** (1900) 369-402.

[28] P. Drude. Zur elektronentheorie der metalle. *Annalen der Physik* **306** (1900) 566-613.

[29] X. Zhang, Z. Meng, D. Rao, Y. Wang, Q. Shi, Y. Liu, H. Wu, K. Deng, H. Liu and R. Lu. Efficient band structure tuning, charge separation, and visible-light response in ZrS_2-based van der Waals heterostructures. *Energy & Environmental Science* **9** (2016) 841-849.

[30] H. Li, K. Yu, C. Li, B. Guo, X. Lei, H. Fu and Z. Zhu. Novel dual-petal nanostructured WS_2@ MoS_2 with enhanced photocatalytic performance and a comprehensive first-principles investigation. *Journal of Materials Chemistry A* **3** (2015) 20225-20235.

[31] M. Ramchandani. Energy band structure of gold. *Journal of Physics C: Solid State Physics* **3** (1970) S1.

[32] Q. Wang, S. Wang, J. Dai and W. Li. First-principles study of ferromagnetism in Pd-doped and Pd-Cu-codoped BN, *IOP Conference Series: Materials Science and Engineering, IOP Publishing* **137** (2016) 012021.

[33] M. Fatmi, B. Ghebouli, M. Ghebouli and Z. Hieba. First-principles study of structural, elastic, electronic, lattice dynamic and optical properties of XN (X= Ga, Al and B) compounds under pressure. *Physica Scripta* **83** (2011) 065702.

[34] R. Garg, N. Dutta and N. Choudhury. Work function engineering of graphene. *Nanomaterials* **4** (2014) 267-300.

[35] N. A. Lanzillo, A. J. Simbeck and S. K. Nayak. Strain engineering the work function in monolayer metal dichalcogenides. *Journal of Physics: Condensed Matter* **27** (2015) 175501.

[36] F. Schulz, R. Drost, S. K. Hämäläinen, T. Demonchaux, A. P. Seitsonen and P. Liljeroth. Epitaxial hexagonal boron nitride on Ir (111): A work function template. *Physical Review B* **89** (2014) 235429.

[37] B. Singh, G. Kaur, P. Singh, K. Singh, B. Kumar, A. Vij, M. Kumar, R. Bala, R. Meena, A. Singh, A. Thakur, and A. Kumar. Nanostructured Boron Nitride With High Water Dispersibility For Boron Neutron Capture Therapy. *Scientific Reports* **6** (2016) 35535.

[38] K.-J. Huang, Y.-J. Liu, J.-T. Cao and H.-B. Wang. An aptamer electrochemical assay for sensitive detection of immunoglobulin E based on tungsten disulfide–graphene composites and gold nanoparticles. *RSC Advances* **4** (2014) 36742-36748.

[39] A. O. Osikoya, O. Parlak, N. A. Murugan, E. D. Dikio, H. Moloto, L. Uzun, A. P. Turner and A. Tiwari. Acetylene-sourced CVD-synthesised catalytically active graphene for electrochemical biosensing. *Biosensors and Bioelectronics* **89** (2017) 496-504.

[40] W. Yan, V. Petkov, S. M. Mahurin, S. H. Overbury and S. Dai. Powder XRD analysis and catalysis characterization of ultra-small gold nanoparticles deposited on titania-modified SBA-15. *Catalysis Communications* **6** (2005) 404-408.

[41] A. J. Bard, L. R. Faulkner, J. Leddy and C. G. Zoski. Electrochemical methods: fundamentals and applications. *Wiley New York* **2** (1980).

[42] P. T. Kissinger and W. R. Heineman. Cyclic voltammetry. *Journal of Chemical Education* **60** (1983) 702-706.

[43] O. Parlak, A. İncel, L. Uzun, A. P. Turner and A. Tiwari. Structuring Au nanoparticles on two-dimensional MoS_2 nanosheets for electrochemical glucose biosensors. *Biosensors and Bioelectronics* **89** (2017) 545-550.

[44] K. K. Reza, M. A. Ali, S. Srivastava, V. V. Agrawal and A. Biradar. Tyrosinase conjugated reduced graphene oxide based biointerface for bisphenol A sensor. *Biosensors and Bioelectronics* **74** (2015) 644-651.

[45] B. G. Choi, H. Park, T. J. Park, M. H. Yang, J. S. Kim, S.-Y. Jang, N. S. Heo, S. Y. Lee, J. Kong and W. H. Hong. Solution chemistry of self-assembled graphene nanohybrids for high-performance flexible biosensors. *ACS Nano* **4** (2010) 2910-2918.

[46] R. S. Nicholson. Theory and application of cyclic voltammetry for measurement of electrode reaction kinetics. *Analytical Chemistry* **37** (1965) 1351-1355.

[47] B.-Y. Chang and S.-M. Park. Electrochemical impedance spectroscopy. *Annual Review of Analytical Chemistry* **3** (2010) 207-229.

[48] M. Levi and D. Aurbach. Simultaneous measurements and modeling of the electrochemical impedance and the cyclic voltammetric characteristics of graphite electrodes doped with lithium. *The Journal of Physical Chemistry B* **101** (1997) 4630-4640.

[49] L. Alfonta, A. Bardea, O. Khersonsky, E. Katz and I. Willner. Chronopotentiometry and Faradaic impedance spectroscopy as signal

transduction methods for the biocatalytic precipitation of an insoluble product on electrode supports: routes for enzyme sensors, immunosensors and DNA sensors. *Biosensors and Bioelectronics* **16** (2001) 675-687.

[50] O. Parlak, A. Tiwari, A. P. Turner and A. Tiwari. Template-directed hierarchical self-assembly of graphene based hybrid structure for electrochemical biosensing. *Biosensors and Bioelectronics* **49** (2013) 53-62.

[51] R. Kumari, A. O. Osikoya, W. W. Anku, S. K. Shukla and P. P. Govender. Hierarchically Assembled Two-Dimensional Hybrid Nanointerfaces: A Platform for Bioelectronic Applications. *Electroanalysis* **30** (2018) 2339-2348.

Appendix A2

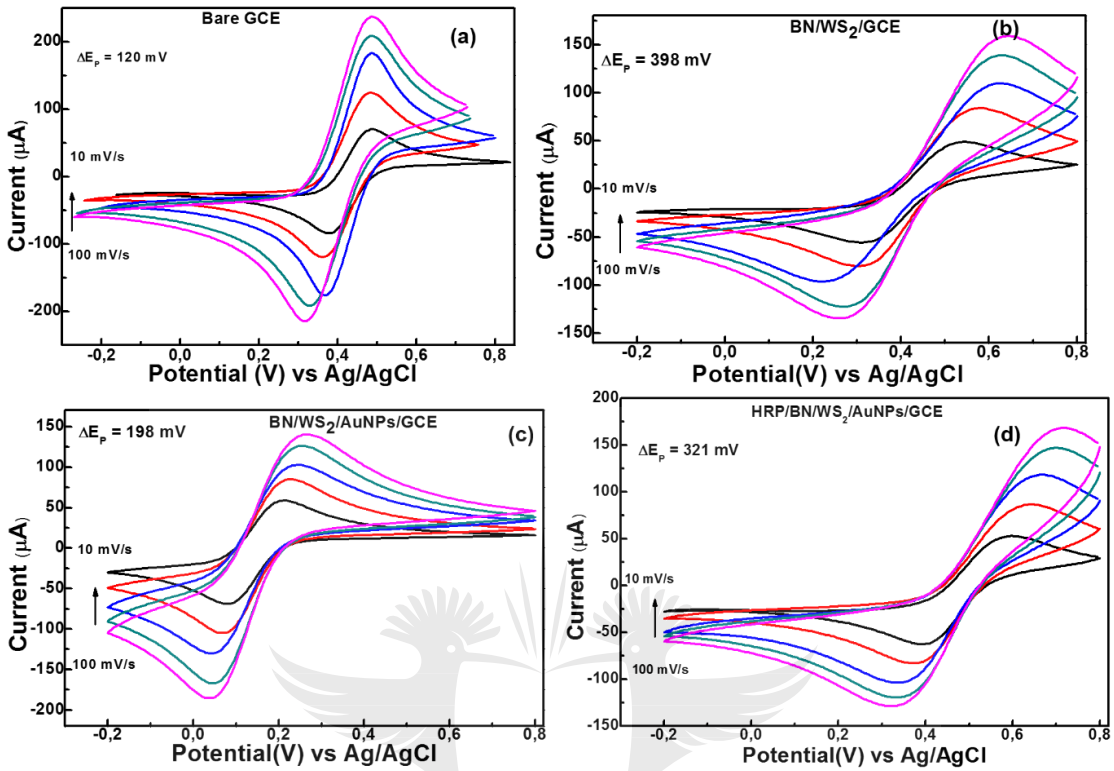

Figure A2.1 Cyclic voltammetry response showing the effect of scan rates on the cathodic peak I_{p_c}, and the anodic peak I_{p_a}, in 10 mM PBS and 10 mM KCl and 10 mM $[Fe(CN)_6^{3-/4-}]$ vs Ag/AgCl reference electrode for (a) Bare GC electrode; (b) BN/WS2/GCE; (c) BN/WS2/AuNPs/GCE; (d) BN/WS2/AuNPs/HRP/GCE respectively.

CHAPTER 6

CVD GROWN GRAPHENE ON WS_2 AND AuNPs: A TWO-DIMENSIONAL NANOHYBRID INTERFACE FOR DETECTION OF H_2O_2

6.1 INTRODUCTION

Significant attention has been given to 2D layered materials in recent years [1, 2] after the discovery of graphene in 2004 [3, 4]. These 2D layered materials have generated huge interest due to their potential for being used in diverse applications such as nanoelectronics, electrochemical sensors, photonics, and catalysis and energy storage devices [5-7].

Although graphene with its extraordinary properties is a choice material for the fabrication of novel smart and flexible devices, it however has limitation in electronic and optoelectronic applications [8-10] due to its zero band gap which then becomes a major drawback to it being used in different advanced energy and biomedical applications. This limitation of graphene has triggered more research interest toward other 2D layered materials that include conductors, semiconductors and insulators with different band gaps [2]. These broad class of 2D layered materials with tunable material properties create the possibility of fabricating novel nanohybrid structures with unique functionalities which involves the formation of graphene heterostructures [11-16].

2D layered materials could be single or multi-layered, with well-ordered 2D planar structures. The layered nanomaterials usually possess strong intralayer covalent bonding while the interactions between neighbouring layers are held by weak

The work presented in this chapter is under review in the journal Material Research Bulletin.

interlayer van der Waals forces [15, 17]. The ultrathin thickness and large surface area of these 2D nanomaterials make them suitable for the fabrication of novel nanohybrid structures with unique structural characteristics [18].

Graphene, possessing honeycomb lattice arrangement of sp^2 bonded carbon atoms with high crystallinity is reported to possess excellent thermal, mechanical and electronic properties [3, 19, 20]. Graphene has many intrinsic properties like high carrier mobility (~ 200000 $cm^2\ V^{-1}\ s^{-1}$), high specific surface area (2630 $m^2\ g^{-1}$), good mechanical strength (~ 1.0 TPa), superior thermal conductivity (between 3080 and 5150 W $m^{-1}\ K^{-1}$) and room-temperature quantum Hall effect [8, 21]. It also possesses other promising properties like good biocompatibility, good conductivity and fast electron transport rate which makes it (graphene) an excellent material for the designing of electrochemical and bioelectronics devices [7].

Besides chemical reduction and mechanical exfoliation methods, CVD technique is one of the most practical and common methods for the scalable synthesis of highly-crystalline 2D heterostacks and high-quality 2D materials with thicknesses from a single to few atomic layers [22, 23].

Inorganic 2D layered materials are generally, TMDs with general formula MX_2 where M is a transition metal of groups 4-10 (typically Mo, Nb, W, Ni, V, or Re) and X represents the chalcogen atom (typically S, Se or Te), M is sandwiched between two chalcogen atom layers in which each monolayer has thickness of about 6-7 Å [24, 25]. They involve van der Waals interactions between adjacent sheets with strong covalent bonding within each sheet.

Based on the co-ordination and oxidation state of the metal atoms, TMDs are classified either as semiconductors such as WS_2 [26], MoS_2 [27], tungsten diselenide (WSe_2), molybdenum diselenide ($MoSe_2$), or as semimetals such as tungsten ditelluride (WTe_2), titanium diselenide ($TiSe_2$) [6] or as metals such as vanadium diselenide (VSe_2) etc. [2, 25]. These materials are mostly newly developed and have been reported to be useful in a wide range of potential applications in past few years, but there is a need for more extensive investigation into their properties and applications [2, 15, 28]. These layered materials can either be synthesized through exfoliation methods [29, 30] or by using CVD technique [31, 32].

2D TMD nanomaterials have been reported to have the ability to enhance interfacial electron transfer properties and are consequently quite useful in the fabrication of efficient and highly sensitive nano bioelectronic devices. An emerging trend in device fabrication is the use of novel hybrid materials involving the combination of graphene, 2D TMDs and other nanostructured materials in the design and fabrication of smart nano bioreactors for environmental and health applications [33-35].

One of the inorganic-layered materials, WS_2 has been reported to have excellent properties with wide band gap and lower defect density than graphene which makes it a very promising material for electrochemical applications [36-38]. Layered WS_2 nanosheets consist of S–W–S sandwich structures that are stacked vertically with interplanar van der Waals interactions [37], good intrinsic electric conductivity and good theoretical specific capacity. Due to these properties, it is used as an electrode

material for lithium-ion batteries, as a semiconducting material for field-effect transistors and as an electrode material in bioelectronics devices [38-40].

WS_2 has received great attention in the field of energy storage and hydrogen evolution catalysis [41, 42] although it is still in the very initial stage in the field of biosensors [43].

The WS_2 nanocomposites along with graphene have been used as an active material for improving the performance of electrochemical sensors [42, 43, 45, 46]. Consequently, the interaction between WS_2 with other 2D materials can offer further prospects in designing devices with greater efficiency, stability and sensitivity [6, 11, 44, 47, 48]. It has been reported that the combination of tailored heterostructures involving graphene and WS_2 has led to the fabrication of new field effect transistors [42].

The stable and conductive nanointerfaces of hybrid structure involving WS_2 and graphene has been studied and reported to be useful for the electrochemical detection of DNA [47], and also for the simultaneous determination of hydroquinone, catechol and resorcinol [45]. Similarly, detection by layered WS_2 nanosheet/AuNPs nanocomposites has extended to other analytes, such as H_2O_2 where WS_2/Au act as an efficient electrobiocatalytic platform [11].

The incorporation of AuNPs on the surface of TMD materials have been reported to lead to improved sensing performance as observed in the enhancement of current response in their electrochemical signals [49].

In this chapter, CVD-synthesized graphene has been successfully combined with WS_2 (Gr/WS_2) to fabricate a novel H_2O_2 electrochemical biosensor. HRP enzyme

was immobilized on Gr/WS_2/AuNPs for sensing of H_2O_2. These self-assembled structures were characterized using XRD for structural properties. Electrochemical characterization and electrocatalytic activity of the modified bioelectrodes were explored through CV, EIS and chronoamperometry.

6.2 EXPERIMENTAL

6.2.1 Apparatus

Electrochemical measurements were performed on a Bio-logic SP-300 electrochemical workstation potentiostat connected to a data controller.

XRD patterns were recorded on a Bruker D8 Advance X-ray diffractometer operating at 20 kV using Cu-Kα radiation (kα ~ 0.1542 nm). The measurements were performed over a diffraction angle range of 2θ=10° to 70° and data analysis was done by X'pert XRD software.

6.2.2 Preparation of CVD-synthesized Graphene

The synthesis procedure for acetylene-sourced CVD grown graphene was discussed in section 3.6.1.1.

6.2.3 Fabrication of graphene-WS_2-enzyme self-assembled nanohybrid structures

The detailed preparation method was elaborated in section 3.6.1.2.

6.2.4 Preparation of modified bioelectrodes

The preparation of bioelectrodes was explained in section 3.6.1.3.

6.3 RESULTS AND DISCUSSION

Scheme 6.1 demonstrates the general method for the structuring of the AuNPs on CVD grown graphene and WS_2 nanosheets and HRP based nanohybrid structure for electrobiocatalytic detection of H_2O_2 at the interface.

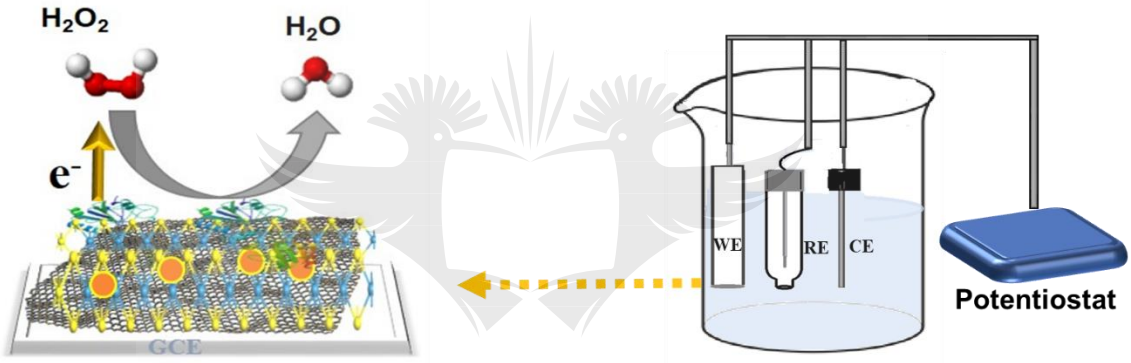

Scheme 6.1 Schematic representation of AuNPs structuring on a CVD grown graphene and WS_2 interface and electron transfer process in the Gr/WS_2/AuNPs/HRP nanohybrid structure on the glassy carbon electrode in an electrochemical cell which is connected to a potentiostat. (Note: Scheme not drawn to scale)**.**

To determine the crystallinity of the sample, XRD analysis was performed on Gr/WS_2/AuNPs nanohybrid structure which had been prepared by dispersing 1000 µL of the composite solution of graphene, WS_2 and gold nanoparticles on silica disk for XRD experiment.

An XRD pattern for the Gr/WS_2/AuNPs sample is presented in Figure 6.1. It was observed that the diffraction peaks of WS_2 centered at 2θ=14.2°, 31.7°, 33.3°, 45.4°,

50.4°, 66.2° which corresponds to (002), (004), (100), (105) and (114) planes of WS_2 (JCPDS No. 37-1492) respectively [50-52]. Two diffraction peaks centered at 26.5° and 44.8° corresponding to (002) and (101) planes of graphene were also observed [22] and two other diffraction peaks at 38.1° and 45.4° corresponding to (111) and (200) planes of gold [53]. XRD results revealed the presence of all the elements of Gr/WS_2/AuNPs nanocomposites.

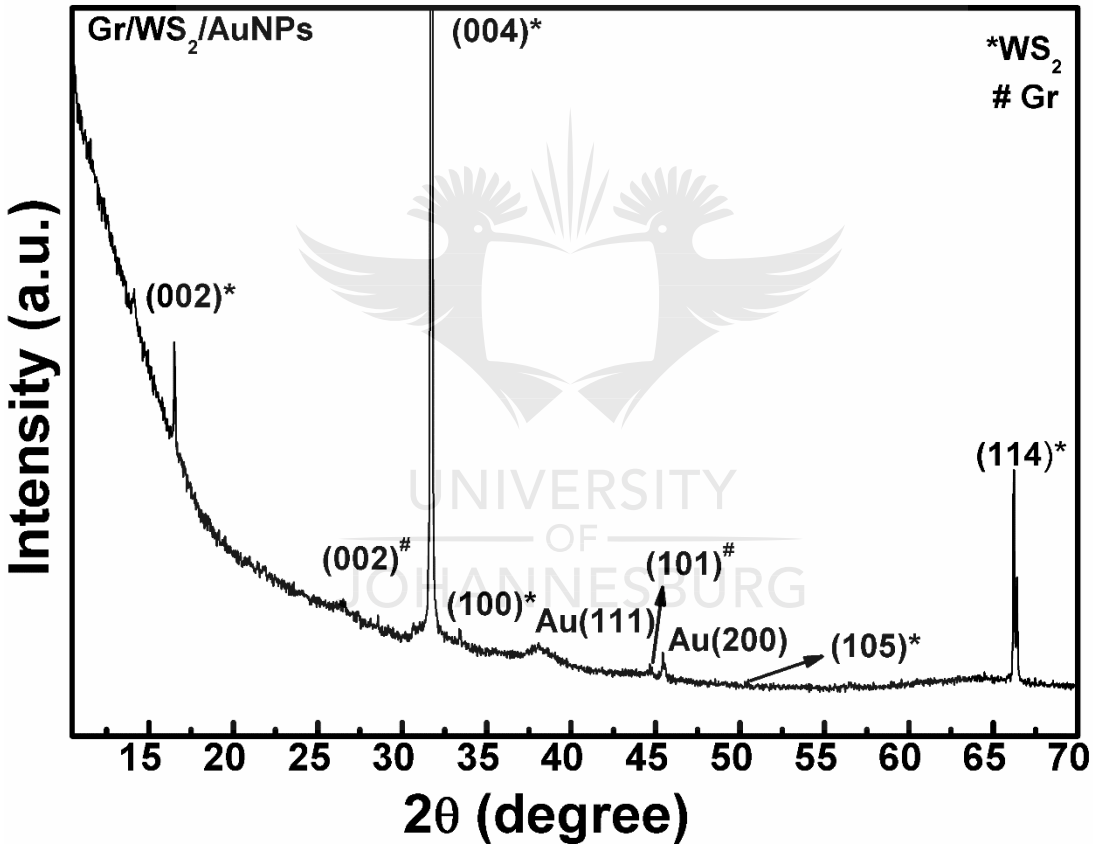

Figure 6.1 XRD spectra for Gr/WS_2/AuNPs nanointerface structure where * and # denote WS_2 and Gr peaks respectively.

Figure 6.2 (I) presents the CV of bare GCE (a), Gr/GCE (b), Gr/WS_2/HRP/GCE (c), and Gr/WS_2/HRP/AuNPs/GCE in 5.0 mM $[Fe(CN)_6]^{3-/4-}$ solution containing 0.1 M

PBS and 0.1 M KCl. The figure showed typical pair of well-defined reversible redox peaks of the probes with different peak-to-peak potential separation.

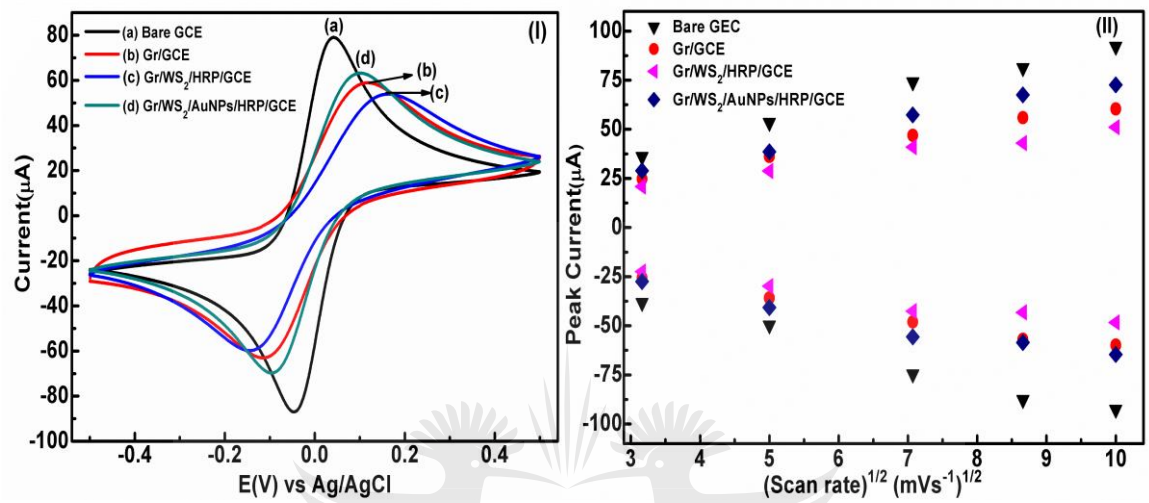

Figure 6.2 Bioelectrode characterization showing (I) CV responses ; (II) The effect of scan rates on the cathodic (I_{p_c}) and anodic peaks (I_{p_a}) of bare and all modified electrodes at 50 mV/s vs. Ag/AgCl reference electrode in 5 mM $[Fe(CN)_6]^{3-/4-}$ containing 0.1 M PBS and 0.1 M KCl.

The CV responses of $[Fe(CN)_6]^{3-/4-}$ in 0.1 M PBS and 0.1 M KCl supporting electrolyte for the bare GCE and all modified electrodes were studied at the scan rate of 50 mV/s and the result is presented in Figure 6.2 (I). It can be seen that a pair of redox peaks with I_{p_a} of 82.8 µA and I_{p_c} of −77.4 µA appear at the bare GCE (curve a) with 90 mV ΔE_p which indicated fast electron transfer between electrode and redox probe. The peak currents of the Gr/GCE (curve b, I_{p_a} 51.5 µA and I_{p_c}−50.0 µA) decreased from bare GCE since immobilization of CVD grown Gr nanosheets occurred and there was an increase in ΔE_p (229.1 mV). The lowest redox peaks (I_{p_a}, 48.1 µA and I_{p_c}−35.1 µA) at the Gr/WS2/HRP/GCE (curve c)

indicate that with the introduction of HRP to Gr/WS_2 decreased the peak currents of $[Fe(CN)_6]^{3-/4-}$. Also the value of ΔE_p for Gr/WS_2/HRP/GCE increased as compared with bare GCE and Gr/GCE. This could be ascribed to the insulating effect of immobilized enzyme (HRP) on Gr/WS_2, which slowed the electrochemical response. With the introduction of AuNPs to HRP immobilized Gr/WS_2/GCE, peak current (curve c, I_{p_a} 54.0 µA and I_{p_c} −50.1 µA) was increased as compared to Gr/GCE (curve b) and Gr/WS_2/HRP/GCE (curve c). The peak to peak potential ΔE_p (194.8 mV) was observed to decrease. The amplification of current and decrease of ΔE_p value was due to the integration of AuNPs which has properties such as large surface area and good electronic conductivity.

Figure 6.2 (II) shows the effect of scan rate on the anodic and cathodic peak currents at the bare GCE (a), Gr/GCE (b), Gr/WS_2/HRP/GCE (c), and Gr/WS_2/HRP/AuNPs/GCE. As shown in Figure 6.2 (II), the anodic and cathodic peak currents of the bare and all the modified electrodes increase linearly with increase in scan rate from 10 to 100 mV s^{-1} and the results are presented in Figure A3.1 (a-d) Appendix A3. The oxidation and reduction peak currents are directly proportional to the square root of scan rate, indicating a diffusion controlled electrode process based on following Randles-Sevcik equation (6.1) [54]:

$$I_p = 2.69\, x10^{-5}\, AD^{1/2}n^{3/2}\gamma^{1/2}C \quad \text{.....(6.1)}$$

Here, n is the number of electrons participating in the redox reaction, D is the diffusion coefficient of the ions, C is the concentration of the probe molecule in the solution (mol/dm^3), and γ is the scan rate ($V \cdot s^{-1}$).

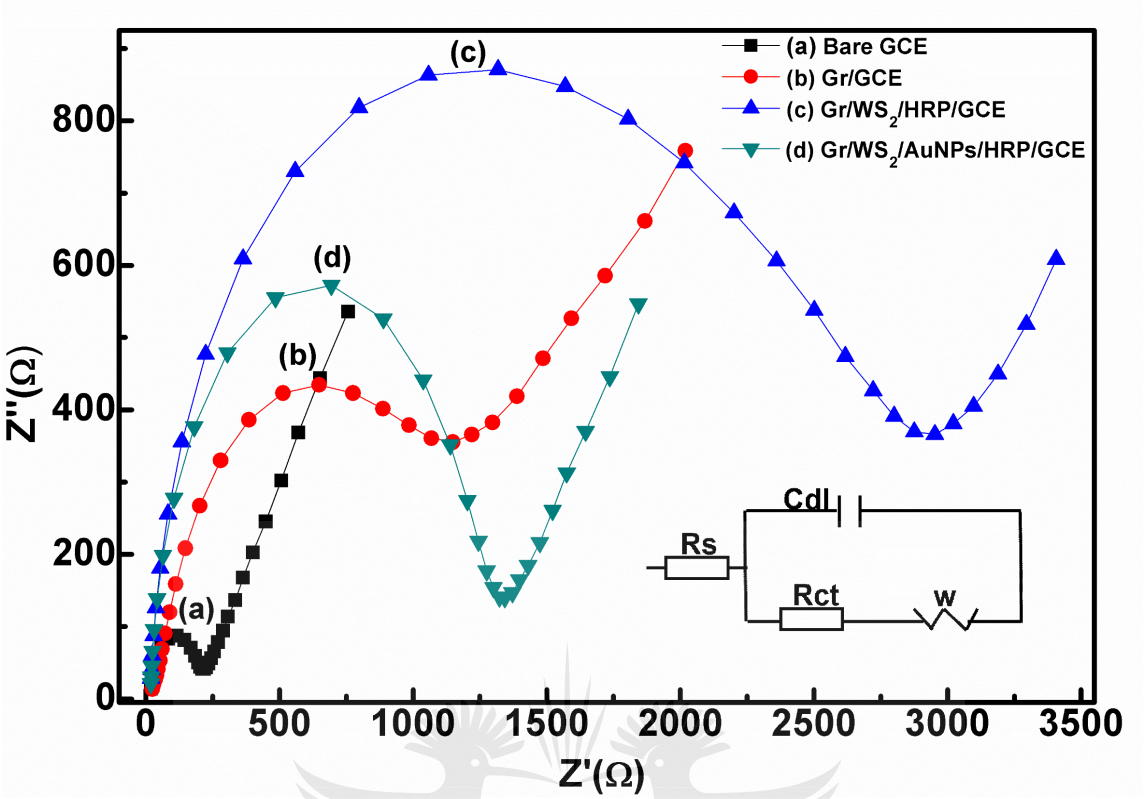

Figure 6.3 EIS's Nyquist plots for the bare GC and all modified electrodes at 50 mV/s vs. Ag/AgCl reference electrode in 5 mM $[Fe(CN)_6]^{3-/4-}$ containing 0.1 M PBS and 0.1 M KCl. The inset is the equivalent of Randles circuit which is used to fit the data.

EIS is a useful technique for probing the charge transfer properties of modified electrodes. Figure 6.3 shows EIS's Nyquist plot for all modified electrodes in 5 mM $[Fe(CN)_6]^{3-/4-}$ in 0.1 M PBS and 0.1 M KCl. The data of impedance outputs were fit by Randles equivalent circuit (inset, Figure 6.3) [55]. The Nyquist plot contains a semi-circular portion and a linear portion. This indicates that both electron transfer limited process and diffusion controlled process occurred simultaneously. The charge transfer resistance [2] (R_{ct}) at the electrode surface can be calculated based on the diameter of the semi-circular part of the plot. It is observed that the R_{ct} of bare GCE was about 0.09 kΩ (curve, a). When dispersed graphene sheet was immobilized on the bare GC electrode, the value of R_{ct} increased to 0.79 kΩ (curve,

b), thus indicating that the immobilization of graphene on GCE caused a slight increase in charge transfer resistance due to kinetics. When the enzyme (HRP) is immobilized on Gr/WS_2/GCE, the value of R_{ct} increase to 2.1 kΩ (curve, c) which shows that the presence of HRP causes an increase in electron transfer resistance R_{ct} in the redox probe ($[Fe(CN)_6]^{3-/4-}$). This phenomenon may be attributed to the insulating effect of HRP that restrict the interfacial electron transfer [12]. When AuNPs are further introduced at Gr/WS_2/HRP/GCE, the value of R_{ct} decreased to 1.2 kΩ (curve, d) as compared to Gr/WS_2/HRP/GCE which indicates that the presence of AuNPs facilitates electron transfer at electrode surface. These phenomena is consistent with the observations in the CV experiment results (Figure 6.2 (I)).

The electrocatalytic activity of the fabricated Gr/HRP, Gr/WS_2/HRP and Gr/WS_2/AuNPs/HRP interface system towards the reduction of H_2O_2 in PBS (0.1 M, pH = 7.4) and 0.1 M KCl was evaluated using chronoamperometric technique and the results presented in Figure 6.4 [(a1, a2), (b1, b2) and (c1, c2)] respectively.

Chronoamperometric experiment was carried out at a constant potential of +0.7 V versus Ag/AgCl in 0.1 M PBS. The chronoamperometric response for the Gr/HRP modified electrodes to the successive addition of H_2O_2 in 0.1 M PBS (pH 7.4) and at an applied potential of +0.7 V is presented in Figure 6.4 (a1), while the corresponding calibration curve is presented in Figure 6.4 (a2). It was observed that there is a stepwise increase in current response of Gr/HRP/GCE modified electrode with the successive addition of H_2O_2 (in Figure 6.4 (a1)). The catalytic current display a linear relationship to H_2O_2 concentration in a range from 0.27 mM to 29.1 mM, a sensitivity of 6.06 μA/mM/cm^2 and the LoD was calculated to be 2.8 mM.

Chronoamperometry experiment was also done using Gr/WS_2/HRP/GC fabricated modified electrode, the results are presented in Figure 6.4 (b1-b2) (Current-time and calibration curves) respectively. The fabricated Gr/WS_2/HRP/GCE showed a linear response from 0.32- 20 mM H_2O_2 concentration with a sensitivity of 9.23 µA/mM/cm^2 (R^2= 0.999) and a detection limit of 2.06 mM based on S/N = 3.

The typical amperometric response for the modified electrode containing Gr/WS_2, AuNPs and HRP immobilized electrode (Gr/WS_2/AuNPs/HRP/GCE) exhibited higher current response per unit analyte added as compared to Gr/WS_2/HRP/GCE (without AuNPs) as shown in Figure 6.4 (c1) while the corresponding calibration curve was presented in Figure 6.4 (c2). This increase of performance may be ascribed to the homogenous assembly of AuNPs on the surface modified electrode leading to increased surface area which favour electron transfer. The sensitivity and detection limit of Gr/WS_2/AuNPs/HRP/GCE were 11.07 µA/mM/cm^2 and 3.23 mM (S/N=3), respectively. Accordingly, Gr/WS_2/AuNPs/HRP/GC electrode provided good catalytic performance for the detection of H_2O_2 over a relatively wider linear range (0.40 mM to 23 mM), higher sensitivity than Gr/WS_2/HRP/GCE as listed in Table 6.1.

Table 6.1 Summary of electrobiocatalytic responses of differently modified bioelectrodes with H_2O_2 stepwise additions

	Gr/HRP/GCE	Gr/WS_2/HRP/GCE	Gr/WS_2/AuNPs/HRP/GCE
LoD	2.8	2.06	3.23
Linear range (mM)	1.57 – 11.33	0.32 - 20	0.40-23
Sensitivity (μA/mM/cm^2)	6.06	9.23	11.07
Regression (R^2)	0.975	0.999	0.940

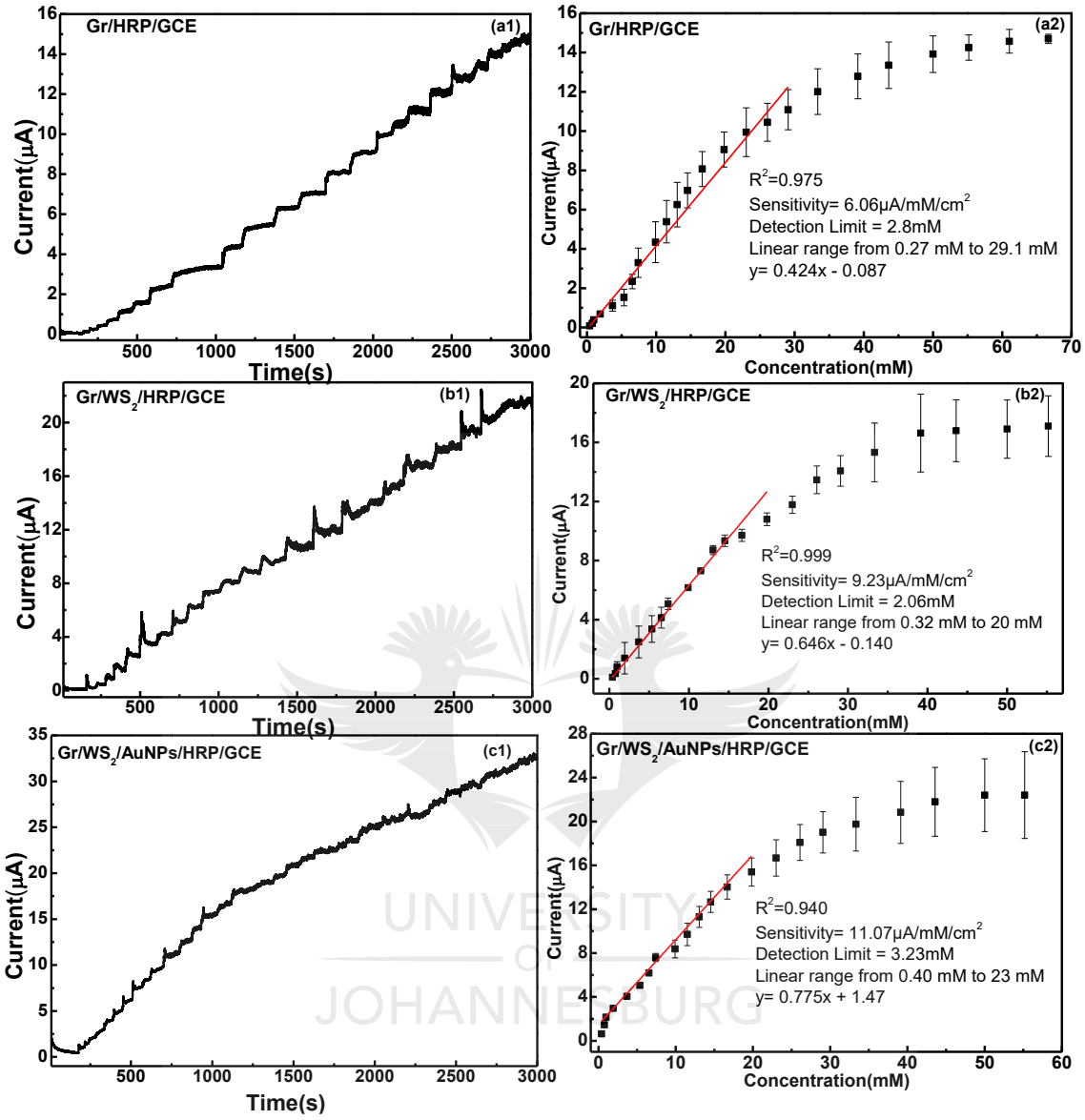

Figure 6.4 Chronoamperometry response showing current-time plot at an applied potential of +0.7 V in 0.1 M PBS and 0.1 M KCl and calibration curve for the chronoamperometric response for fabricated Gr/HRP/GCE (a1, a2), Gr/WS_2/HRP/GCE (b1, b2) and Gr/WS_2/AuNPs/HRP/GCE (c1, c2) nanohybrid structures.

6.4 SUB-CONCLUSION

In this study, CVD graphene based nanohybrid interfaces including WS_2, and nano structuring with AuNPs have been successfully fabricated which is followed by immobilization of HRP by self-assembled method. Few-layer graphene was

synthesized by CVD method and then combined with other 2D materials WS_2. The XRD results revealed that the Gr/WS_2/AuNPs nanohybrid interface was crystalline in nature. Electrochemical characterizations of modified Gr/WS_2 based interface structure indicated that this novel nanostructured hybrid interface material can be applied in the design, fabrication and development of flexible, thin, smart and highly sensitive bioelectronics and biosensing devices.

6.5 REFERENCES

[1] X. Huang, Z. Zeng and H. Zhang. Metal dichalcogenide nanosheets: preparation, properties and applications. *Chemical Society Reviews* **42** (2013) 1934-1946.

[2] M. Chhowalla, H. S. Shin, G. Eda, L. J. Li, K. P. Loh and H. Zhang. The chemistry of two-dimensional layered transition metal dichalcogenide nanosheets. *Nature Chemistry* **5** (2013) 263-275.

[3] K. S. Novoselov, A. K. Geim, S. V. Morozov, D. Jiang, Y. Zhang, S. V. Dubonos, I. V. Grigorieva and A. A. Firsov. Electric field effect in atomically thin carbon films. *Science* **306** (2004) 666-669.

[4] K. Novoselov, D. Jiang, F. Schedin, T. Booth, V. Khotkevich, S. Morozov and A. Geim. Two-dimensional atomic crystals. *Proceedings of the National Academy of Sciences of the United States of America* **102** (2005) 10451-10453.

[5] J. Wan, S. D. Lacey, J. Dai, W. Bao, M. S. Fuhrer and L. Hu. Tuning two-dimensional nanomaterials by intercalation: materials, properties and applications. *Chemical Society Reviews* **45** (2016) 6742-6765.

[6] P. Bollella, G. Fusco, C. Tortolini, G. Sanzo, G. Favero, L. Gorton and R. Antiochia. Beyond graphene: Electrochemical sensors and biosensors for biomarkers detection. *Biosensors and Bioelectronics* **89** (2017) 152-166.

[7] B. Radisavljevic, A. Radenovic, J. Brivio, i. V. Giacometti and A. Kis. Single-layer MoS_2 transistors. *Nature Nanotechnology* **6** (2011) 147-150.

[8] V. Singh, D. Joung, L. Zhai, S. Das, S. I. Khondaker and S. Seal. Graphene based materials: Past, present and future. *Progress in Materials Science* **56** (2011) 1178-1271.

[9] D. Jariwala, V. K. Sangwan, L. J. Lauhon, T. J. Marks and M. C. Hersam. Emerging device applications for semiconducting two-dimensional transition metal dichalcogenides. *ACS Nano* **8** (2014) 1102-1120.

[10] D. Akinwande, N. Petrone and J. Hone. Two-dimensional flexible nanoelectronics. *Nature Communication* **5** (2014) 5678.

[11] O. Parlak, P. Seshadri, I. Lundström, A. P. Turner and A. Tiwari. Two-Dimensional Gold-Tungsten Disulphide Bio-Interface for High-Throughput Electrocatalytic Nano-Bioreactors. *Advanced Materials Interfaces* **1** (2014) 1400136.

[12] H. Song, Y. Ni and S. Kokot. Investigations of an electrochemical platform based on the layered MoS_2–graphene and horseradish peroxidase nanocomposite for direct electrochemistry and electrocatalysis. *Biosensors and Bioelectronics* **56** (2014) 137-143.

[13] A. Azizi, S. Eichfeld, G. Geschwind, K. Zhang, B. Jiang, D. Mukherjee, L. Hossain, A. F. Piasecki, B. Kabius and J. A. Robinson. Freestanding van der Waals heterostructures of graphene and transition metal dichalcogenides. *ACS Nano* **9** (2015) 4882-4890.

[14] M. Xu, T. Liang, M. Shi and H. Chen. Graphene-like two-dimensional materials. *Chemical Reviews* **113** (2013) 3766-3798.

[15] Y. Liu, N. O. Weiss, X. D. Duan, H. C. Cheng, Y. Huang and X. F. Duan. Van der Waals heterostructures and devices. *Nature Reviews Materials* **1** (2016) 16042.

[16] C. Zhu, D. Du and Y. Lin. Graphene-like 2D nanomaterial-based biointerfaces for biosensing applications. *Biosensors and Bioelectronics* **89** (2017) 43-55.

[17] G. Yang, C. Zhu, D. Du, J. Zhu and Y. Lin. Graphene-like two-dimensional layered nanomaterials: applications in biosensors and nanomedicine. *Nanoscale* **7** (2015) 14217-14231.

[18] D. Chimene, D. L. Alge and A. K. Gaharwar. Two-dimensional nanomaterials for biomedical applications: emerging trends and future prospects. *Advanced Materials* **27** (2015) 7261-7284.

[19] C. Mattevi, G. Eda, S. Agnoli, S. Miller, K. A. Mkhoyan, O. Celik, D. Mastrogiovanni, G. Granozzi, E. Garfunkel and M. Chhowalla. Evolution of electrical, chemical, and structural properties of transparent and conducting chemically derived graphene thin films. *Advanced Functional Materials* **19** (2009) 2577-2583.

[20] A. K. Geim and K. S. Novoselov. The rise of graphene. *Nature materials* **6** (2007) 183-191.

[21] Y. Zhang, Y.-W. Tan, H. L. Stormer and P. Kim. Experimental observation of the quantum Hall effect and Berry's phase in graphene. *Nature* **438** (2005) 201-204.

[22] A. O. Osikoya, O. Parlak, N. A. Murugan, E. D. Dikio, H. Moloto, L. Uzun, A. P. Turner and A. Tiwari. Acetylene-sourced CVD-synthesised catalytically active graphene for electrochemical biosensing. *Biosensors and Bioelectronics* **89** (2017) 496-504.

[23] C. Mattevi, H. Kim and M. Chhowalla. A review of chemical vapour deposition of graphene on copper. *Journal of Materials Chemistry* **21** (2011) 3324-3334.

[24] M. Osada and T. Sasaki. Two-dimensional dielectric nanosheets: novel nanoelectronics from nanocrystal building blocks. *Advanced Materials* **24** (2012) 210-228.

[25] J. A. Wilson and A. Yoffe. The transition metal dichalcogenides discussion and interpretation of the observed optical, electrical and structural properties. *Advances in Physics* **18** (1969) 193-335.

[26] H. Zeng, G.-B. Liu, J. Dai, Y. Yan, B. Zhu, R. He, L. Xie, S. Xu, X. Chen and W. Yao. Optical signature of symmetry variations and spin-valley coupling in atomically thin tungsten dichalcogenides. *Scientific Reports* **3** (2013) 1608.

[27] H. J. Conley, B. Wang, J. I. Ziegler, R. F. Haglund Jr, S. T. Pantelides and K. I. Bolotin. Bandgap engineering of strained monolayer and bilayer MoS_2. *Nano Letters* **13** (2013) 3626-3630.

[28] M. Chhowalla, D. Jena and H. Zhang. Two-dimensional semiconductors for transistors. *Nature Reviews Materials* **1** (2016) 16052.

[29] V. Nicolosi, M. Chhowalla, M. G. Kanatzidis, M. S. Strano and J. N. Coleman. Liquid Exfoliation of Layered Materials. *Science* **340** (2013) 1226419.

[30] H. Li, G. Lu, Y. Wang, Z. Yin, C. Cong, Q. He, L. Wang, F. Ding, T. Yu and H. Zhang. Mechanical Exfoliation and Characterization of Single-and Few-Layer Nanosheets of WSe_2, TaS_2, and $TaSe_2$. *Small* **9** (2013) 1974-1981.

[31] J. Yu, J. Li, W. Zhang and H. Chang. Synthesis of high quality two-dimensional materials via chemical vapor deposition. *Chemical science* **6** (2015) 6705-6716.

[32] Y. Zhang, Y. Zhang, Q. Ji, J. Ju, H. Yuan, J. Shi, T. Gao, D. Ma, M. Liu and Y. Chen. Controlled growth of high-quality monolayer WS_2 layers on sapphire and imaging its grain boundary. *ACS Nano* **7** (2013) 8963-8971.

[33] A. K. Geim and I. V. Grigorieva. Van der Waals heterostructures. *Nature* **499** (2013) 419-425.

[34] H. Ramakrishna Matte, A. Gomathi, A. K. Manna, D. J. Late, R. Datta, S. K. Pati and C. Rao. MoS_2 and WS_2 analogues of graphene. *Angewandte Chemie International Edition* **49** (2010) 4059-4062.

[35] J. Li, N. V. Medhekar and V. B. Shenoy. Bonding charge density and ultimate strength of monolayer transition metal dichalcogenides. *The Journal of Physical Chemistry C* **117** (2013) 15842-15848.

[36] C. Tan and H. Zhang. Two-dimensional transition metal dichalcogenide nanosheet-based composites. *Chemical Society Reviews* **44** (2015) 2713-2731.

[37] X. Chia, A. Y. S. Eng, A. Ambrosi, S. M. Tan and M. Pumera. Electrochemistry of nanostructured layered transition-metal dichalcogenides. *Chemical Reviews* **115** (2015) 11941-11966.

[38] M. Pumera and A. H. Loo. Layered transition-metal dichalcogenides (MoS_2 and WS_2) for sensing and biosensing. *TrAC Trends in Analytical Chemistry* **61** (2014) 49-53.

[39] D. Chen, G. Ji, B. Ding, Y. Ma, B. Qu, W. Chen and J. Y. Lee. In situ nitrogenated graphene–few-layer WS_2 composites for fast and reversible Li^+ storage. *Nanoscale* **5** (2013) 7890-7896.

[40] Y. Niu, R. Zou, H. A. Yones, X. Li, X. Li, X. Niu, Y. Chen, P. Li and W. Sun. Electrochemical behavior of horseradish peroxidase on WS_2 nanosheet-modified electrode and electrocatalytic investigation. *Journal of the Chinese Chemical Society* **65** (2018) 1127-1135.

[41] D. Voiry, H. Yamaguchi, J. Li, R. Silva, D. C. B. Alves, T. Fujita, M. Chen, T.Asefa, V. B. Shenoy, G. Eda and M. Chhowalla. Enhanced catalytic activity

in strained chemically exfoliated WS_2 nanosheets for hydrogen evolution. *Nature Material*s **12** (2013) 850-855.

[42] T . Georgiou, R. Jalil, B. D. Belle, L. Britnell, R. V. Gorbachev, S. V. Morozov, Y. -J. Kim, A. Gholinia, S. J Haigh, O. Makarovsky, L. Eaves, L. A. Ponomarenko, A. K. Geim, K. S. Novoselov and A. Mishchenko. Vertical field-effect transistor based on graphene-WS_2 heterostructures for flexible and transparent electronics. *Nature Nanotechnolgy* **8** (2013) 100-103.

[43] Y. Yuan, R. Li and Z. Liu. Establishing water-soluble layered WS_2 nanosheet as a platform for biosensing. *Analytical Chemistry* **86** (2014) 3610-3615.

[44] X. Huang, C. Tan, Z. Yin and H. Zhang. 25th anniversary article: hybrid nanostructures based on two-dimensional nanomaterials. *Advanced Materials* **26** (2014) 2185-2204.

[45] K.-J. Huang, L. Wang, Y.-J. Liu, T. Gan, Y.-M. Liu, L.-L. Wang and Y. Fan. Synthesis and electrochemical performances of layered tungsten sulfide-graphene nanocomposite as a sensing platform for catechol, resorcinol and hydroquinone. *Electrochimica Acta* **107** (2013) 379-387.

[46] N. Rohaizad, C. C. Mayorga-Martinez, Z. k. Sofer and M. Pumera. 1T-Phase Transition Metal Dichalcogenides (MoS_2, $MoSe_2$, WS_2, and WSe_2) with Fast Heterogeneous Electron Transfer: Application on Second-Generation Enzyme-Based Biosensor. *ACS Applied Materials & Interfaces* **9** (2017) 40697-40706.

[47] K.-J. Huang, Y.-J. Liu, H.-B. Wang, T. Gan, Y.-M. Liu and L.-L. Wang. Signal amplification for electrochemical DNA biosensor based on two-dimensional

graphene analogue tungsten sulfide–graphene composites and gold nanoparticles. *Sensors and Actuators B: Chemical* **191** (2014) 828-836.

[48] O. Parlak, A. İncel, L. Uzun, A. P. Turner and A. Tiwari. Structuring Au nanoparticles on two-dimensional MoS_2 nanosheets for electrochemical glucose biosensors. *Biosensors and Bioelectronics* **89** (2017) 545-550.

[49] A. Chen and S. Chatterjee. Nanomaterials based electrochemical sensors for biomedical applications. *Chemical Society Reviews* **42** (2013) 5425-5438.

[50] J. Yang, D. Voiry, S. J. Ahn, D. Kang, A. Y. Kim, M. Chhowalla and H. S. Shin. Two-dimensional hybrid nanosheets of tungsten disulfide and reduced graphene oxide as catalysts for enhanced hydrogen evolution. *Angewandte Chemie* **125** (2013) 13996-13999.

[51] X. Mao, Y. Xu, Q. Xue, W. Wang and D. Gao. Ferromagnetism in exfoliated tungsten disulfide nanosheets. *Nanoscale Research Letters* **8** (2013) 430.

[52] Y. Cheng, J. Peng, B. Xu, H. Yang, Z. Luo, H. Xu, Z. Cai and J. Weng. Passive Q-switching of a diode-pumped Pr: $LiYF_4$ visible laser using WS_2 as saturable absorber. *IEEE Photonics Journal* **8** (2016) 1-6.

[53] H.-L. Shuai, K.-J. Huang and Y.-X. Chen A layered tungsten disulfide/acetylene black composite based DNA biosensing platform coupled with hybridization chain reaction for signal amplification, *Journal of Materials Chemistry B*, **4** (2016) 1186-1196.

[54] M. A. Uppal, A. Kafizas, M. B. Ewing and I. P. Parkin. The room temperature formation of gold nanoparticles from the reaction of cyclohexanone and auric acid; a transition from dendritic particles to compact shapes and nanoplates. *Journal of Materials Chemistry A* **1** (2013) 7351-7359.

[55] A. J. Bard, L. R. Faulkner, J. Leddy and C. G. Zoski. Electrochemical methods: fundamentals and applications. *Wiley New York* (1980).

[56] B.-Y. Chang and S.-M. Park. Integrated description of electrode/electrolyte interfaces based on equivalent circuits and its verification using impedance measurements. *Analytical Chemistry* **78** (2006) 1052-1060.

APPENDIX A3

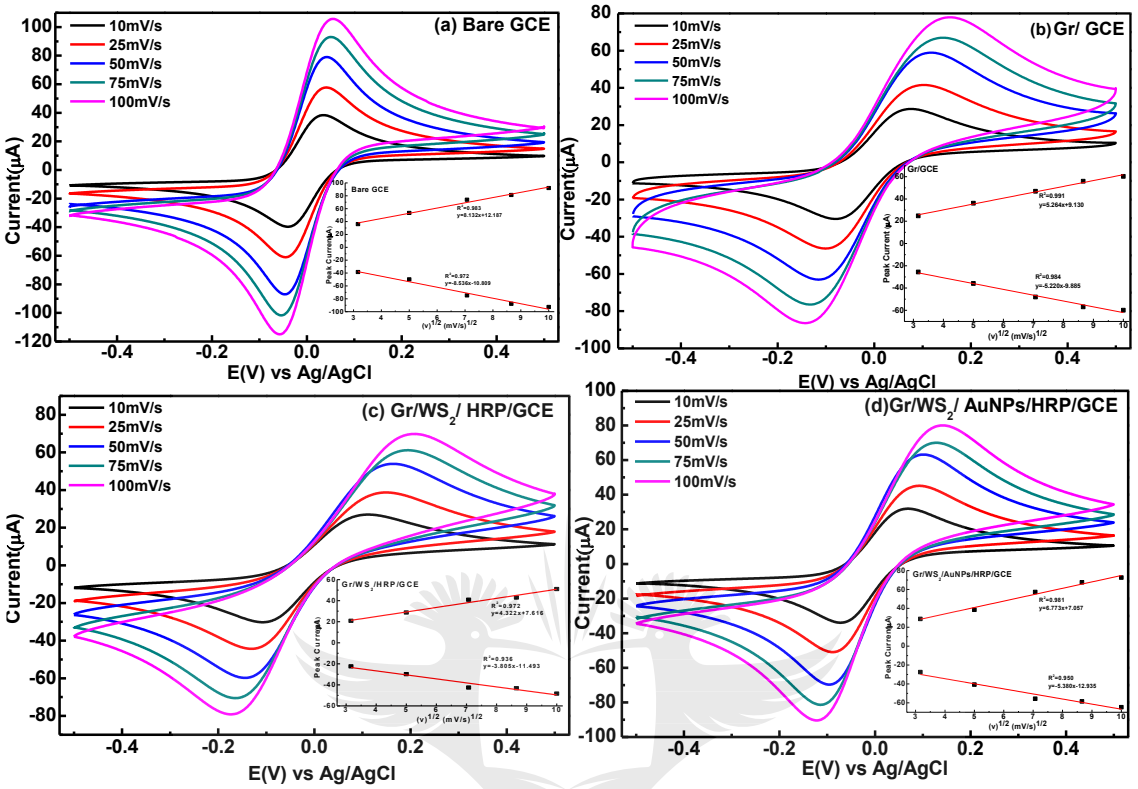

Figure A3.1 Cyclic voltammetry response showing the effect of scan rates on the cathodic peak I_{p_c}, and the anodic peak I_{p_a}, in 0.1 M PBS and 0.1 M KCl and 5 mM $[Fe(CN)_6^{3-/4-}]$ vs Ag/AgCl reference electrode for (a) bare GC electrode; (b) Gr/GCE; (c) Gr/WS_2/HRP/GCE; (d) Gr/WS_2/AuNPs/HRP/GCE respectively.

CHAPTER 7

CONCLUSION AND FUTURE PERSPECTIVES

This research study has successfully combined dual 2D hybrid layered structures using different 2D materials (Gr, MoS_2, BN and WS_2) then doped the layered structure with metal nanoparticles (AuNPs), followed by the immobilization of bio-recognition element (HRP) using a self-assembled procedure. This has led to the fabrication of novel electrode interface materials with very high surface areas coupled with the excellent electron transport properties which was facilitated by the presence of these 2D materials.

The electrobiocatalytic activities of the fabricated 2D nanointerface platforms were evaluated by using H_2O_2 as a model analyte throughout the study.

It has been found that the hierarchically self-assembled 2D nanointerface structures showed good electrocatalytic properties for detection of H_2O_2. The AuNPs incorporated into the 2D nanohybrid structure further endowed the nanohybrid with good electron transfer properties leading to the efficient electrocatalytic properties of the fabricated nanohybrid structures.

A theoretical study using DFT calculations indicated that the observed increase in electrobiocatalytic performance was due to the synergistic effects of the dual 2D hybrid materials and the gold nanoparticles. The presence of horseradish peroxidase was observed to cause an improvement in electrobiocatalysis performance of the novel hybrid interface structure.

This study has thus set the stage for the incorporation of nanostructured dual 2D hybrid materials as electrocatalytic interface materials in the design and fabrication of novel smart and highly sensitive bioelectronics, bioreactors and biosensing devices.

For future work, it is suggested that the 2D materials should be functionalized for the betterment of biosensor applications. Similarly, this developed dual 2D hybrid interface materials may be incorporated in the fabrication of sensors for environmental pollutants in air, soil and water. The resulting fabricated platform could be modified for specificity in detecting either organic or metallic pollutants.